1 Introduction

There are two key methods of generating short pulses of laser light: mode-locking and Q-switching. While mode-locking generates extremely short pulses, between femto- and pico-second durations, the pulse energy for the simplest systems tends to be of the order of tens of nanojoules. In contrast, Q-switched devices generate longer pulses, in the hundreds of pico- to nano-second regime, while delivering pulse energies in the micro- to milli-joule range. Mode-locked pulses are typically generated at repetition rates of tens of megahertz, and Q-switched pulses from single shot to tens of kilohertz.

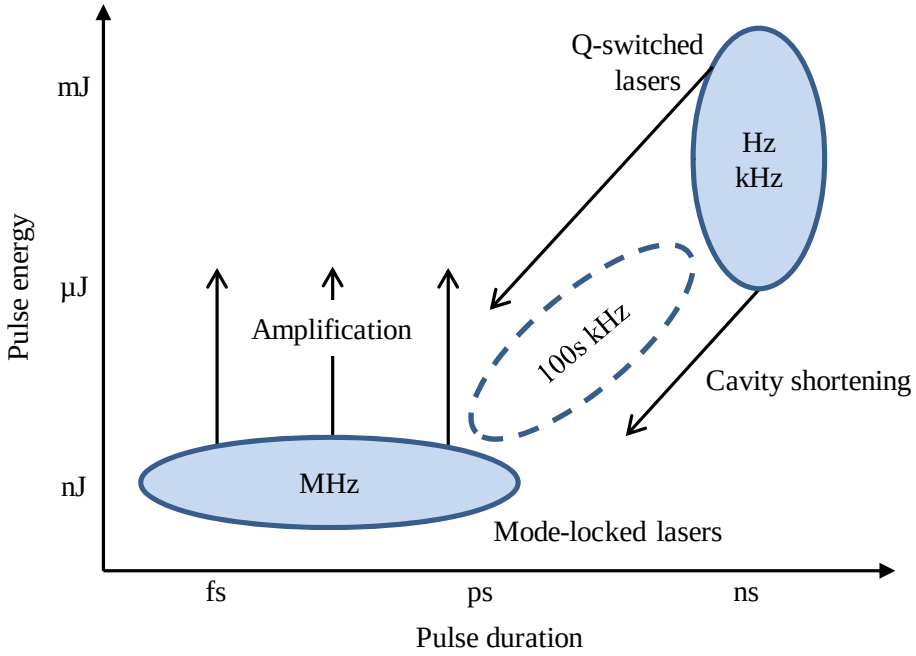

Figure 1.1: Pulse durations and pulse energies of typical mode-locked and Q-switched systems.

As depicted in Figure 1.1, there is a gap between the basic embodiments of these two technologies for a laser that delivers pulses of tens of picoseconds, with microjoule energy. In this chapter we highlight a selection of applications that need lasers that perform in this regime, and discuss laser systems that currently approach this region of operation.

1.1 Applications

We identify three separate application areas that are defined by their requirements from a laser pulse. They are: non-linear processes requiring high peak intensity, time-resolved applications requiring short pulses at either controllable or low repetition rates, and material processing requiring short pulses and high pulse energy. The additional factors of cost and space constraints are of constant consideration to applications in all three of these areas, especially the highly commercialised area of material processing.

A key non-linear laser process that would benefit from a laser source occupying the gap in Figure 1.1 is coherent anti-Stokes Raman spectroscopy (CARS) [1-4]. CARS requires two laser pulses as pump and Stokes sources, with the anti-Stokes signal

generated when the Stokes shift coincides with a Raman-active mode in the target species. This can potentially provide excellent contrast against non-resonant background substances in cases where other invasive contrast enhancement methods are undesirable. An example application of CARS, used to track the diffusion of oil through a skin sample, is shown in Figure 1.2.

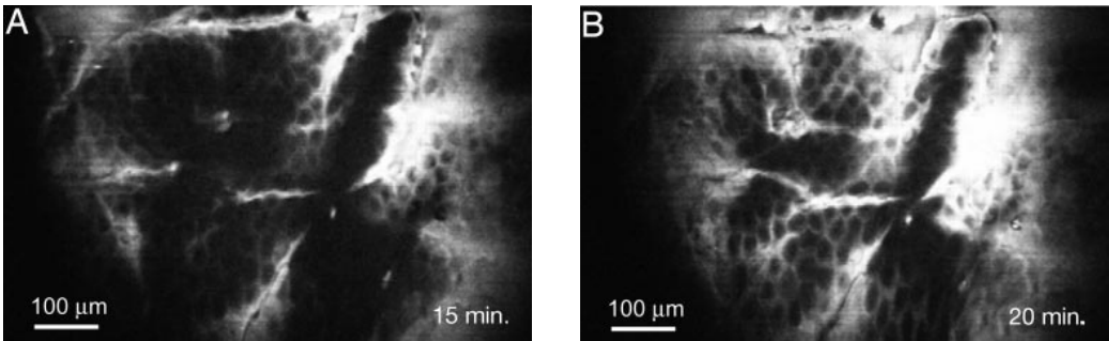

Figure 1.2: *In vivo* CARS images of oil diffusing through a sample of skin (a) 15 minutes after application and (b) 20 minutes after application. From [5].

The intensity of the CARS signal is nonlinearly dependent on the incident beam intensities, $I_{CARS} \sim I_p{}^2 I_{Stokes}$, and so short pulsed sources are used to deliver high intensities with low pulse energy to avoid thermal damage to the sample. While femtosecond pulses can lead to the lowest incident energy, the large bandwidth of femtosecond pulses can exceed the bandwidth of the Raman resonance, reducing the CARS signal and compromising the contrast [2, 6]. In fact, pulse durations between 2 and 7 ps are optimal to match the typical bandwidth of the resonances [2]. A summary of the desired laser properties for CARS is given in [2]. Ideally, excitation lasers with small footprints are desired for this application since an attractive prospect for CARS is its incorporation into portable field-kits for extra-laboratory substance identification.

Supercontinuum (SC) generation is another non-linear process that requires high intensities for maximum efficacy. In SC generation the pump radiation is spectrally broadened via non-linear processes to generate a high power, broadband white-light, as shown in Figure 1.3. It is most commonly demonstrated in photonic crystal fibres that have high $\chi^{(3)}$ non-linearities and controlled dispersion characteristics [7].

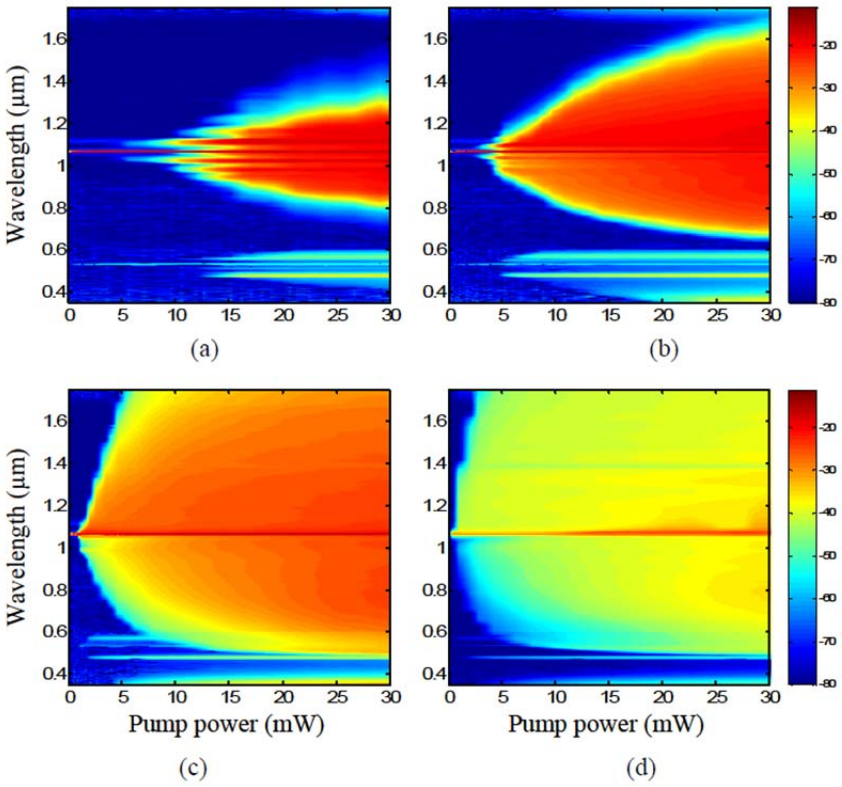

Figure 1.3: Broadband supercontinuum generation from a 600 ps 1064 nm Q-switched laser source after propagation through (a) 1 m, (b) 3 m, (c) 20 m and (d) 100 m of photonic crystal fibre. Colour scale is in dBm/5 nm bandwidth. From [8].

In the femtosecond regime, SC generation occurs through self-phase modulation, whereas in the picosecond regime it is caused by Raman scattering and four-wave mixing [9]. The pulse durations commonly used in SC generation experiments span from femtoseconds to nanoseconds [10, 11], and even high-power CW [12], and the suitability of picosecond Q-switched lasers to SC generation has been successfully demonstrated [8, 13, 14]. For more details of SC generation and its laser requirements, see [15].

Time-of-flight (TOF) distance ranging using pulsed laser sources is an application that would benefit greatly from an inexpensive, compact short-pulse laser source [16]. Laser range finding using the TOF approach simply measures time taken for a pulse of laser light to cover the round-trip distance to the target and can be used over long distance, of the order of 10s of km, and over shorter distances to perform accurate surface scans of sample materials [17]. A common recent use of these lasers is

in automotive cruise control systems, to determine and maintain a safe distance from other vehicles. This particular application has a common requirement for TOF laser sources to be eye-safe [18]. The accuracy of TOF distance measurements depends directly on the laser pulse duration [13, 19]. In high resolution, surface scanning applications the pulse duration is required to be in the picosecond range to give micrometre resolutions, although in these ranges the bandwidth of the detectors and analysis electronics start to pose limitations. Picosecond pulsed sources are also desirable compared to nanosecond sources to satisfy the eye-safe condition since, for high-speed measurement, high pulse repetition rate is required and picosecond pulses can maintain high intensity (for good signal-noise ratio) while reducing the pulse energy and time-averaged power. To reach the right balance between eye safety, accuracy and high speed imaging, an ideal solution would be a picosecond source with a controllable pulse repetition frequency.

TOF distance measuring is an application where laser compactness and portability are key factors. The incorporation of these devices into aircraft, cars and standalone units that are portable by humans requires that they are small and have low power requirements. A particular design that has been successfully demonstrated in this field and is extremely compact, robust and inexpensive is the Q-switched microchip laser [13, 18, 20].

Fluorescence lifetime measurements, and by extension time-resolved fluorescence imaging, of materials can only be achieved using pulses of light with duration shorter than the fluorescence lifetime, and of sufficient fluence to cause substantial upper level population of the sample. For many biological and semiconductor materials the fluorescence lifetime is in the nanosecond range, requiring picosecond-or-faster sources for effective fluorescence measurement [21, 22]. Fluorescence imaging is possible through raster scanning, with a false colour image of the sample generated indicating the fluorescence lifetime measured for the particular pixel. Provided that a laser source with sub-ns pulses is used, *in vivo* fluorescence imaging is possible, allowing functional observation of biological processes [23, 24].

For bulk sheet metal processing, non-laser processes such as inert gas shielding and flame cutting can reliably and efficiently give millimetre accuracy. In cases where

greater machining accuracy is required, laser micromachining is an effective option. The key considerations for laser sources used in the material processing industry are the rates at which they can modify the material, the quality of the finish they leave on the material and their cost and reliability. Currently, the majority of metal processing by laser is carried out using nanosecond pulses from Q-switched lasers, or high-power CW lasers, and although better than the non-laser processes, they can still leave considerable debris in the machined area. This is due to material modification outside the area of laser focus being caused by a thermally-driven process arising from energy deposition in the material. To achieve clean, accurate modification of the material, it is desirable to perform laser ablation in a fluence regime where damage through heat transfer by diffusion to the area surrounding the target is prevented [25].

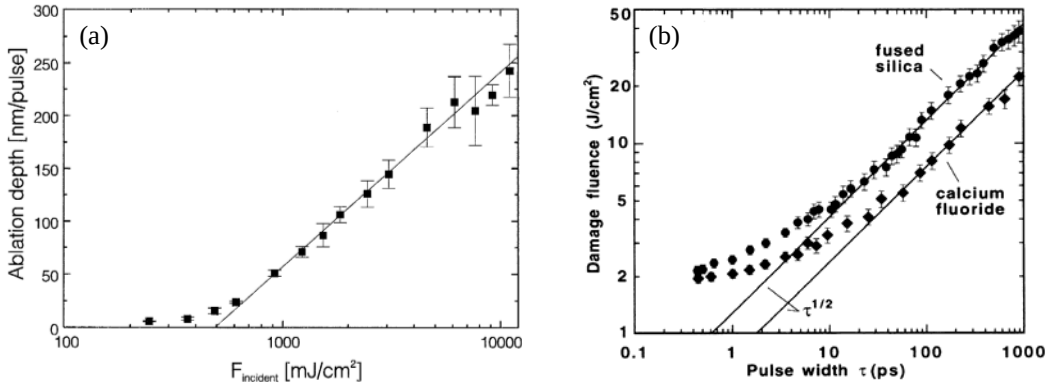

Figure 1.4: Plots showing the thermal diffusion regimes (straight lines) for machining (a) copper with 150 fs pulses [26], and (b) fused silica and calcium fluoride dielectrics with varying pulse durations [27].

The ablation threshold of materials drops as pulse duration is reduced, allowing effective machining at reduced fluences, thus minimising the spread of heat into the material [27-33]. For most materials, the thermal diffusion effects can be drastically reduced by using femtosecond or few-picosecond pulses, as seen in Figure 1.4, meaning that material ablation is tightly confined to the region of optical focus, rather than spreading over a wide area through heat transfer by electron diffusion [34]. Although not fully understood, the ablation process at short duration, low fluence pulses is thought to be a multi-photon ionisation effect, leading to inverse Bremsstrahlung heating and Coulombic explosion [35-39]. An example of where high speed, high accuracy machining is required is in the roll-to-roll manufacturing methods currently

employed in the thriving electronic display (LCD and LED) industry – a robust, inexpensive and high energy picosecond source would be hugely valuable in this sector.

The standard of machining afforded by nanosecond and CW lasers is acceptable for many requirements of material processing, especially in view of their economical affordability. However, for effective, clean and accurate machining in the non-thermal regime, picosecond to femtosecond pulses are required with microjoule-scale energies and the industry would benefit greatly from an economical and robust low-picosecond source. Excellent summaries of material processing with laser pulses are given in [25, 40, 41].

1.2 Current pulsed sources

A trend for the applications discussed in the previous section is a requirement for pulses with short duration, picosecond or lower, and energies in the high nanojoule to microjoule range. For the applications discussed, there currently exist laser solutions that are suitable but perhaps not ideally fulfilling the requirements. We now discuss laser systems in light of their suitability for short, high energy pulse generation.

By far the most common method of generating sub-nanosecond pulses is through mode-locking, a process that provides trains of short pulses. From the discovery in 1966 of Q-switched mode-locking [42], through the development to CW mode-locking by first dye saturable absorber [43], Kerr-lens mode-locking [44], and semiconductor saturable absorber mirror (SESAM) [45], mode-locked pulses have set all the records for shortest pulse duration from an oscillator. Without utilising additional compression techniques, the shortest pulses of light ever achieved were 5.8 fs long from a SESAM-assisted, Kerr lens mode-locked Ti:Sapphire laser [46]. In terms of the pulse durations required by the above applications, this is perhaps extreme but by using various mode-locking techniques and cavity designs, solid-state mode-locked lasers have the ability to generate a wide range of pulse durations from femtoseconds to picoseconds.

Mode-locked pulses are created from the preferential propagation of a high intensity short pulse in a laser oscillator, requiring a suitable non-linear loss mechanism

[47, 48]. For picosecond pulse generation this non-linear loss is provided by a saturable absorber, such as from dyes or more recently SESAMs, but for shorter femtosecond pulses the Kerr-lens non-linearity [49, 50], is necessary for its high speed response. The single intracavity pulse generates an output pulse train with a pulse repetition rate equal to the inverse of the round-trip period, of the order of 100 MHz for metre-long cavities. Mode-locking typically generates low pulse energies owing to the high repetition rate of conventional lasers. Typical mode-locked pulse energies are only in the tens of nanojoule range, preventing direct use in the applications mentioned in the previous section. It wasn't until 2003, nearly 40 years after mode-locking was discovered, that mode-locked pulse energies over the 1 µJ barrier were generated directly from an oscillator [51], with thin disk architectures allowing impressive power scaling [52]. Before discussing the technology that enables higher pulse energy oscillators, we will cover the various amplification schemes applicable to conventional mode-locked oscillators.

The maximum repetition rate of an amplifier is determined by the rate at which the gain medium can be pumped to a high inversion. Q-switched pump pulses can be used to rapidly invert the gain medium, with repetition rate then set by that of the pump laser (normally kHz); for gain media with long upper-state lifetimes CW pumping can also be used. Where amplifier gains are low, very many passes through an amplifier crystal are required to achieve the desired amplification: a common way to achieve this is a regenerative amplifier where the pulse makes many round-trips through the same gain medium inside a cavity, the duration of confinement of the pulse within the amplifier being controlled by a Pockels cell.

A regenerative amplifier arrangement is shown in Figure 1.5. The amplifier cavity is defined by the pump-input mirror in the bottom right-hand corner and the HR mirror just above it. Pulses from a high-repetition rate mode locked oscillator are switched into the amplifier cavity at an appropriately reduced repetition rate, and the amplified pulse is switched out once the amplifier gain has been depleted. The cavity serves to ensure that the transverse profile of the pulse is preserved.

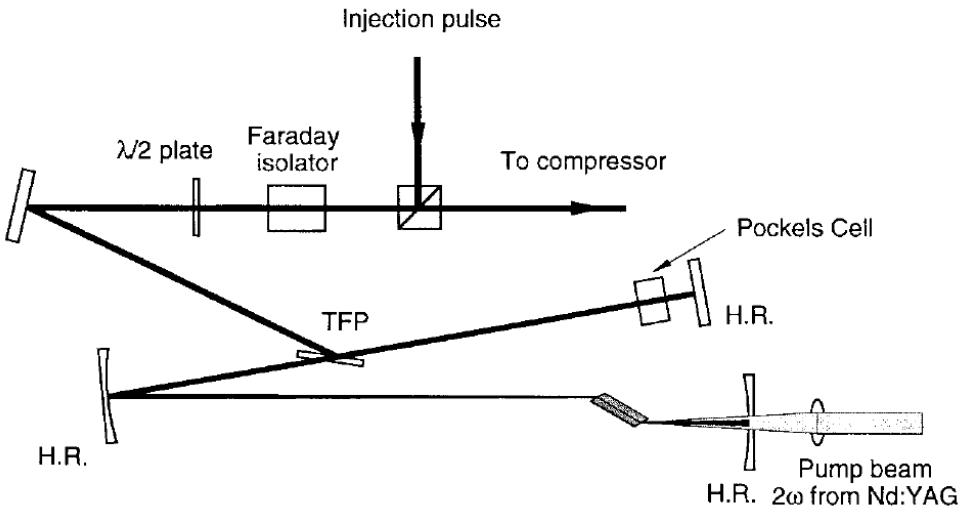

Figure 1.5: A schematic of a typical regenerative amplifier design. From [25].

A few examples of early regeneratively amplified mode-locked systems achieved pulses of a few picoseconds duration at hertz to kilohertz repetition rates (CW and Q-switched pumped) and with microjoule to millijoule pulse energies [53, 54]. The output of these amplified mode-locked systems is heavily dependent on both oscillator and amplifier designs, meaning that the range of final characteristics achievable by such systems is extremely large.

In contrast to the multi-pass approach of the regenerative amplifier, doped optical fibres have sufficient length to provide high-gain amplification in a single pass [55-57]. Substantial issues that are inherent in high-gain devices are amplified stimulated emission (ASE) and parasitic lasing from reflection at the fibre input and output. The latter can be prevented through modification of the fibre input and output faces, although ASE remains a problem with few solutions, limiting the maximum gain achievable. For femtosecond pulse amplification, the fibre dopant must have comparable bandwidth to the pulse, achievable in ytterbium, erbium and neodymium-doped fibres [58, 59]. In addition, as discussed for supercontinuum generation, non-linear effects in the fibre can cause distortion and modification of the spectral and temporal profiles of the pulse at high intensities.

A design exists for mode-locked oscillators that generate high energy pulses directly from the oscillator. By dramatically increasing the cavity length, through employment of such geometries as a Heriott cell [60] one can lower the pulse repetition

rate, and increase the pulse energy. To avoid excessive non-linear effects in the cavity at such increased energies, the cavity is left with a small amount of dispersion resulting in a chirping of the intracavity pulse; these systems are thus known as chirped pulse oscillators. This technique has been applied to standard Ti:Sapphire lasers [61], but is particularly useful for more scalable geometries based on the thin disk laser concept [62].

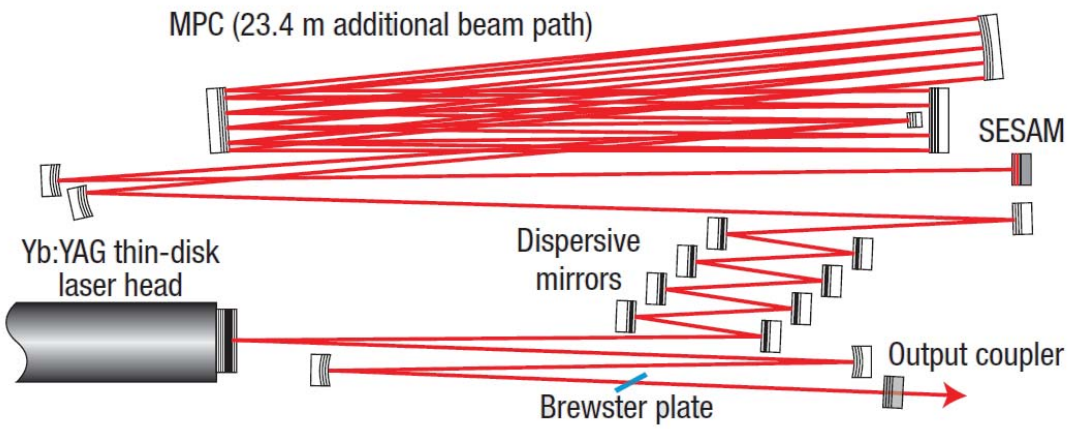

Figure 1.6: A thin-disk mode-locked laser. From [62].

In Figure 1.6 a thin-disk cavity is demonstrated, including an additional 23 m of folded beam path [62]. This approach drops the repetition rate from typical values of around 100 MHz to just a few 10s of MHz, allowing an extra order of magnitude of inter-pulse pumping of the Yb:YAG gain medium. Pulse energies in the microjoule range have been demonstrated in these thin-disk oscillators [52, 63-65], and although they are not comparable to those achievable from the amplification processes already discussed, this novel technique is simpler and more compact and can provide pulses suitable for most of the applications discussed. However, in wider terms, thin-disk oscillators with folded cavity geometries can still be considered bulky and expensive solutions.

Since the demonstration of short-cavity microchip lasers in 1989 [66], the possibility of using a Q-switched laser to generate sub-ns pulses has been investigated and demonstrated [67-72]. Compared to the mode-locked examples above, these solid-state, diode-pumped devices are by design extremely compact and simple, but also very cheap. Typical cavity lengths (≤ 2 mm) are sufficiently short to sustain just a single

longitudinal mode, resulting in single frequency output. These miniature oscillators represent the focus of this thesis and are covered in detail in the next chapter, but we present a brief summary here of their capability in terms of pulse duration and energy scaling. A typical Q-switched microchip laser design is shown in Figure 1.7 for comparison with the mode-locked designs in Figure 1.5 and Figure 1.6.

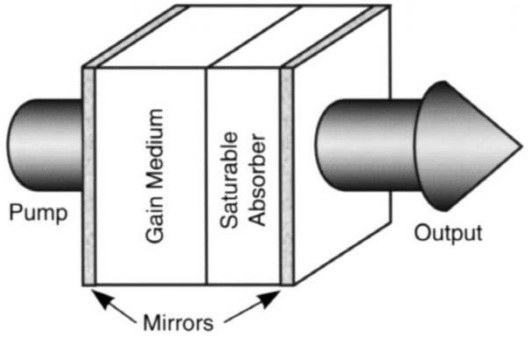

Figure 1.7: A schematic of a Q-switched microchip laser cavity, with a bulk solid-state saturable absorber as Q-switch, from [13].

The shortest pulses generated by a Q-switched microchip laser are reported by Spühler *et al.* to be 37 ps [69], achieved by using a SESAM as the cavity Q-switch. Other Q-switching approaches use active devices such as an electro-optic coupled cavity [71, 73], but the passive Q-switching approach, either by SESAM or crystalline saturable absorber, is by far the most common. Microchip oscillators produce pulse energies in the tens-of-nanojoule to microjoule range. By utilising diode-pumped fibre amplifiers, the pulse energies are boosted to the millijoule regime, suitable, for example, for micromachining applications [40, 74-76].

Initial research into extra-cavity compression of Q-switched microchip laser pulses has been carried out by two groups. Mok *et al.* observed a twelve-fold compression of a 580 ps pulse to 45 ps by soliton effect compression in a fibre Bragg-grating [77], while Steinemtz *et al.* more recently compressed 100 ps pulses to 6 ps using a fibre amplifier to first spectrally broaden and chirp the pulse before compressing it with a grating compressor [78].

Intra-cavity pulse compression in Q-switched microchip lasers through stimulated Raman scattering (SRS) has also been observed [79, 80], and pulse compression factors of 4 times have been demonstrated. The high peak powers resulting

from this process demand that components with high damage thresholds be used, which prevents the use of semiconductor Q-switches.

1.3 Summary

Even though we have outlined some specific applications where picosecond pulses are either necessary or highly desirable, there are many more applications, particularly in high-speed imaging and microscopy, where inexpensive picosecond sources are desirable. Currently, laser requirements restrict many of these applications to specialist laboratory settings as the laser sources are large, expensive and require significant laser knowledge to maintain and operate. In particular, amplified mode-locked systems are not well suited for long-term use in the discussed applications outside of a laboratory setting. The footprint of mode-locked lasers, including cooling, pump sources, oscillator, pulse picker and amplifier are typically of the order of a few square metres, particularly in the case of long-cavity oscillators for high pulse energy generation.

In tandem with the complexity of mode-locked lasers comes a substantial price tag. A complete amplifier and oscillator set that generates microjoule, picosecond pulses can easily cost upwards of AU$100 000. For many applications this cost is prohibitive, forcing users to opt for cheaper, less capable options. A key example is the laser materials processing industry: Q-switched and CW lasers currently perform the job well enough, but ready access to short, high energy pulses would enable exact, accurate machining to become more widely available.

In comparison to mode-locked systems, Q-switched microchip lasers are an outwardly less complex, and therefore cheaper, alternative, and have the potential to be packaged into extremely small, portable units. Provided that their typically longer pulse durations can be scaled to the low-end of the picosecond range, ideally sub-10 ps, Q-switched microchip lasers represent a very viable alternative to mode-locked lasers. A thorough analysis of microchip laser technology and the current state of the art is presented in the following chapter.

2 SESAM Q-Switched Microchip Lasers

2.1 Q-Switching

As described in Section 1.2, there are two methods of producing pulses of light from a laser. Mode-locked lasers generate pulses of the order of picosecond to femtosecond duration at rates of tens of megahertz, while Q-switched lasers produce pulses with durations in the nanosecond to picosecond range at repetition rates of megahertz to hertz. Each process is enabled by the incorporation of an intra-cavity device that modulates the intra-cavity intensity and while the mode-locking process and its benefits and limitations are described briefly in 1.2, the Q-switching method is more suited to generating picosecond, microjoule pulses of light with reduced complexity.

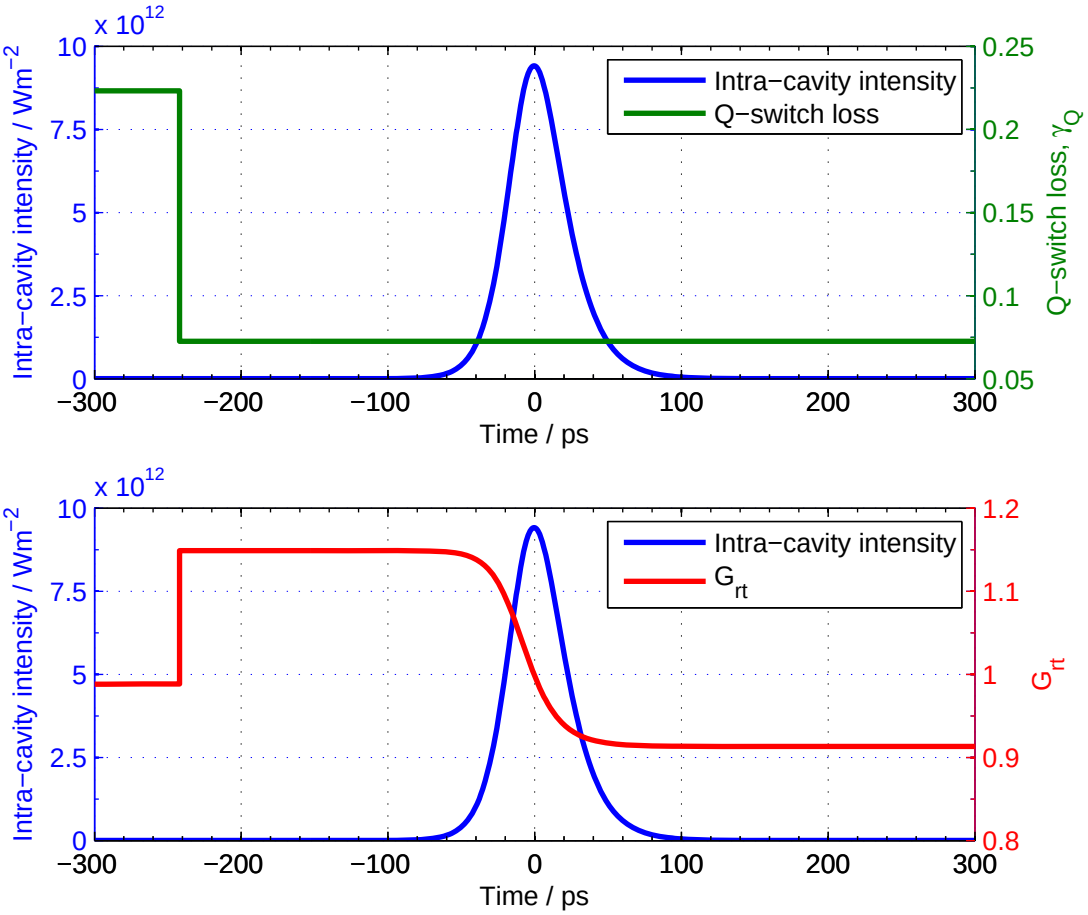

Figure 2.1: A typical profile in time of a pulse from an actively Q-switched laser, showing the evolution of intra-cavity intensity in reference to the Q-switch loss (top) and resulting net round-trip gain coefficient (bottom).

In practice, Q-switching is achieved by introducing a time-varying loss mechanism into the laser resonator cavity that in its high-loss state inhibits the laser action, allowing the inversion to build to a high level before switching to its low-loss state. The two implementations that enable the loss modulation are active Q-switching and passive Q-switching. The former involves the use of an intra-cavity Q-switch device, the loss properties of which are externally controlled and are independent of the laser behaviour. The latter also requires the insertion of an intra-cavity element, although its loss properties are dictated solely by the state of the laser field within the cavity. Active Q-switching offers complete control over repetition rate and pulse energy, although the controlling architecture is often complex, bulky and can involve high voltages (> 2 kV). Passive Q-switching is considerably more simple, although the

initial choice of device and control over its characteristics can be difficult to tailor to the desired application.

Figure 2.1 shows the stages of the active Q-switching process:

- The laser is pumped with the Q-switch in its high-loss state and before the net round-trip gain, G_{rt}, reaches unity, the loss is withdrawn. The value of the net round-trip gain is pushed above unity by the switch and the stimulated emission of photons starts to overcome the cavity losses resulting in a net increase in cavity photon density.
- The cavity field builds up rapidly and starts to deplete the gain. The field reaches a peak as the net gain is reduced below unity, and then starts to decay while still further depleting the gain.
- Well after the pulse has died away, the Q-switch is reset to its high-loss state to suppress further lasing while the inversion population is re-pumped.

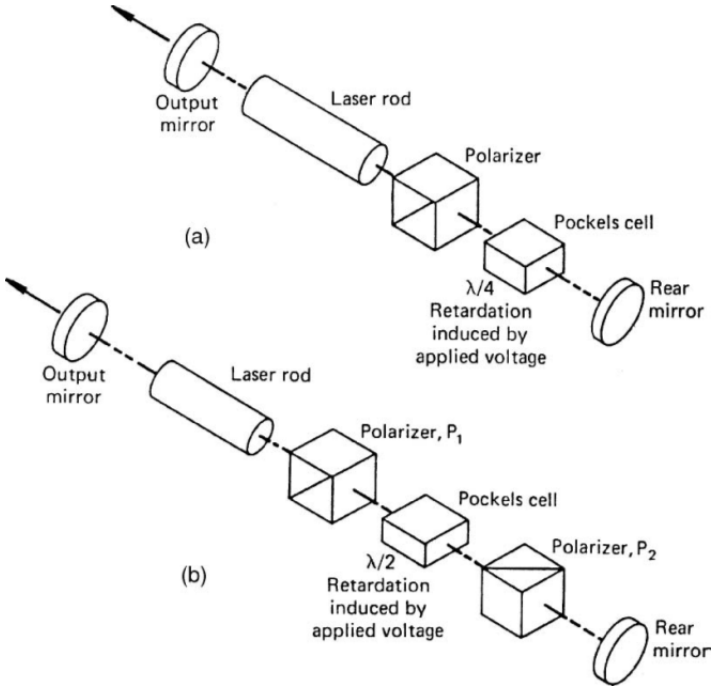

Figure 2.2: Electro-optic Q-switches in (a) $\lambda/4$ and (b) $\lambda/2$ retardation schemes, from [81].

There are a large number of ways to actively Q-switch a laser, ranging from mechanical devices that periodically block the flow of intra-cavity photons such as chopper wheels or spinning cavity end mirrors, to electro- and acousto-optical devices

that eject light from the cavity by more exotic means. A common electro-optic Q-switch design is depicted in Figure 2.2, where the presence of the active Q-switch device necessitates cavity elongation, rarely by less than 5 mm.

Passive Q-switches take the form of an intra-cavity element – a saturable absorber – that absorbs the laser radiation until it saturates and its contribution to the cavity loss is lessened. Whereas transmission-varying saturable absorbers are inserted into a cavity between the gain medium and a fixed reflectivity end mirror, reflectivity-varying saturable absorber mirrors (SAMs) are incorporated into the cavity by replacing one of the constant-reflectivity end mirrors. The most common SAMs are semiconductor saturable absorber mirrors, or SESAMs. Typical Q-switched cavities employing a saturable absorber or a SESAM are shown in Figure 2.3.

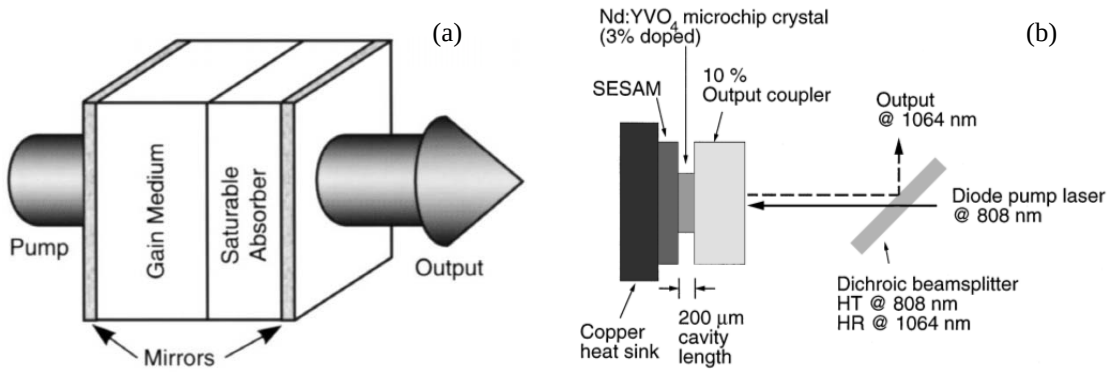

Figure 2.3: Microchip laser designs incorporating (a) saturable absorber (from [13]) and (b) SESAM (from [69]) passive Q-switches.

Passive Q-switches, whether bulk saturable absorber or SESAM, share common properties that govern their behaviour when used in a laser design. Each has a high-loss state (low-T and low-R respectively) and a low-loss state (high-T, high-R), the difference between which is known as the modulation depth, ΔT or ΔR. Technically, it is the transmission of an absorber layer within the SESAM structure that increases when saturated, although the net response of the SESAM unit is that of an apparent increase in reflectivity and this is the treatment given in most design and modelling considerations.

The parameters that describe absorber saturation and relaxation behaviour are also analogous between the two. Saturation of the passive Q-switch absorption occurs

through excitation of the absorber elements – ions or molecules in saturable absorbers and charge carriers in semiconductor devices – to less absorbing excited states. The absorber elements decay from these excited states according to an exponential time constant, τ_A (later referred to as τ_{SESAM} for SESAMs). A saturation fluence, F_{SAT} is defined as the incident pulse fluence required to reduce the saturable absorption to e^{-1} of its original value, provided the pulse duration is much shorter than τ_A. In the case where the pulse duration is much longer than τ_A, it is useful to define:

$$I_{SAT} = \frac{F_{SAT}}{\tau_A} \tag{2.1}$$

which describes the CW intensity required to maintain a saturation of e^{-1} in the absorber. In the case where the absorber relaxation timescale is similar to that of the pulse duration, i.e. the absorber relaxation directly affects the pulse formation, a more complex approach is required to calculate the instantaneous absorption state. This is achieved later in Section 3.2 by defining an “effective fluence” that tracks the history of incident fluence while also accounting for the relaxation of the absorber elements.

As already mentioned, a passive Q-switch differs from an active Q-switch in that its loss state is dictated by the history of the intra-cavity intensity, rather than by external modulation. Although the control mechanisms are completely different, the passive process, depicted in Figure 2.4, can produce an almost identical pulse to that generated by the active Q-switch demonstrated in Figure 2.1.

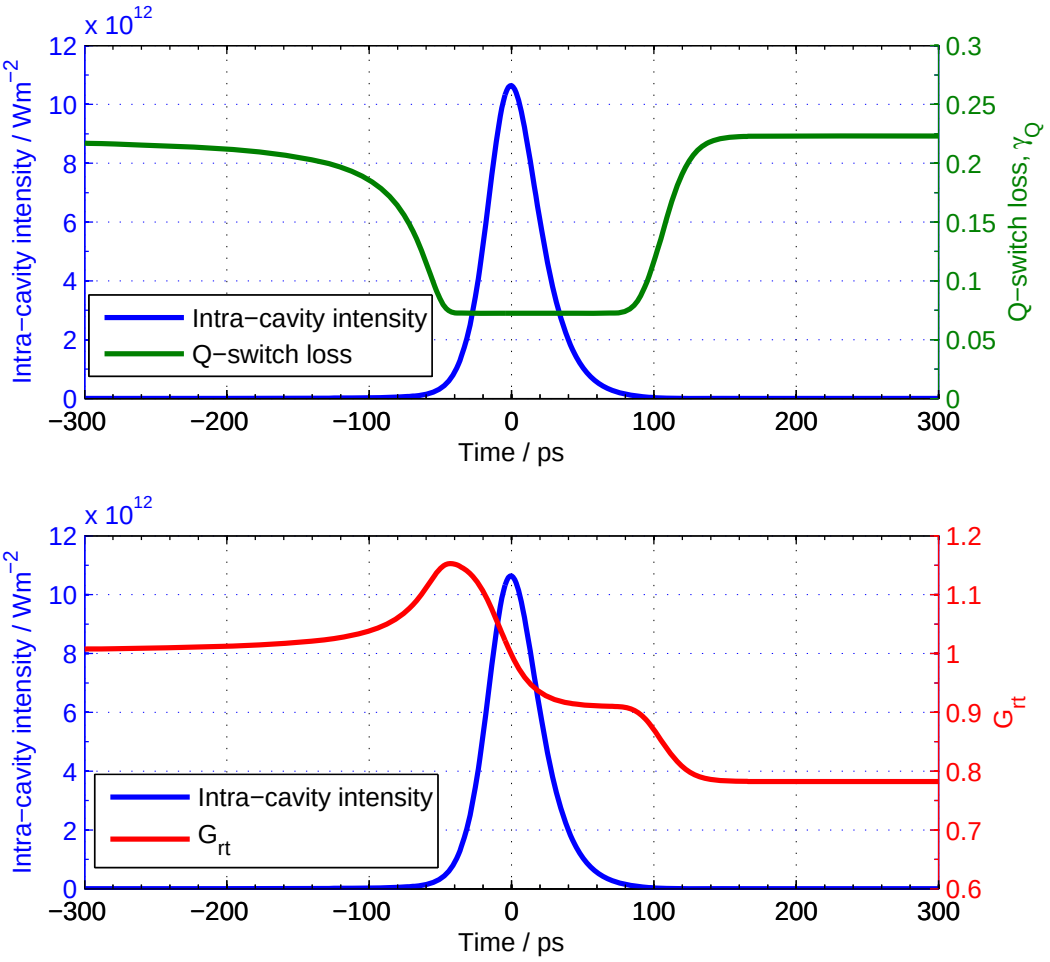

Figure 2.4: A pulse from a passively Q-switched laser, showing the evolution of intra-cavity intensity in reference to the Q-switch loss (top) and resulting net round-trip gain coefficient (bottom).

The Q-switching process demonstrated in Figure 2.4 is typical of a passive Q-switch and describes the dynamics clearly:

- At a time before the main body of the pulse (~ 10 ns in this example), the inversion population density reaches the inversion threshold value set by the high-loss state of the Q-switch and G_{rt} exceeds unity.
- The rate of photons contributed to the cavity by stimulated emission starts to grow as the round-trip gain overcomes the round-trip losses. Once the intra-cavity intensity incident on the Q-switch approaches I_{SAT}, the photon field starts to slightly bleach the absorber, lowering its loss and causing the net round-trip gain coefficient to increase.

- The cavity photon population rises even faster as the net gain is increased by the reduced cavity loss. The saturation of the Q-switch increases further, creating an avalanche effect.
- Once the passive Q-switch has absorbed enough energy to become completely saturated and reached its low-loss state, evidenced by the peak in G_{rt}, the maximum gain is made available to the cavity photons.
- As with the active Q-switch, the field reaches a peak as the gain coefficient is reduced below unity, and then starts to decay while further depleting the gain.
- When the intra-cavity intensity becomes insufficient to sustain the low-loss (saturated) state of the Q-switch, the absorber reverts to its high-loss (unsaturated) state.

An important difference between actively and passively Q-switched lasers is their behaviour under different pump powers. It is possible to increase the pulse energy and decrease the pulse duration of an actively Q-switched laser by lowering the Q-switch repetition rate or increasing the incident pump power. When the pump power is increased in a passively Q-switched laser, the pulse energy and duration are maintained while the repetition rate and average output power increase correspondingly.

While the actively and passively Q-switched lasers already described are quite common, the use of combinations of Q-switches, providing a double-switching effect, has also been demonstrated. Both active-passive [82-84], and passive-passive [85], pairings have been employed to increase pulse energy and reduce pulse duration by shaping the passively Q-switched pulse. In Section 3.7 the asymmetry of a passively Q-switched pulse is discussed further, but the basic intention of double-Q-switching is to enhance the effective modulation depth of the net Q-switch effect to release a greater proportion of the inversion density during the pulse, shortening the pulse and increasing the amount of energy released.

2.2 Passive Q-switches – bulk saturable absorbers

The saturable absorber style of Q-switch typically takes the form of a slab of doped crystalline laser material or an organic dye cell, although the latter has declined

in popularity in favour of the former owing to dye degradation with time. By far the most common of these used in solid-state lasers is chromium-doped yttrium aluminium garnet, or Cr^{4+}:YAG [86].

In simple terms, the chromium ions absorb the laser radiation (in the 850 – 1200 nm range [87]) and transition from the ground state to an excited state. Ground state absorption far outweighs excited state absorption (ESA) in Cr^{4+}:YAG , but even in its saturated state, Cr^{4+}:YAG will not reach 100% transmission due to excited state absorption of the laser radiation [88, 89]. This loss is non-saturable since the decay from the ESA end states is very fast. The unsaturated and saturated transmissions of the saturable absorber, and hence the modulation depth, can be tailored to meet particular Q-switching applications by altering the thickness of the saturable absorber and its doping levels.

Other crystalline saturable absorber materials exist that work on the same principles and are more suitable for use at longer wavelengths. For example, V^{3+}:YAG [85, 90-93], V^{3+}:LuAG [94], and Co:LMA [85, 95] are used in lasers that operate on the 1.34 µm and 1.44 µm transitions of Nd-doped materials and Cr^{2+}:$Cd_{0.55}Mn_{0.45}Te$ and Co^{2+}:spinel can be used between 1030 nm and 1660 nm [96-100]. A comprehensive review of a wide range of saturable absorber crystals can be found in [101]. Crystalline saturable absorbers are well understood devices and highly configurable that, combined with their high damage thresholds and high heat dissipation ratings, makes them candidates for most Q-switching applications.

Since the YAG hosting structure is common to both Cr^{4+}:YAG saturable absorbers and YAG-based laser materials, it is possible to co-dope a single slab of YAG with both absorber ions and laser gain ions to produce a self-Q-switching, monolithic laser. Such examples are Cr,Nd:YAG [102, 103], and Cr,Yb:YAG [104, 105], which produce simple, monolithic Q-switched lasers with high damage thresholds at low cost. Unfortunately, the attainable level of Cr-doping in each, and hence the modulation depth of the Q-switch, is limited since increasing the Cr^{4+} concentration introduces more defects in crystalline Cr,Nd:YAG and increases fluorescence quenching effects in Cr,Yb:YAG [67].

Semiconductor materials have also been successfully used as passive Q-switches, both in a simple form [82, 106], and as quantum well structures [107-109]. Both approaches behave very much the same as the crystalline saturable absorbers already mentioned although the latter affords extra control over transmission properties and absorber relaxation time. In addition, carbon nanotubes, quantum dots and graphene have been used as saturable absorbers in mode-locking [110-115], and Q-switching [111, 116, 117], although these technologies have so far not been demonstrated generating ultrashort Q-switched pulses.

2.3 Passive Q-switches – SESAMs

Invented in the early 1990s, semiconductor saturable absorber mirrors (SESAMs) were primarily used to initiate and sustain mode-locking in solid-state lasers [45, 118, 119], and later as passive Q-switches [120-122]. In each case they provide a modulation of the net gain within the laser cavity; in mode-locking to initiate the mode-locking action by enabling the preferential propagation of a high intensity pulse and in Q-switching to form the pulse itself. As described above they can be treated simply as devices that change their reflectivity based on the fluence through the face of the SESAM, although the construction and design needed to achieve this effect are non-trivial. Their optical properties and responses are widely selectable through design of the SESAM structure and choice of semiconductor materials, making them suitable for both mode-locking and Q-switching throughout the NIR range.

The structure of a typical SESAM design used for Q-switching is shown in Figure 2.5. The three main components are the high-reflectivity Bragg mirror, the saturable absorber layer and a partially reflecting second Bragg mirror, or top reflector. Although the bottom Bragg mirror is usually designed simply to provide high-reflectivity at the central operating wavelength, changing the parameters of the other two components offers a large degree of control over the overall performance of the SESAM. The absorber layer consists of a series of quantum wells positioned in relation to the nodes of the standing-wave pattern created in the SESAM. Transparent spacer layers are included to adjust the quantum well position and control the overall thickness (d in Figure 2.5) of the absorber layer, but also, significantly, to control the thickness of

the etalon formed between reflectors. The reflectivity of the top reflector can range from high reflectivity to anti-reflective depending on the requirements of the SESAM.

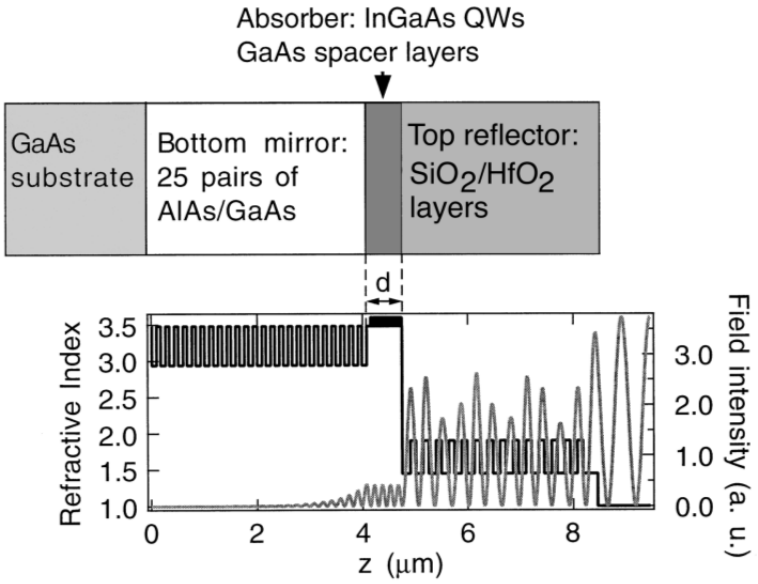

Figure 2.5: A typical SESAM structure showing bottom Bragg reflector, absorber layer and top reflector. The standing wave field intensity within the structure is shown to penetrate only a few μm into the SESAM. From [69].

In SESAM design, each component of the SESAM has its own microscopic properties – details such as layer thickness, layer spacing and composite materials. In laser design, the important parameters of the SESAM are its macroscopic properties – the key performance characteristics that are determined by the microscopic component properties and dictate how the SESAM, and hence the laser, behave. These are: the modulation depth, ΔR; the saturation fluence, F_{SAT} and the absorber recovery time (or relaxation time) constant, τ_{SESAM}. In addition, a non-saturable loss, $A_{n\text{-}s}$, is defined that gives an upper limit to the reflectivity of the saturated SESAM, allowing an unsaturated SESAM reflectivity, $R_U = 1 - A_{n\text{-}s} - \Delta R$ to be inferred. Typical characteristics for a SESAM with $R_U = 80\%$, $\Delta R = 13\%$ and $A_{n\text{-}s} = 7\%$ are shown in Figure 2.6.

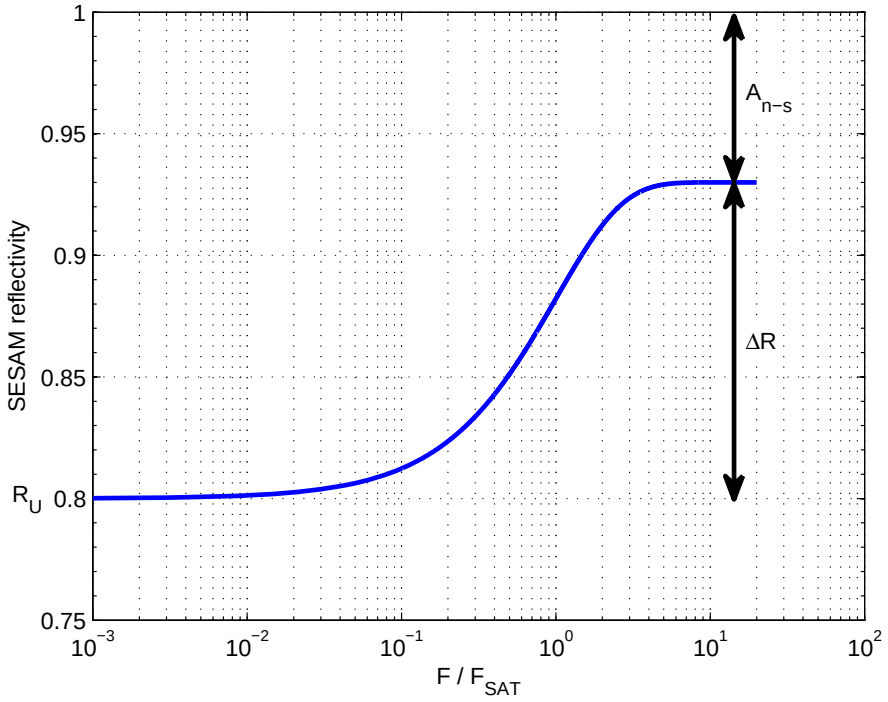

Figure 2.6: The reflectivity cycle of a SESAM as a function of instantaneous incident fluence.

It will be shown later in Sections 2.6 and 3.7 that in addition to requiring a short cavity, a large SESAM modulation depth, ΔR, is key to achieving short, high energy Q-switched pulses. Ideally, a modulation depth of 100% is desired although this is not realisable in practice due to limitations of the SESAM design. Crystal defects, introduced in the growing process to control the absorber relaxation time, as well as other mechanisms such as residual transmission through the bottom reflector and Auger recombination [123], prevent the SESAM from reaching 100% reflectivity as they result in an ever-present non-saturable absorption. In most SESAM designs, the reflectivity of the top reflector is > 0, preventing 100% absorption [124]. Ultimate control of ΔR within these limits is given to the number, material and placement of the quantum wells in the absorber structure.

It is a general rule that lower values of F_{SAT} are preferred to ensure Q-switch initiation and fast switching. The intensity incident on the SESAM in a mode-locked laser can be adjusted by changing the laser mode size on the SESAM [124], an option not available to short-cavity Q-switched lasers. The fixed mode size demands that F_{SAT}, or more precisely the saturation intensity $I_{SAT} = F_{SAT} / \tau_{SESAM}$, be low enough to ensure

the saturation of the absorber given the intra-cavity intensity of the laser, although this is shown later in Section 3.10 not to be a hard limit based simply on the CW level of the un-switched laser.

As with the modulation depth, the saturation fluence is influenced by the material, number and position (in relation to the nodes of the standing wave) of the absorber layers and by the field-enhancement effect of the etalon formed about the absorber by the two reflectors. Increasing the reflectivity of the top reflector in a resonant design increases field enhancement within the etalon and lowers F_{SAT}. Conversely, increasing the reflectivity of the top reflector in an anti-resonant design will suppress the field within the absorber and increase F_{SAT} [124-126]. Using resonant effects to lower F_{SAT} also increases the effective non-saturable loss of the SESAM (for high-reflectivity bottom reflectors) and limits its operational bandwidth, although this is not as important for single-frequency Q-switched lasers as it is for mode-locked lasers. The use of resonant and anti-resonant etalons in relation to apparent SESAM performance is covered in more detail in Sections 3.9 and 3.10.

From the discussion above, it is clear that long absorber recovery times are required to minimise saturation intensity. Slow recovery is also desirable to ensure that the SESAM stays switched for the duration of the Q-switched pulse although this is often fulfilled anyway since the intensity in the trailing edge of the pulse is more than sufficient to keep the SESAM saturated. Since this is the case, we make the point that a fast SESAM recovery time could truncate the trailing edge of a Q-switched pulse, assisting in short pulse generation, although final choice of τ_{SESAM} is dictated by its effect on I_{SAT}. The magnitude of τ_{SESAM} depends largely on the defects introduced during the SESAM growing process with higher growth temperatures producing fewer defects and hence longer electron trapping times [124, 125], as shown in Figure 2.7 (a).

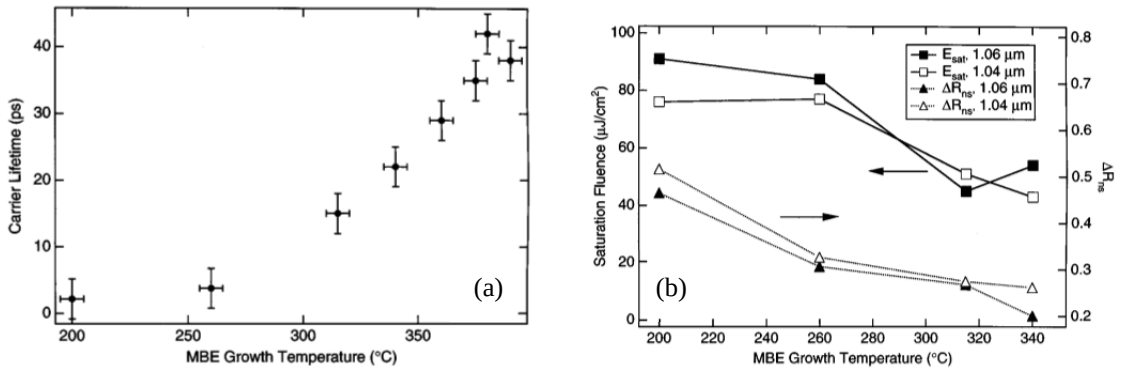

Figure 2.7: (a) The carrier lifetimes, or electron trapping times, of absorbers grown by molecular beam epitaxy at different temperatures. (b) The saturation fluence and non-saturable loss (right-hand axis, where $\Delta R_{ns} \equiv A_{n\text{-}s}$) of absorbers grown by molecular beam epitaxy at different temperatures. Both from [125].

Having fewer defects also has the benefit of decreasing the non-saturable loss, Figure 2.7 (b). However, there can exist a lattice mismatch between the spacer layer (GaAs) and quantum well (InGaAs) materials of the absorber that, under strain, can cause crosshatching leading to poor surface quality [69, 122, 125], and hence large, unwanted non-saturable losses. This imposes an upper limit on the thickness of the absorber that can be successfully grown, which in turn compromises the range of ΔR available. The thickness limit increases for lower growing temperatures meaning that while growing at high temperatures extends the SESAM recovery time and lowers non-saturable loss, consideration must be given to its effect on modulation depth.

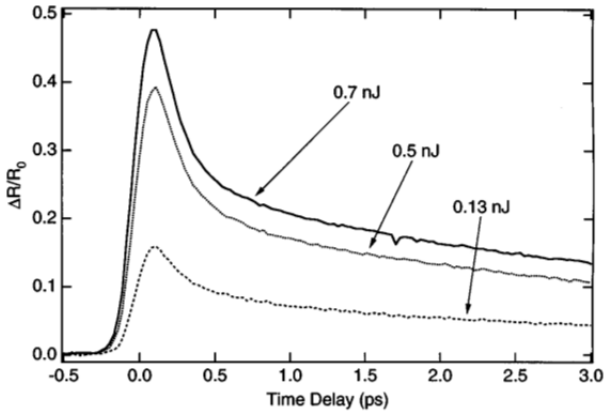

Figure 2.8: The reflectivity decay of a SESAM ($R_0 \equiv R_U$), measured for different pulse energies. From [125].

It is important to note that the carrier relaxation in SESAMs is due to both thermal relaxation and carrier recombination [124, 125, 127], so the relaxation rate

should strictly be described by two time constants. However, thermal relaxation happens on a scale of 100s of fs, compared to the ps scale of recombination, so is not appreciable on the 10-100s ps time scale of Q-switched pulses [128]. The two mechanisms are shown in Figure 2.8 with rapid thermal relaxation dominating up to ~ 0.3 ps before carrier recombination continues the relaxation process. The quoted relaxation time constant for SESAMs typically attempts to describe both relaxation mechanisms in one constant.

Designing a SESAM with particular parameters for a particular application is a non-trivial process. The interdependence of the macroscopic parameters on the microscopic properties means that many compromises and trade-offs must be considered. However, as a passive Q-switch, the SESAM remains extremely customisable with the added benefit of negligible contribution to the cavity length. SESAMs are commercially available through BATOP GmbH [129] and RefleKron Ltd [130], either as off-the-shelf units with preset operating characteristics or grown to specification. Comprehensive details of SESAM design, manufacture and implementation are given by the inventors, Keller *et al.* in [69, 122, 124-126].

2.4 Microchip lasers

The microchip laser represents the simplest interpretation of a laser oscillator [66]. A thin, solid-state gain medium is placed between two flat, plane-parallel mirrors and end-pumped through one of these mirrors with an appropriate source, typically a diode laser. The end mirrors (one high-reflector and one output coupler) are usually coated directly onto the gain medium but may be external, bulk-optic mirrors contacted directly with the gain medium faces, fulfilling the primary purpose of the microchip laser design – to provide as short a cavity as possible. In this case, the length of the laser cavity is equivalent to the length of the gain medium. A generally accepted definition of a microchip laser describes the cavity length as being less than 2 mm. A basic, CW microchip resonator is shown in Figure 2.9.

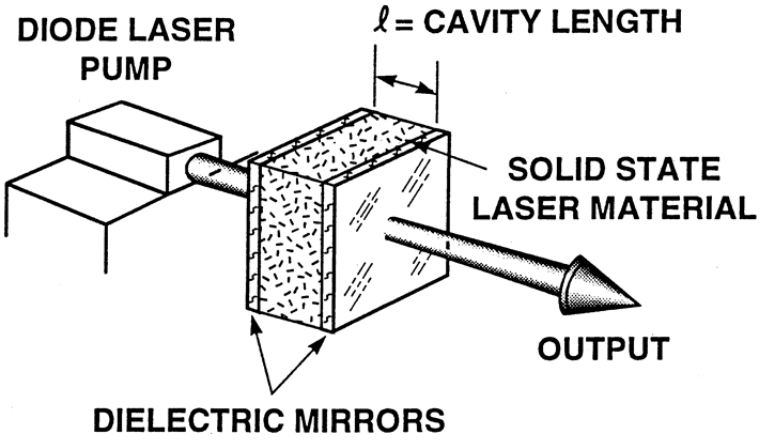

Figure 2.9: A basic CW microchip design. From [131].

As demonstrated in the literature and analytic models (both discussed later in this chapter), the short cavity is a key factor is generating short pulses from Q-switched lasers although an additional benefit of this is their potential to give a single-frequency output. The longitudinal mode spacing in a short cavity of length l_L and filled with a gain medium of refractive index n_{RI} according to $\Delta\nu = c/(2n_{RI}l_L)$, can exceed the bandwidth of the emission peak of the gain material, enabling single-mode, single-frequency operation. Single longitudinal mode operation, without additional intra-cavity elements, has been demonstrated in 5 mm, non-microchip Nd:YAG lasers [132, 133], although it is much more commonly found in microchip Nd:YAG lasers with cavities less than 2 mm long [66].

Owing to their simple, compact design, microchip lasers are well suited to wafer-like bulk manufacture methods. Once the desired cavity end mirrors have been coated onto a thin, large surface-area slab of gain material, the wafer can be diced to provide a large quantity of identical microchip laser units. Typical mode sizes in microchip lasers are less than 100 µm meaning that their planar dimensions rarely exceed a few mm, thus allowing tens to hundreds to be produced from a single centimetre-sized wafer. The suitability of microchip lasers to this batch process, near identical to silicon wafer processing methods, means that identical units with repeatable performance characteristics can be produced in large volume at low cost.

Shortening the laser resonator length imposes a limit on the thickness of the gain medium within, which can compromise the absorption of the diode pump light and the

overall optical-optical conversion efficiency of the laser. Once the length of the gain material drops below the material's absorption length, a likelihood for microchip lasers, efficiency decreases dramatically. Using a highly-absorptive gain medium to absorb as much of the incident pump light as possible can counter this, but only to a certain extent. By choosing to use a microchip design for the purpose of generating short, Q-switched pulses, the choice is also made to sacrifice laser efficiency.

Since their invention in 1989, microchip lasers have been demonstrated using a variety of solid-state gain media such as; Nd:YAG, Nd:YVO_4, Yb:YAG, Yb:LuAG, Nd:$GdYVO_4$ and Tm:Ho:$GdVO_4$ [66, 121, 134-139], and in a variety of active and passive Q-switching cavity configurations [68, 69, 72, 73, 100, 122, 126, 131, 140-142], with great success. The shortest Q-switched laser pulse ever emitted was reported by Spühler *et al.*, using a SESAM in a 185 µm microchip cavity to generate a pulse of just 37 ps duration.

2.5 Literature summary

Table 2.1 contains a summary of Q-switched lasers from the literature that generate sub-ns pulses, and these durations are represented graphically in Figure 2.10.

Author	Pulse duration / ps	Pulse Energy / µJ	Q-switch	Laser medium	Doping / at. %	Cavity length / mm
Spühler *et al.* [69]	37	0.053	SESAM	Nd:YVO_4	3	0.185
Nodop *et al.* [68]	50	1	SESAM	Nd:YVO_4	3	0.2
Braun *et al.* [122]	56	0.062	SESAM	Nd:YVO_4	3	0.2
Braun *et al.* [122]	68	0.37	SESAM	Nd:YVO_4	3	0.2
Nodop *et al.* [68]	110	0.6	SESAM	Nd:YVO_4	3	0.2
Zayhowski *et al.* [71]	115	12	EO	Nd:YVO_4	1.1	0.44
Braun *et al.* [121]	180	0.1	SESAM	Nd:LSB	25	0.22
Steinmetz *et al.* [72]	200	0.145	SESAM	Nd:YVO_4	3	0.25
Zayhowski *et al.* [131]	218	4	Cr^{4+}:YAG	Nd:YAG		
Fluck *et al.* [141]	230	0.12	SESAM	Nd:YVO_4	3	0.2
Dong *et al.* [67]	237	172	Cr^{4+}:YAG ceramic composite	Yb:YAG		1.2 + 1.5
Wang *et al.* [103]	290	8	Cr^{4+}:YAG monolithic	Nd:YAG	1 wt	1
Zayhowski et al. [73]	< 300		EO	Nd:YAG	1.8 wt	0.532
Zayhowski *et al.* [143]	337	11	Cr^{4+}:YAG	Nd:YAG	1.8	0.5 + 0.25
Dong *et al.* [144]	350	3.2	Cr^{4+}:YAG	Yb:YAG	20	0.5 + 0.5
Braun *et al.* [121]	360	0.6	SESAM	Nd:LSB		0.22
Zayhowski [70]	440	8	Cr^{4+}:YAG	Nd:YAG		1 + 0.25
Spühler *et al.* [135]	530	1.1	SESAM	Yb:YAG	20	0.2
Haring *et al.* [126]	840	11.2	SESAM	Er:Yb:Glass	2.75:21 wt	0.5

Table 2.1: A summary of sub-ns Q-switched lasers. Cavity lengths expressed as sums take into account the thickness of the gain medium and also the intra-cavity Q-switch.

An important laser performance indicator, pulse repetition rate, is omitted from Table 2.1. Spühler *et al.* observed an obtainable range of 27 kHz – 7 MHz across a range of similar SESAM Q-switched microchip laser designs, which varied according to Q-switch and gain medium, but was largely dependent on incident pump power. This behaviour is commonly reported for passively Q-switched lasers and it is shown later in Section 2.6 that pump power linearly affects repetition rate without altering other output behaviour. As a result, pulse repetition rate can be arbitrarily chosen.

It is clear from Table 2.1 that the shortest pulses are achieved by lasers with short cavities, employing Nd:YVO_4 as a gain medium and with a SESAM as a passive Q-switch. The last two criteria are actually requirements dictated by the first: if thin cavities generate short Q-switched pulses, a highly-absorptive gain medium is required to absorb the pump light efficiently and a Q-switch that does not contribute to the length of the cavity is needed. Only two entries in Table 2.1 are from actively Q-switched lasers and although they still require high voltages for switching, they are not standard examples of EO Q-switches. In each case, $LiTaO_3$ is used to form an output coupling etalon, the thickness of which, and therefore the transmission of which, can be varied from anti-resonant to resonant to perform the Q-switching action. As can be inferred from Figure 2.2, standard electro-optic and acousto-optic Q-switching elements typically add 10’s of mm to a cavity length and give pulse durations in the region of 10’s of ns [140, 145, 146].

Author	l_L / mm	ΔR / %	F_{SAT} / Jm^{-2}	τ_{SESAM} / ps	R_{OPC} / %	σ_{em} / 10^{-23} m^2	τ_p / ps	E_p / µJ
Spühler *et al.* [69]	0.185	13			90	25	37	0.053
Nodop *et al.* [68]	0.2	20.5	5	320		25	50	1
Braun *et al.* [122]	0.2	13			90	25	56	0.062
Braun *et al.* [122]	0.2	11			90	25	68	0.37
Nodop *et al.* [68]	0.2	11	5	320		25	110	0.6
Braun *et al.* [121]	0.22	2.3	0.5	24	90	1.3	180	0.1
Steinmetz *et al.* [72]	0.25	10	5		90	25	200	0.145
Fluck *et al.* [141]	0.2	7	6.7	330	91.5	25	230	0.12
Braun *et al.* [121]	0.22	3.1	0.5	24	90	1.3	360	0.6
Spühler *et al.* [135]	0.2	3.8	2.1	78	95.2	0.25	530	1.1
Haring *et al.* [126]	0.5	1.2			96	0.08	840	11.2

Table 2.2: An extended summary of the SESAM Q-switched microchip lasers in Table 2.1, showing details of the SESAMs used. The total cavity length, in all these cases equivalent to just the gain material thickness, is denoted l_L.

A collection of SESAMs used in the results in Table 2.1 and their parameters are summarised in Table 2.2 and graphically in Figure 2.10. As with decreasing cavity length in Table 2.1, a trend between increasing SESAM modulation depth and decreasing pulse duration is evident.

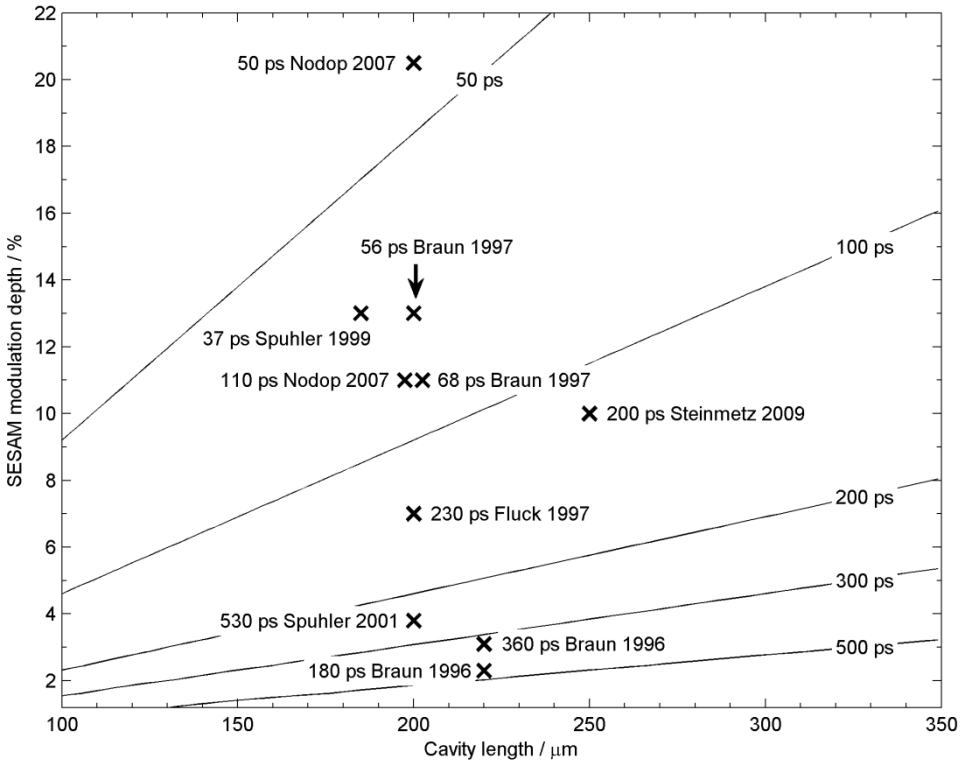

Figure 2.10: The pulse duration results from the literature expressed as functions of cavity length and SESAM modulation depth. The background contour lines are calculated using the analytic expressions later discussed in Section 2.6.

It is clear from the literature, and later proven in modelling and experiment, that making the oscillator cavity as short as possible and having a Q-switch with a large modulation depth are the keys to generating short Q-switched pulses. This can be achieved simply by using a passive SESAM Q-switch in a microchip laser arrangement, negating the need for additional active Q-switch-supporting architecture and without adding extra length to the cavity.

2.6 Analytic models of Q-switched microchip lasers

In Chapter 3 a rate equation model is derived and solved numerically to predict the performance of SESAM Q-switched microchip lasers, given their component parameters. Analytic expressions derived from the laser rate equations also exist and can be used to indicate key relationships between laser component parameters and laser performance without the extended computation time associated with numerical solutions.

Zayhowski and Kelley [147], derive an explicit expression for the pulse energy achievable by a Q-switched microchip laser by considering the size of the inversion depletion from the pulse:

$$E_p = \eta_q n_0 A l_L h\nu_L \frac{\gamma_{OPC}}{\gamma_{n\text{-}s}} \tag{2.2}$$

The quantum extraction efficiency, η_q, is the fraction of the total extractable inversion density, n_0, released during a pulse. The beam area in the gain medium is A and $\gamma_{OPC}/\gamma_{n\text{-}s}$ is the ratio of the output coupling loss constant to the total non-saturable round-trip loss constant, or the output coupling efficiency. In this case, $\gamma_{n\text{-}s} = \gamma_{OPC} + \gamma_p$, is the sum of the round-trip non-saturable losses, including the loss due output coupling, γ_{OPC}, and other parasitic losses, γ_p, typically dominated by the non-saturable loss of the passive Q-switch.

Assuming a particular pulse shape, Zayhowski and Kelley derive an expression for the pulse duration:

$$\begin{aligned} \tau_{p,\min} &= \frac{8.1 n_{RI}}{n_0 \sigma_{em} c} \\ &= \frac{8.1 \tau_{rt}}{2\sigma_{em} l_L n_0} \end{aligned} \tag{2.3}$$

which is later written as [13, 71, 148]:

$$\tau_{p,\min} = \frac{8.1 \tau_{rt}}{\ln\left(G_{rt,S}\right)} \tag{2.4}$$

where $G_{rt,s} = e^{2\sigma_{em} l_L n_0}$ is the round-trip gain provided by the extractable inversion density n_0. $\tau_{rt} = 2 l_L n_{RI}/c$ is the round-trip time for a photon in a cavity of length l_L, filled with a medium of refractive index n_{RI} and emission cross-section σ_{em}. The factor of 8.1 is determined by assuming the output coupling efficiency is optimised to give the shortest pulse duration and is further fine-tuned by numerical simulation to account for

additional shaping by the output coupling loss. A simpler derivation of equation (2.3) is given by Zayhowski and Kelley, where the rise and decay times of the pulse are each approximated to $2\tau_c = 2 \cdot 2n_{RI} l_L / (\gamma_{n\text{-}s} c)$, giving a minimum pulse duration of:

$$\tau_{p,\min} = \frac{8n_{RI} l_L}{\gamma_{n\text{-}s} c} = \frac{8n_{RI}}{n_0 \sigma_{em} c} \tag{2.5}$$

when the output coupling is optimised $\gamma_{n\text{-}s} = \gamma_{OPC} + \gamma_p = n_0 \sigma_{em} l_L$. The cavity photon lifetime, τ_c, also described later in Section 3.2, does not take into account the effect of gain saturation on rise and decay times, so the factor of 2 is included to approximately compensate for this.

Expressions for E_p and τ_p from Spühler *et al.* [69], are more specific to SESAM Q-switched microchip lasers, although are derived in a similar manner and give the same results as Zayhowski and Kelley within limits. The pulse-formation approach taken by Spühler *et al.* is summarised in Figure 2.11: when the total round-trip loss is reduced by an amount q_0 ($l + q_0$ in Figure 2.11 is equivalent to $\gamma_{n\text{-}s} + q_0$ in our nomenclature), the resulting pulse depletes the gain by q_0 in both the leading and trailing edges of the pulse.

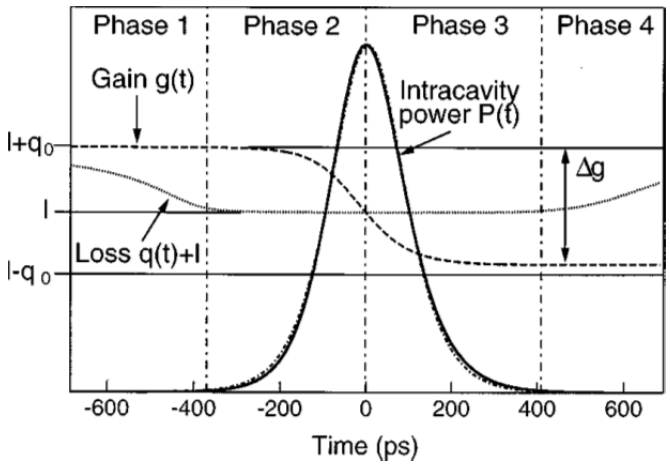

Figure 2.11: The evolution of a pulse from a SESAM Q-switched microchip laser as described by Spühler *et al*, showing the reduction in loss pre-pulse, the depletion of the gain and the pulse. From [69].

This treatment allows the pulse energy expression to be formed:

$$E_p = \frac{h\nu_L}{2\sigma_{em}} A 2q_0 \frac{\gamma_{OPC}}{\gamma_{n\text{-}s}} = \frac{h\nu_L}{2\sigma_{em}} A 2\Delta R \frac{\gamma_{OPC}}{\gamma_{n\text{-}s}} \tag{2.6}$$

where $q_0 = -\ln(1-\Delta R)$ is the saturable loss coefficient of the SESAM and $q_0 \approx \Delta R$ for small ΔR. The quantity $Ah\nu_L/(2\sigma_{em})$ is the saturation energy of the gain medium, $2q_0$ is the total gain depletion and $\gamma_{OPC}/\gamma_{n\text{-}s}$ again the output coupling efficiency. The product of these three quantities will represent the amount of stored energy that is released through the output coupler during the pulse. Assuming that the gain made available by the switching of the Q-switch is $2q_0$ and it is entirely depleted during the pulse, $2\sigma_{em} l_L n_0 = 2q_0$ and $\eta_q = 1$, making (2.2) identical to (2.6).

The expression for pulse duration from Spühler *et al.* is derived from the assumption that the exponential growth and decay rates of the pulse are both q_0/τ_{rt}, resulting in a FWHM duration of $2\ln(2)\tau_{rt}/q_0$.

$$\tau_p \approx \frac{3.52\tau_{rt}}{q_0} \approx \frac{3.52\tau_{rt}}{\Delta R} \tag{2.7}$$

An additional correction factor of ~ 2 is included to account for the decrease in the growth and decay of the pulse during gain saturation, determined from numerical simulation. The earlier approach of Braun *et al.* for SESAM Q-switched microchip lasers is similar although rather than approximate to an exponential growth and decay, they include a term to shape for sech^2 pulses and a factor of 2, with the same result. Again by setting $2\sigma_{em} l_L n_0 = 2q_0$, and including a factor of 0.88 to account for the half-maximum rise and fall time width of a sech^2 pulse, (2.5) is identical to (2.7).

Spühler *et al.* also derive a pulse repetition rate by dividing an empirically determined expression for average output power by pulse energy:

$$f_{rep} = \frac{\eta\left(P_P - P_{P,th}\right)}{E_p} = \frac{g_0 - \left(\gamma_{n\text{-}s} + q_0\right)}{2q_0\tau_L} \tag{2.8}$$

The average output power is simply the product of the optical-optical slope efficiency η, later defined in (2.11), and the pump power supplied to the laser, P_P, that is excess over that required to reach threshold, $P_{P,th}$. g_0 is the round trip gain achievable with a given pump power and can be expressed as:

$$g_0 = \frac{2\sigma_{em}\tau_L\eta_P}{h\nu_P A} P_P \tag{2.9}$$

where τ_L is the upper-state lifetime of the gain material and η_P is the pump absorption efficiency. Using $\gamma_{n\text{-}s} = \gamma_{OPC} + \gamma_p = -\ln\left(R_{OPC}\right) - \ln\left(R_U + \Delta R\right)$, (2.8) can be given in terms of SESAM parameters and other known or calculable properties:

$$f_{rep} = \frac{\sigma_{em}\eta_P}{-Ah\nu_P \ln\left(1-\Delta R\right)} P_P + \frac{\ln\left(1-\Delta R\right) + \ln\left(R_{OPC}\right) + \ln\left(R_U + \Delta R\right)}{-2\tau_L \ln\left(1-\Delta R\right)} \tag{2.10}$$

where R_{OPC} is the reflectivity of the output coupler.

Since the optical-optical slope efficiency of a laser is defined $\eta = P_{ave}/P_P = E_p f_{rep}/P_P$ and as the second term of (2.10) is negligible for most cases:

$$\eta = \frac{\gamma_{OPC}}{\gamma_{n\text{-}s}} \frac{\nu_L}{\nu_P} \eta_P = \frac{\ln\left(R_{OPC}\right)}{\ln\left(R_{OPC}\right) + \ln\left(R_U + \Delta R\right)} \frac{\lambda_P}{\lambda_L} \eta_P \tag{2.11}$$

which is the product of the output coupling efficiency, quantum defect and pump efficiency and is identical to the expression for slope efficiency given by Zayhowski and Kelley.

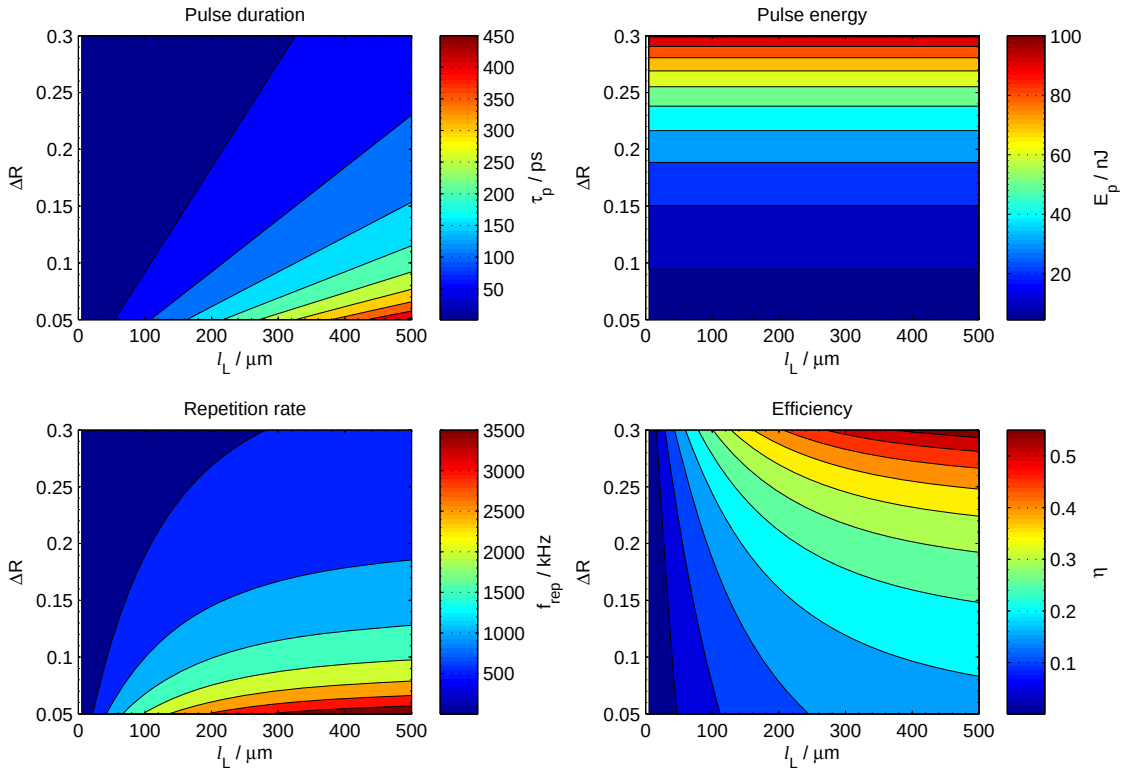

Figure 2.12: Laser output behaviour according to (2.6) - (2.11), for common ranges of ΔR and l_L demonstrated in Table 2.2. All other parameters used to generate these plots are taken from the common design in Section 3.6. Note that in varying ΔR, R_U is chosen to remain constant at 0.7 with the non-saturable SESAM loss, $A_{n\text{-}s}$, changing to satisfy $R_U + \Delta R + A_{n\text{-}s} = 1$.

Figure 2.12 shows the trends in analytic model results for a range of cavity lengths and SESAM modulation depths commonly found in SESAM Q-switched microchip lasers. These results confirm the trends found in the literature in Section 2.5 that short pulse are generated by short, high modulation depth cavities.

The expressions (2.2) - (2.11) are derived either analytically from the laser rate equations or empirically from the behaviour of the rate equation solutions. They are applicable to four-level laser systems although extensions to three-level systems are also presented in [69, 147]. The primary assumption around which they are based is that the gain depletion is symmetric about the pulse peak and is $2q_0$ in magnitude and requires that the saturable loss of the Q-switch, q_0, is of the order of or smaller than the non-saturable cavity loss, $\gamma_{n\text{-}s}$. Additionally, the switch from high-loss to low-loss must be much faster than the pulse duration and last for the entire duration of the pulse. It is

shown in Section 3.7 that the symmetry assumption breaks down under certain conditions and that the analytic models are insufficient to completely describe a SESAM Q-switched microchip laser. However, the expected dependency of the laser output behaviour on its component parameters is clearly indicated in the analytic expressions and Figure 2.12.

2.7 Amplification

For cases where the cavity length of a microchip laser, and hence gain material thickness, can be of the order of or less than the absorption length of the gain material, the efficiency of the microchip laser can be poor through incomplete pump absorption. Microchip lasers have been used as seed sources for conventional amplification schemes with the primary intent of increasing pulse energy rather than efficiency and require additional pump sources [40, 75, 76]. In order to directly reclaim oscillator efficiency, Zayhowski and Wilson [149], demonstrated an energy-scavenging amplifier design (Figure 2.13) that makes use of the unabsorbed pump light from the resonator cavity.

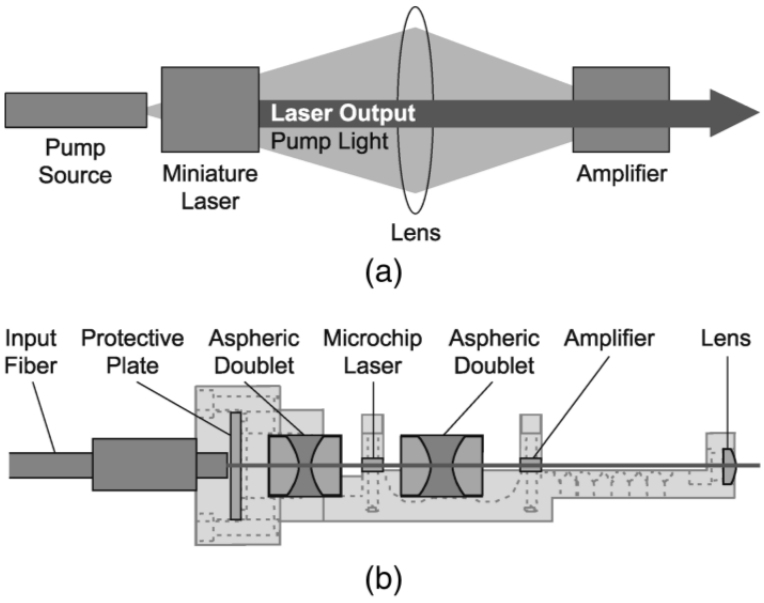

Figure 2.13: (a) The concept of a pump-scavenging amplifier and (b) the design of an amplified microchip laser. From [149].

Zayhowksi and Wilson reported as much as a factor of 2.8 increase in pulse energy and efficiency, resulting in pulses of 250 ps duration and 59 µJ energy. This was achieved using an Nd:YAG microchip laser passively Q-switched with Cr^{4+}:YAG and a 4 mm-thick 1 at.% Nd:YVO_4 amplifier crystal. The amplifier material is chosen to have large absorption and emission cross-sections at wavelengths similar to those of the laser material in order to efficiently absorb the unabsorbed pump light and enable efficient gain extraction. In this scheme, the diode pump source is detuned slightly from the narrow absorption band of the Nd:YAG while still remaining in the broader absorption band of Nd:YVO_4, so as to maximise the period of amplifier pumping before the laser reaches threshold and pulses.

2.8 Summary

The SESAM Q-switched microchip laser approach has been shown in Table 2.1 to deliver pulses of duration in the 10-100s ps range, comparable to that of some mode-locked systems but with considerably reduced complexity. The trends in Table 2.1 and Table 2.2 show that this is achieved by using a Q-switch with a large modulation depth in a short cavity. The shortest reported pulse generated by a Q-switched laser, prior to the work reported in this thesis, is 37 ps from a 185 µm long cavity using a SESAM Q-switch with 13% modulation depth. The need for short cavities and large modulation depths is further confirmed by the analytic expressions in Section 2.6. The analytic models have been used to predict scaling relationships between laser component parameters and other output indicators such as pulse energy and repetition rate, while also predicting realistic ball-park values for these indicators.

In addition to producing short pulses, SESAM Q-switched microchip lasers also have the additional benefits of generating single-frequency output and are compact, self-contained and simple, requiring minimal supporting architecture. The output pulse rate is highly controllable by modulating the incident pump power, without otherwise affecting the performance of the laser. The cost of reducing the cavity and gain medium length to generate short pulses is a reduction in overall efficiency, although it has been shown that this can be partially countered through introduction of an energy-scavenging amplifier.

3 Numerical Modelling of SESAM Q-Switched Microchip Lasers

Although the design of these lasers is outwardly simple, the parameter field that determines the laser's behaviour is large and varied. While the analytic models discussed in Section 2.6 incorporate a large proportion of these variables, there remain approximations that can limit their validity, particularly as the limits of scaling are approached, such as moving to very short cavity lengths. The two key approximations are that the SESAM relaxation time is much longer than the pulse duration and that the saturable loss is of the order of or smaller than the non-saturable loss, leading to a symmetric pulse of a particular shape.

In this chapter we develop a numerical model to accurately model a microchip laser without these approximations. We also add a consideration of two-photon absorption (TPA) that can be significant for SESAMs at higher fluence levels [150, 151]. We use this model to predict the limitations of scaling the behaviour of microchip lasers, particularly with a view to generating the shortest pulses possible.

3.1 Laser design and component selection

As shown below, the arrangement of components in a SESAM Q-switched microchip laser is very straightforward, a characteristic that makes these devices especially attractive. The laser gain medium is sandwiched between the Q-switch element and a bulk output coupler. Pump light is delivered through the output coupler and double-passed through the cavity by virtue of a high reflectivity coating on the SESAM face.

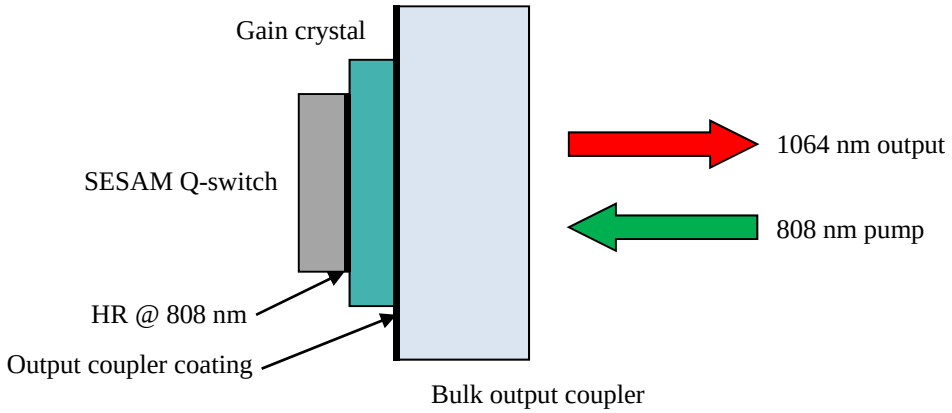

Figure 3.1: A schematic of a basic microchip laser design, incorporating a SESAM as a passive Q-switch and a bulk output coupler.

The choice of solid-state gain material in this case is mainly dictated by the need for a thin, or short, cavity. If the thickness of the absorbing material approaches or is even less than its absorption length, as can be the case with microchip lasers, the absorption of the pump light by the gain medium can be low causing the laser to become extremely inefficient. Part of the solution is to double-pass the pump light through the cavity, effectively doubling the length presented to the pump beam for absorption.

The second part of the solution is to choose a highly absorptive gain medium. The absorption coefficient of a material, α_{abs}, is given by $\alpha_{abs} = \sigma_{abs} n_{tot}$ where σ_{abs} is the absorption cross-section of the material and n_{tot} is the total number density of absorber particles, in this case laser gain ions. Increasing either σ_{abs} or n_{tot} will increase the absorption coefficient (and shorten the absorption length) and hence increase the overall absorption efficiency of the material. Efficiency considerations thus suggest choosing materials with high absorption cross-sections, and which are amenable to high levels of ion doping.

Other considerations include: thermal conductivity, that will determine maximum pump powers; the output wavelength and polarisation of the laser, although many applications do not require a specific wavelength or polarisation state; and emission cross-section, which we will see below affects the output pulse energy.

Property	Laser Crystal				
	Nd:YAG [69]	Nd:YVO_4 [69]	Nd:LSB [121, 152]	Nd:LSB [153]	Yb:YAG [69]
Doping / at. %	1.1	3	25	10	20
Main lasing wavelength / nm	1064	1064	1062	1063	1030
Main absorption wavelength / nm	808	808	808	808	968
Doping concentration / $\times 10^{26}$ m^{-3}	1.52 [154]	3.75 [154]	12.8	4.3 (5.1 [152])	27.5
Absorption cross-section / $\times 10^{-23}$ m^2	1.5	2.7	0.71	0.71 [152]	0.056
Absorption coefficient / m^{-1}	2280	10125	9091	3053 (3621 [152])	1538
Emission cross-section / $\times 10^{-23}$ m^2	3.3	25	1.3 (effective)	2.3 (spectro-scopic)	0.25
Upper state lifetime / μs	250	50	87	100 (118 [152])	950
Refractive index	1.84	1.96	1.82	1.83	1.84
Thermal conductivity / $Wm^{-1}K^{-1}$	13	5.2	2.8	2.8	13

Table 3.1: Properties for the most common microchip laser materials.

Table 3.1 shows properties for the most frequently used microchip laser materials. The most common crystal used in microchip lasers is neodymium-doped yttrium aluminium garnet, or Nd:YAG [66, 155, 156]. Nd:YAG is a very well-known solid-state material with excellent thermal properties but does not have as high an absorption coefficient as other solid-state crystals. Due to a low segregation coefficient for Nd in YAG sites, monocrystalline Nd:YAG cannot be reliably doped much over 1% before the structural integrity and optical properties break down, meaning that the upper limit for ion concentration is low compared to other crystals. Additionally, Nd:YAG output is unpolarised, which is undesirable for amplification, frequency conversion and is problematic for some applications.

In terms of absorption, Nd:YVO_4 [71, 122, 157, 158], or neodymium-doped yttrium orthovanadate, is by far the better candidate since the Nd-doping level can be set moderately high, up to 4 at.% commercially, and the absorption cross-section is nearly double that of its nearest rival, Nd:YAG.

To increase the pulse energy, a low emission cross-section should be chosen: the less common materials, Nd:LSB [121, 152, 153], and Yb:YAG [135, 144, 159], are very favourable in this regard. Yb:YAG has high thermal conductivity but has the worst absorption coefficient of the selection. Conversely, Nd:LSB is more absorptive but with poor heat management properties. Note that, as Nd:YVO_4 is an anisotropic crystal it can present two different emission cross-sections depending on the axis along which it is cut. The c-cut crystal has a lower emission cross-section than the a-cut crystal, which is beneficial for high pulse energies [160]. However, in this instance the a- and b-axes of the crystal have equal emission cross sections and both tend to lase, resulting in un-polarised light. In an a-cut crystal, the emission cross section of the c-axis is greater than that of the b-axis and so lasing occurs preferentially in this polarisation, giving output in a single linear polarisation.

Ceramic solid-state media have also been considered [161, 162]. Ceramic laser materials are composed of grains of highly-doped crystalline material, compressed together and heated to form a single polycrystalline structure. Although the majority of research on ceramic media has been on Nd:YAG [163-166], with doping as high as 6.6 at.% [167], successful lasing of other materials in ceramic form has also recently

been demonstrated [146, 168]. Their randomly-orientated polycrystalline nature also prevents polarised output although this can be partially remedied with polarization-selective output coupling techniques [169].

The material considered in the following modelling and experimental chapters will be Nd:YVO_4. Its attractive absorption properties make it more likely to operate efficiently at low thicknesses. While its high emission cross-section makes this an ideal material for CW microchip applications, it will compromise the output pulse energy in a Q-switched system. However, our primary goal will be to generate the shortest possible pulses from the Q-switched architecture, with pulse energy a secondary consideration for the oscillator component, making Nd:YVO_4 the gain medium of choice for our Q-switched microchip laser.

As the Q-switching element, the SESAM has a comparable degree of control over the output pulse duration to that of the resonator cavity length. The key properties of the SESAM that effect the pulse duration are the modulation depth, ΔR, the saturation intensity, $I_{SAT} = F_{SAT} / \tau_{SESAM}$, and the unsaturated reflectivity, R_U. These between them control most aspects of the laser performance, including whether it lases pulsed, CW or not at all. The factors influencing the choice of these parameters are one of the key results of this chapter.

The complete variable set for consideration in numerical modelling and their associated normal operating regimes are summarised in Table 3.2. Although the range of gain media and SESAMs available will set the parameters to specific values when modelling to reflect real-world systems, the numerical model's primary function is still to indicate the general relationships between input parameters and output performance even when the particular variable sets do not replicate real-world components.

Component	Property	Symbol	Typical Values
Gain crystal	Absorption cross-section	σ_{abs}	~ 10^{-23} m^2
	Emission cross-section	σ_{em}	~ 10^{-23} m^2
	Total laser ion density	n_{tot}	~ 10^{26} m^{-3}
	Upper state lifetime	τ_L	10-100's of μs
	Speed of light in crystal	$c_L = c/n_{RI}$	$1.8 \le n_{RI} \le 2$
	Emission light frequency	$\nu_L = c/\lambda_L$	λ_L = 1064 nm
	Spontaneous photon to cavity coupling efficiency	M	~ 10^{-5}
Pump source	Pump light frequency	$\nu_P = c/\lambda_P$	λ_P = 808 nm
	Power	P_P	mW to W
	Spot size	r_P	10's of μm
Cavity	Length	l_L	μm to mm
	Laser mode radius	r_L	10's of μm
	Output coupling reflectivity	R_{OPC}	0-100%
SESAM	Modulation depth	ΔR	10's of %
	Unsaturated reflectivity	R_U	10's of %
	Relaxation time constant	τ_{SESAM}	10's of ps
	Saturation fluence	F_{SAT}	~ 1 Jm^{-2}

Table 3.2: A summary of the variables used in numerical modelling of a SESAM Q-switched microchip laser and their common ranges.

3.2 Rate equations

Here we derive the time-dependent rate equations for the laser field and inversion density suitable for describing SESAM Q-switched microchip lasers [81, 170, 171]. We focus on the treatment of the SESAM reflectivity, the addition of two-photon absorption, and highlight the assumptions that underlie this approach.

We model the laser as a perfect 4-level system, and track the upper laser population, n, leaving the ground state population density simply expressed as $n_{tot} - n$ where n_{tot} is the total number density of ions present in the gain medium. When a beam of light of intensity I passes through a medium of length l_L, emission cross-section, σ_{em} and with an inversion population n, the resulting intensity I' is:

$$I' = Ie^{\sigma_{em} n l_L} \tag{3.1}$$

If two mirrors of reflectivity R_1 and R_2 are placed at either end of the medium, forming a resonator cavity, and neglecting the scattering loss in the thin laser crystal, the intensity after a complete round-trip, I'', is:

$$I'' = R_1 R_2 e^{\sigma_{em} n l_L} I' = R_1 R_2 e^{2\sigma_{em} n l_L} I \tag{3.2}$$

By expressing both R_1 and R_2 in the form, $R = e^{-\gamma}$ and incorporating them into the exponent, the change in intensity due to the round-trip is given by:

$$\Delta I = \left(e^{2\sigma_{em} n l_L - (\gamma_1 + \gamma_2)} - 1 \right) I \tag{3.3}$$

Assuming $2\sigma_{em} n l - (\gamma_1 + \gamma_2) \ll 1$, the exponential in (3.3) can be expanded as a power series, and we get:

$$\Delta I \approx \left[2\sigma_{em} n l_L - (\gamma_1 + \gamma_2) \right] I \tag{3.4}$$

Considering the time over which this change takes place, the round-trip time:

$$\tau_{rt} = \Delta t = \frac{2 l_L n_{RI}}{c} = \frac{2 l_L}{c_L} \tag{3.5}$$

allows the relationship to be formed:

$$\begin{aligned} \frac{\Delta I}{\Delta t} &= \left(\frac{2\sigma_{em} n l_L}{\tau_{rt}} - \frac{\gamma_1 + \gamma_2}{\tau_{rt}} \right) I \\ &= \left(\sigma_{em} n c_L - \frac{-\ln R_1 - \ln R_2}{\tau_{rt}} \right) I \end{aligned} \tag{3.6}$$

Finally, approximating $\Delta I / \Delta t$ to dI/dt and knowing that the intra-cavity intensity is directly proportional to the intra-cavity photon density, ϕ, one of the laser rate equations is formed:

$$\frac{d\phi}{dt} = c_L \sigma_{em} n \phi - \frac{-\ln(R_1 R_2)}{\tau_{rt}} \phi \tag{3.7}$$

It is common to write the last term in (3.7) as ϕ/τ_c where τ_c is the cavity photon lifetime:

$$\tau_c = \frac{-2l_L}{c_L \ln\left(R_1 R_2\right)} \tag{3.8}$$

however, it is clearer in this instance to express round-trip loss occurring per round-trip period.

The first term on the right-hand side of (3.7) is clearly the rate of increase of cavity photon density due to stimulated emission of photons by the transition of ions from the excited state to the ground state. Using the fact that one photon is released by one transition, it is possible to begin constructing an expression for the rate of change of the inversion population density:

$$\frac{dn}{dt} = -c_L \sigma_{em} n\phi + R_P + R_f \tag{3.9}$$

R_P and R_f denote the rate of change of inversion density through absorption of pump light and by spontaneous emission respectively. R_f is straightforward to derive knowing that the fluorescence decay is an exponential process, with lifetime τ_L, and neglecting stimulated emission and pumping:

$$n = e^{\frac{-t}{\tau_L}} \Rightarrow \frac{dn}{dt} = -\frac{n}{\tau_L} \Rightarrow R_f = -\frac{n}{\tau_L} \tag{3.10}$$

To derive the pumping term, we consider the intensity of pump light transmitted through the medium, with absorption cross-section σ_{abs} and lower state population density $n_{tot} - n$, after a single and then a double-pass:

$$\begin{aligned} I' &= Ie^{-(n_{tot}-n)\sigma_{abs}l_L} \\ I'' &= I'e^{-(n_{tot}-n)\sigma_{abs}l_L} = Ie^{-2(n_{tot}-n)\sigma_{abs}l_L} \end{aligned} \tag{3.11}$$

allowing the pump photon transmission ratio, and then absorption ratio to be calculated:

$$T_P = \frac{I''}{I} = e^{-2(n_{tot}-n)\sigma_{abs}l_L}$$
$$A_P = 1 - T_P = 1 - e^{-2(n_{tot}-n)\sigma_{abs}l_L} \tag{3.12}$$

The fraction of pump photons absorbed is expressed by (3.12), and combined with the rate of pump photons arriving in the pumped gain volume, V_P, the expression for the rate of pump photon absorption per unit volume is formulated:

$$R_P = \frac{P_P}{h\nu_P}\frac{1}{V_P}A_P = \frac{P_P}{h\nu_P}\frac{1}{\pi r_P{}^2 l_L}\left(1 - e^{-2(n_{tot}-n)\sigma_{abs}l_L}\right) \tag{3.13}$$

assuming that the pump beam has a top-hat intensity profile and hence the pump volume cylindrical with volume $V_P = \pi r_P{}^2 l_L$.

By placing (3.10) and (3.13) into (3.9), the rate equation for inversion population density is given:

$$\frac{dn}{dt} = -c_L\sigma_{em}n\phi + \frac{P_P}{h\nu_P}\frac{1}{\pi r_P{}^2 l_L}\left(1 - e^{-2(n_{tot}-n)\sigma_{abs}l_L}\right) - \frac{n}{\tau_L} \tag{3.14}$$

By comparing (3.7) and (3.14), it is evident that a term is missing from the photon density expression, and we must account for spontaneous decay photons that enter the laser mode:

$$\frac{d\phi}{dt} = c_L\sigma_{em}n\phi - \frac{-\ln\left(R_1R_2\right)}{\tau_{rt}}\phi + M\frac{n}{\tau_L} \tag{3.15}$$

The spontaneous photon to cavity mode coupling efficiency, M is typically of the order of 10^{-5} or 10^{-6}. In reality, the value of M has little effect on the output parameters of the laser since it is only required to seed the laser cavity with photons and initiate the laser action.

The rate equations are now in a form that is directly applicable to a CW microchip laser. All the variables in (3.14) and (3.15) are known or easily calculable and CW behaviour can be derived. To make the equations specific to a Q-switched system, the reflectivities of the mirrors are now made to reflect the design in Figure 3.1

with R_1 becoming the reflectivity of the output coupler, R_{OPC}, and R_2 becoming the reflectivity of the SESAM, R_{SESAM}. R_{SESAM} varies over time depending on the fluence incident on the SESAM, F, which is calculated with an additional rate equation coupled to the cavity photon density.

The intra-cavity intensity incident on the face of the SESAM is related to the cavity photon density by the expression:

$$I = \frac{\phi}{2} c_L h\nu_L \tag{3.16}$$

The factor of $1/2$ in (3.16) arises from the fact that ϕ is the total intra-cavity photon density, i.e. a total density of photons travelling both towards and away from the SESAM. Only those travelling towards the SESAM at any point in time are included in the intensity incident on the face of the SESAM. The fluence that has impinged on the SESAM can then be written as a differential equation as:

$$\frac{dF}{dt} = I = \frac{\phi}{2} c_L h\nu_L \tag{3.17}$$

In the case where the relaxation time constant of the SESAM (or any passive Q-switch) is much longer than the pulse duration, $\tau_{SESAM} \gg \tau_p$, the fluence as defined in (3.17) is an acceptable approximation for use in determining the reflectivity of the SESAM for each pulse. However, the relaxation time constants of most commercially available SESAMs are either of the order of the pulse duration from Q-switched microchip lasers or even shorter. Since the increase in R_{SESAM} is owing to the excitation of electrons in the SESAM absorber layer, the lifetime of these carriers determines the timescale for the memory of the incident fluence history. This fact enables us to define an effective SESAM fluence that accounts for the relaxation of the carriers by including a decay term:

$$\frac{dF}{dt} = \frac{\phi}{2} c_L h\nu_L - \frac{F}{\tau_{SESAM}} \tag{3.18}$$

This effective SESAM fluence is not strictly a physical quantity, but it represents the effective fluence determining the instantaneous SESAM reflectivity at a given time. Note that for $\tau_{SESAM} \gg \tau_p$, (3.18) is equivalent to (3.17) as required; for $\tau_{SESAM} \ll \tau_p$, the steady state value of F is $I\tau_{SESAM}$, and so an incident intensity of $I_{SAT} = F_{SAT}/\tau_{SESAM}$ will result in an effective fluence of F_{SAT}, the fluence required to bleach the SESAM absorption to e^{-1}, as required by (2.1).

The value calculated by solving (3.18) is used to derive SESAM reflectivity. As described in 2.3, the SESAM can be modelled as a device with an unsaturated reflectivity, R_U, a saturable loss, $A_{s\text{-}l}$ (variable according to F but with maximum magnitude A_s), and an unchanging non-saturable loss, $A_{n\text{-}s}$.

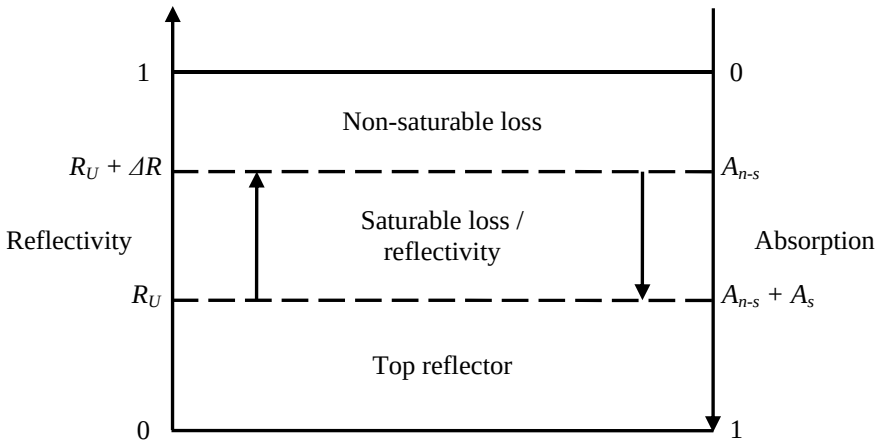

Figure 3.2: A representation of the SESAM reflectivity and absorption. When a SESAM switches, it switches from an initial reflectivity, R_U, to a switched reflectivity, $R_U + \Delta R$, or equivalently from an absorption $A_{n\text{-}s} + A_s$ to $A_{n\text{-}s}$.

These three regimes are depicted in Figure 3.2. It is the saturable loss that changes to provoke pulse formation and is dependent upon the effective fluence incident on the SESAM face. By modelling the saturable loss as a three-level system with saturation fluence F_{SAT}, we write:

$$A_{s\text{-}l} = A_s e^{\frac{-F}{F_{SAT}}} \tag{3.19}$$

Using the relationships $A_{n\text{-}s} = 1 - (R_U + \Delta R)$ and $A_s = \Delta R$, the reflectivity of the SESAM given an incident fluence, F, is then:

$$\begin{aligned} R_{SESAM}(F) &= 1 - A_{n\text{-}s} - A_s e^{\frac{-F}{F_{SAT}}} \\ &= R_U + \Delta R\left(1 - e^{\frac{-F}{F_{SAT}}}\right) \end{aligned} \tag{3.20}$$

It is important to note that the SESAM reflectivity calculation is often found in the literature in a form that predicts the average reflectivity over a pulse of particular fluence and duration [123, 125, 128]. This is not suitable for considering the pulse formation by SESAMs for which we need the instantaneous reflectivity for all times during the pulse.

The three rate equations in their final form for numerical simulation of a SESAM Q-switched microchip laser are written:

$$\frac{dn}{dt} = -c_L \sigma_{em} n\phi + \frac{P_P}{h\nu_P}\frac{1}{\pi r_P{}^2 l_L}\left(1 - e^{-2(n_{tot}-n)\sigma_{abs} l_L}\right) - \frac{n}{\tau_L} \tag{3.21}$$

$$\frac{d\phi}{dt} = c_L \sigma_{em} n\phi - \frac{-\ln\left[R_{OPC} R_{SESAM}(F)\right]}{\tau_{rt}}\phi + M\frac{n}{\tau_L} \tag{3.22}$$

$$\frac{dF}{dt} = \frac{\phi}{2} c_L h\nu_L - \frac{F}{\tau_{SESAM}} \tag{3.23}$$

where $R_{SESAM}(F)$ is calculated using (3.20).

The dynamics of a Q-switched laser system follow the pattern of long periods of pumping (inter-pulse), punctuated by comparatively brief but intense periods of action (pulse). For this reason we choose a stiff numerical solving algorithm, such as MATLAB's `ode15s` which is based on the numerical differentiation formulae [172], and decreases computation time dramatically without compromising accuracy.

The form taken by the solver's output variables, n, ϕ and R_{SESAM} from the numerical modelling solution is a detailed history of their evolution over time for a series of pulses. The total time period under examination is made long enough that a pulse train of uniform pulses is attained and the initial pulses before equilibrium is reached are ignored. The principle performance indicators that need to be interpreted from the raw model outputs are the pulse duration at FWHM, τ_p, the pulse repetition rate, f_{rep}, and the pulse energy, E_p.

The instantaneous output power of the laser is calculated directly from ϕ as follows:

$$P_L = \frac{\phi}{2} c_L \pi r_L^2 h\nu_L \left(1 - R_{OPC}\right) \tag{3.24}$$

(3.24) is the intra-cavity intensity in (3.16) integrated over the beam area and scaled for the output coupler transmission. Pulse energy, E_p, can be calculated by integrating P_L over a pulse and pulse duration, τ_p and repetition rate, f_{rep} can be determined directly from the ϕ output of the model.

3.3 Numerical model assumptions

Beyond the assumptions and approximations made in Section 3.2, the use of this rate equation model is made under the following extra understandings.

The overlap factor between the pump beam and cavity laser mode is considered to be unity i.e. $r_L = r_P$, and both the pump beam and laser mode are uniform within the laser cavity. In reality, matching the pump spot size to the laser mode is very achievable and for cavity lengths of the order of a Rayleigh range, the cylindrical assumption is also reasonable.

In the formation of (3.7), it was assumed that the discrete quantity $\Delta I/\Delta t$, which expresses the change in intra-cavity intensity over one round-trip, could be approximated to a continuous derivative, dI/dt. This treats the mirror-loss, experienced

by photons as they reach either end of the cavity, and the crystal gain as distributed evenly throughout the cavity, discarding any notion of interaction order. Since the cavity round-trip time is considerably less than the pulse duration, as is the case from (2.7) even for large ΔR, and the non-saturable losses and gain are of comparable magnitude in typical microchip laser designs, this approximation holds. We have tested models that model discrete losses and generated results to within a few per cent of the distributed loss model, with the drawback of drastically increased computation time.

The derivation of the amplification factor in (3.2) assumes that the inversion population density is spread homogeneously throughout the gain medium. In reality, there is a greater inversion density at the pump-input, or front, end of the crystal since the dopant ions in this location see the greatest intensity of pump light.

The effect of uneven distribution of the inversion density throughout the longitudinal thickness of the crystal can be considered by using the differential form of (3.1), which is appropriate for spatially varying inversions:

$$\frac{dI'}{dl} = \sigma_{em} n(l) I' \tag{3.25}$$

which can be integrated for spatially-varying inversion to give:

$$I' = Ie^{\sigma_{em}\int_0^{l_L} n(l)dl} \tag{3.26}$$

The integral $\int_0^{l_L} n(l)\,dl$ is equal to $n_{ave} l_L$ where n_{ave} is the inversion density averaged across the entire length of the gain medium, showing that the longitudinal distribution of inversion density throughout the length of the medium has no effect on the single-pass gain.

We neglect the effects of the standing wave formation inside the laser cavity. We assume that the photon density ϕ is uniformly distributed, whereas for a single longitudinal mode (as most often is seen in lasers under 300 μm) the photon density is distributed as $2\phi \sin^2(2\pi z/\lambda)$. We note that changing this distribution does not affect the predicted threshold for the laser, nor does it affect the behaviour of the laser for

small depletions of the gain: this is because the spatial average of the field is unchanged, and enhanced interaction around the field antinodes compensates for the reduced interaction around the nodes. There may begin to be differences in predicted behaviour for pumping far above threshold, and a full description should account for this spatial variation, the 'diffusion' of gain, and competition of second longitudinal modes – the components of such a model are described in [173]. This is left for future work.

The rate equation model also uses the assumption that both the laser and pump photon distributions have a top-hat transverse distribution rather than the realistic Gaussian formation [174]. For generality, we should integrate transversely the stimulated emission term from the rate equations (3.21) and (3.22) for arbitrary distributions of n and ϕ, resulting in a term $c_L \sigma_{em} n_{total} \phi_{total} K$. n_{total} and ϕ_{total} are the total numbers across the distribution of the inversion population and cavity photons respectively and retain the same values regardless of distribution. The normalising overlap factor, K, takes into account the shape of the particular distribution and is defined in a normalised overlap integral:

$$K = \frac{\int_0^\infty n(r)\phi(r)2\pi r dr}{\int_0^\infty n(r)2\pi r dr \int_0^\infty \phi(r)2\pi r dr} \tag{3.27}$$

Calculating K first for top-hat distributions of n and ϕ of radius r_B and then for Gaussian distributions of radius r_B at e^{-2} gives:

$$\begin{aligned} K_{T\text{-}H} &= \frac{\int_0^\infty n_0 \phi_0 2\pi r dr}{\int_0^\infty n_0 2\pi r dr \int_0^\infty \phi_0 2\pi r dr} \\ &= \frac{4 n_0 \phi_0 2\pi {r_B}^2}{2 n_0 2\pi {r_B}^2 \phi_0 2\pi {r_B}^2} \\ &= \frac{1}{\pi {r_B}^2} \end{aligned} \tag{3.28}$$

$$K_G = \frac{\int_0^\infty n_0 e^{\frac{-2r^2}{r_B^2}} \phi_0 e^{\frac{-2r^2}{r_B^2}} 2\pi r dr}{\int_0^\infty n_0 e^{\frac{-2r^2}{r_B^2}} 2\pi r dr \int_0^\infty \phi_0 e^{\frac{-2r^2}{r_B^2}} 2\pi r dr}$$
$$= \frac{\int_0^\infty r e^{\frac{-4r^2}{r_B^2}} dr}{2\pi \int_0^\infty r e^{\frac{-2r^2}{r_B^2}} dr \int_0^\infty r e^{\frac{-2r^2}{r_B^2}} dr}$$
$$= \frac{1}{\pi r_B^{\,2}} \qquad (3.29)$$

The results in (3.28) and (3.29) show that matched top-hat distributions of radius r_B are equivalent to matched Gaussian distributions of e^{-2} radius r_B. It is simpler to consider top-hat distributions with uniform values and area $\pi r_B^{\,2}$ and these results are still appropriate for Gaussian beams. This fact is employed when determining the pump volume in (3.13) and again when calculating the laser output power in (3.24).

A final concern raised by neglecting the Gaussian intensity profile within the cavity is that of beam-SESAM interaction. The SESAM is modelled under the assumption that the intensity incident on its face is spatially uniformly distributed whereas in reality, it is reasonable to suggest that the central area of the SESAM, seeing the greater intensity, will switch to high reflectivity sooner than the edges which see a lower intensity. Realistically, the intensity even in the wings of the Gaussian wavefront is more than sufficient to cause the SESAM to switch and so the effects of the Gaussian profile are not considered in the rate equation model.

3.4 Two-photon absorption in the rate equation model

It has been shown in cases where the pulse fluence of mode-locked lasers far exceeds that of the SESAM saturation fluence that the reflectivity of the SESAM does not reach and maintain a maximum value, but rather rolls-over as pulse fluence increases [150, 151]. This effect is shown in Figure 3.3 for both experimental data and a theoretical fit. The causes of this roll-over effect are non-linear absorption effects, mainly two-photon absorption (TPA), occurring in the SESAM spacer layer (typically,

GaAs), the distributed Bragg reflector (GaAs/AlAs) and additionally in the top reflector (SiO_2/Al_2O_3). Preliminary modelling of the rate equations in Section 3.2 showed that typical pulse fluences incident on the face of the SESAM of a Q-switched microchip laser were of the order of tens of times the SESAM saturation fluence, so investigation of TPA in the SESAM Q-switched model became a practical consideration.

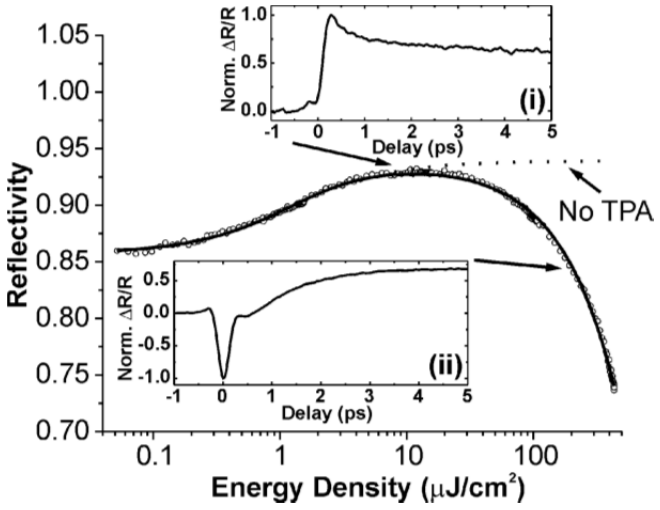

Figure 3.3: SESAM reflectivity roll-over at high pulse fluences, from [151].

Expressions heuristically modified for calculating the SESAM reflectivity incorporating the TPA effect using a TPA fluence parameter, F_{TPA}, have been demonstrated [123, 151, 175, 176] and one form is shown in (3.30) [176].

$$R_p\left(F_p\right)=1-A_{n\text{-}s}-\Delta R\left(1-e^{\frac{-F_p}{F_{SAT}}}\right)\frac{F_{SAT}}{F_p}-\frac{F_p}{F_{TPA}} \tag{3.30}$$

Similar to the reflectivity calculation mentioned at the end of Section 3.2, this model predicts the average reflectivity for a short pulse of specific duration, and indeed it is the *averaged* reflectivity rather than an instantaneous reflectivity. By taking an approach that employs an instantaneous intensity rather than pulse fluence, we here derive a TPA coefficient, β, determined according to the measured TPA behaviour of the SESAM, to derive an instantaneous reflectivity for arbitrary pulse durations.

The TPA effect is included in the overall SESAM response by including an additional loss term derived from assuming the TPA effect modifies the transmission

properties, $T_{TPA}(t)$, of a zero-thickness layer on top of the usual SESAM device where the transmission is calculated from a TPA coefficient, β, and the instantaneous intensity incident on the SESAM, $I(t)$:

$$T_{TPA}(t) = \frac{1}{1+\beta I(t)} \tag{3.31}$$

where β captures both the effective TPA absorption coefficient and the effective absorption path length in the SESAM. Values of F_{TPA} are known from experimental measurements of average SESAM reflectivity for short Gaussian pulses. In order to calculate the appropriate β for our instantaneous SESAM reflectivity, we must calculate the pulse-averaged reflectivity, R_p, for a range of pulse fluences to compare to experimental measurements.

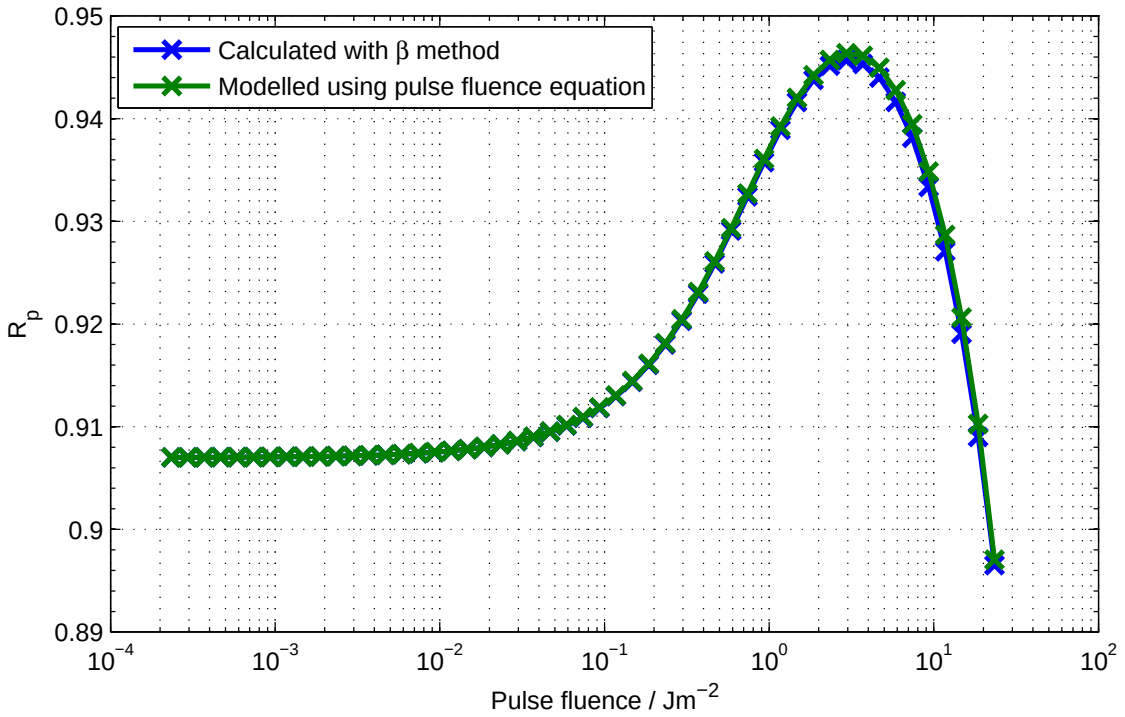

Figure 3.4: The pulse reflectivity calculated using the β method described above, compared to the pulse fluence approach described by (3.30). In this case, F_{TPA} = 356 Jm^{-2} for τ_p = 220 fs and $\beta = 1.0564\times10^{-15}$ W^{-1}m^2.

Such a calculation is shown in Figure 3.4, showing agreement with experimentally determined behaviour and our model using $\beta = 1.0564 \times 10^{-15}$ $\mathrm{W^{-1}m^2}$, for a SESAM with $F_{TPA} = 356$ $\mathrm{Jm^{-2}}$, measured using a pulse of 220 fs duration. Once β is established for a particular SESAM, $R_{SESAM,TPA} = R_{SESAM} T_{TPA}$ replaces R_{SESAM} in (3.22), with R_{SESAM} calculated as usual from (3.20).

Below are two examples to show the effect of TPA on the SESAM performance. The instantaneous SESAM response for a fast pulse is shown in Figure 3.5 for a low pulse-fluence case, which does not even fully switch the SESAM, and a high fluence case where the SESAM fully switches although its net reflectivity is diminished due to the large TPA component. We will show that TPA can be substantial in microchip lasers, particularly as we scale the lasers to generate the shortest possible pulses.

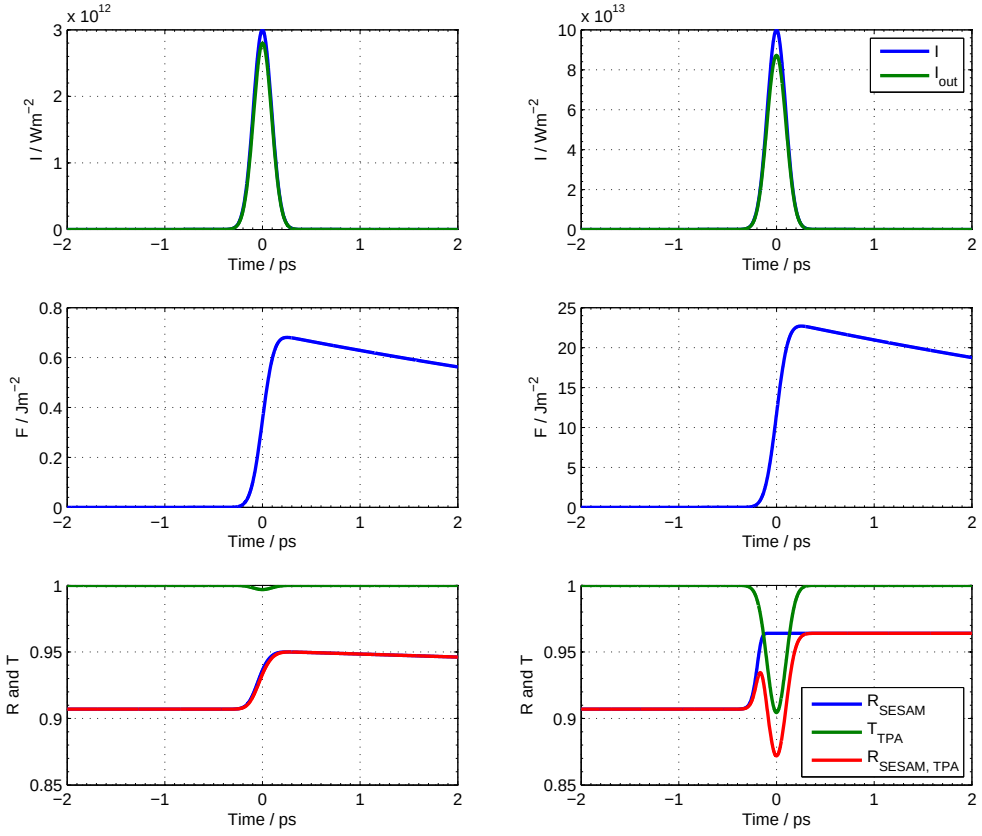

Figure 3.5: Left hand side shows the intensity of the input and output pulses (top), the fluence in the SESAM (middle) and the resulting SESAM responses (bottom) for a low fluence pulse. Right hand side shows the same for a high fluence pulse for the same SESAM parameters. Please note the difference in y-axis scales between cases.

3.5 Analytic results derived from the rate equations

Although the rate equations in 3.2 are intended to be solved numerically, we first look in more detail at some analytic results, which will be used later in analysis.

From (3.15) and neglecting the small spontaneous photon contribution, we can calculate some steady state values. Setting the rate of change of photon density to zero:

$$\frac{d\phi}{dt} = c_L \sigma_{em} n_{S\text{-}S} \phi - \frac{-\ln\left(R_{OPC} R_{SESAM}\right)}{\tau_{rt}} \phi = 0$$

$$\Rightarrow n_{S\text{-}S} = \frac{-\ln\left(R_{OPC} R_{SESAM}\right)}{2\sigma_{em} l_L} \tag{3.32}$$

where $n_{S\text{-}S}$ is the value of n for steady-state given the reflectivities of the output coupler and SESAM. If $n > n_{S\text{-}S}$, ϕ increases and if $n < n_{S\text{-}S}$, ϕ decreases. The expression in (3.32) can also be obtained by rearranging (3.2) to give the net round trip gain coefficient, G_{rt}:

$$G_{rt} = \frac{I''}{I} = R_1 R_2 e^{2\sigma_{em} n l_L} \tag{3.33}$$

By setting G_{rt} to 1, (3.32) is derived again. $n_{S\text{-}S}$ and G_{rt} depend on the instantaneous value of R_{SESAM}, and so are themselves dynamic parameters, whose rapid change as the SESAM switches causes the formation of the pulse. The evolution of these values will be tracked through the pulse cycle in the next section.

We can predict the minimum pump power to initiate lasing by solving (3.14) for $dn/dt = 0$ and setting $n = n_{S\text{-}S,\,U\text{-}S}$ for the un-switched, high-loss SESAM state and $\phi = 0$:

$$\frac{dn}{dt} = -c_L \sigma_{em} n_{S\text{-}S,\,U\text{-}S} \phi_{th} + \frac{P_{P,th}}{h\nu_P} \frac{1}{\pi {r_P}^2 l_L} \left(1 - e^{-2\left(n_{tot} - n_{S\text{-}S,\,U\text{-}S}\right)\sigma_{abs} l_L}\right) - \frac{n_{S\text{-}S,\,U\text{-}S}}{\tau_L} = 0$$

$$\Rightarrow P_{P,th} = \frac{-\ln\left(R_{OPC} R_U\right) h\nu_P \pi {r_P}^2}{2\sigma_{em} \tau_L \eta_P} \tag{3.34}$$

3.6 General numerical modelling results

We now move on to using the numerical model to predict the operation of SESAM Q-switched lasers. For the following plots and results in this section and the next, unless otherwise specified, the values of variables used in modelling have been the nominal values for the favoured general laser design used in experiment and are shown in the following table. TPA is not included in the initial results since its effect is analysed later in the chapter, although the β parameter is included in Table 3.3.

Component	Property	Symbol	Value
Gain crystal a-cut 3 at.% Nd:YVO_4	Absorption cross-section, π	$\sigma_{abs,\pi}$	1.392×10^{-23} m^2
	Absorption cross-section, σ	$\sigma_{abs,\sigma}$	5.464×10^{-24} m^2
	Emission cross-section	σ_{em}	25×10^{-23} m^2
	Total laser ion density	n_{tot}	3.75×10^{26} m^{-3}
	Upper state lifetime	τ_L	50 µs
	Speed of light in crystal	$c_L = c/n_{RI}$	1.96
	Emission light frequency	$\nu_L = c/\lambda_L$	λ_L = 1064 nm
	Spontaneous photon to cavity coupling efficiency	M	1.75×10^{-5}
Pump source	Pump light frequency	$\nu_P = c/\lambda_P$	λ_P = 808 nm
	Power	P_P	100 mW
	Spot size	r_P	9 µm
Cavity	Length	l_L	110 µm
	Laser mode radius	r_L	9 µm
	Output coupling reflectivity	R_{OPC}	90%
SESAM	Modulation depth	ΔR	13%
	Unsaturated reflectivity	R_U	80%
	Relaxation time constant	τ_{SESAM}	9 ps
	Saturation fluence	F_{SAT}	0.7 Jm^{-2}
	TPA coefficient	β	1.0564×10^{-15} W^{-1}m^2

Table 3.3: Variable values for use in general numerical modelling results unless otherwise specified.

An item of note in Table 3.3 is the replacement of the absorption cross-section, σ_{abs}, with the polarisation-specific absorption cross-sections, $\sigma_{abs,\pi}$ and $\sigma_{abs,\sigma}$. Figure 3.6 shows the measured absorption spectra, for π and σ polarisations, of a 310 µm thick sample of a-cut 3 at.% Nd:YVO_4 obtained using a Cary 5000 spectrophotometer, configured for an incident beam of 2 nm spectral bandwidth, the same as that of the diode that will be used for pumping. In reality, the absorption peaks have very narrow

bandwidths and considerably higher absorption coefficients, but measuring using a beam of spectral content similar to the pump source allows the determination of effective absorption cross-sections.

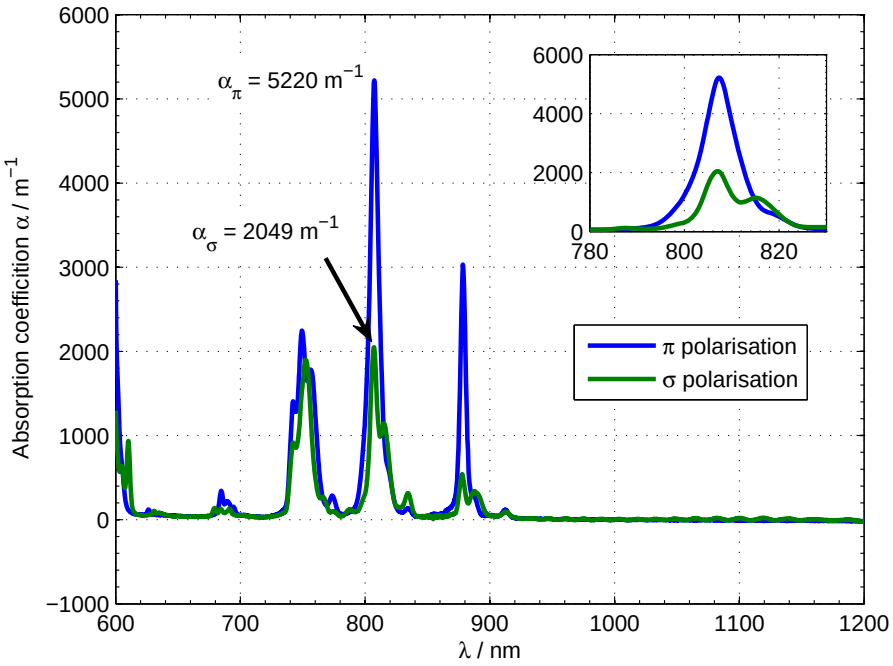

Figure 3.6: Absorption spectra for 3 at.%. Nd:YVO4 in π and σ polarisations for a probe beam with spectral bandwidth of 2 nm. Inset shows detail around 808 nm absorption peak. The thickness of the crystal measured was 310 μm.

Using the peak values from Figure 3.6, the cross-sections are determined using the relationship $\sigma_{abs} = \alpha / n_{tot}$ and included in Table 3.3. To model absorption of an unpolarised pump source these split absorption cross-sections require modification of the rate equations to model separately the two orthogonal polarisations, π and σ. The inversion density rate equation in (3.21) is now modified:

$$\begin{aligned}\frac{dn}{dt} = -c_L \sigma_{em} n\phi + \frac{P_P}{2h\nu_P}\frac{1}{\pi r_P^{\,2} l_L}\left(1 - e^{-2(n_{tot}-n)\sigma_{abs,\pi} l_L}\right) \\ + \frac{P_P}{2h\nu_P}\frac{1}{\pi r_P^{\,2} l_L}\left(1 - e^{-2(n_{tot}-n)\sigma_{abs,\sigma} l_L}\right) - \frac{n}{\tau_L}\end{aligned} \tag{3.35}$$

For ease of reference, (3.35) can be shortened to:

$$\frac{dn}{dt} = -c_L \sigma_{em} n\phi + \frac{P_P}{h\nu_P} \frac{1}{\pi r_P{}^2 l_L} \eta_P - \frac{n}{\tau_L} \tag{3.36}$$

where:

$$\eta_P = \frac{\left(2 - e^{-2(n_{tot}-n)\sigma_{abs,\pi} l_L} - e^{-2(n_{tot}-n)\sigma_{abs,\sigma} l_L}\right)}{2} \tag{3.37}$$

is the pump absorption efficiency.

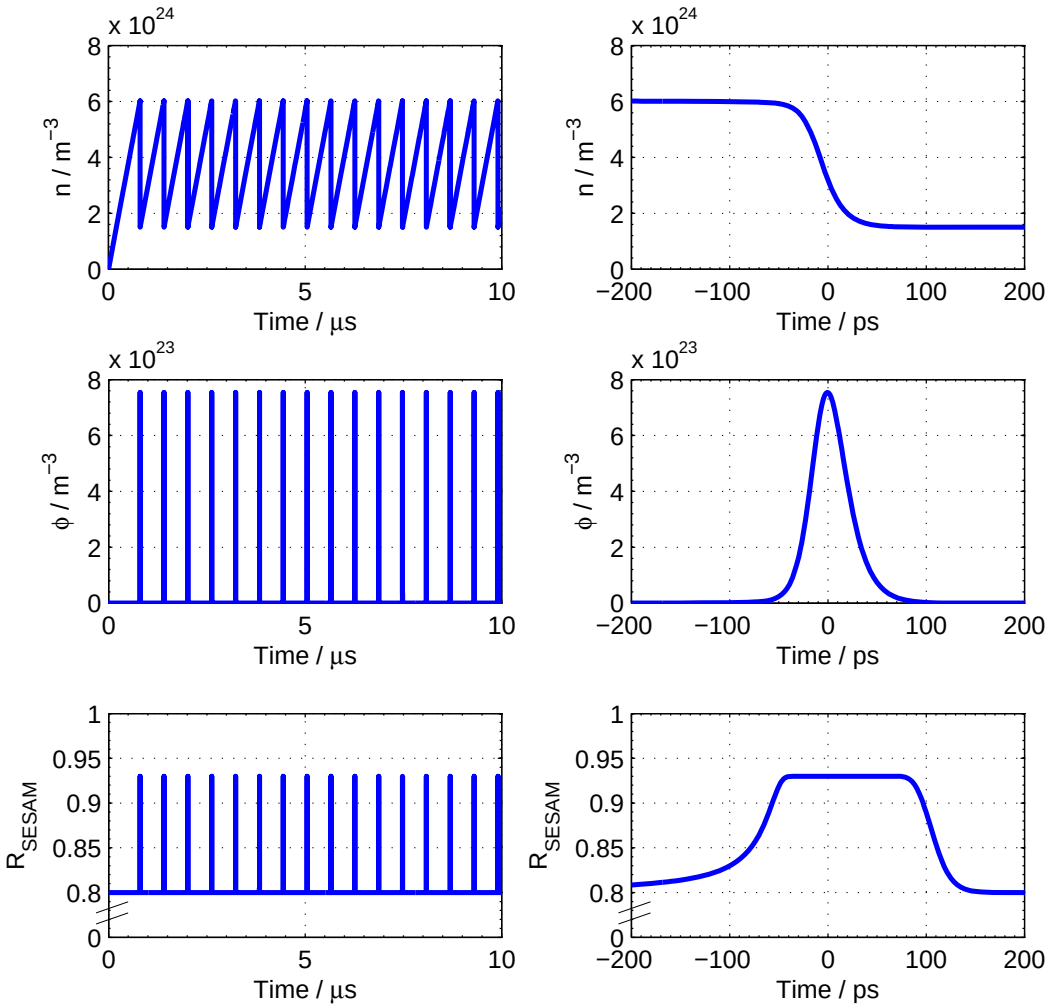

Figure 3.7: The three output variables of the numerical rate equation solution evolving over time for parameters described in Table 3.3, showing a pulse train over 10 µs (LHS) and detail of a pulse over 400 ps (RHS). Top: inversion density, middle: cavity photon density, bottom: SESAM reflectivity.

Figure 3.7 shows the typical numerical model output for a functioning SESAM Q-switched laser. It is characterised by a steady train of pulses in ϕ with corresponding

sharp depletions of n and modulation of R_{SESAM}. The pulse detail in Figure 3.7 shows the pulse shape and SESAM response, demonstrating that the SESAM is fully-switched very early in the pulse, and stays in its high reflectivity state for the entire pulse. The derived pulse duration is 42 ps, the repetition rate is 1.6 MHz and the pulse energy is 13 nJ.

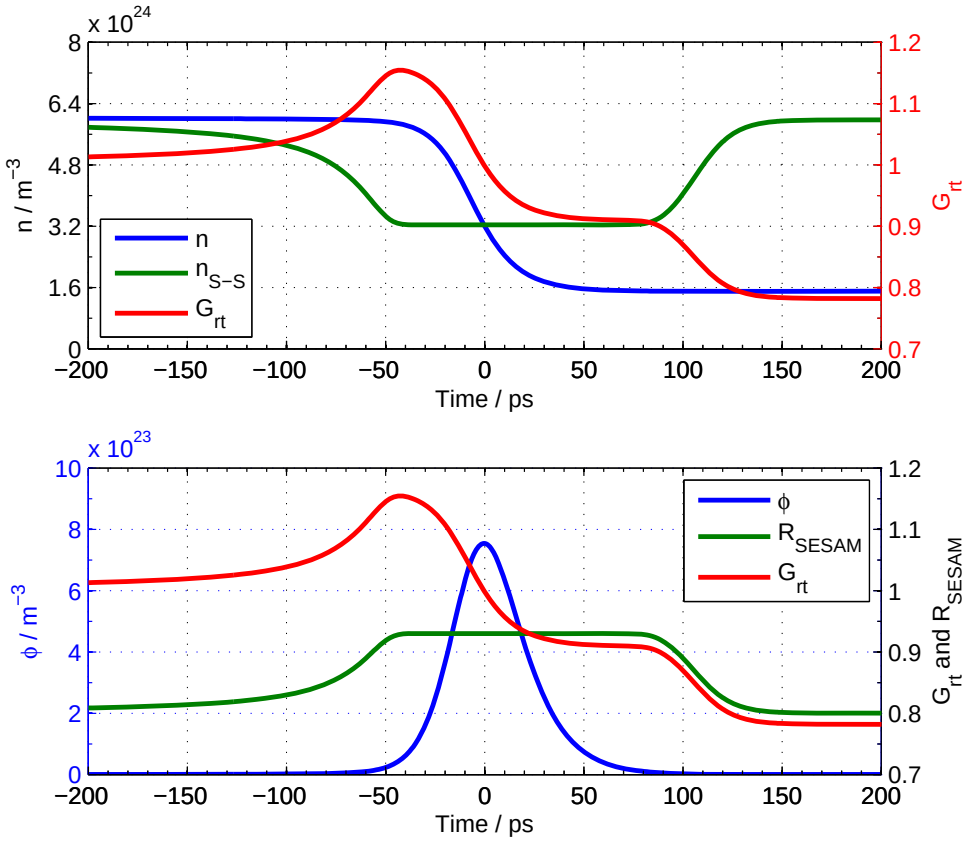

Figure 3.8: The evolution of a Q-switched pulse over time, showing the relationships between n and $n_{S\text{-}S}$ and G_{rt} and ϕ.

In Figure 3.8 the output variables are plotted with the steady-state inversion value, $n_{S\text{-}S}$, and the round-trip gain coefficient, G_{rt}. At a point around 10 ns before the peak of the pulse, the inversion density reaches the threshold value set by the low reflectivity state of the SESAM and the rate of photon emission by stimulated emission exceeds the rate of photon loss. The increased density of photons in this Q-switched cavity causes the SESAM to start switching, lowering the loss component, lowering $n_{S\text{-}S}$ and raising the round-trip gain and increasing the cavity photon density further.

This avalanche effect builds and ϕ increases until the inversion population density is depleted below the threshold value set by the high reflectivity state of the SESAM.

The peak of the pulse corresponds with both $n = n_{S\text{-}S}$ and $G_{rt} = 1$. Note that there is sufficient fluence even in the tail-end of the pulse to keep the SESAM saturated and in its high reflectivity state until long after the body of the pulse has passed.

3.7 Laser design relationships derived from numerical modelling results

Considering that the primary reason for specifically choosing a microchip Q-switched laser design is to generate short pulses, it is important to first examine the design properties that control the pulse duration. From the analytical approaches in Section 2.6, an informed starting point is to investigate the influence of cavity length l_L, and SESAM modulation depth ΔR, with τ_p expected to be $\propto l_L / \Delta R$.

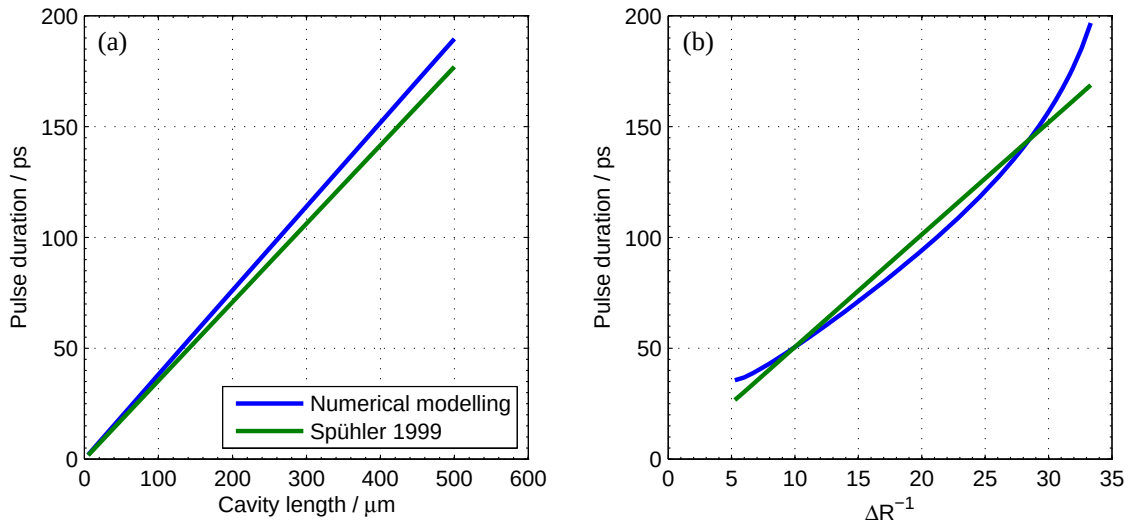

Figure 3.9: Pulse duration scaling with (a) cavity length and (b) SESAM modulation depth. The analytic modelling results from Spühler *et al.* [69], are included for comparison.

The proportional relationship between microchip cavity length and Q-switched pulse duration is clearly evident in Figure 3.9 (a), although it is not a perfect fit with the analytic approach of Spühler *et al.*, outlined in Section 2.6. Similarly, although the expected inverse relationship between pulse duration and modulation depth is approximately reflected in Figure 3.9 (b), there are significant deviations from the

analytic model. These deviations arise from the approximations made during the formation of the analytic expressions.

Note that the predicted pulse duration from the model extends down to extremely low crystal thicknesses, showing that such lasers still switch successfully. We can predict the lower limit of length scaling by replacing $n_{S\text{-}S}$ for the high-loss SESAM state with n_{tot} in (3.32) and rearranging for l_L. This will calculate the minimum gain thickness possible, defined by the point when 100% of the available gain ions must be in the high energy state:

$$l_{L,\min} = \frac{-\ln\left(R_{OPC}R_U\right)}{2\sigma_{em}n_{tot}} \tag{3.38}$$

According to (3.38), the minimum thickness of gain material required to successfully Q-switch a laser that uses 3 at.% Nd:YVO_4 with the SESAM and output coupler described in Section 3.6 is just 1.75 µm. At this thickness, the pulse duration determined from numerical modelling is 675 fs, the pulse energy 13 nJ and the optical-optical slope efficiency 0.08%. This pulse duration is just about sustainable given the gain bandwidth of Nd:YVO_4, although manufacturing and handling crystals a few micrometres thick pose their own limits. Since the penetration depth of the cavity field into the SESAM is generally accepted to be of the order of a few µm [69, 124], it is insignificant in the practically achievable range of cavity lengths we are testing. However, it will require consideration in extremely short cavities and as such the 675 fs prediction is only offered as an estimate. We note that previous experiments have not come close to reaching this fundamental length-scaling limit, and so the scope for decreasing the pulse duration by decreasing the cavity length is substantial. Of course, the efficiency of such thin devices becomes extremely low, but that can be countered by other means.

We now discuss some derived quantities that can give insight into the scaling behaviour of microchip lasers and the shortfalls of the previously discussed analytic models. From examination of the rate equation for cavity photon density in (3.22) using the definition of the inversion density for steady state in (3.32), the rate of change of

cavity photon density is found to be proportional to the difference between the inversion density and the inversion density for steady state:

$$\frac{d\phi}{dt} = \left[c_L \sigma_{em} n - \frac{-\ln\left(R_{OPC} R_{SESAM}\right)}{\tau_{rt}} \right] \phi$$

$$\Rightarrow \frac{d\phi}{dt} \propto c_L \sigma_{em} \left(n - n_{S\text{-}S} \right) \tag{3.39}$$

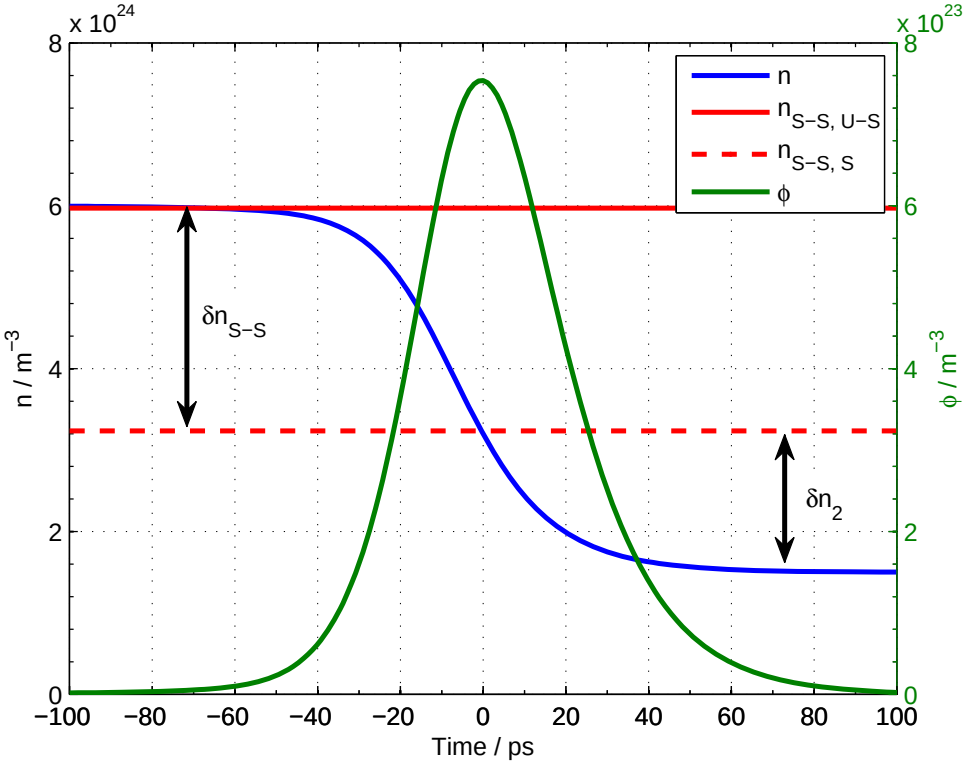

Figure 3.10: The evolution of a pulse in time (green), showing the inversion population density (blue) in relation to the steady-state values determined by the un-switched (red, solid) and switched (red, dashed) SESAM reflectivity values.

Figure 3.10 shows the behaviour of the inversion population density during a pulse in relation to the upper and lower steady-state values, obtained when the SESAM is un-switched ($n_{S\text{-}S,\,U\text{-}S}$) and switched ($n_{S\text{-}S,\,S}$) respectively. Provided that the SESAM switches quickly, the rate of growth in the leading edge of the pulse is proportional to the difference between the two steady-state values, $\delta n_{S\text{-}S}$.

$$\delta n_{S\text{-}S} = n_{S\text{-}S,\,U\text{-}S} - n_{S\text{-}S,\,S} = \frac{-\ln\left(R_{OPC}R_U\right)}{2\sigma_{em}l_L} - \frac{-\ln\left[R_{OPC}\left(R_U+\Delta R\right)\right]}{2\sigma_{em}l_L}$$
$$= \frac{1}{2\sigma_{em}l_L}\ln\left(1+\frac{\Delta R}{R_U}\right) \tag{3.40}$$

Similarly, the rate of decay in the trailing edge of the pulse is proportional to the difference between the switched steady-state value and the final value of the depleted inversion density, δn_2. The analytic models in Section 2.6 were derived on the assumption that δn_2 is the same size as $\delta n_{S\text{-}S}$, leading to a symmetric pulse. This is achieved only if the saturable loss is small compared to the non-saturable losses, which is an unlikely situation when the aim is to generate short pulses from reduced-thickness gain media.

As in the analytic models and since pulse duration is inversely proportional to the rate of decay and growth of the pulse, from (3.39) and (3.40) and by assuming symmetry we can say:

$$\tau_p \propto \frac{l_L}{c_L \ln\left(1+\frac{\Delta R}{R_U}\right)} \tag{3.41}$$

which is independent of variables such as output coupler reflectivity and emission cross-section. In the analytic models, the further approximation is made that for small ΔR the log term approximates to ΔR with $R_U \approx 1$, removing the un-switched SESAM reflectivity from the equation. It is clear from the inversion density levels in Figure 3.10 and indeed from the pulse shape itself that the pulse is not symmetric, i.e. $\delta n_2 \neq \delta n_{S\text{-}S}$. Through numerical modelling we find that these parameters do influence the FWHM pulse duration, as shown compared to an analytic model in Figure 3.11.

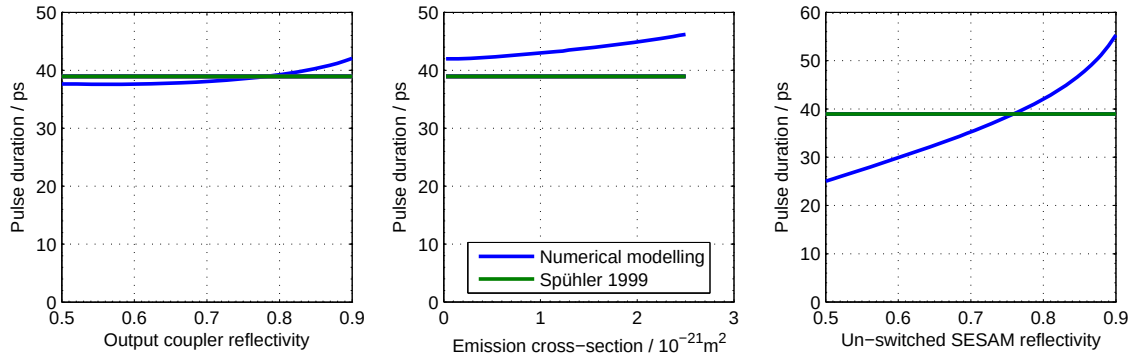

Figure 3.11: Pulse duration dependence on output coupler reflectivity, emission cross-section and un-switched SESAM reflectivity, based on the laser described by parameters in Table 3.3.

It is a similar case for pulse energy where, under the symmetry assumption, $E_p \propto Al_L \delta n_{S\text{-}S}$ since $\delta n_{S\text{-}S}$ represents the density of transiting ions releasing laser photons during depletion. As such, pulse energy should be independent of cavity length. Output coupler reflectivity and un-switched SESAM reflectivity are included in the analytic expressions for pulse energy, but only as cavity losses rather than also accounting for their influence over δn_2. When the relationships between these three variables and pulse energy are tested in the numerical model, the results are again found to deviate from those based on the symmetry assumption as shown in Figure 3.12.

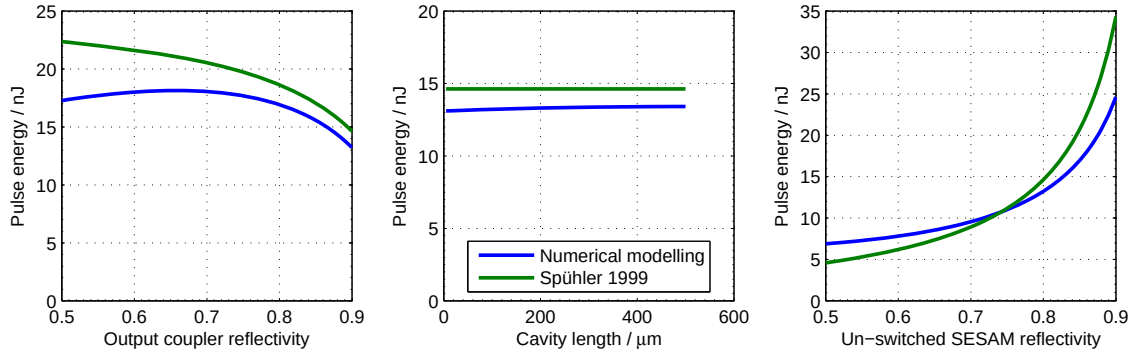

Figure 3.12: Pulse energy dependence on output coupler reflectivity, cavity length and un-switched SESAM reflectivity.

The results given between Figure 3.9 and Figure 3.12 demonstrate the consequences of the symmetry approximation in the analytic models. While we can say that the analytic and numerical models loosely follow the same trends, we also show that component parameters assumed not to influence output behaviour clearly can, and in some cases drastically, affect the performance of the laser. The comprehensive

approach of the numerical model accounts for asymmetry in the laser pulse and more effectively covers regimes where the analytic models are inappropriate e.g. when saturable loss is comparable to non-saturable loss.

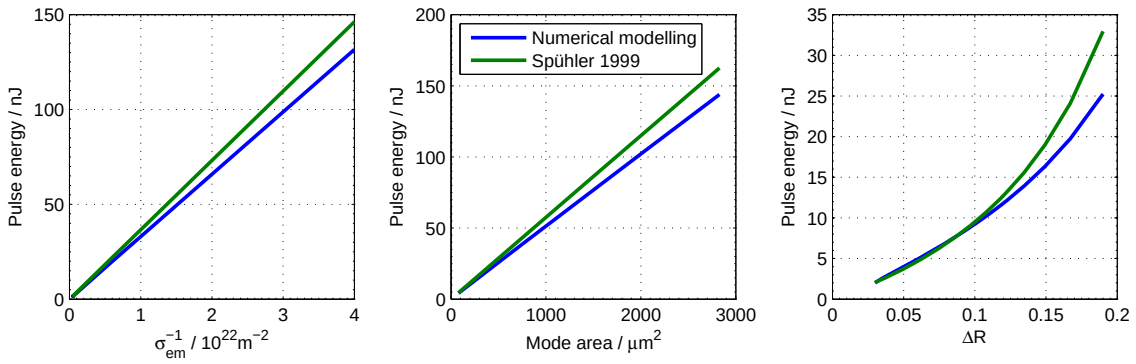

Figure 3.13: The dependence of pulse energy on emission-cross section, laser mode area and SESAM modulation depth.

The dependences of pulse energy on emission cross-section, mode area and modulation depth, three variables that are predicted to directly affect pulse energy by the analytic model in (2.6), are shown in Figure 3.13. In a similar fashion to the dependence of pulse duration on cavity length, and to a lesser extent SESAM modulation depth, the relationships are clear although deviation from the analytically predicted values can be seen, accredited again to pulse asymmetry. In this case, the dependence of pulse energy on modulation depth is not linear owing to the SESAM non-saturable loss ($A_{n\text{-}s}$) varying in tandem with modulation depth to maintain the relationship $A_{n\text{-}s} + R_U + \Delta R = 1$ for constant R_U.

In terms of controlling pulse repetition rate, most of the variables in Table 3.3 have a strong influence. The more strongly the inversion is depleted, the larger the value of $\delta n_{S\text{-}S}$ and the longer the pumping period until threshold is reached again. The inter-pulse period should then scale as $\delta n_{S\text{-}S}/\eta_P$, where η_P is the pump absorption efficiency, as suggested in the analytic model (2.10). Changes in the pump absorption dominate this scaling as gain thickness changes, leading to the saturation of the repetition rate as cavity length is increased in Figure 3.14. Other material parameters that don't appear in the pump absorption efficiency term influence repetition rate through their presence in $\delta n_{S\text{-}S}$, as shown for emission cross-section in Figure 3.14.

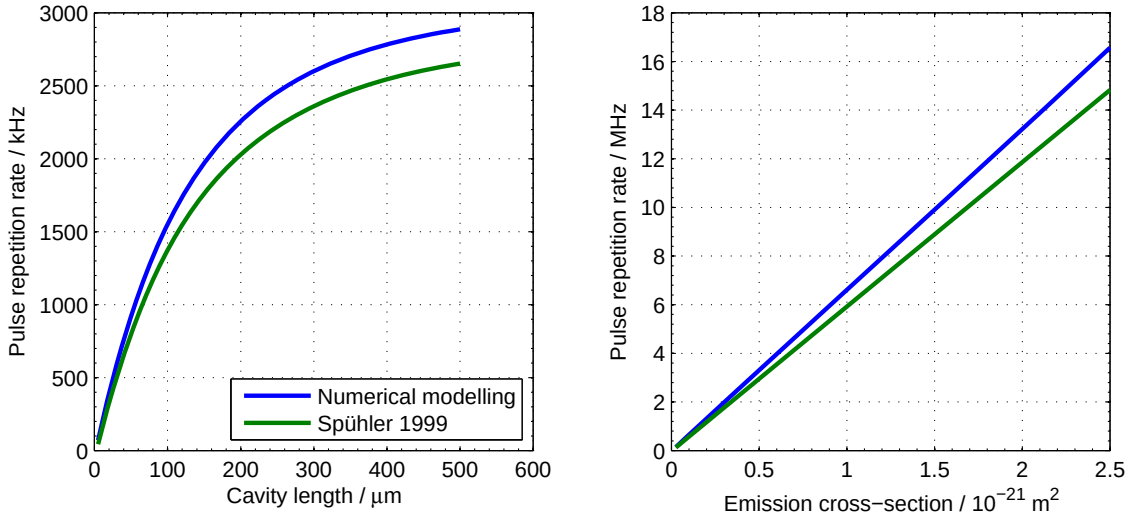

Figure 3.14: The scaling of pulse repetition rate with cavity length and emission cross-section.

Finally the input pump power, P_P, can be increased or decreased to control the pulse repetition rate while leaving other output parameters, such as pulse duration and pulse energy, almost completely unchanged.

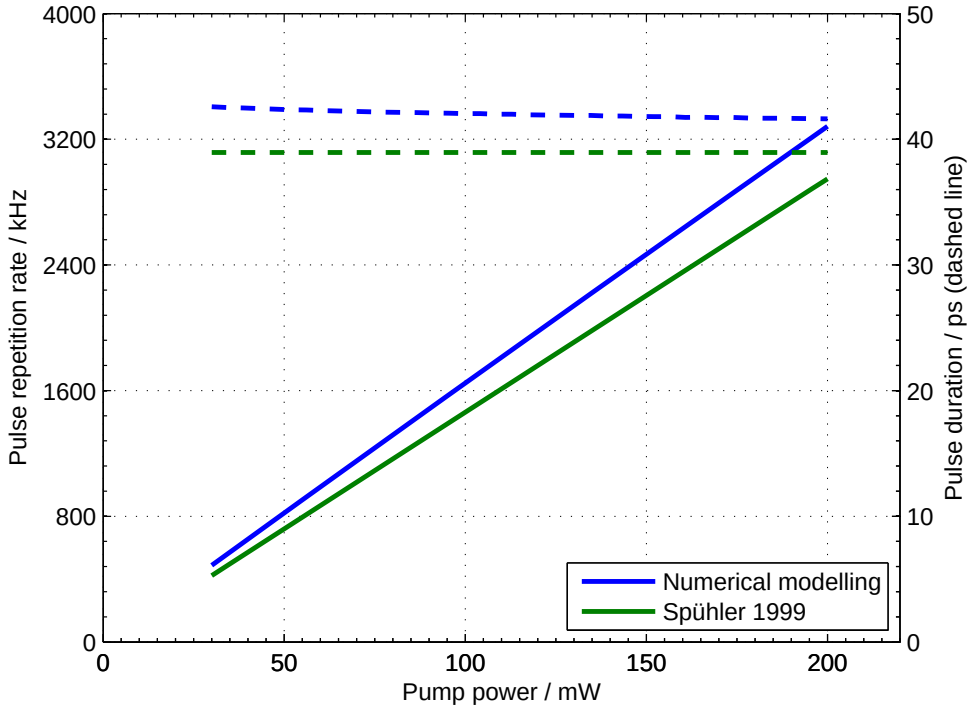

Figure 3.15: The linear relationship between pump power and pulse repetition rate, showing pulse duration (dashed lines) as unaffected.

The rate of increase of inversion density is linearly dependent on the pump power absorbed by the crystal and as such, the pulse repetition rate is proportional to input pump power, as confirmed in Figure 3.15. This result is an extremely useful benefit of the passively Q-switched microchip laser design. Similar control over repetition rate is afforded to actively Q-switched systems by simply varying the frequency of the Q-switch operation. However, to do this without changing the pulse energy requires the pump power to be changed correspondingly. The passively Q-switched system enables repetition rate control by varying only a single input parameter and even allows single pulse operation. The downside of this dependence is that small fluctuations in the diode output power cause inter-pulse timing jitter.

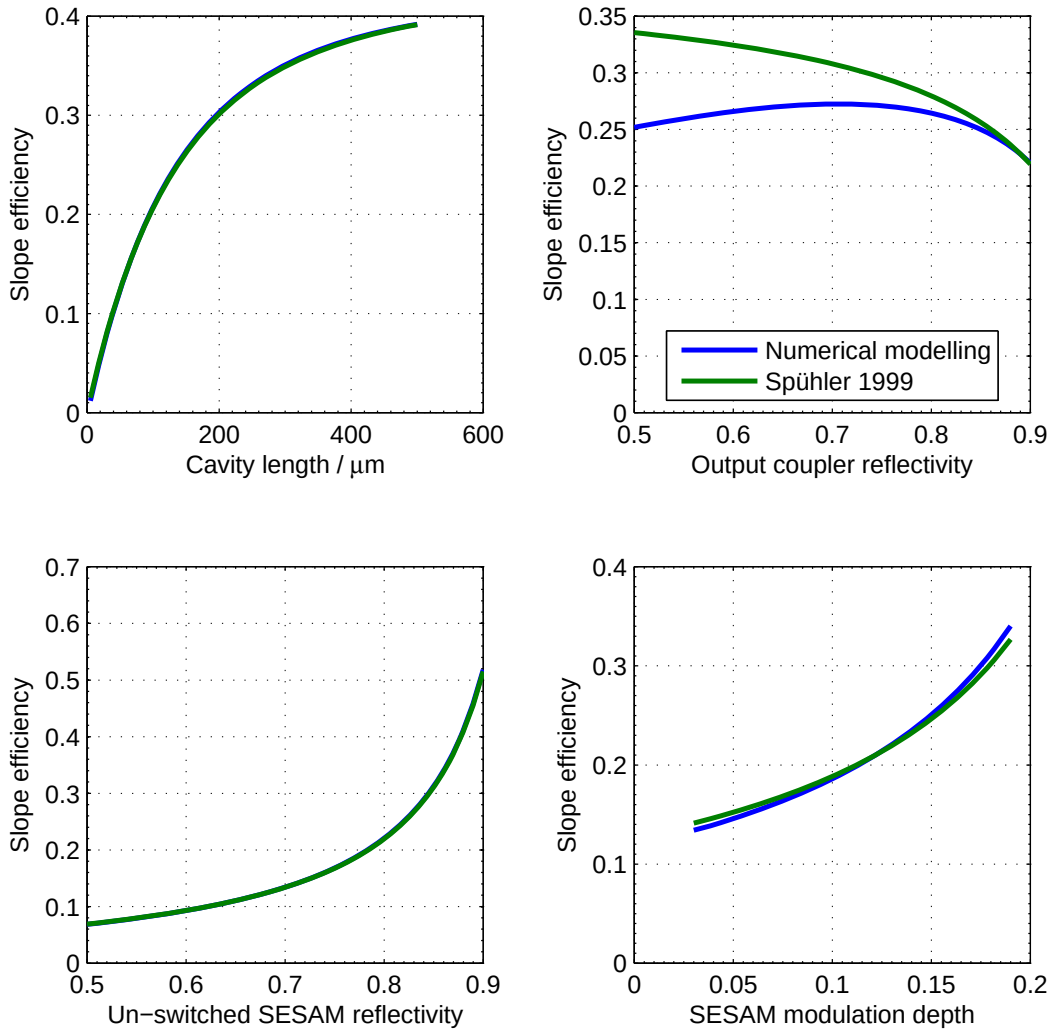

Figure 3.16: The dependence of optical-optical conversion efficiency on cavity length, output coupler reflectivity, un-switched SESAM reflectivity and SESAM modulation depth. Note the change of y-axis scales between plots.

The final useful output parameter of the laser is overall optical-optical efficiency. Overall efficiency is the approximate product of the pump absorption efficiency and output coupling efficiency. Increasing either of these – pump efficiency by increasing crystal length, doping or absorption cross section and output coupling efficiency by decreasing the output coupler reflectivity – will improve the efficiency of the laser.

Figure 3.16 shows the laser optical-optical conversion efficiency as functions of laser parameters. Short cavities, as well as high SESAM losses are seen to lower the laser efficiency, as expected. For the most part, the efficiency prediction appears not to be affected by the symmetry approximation as the numerical results closely match the analytic results. However, the relationship between numerically modelled efficiency and output coupler reflectivity is shown to depart from the analytic prediction at low output coupler reflectivities.

We can breakdown the results for the slope efficiency dependence on cavity length into a power budget, tracking how the input pump power is distributed through the various 'output' channels available to it. As fractions of the input pump power, we calculate the power loss from the cavity caused by the following mechanisms: un-absorbed pump as $1-\eta_P$ from (3.37), the loss due to output from the laser from the model outputs as $E_P f_{rep}/P_P$, the heating loss due to quantum defect as $\eta_P(\lambda_L-\lambda_P)/\lambda_P$ and the loss due to fluorescence as:

$$\frac{n_{ave} l_L \pi r_L^{\,2} h\nu_L}{\tau_L}\frac{1}{P_P} \tag{3.42}$$

where n_{ave} is the average inversion density of the pulsing laser as is recorded in the model. The fractional loss by saturable and non-saturable absorption by the SESAM is calculated as the remainder.

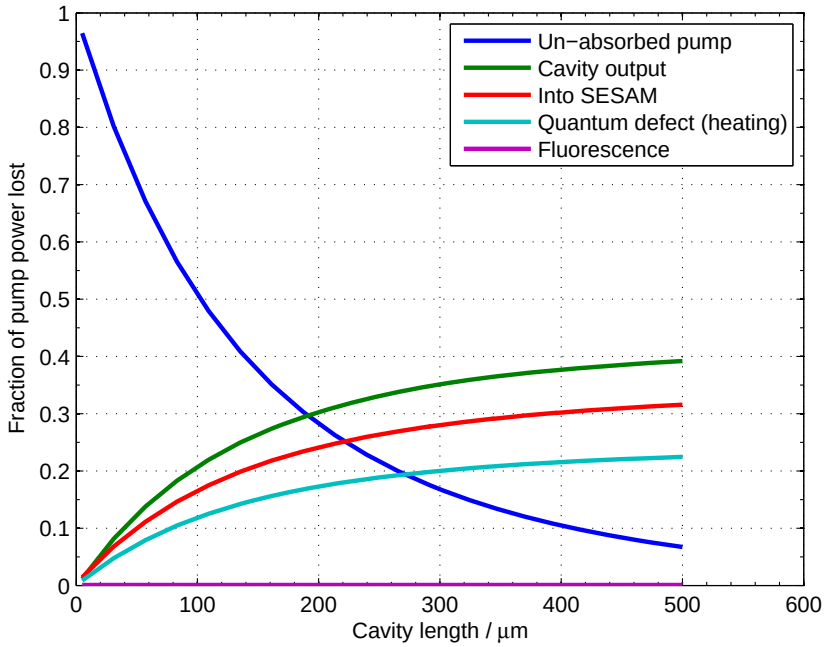

Figure 3.17: The relative sources of cavity loss as fractions of the input pump power.

From Figure 3.17 we see that fluorescence loss is comparatively very small, except for very short cavities. Since fluorescence is proportional to $n_{ave}l_L$ and $n_{ave}l_L$ is fixed at switch by constant ΔR for all cavity lengths, the fluorescence loss must be approximately the same for all cavities and so will become insignificant for longer cavities. We see that the other three output channels are similar in magnitude.

3.8 TPA effect on numerical modelling results

We now examine the effects of TPA on the laser output behaviour. During the period of high intensity incident on the SESAM, the numerical model – incorporating TPA effects from Section 3.4 – predicts a roll-over of the saturated SESAM reflectivity.

The compromised SESAM reflectivity as a result of high intensity on the SESAM is clearly evident in Figure 3.18, the roll-over coinciding with the period of high intra-cavity intensity as per (3.31). Since this is the case, any component configuration that increases the intra-cavity intensity, by either increasing the pulse energy or decreasing the pulse duration, will increase the TPA effect.

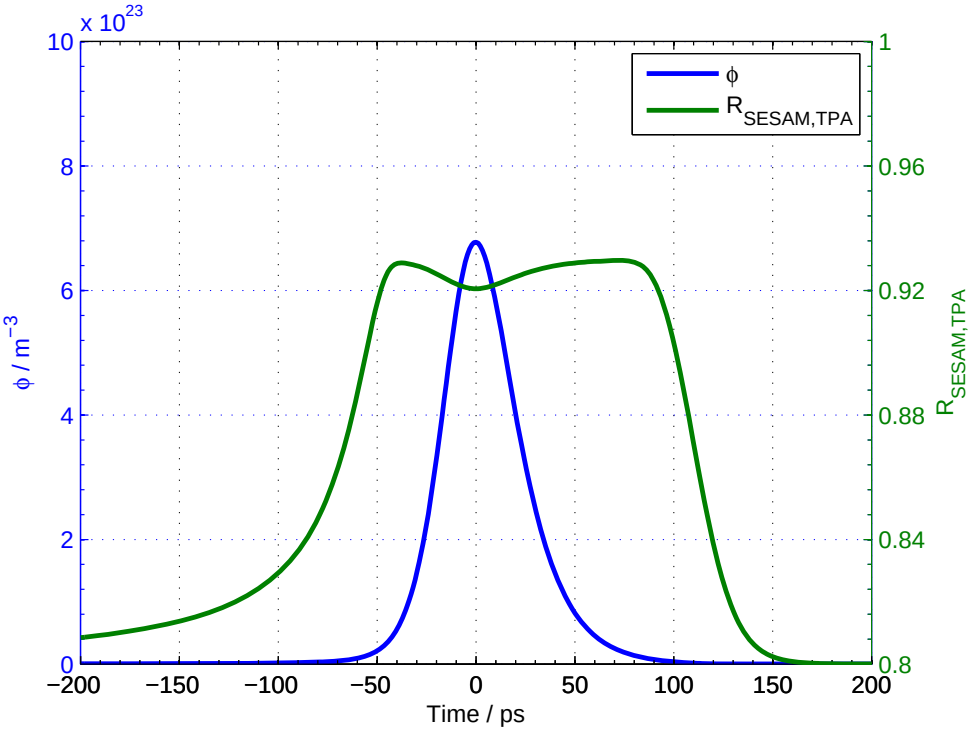

Figure 3.18: The effect of TPA in the SESAM spacer layer and distributed Bragg reflector on the reflectivity of the SESAM during a Q-switched pulse.

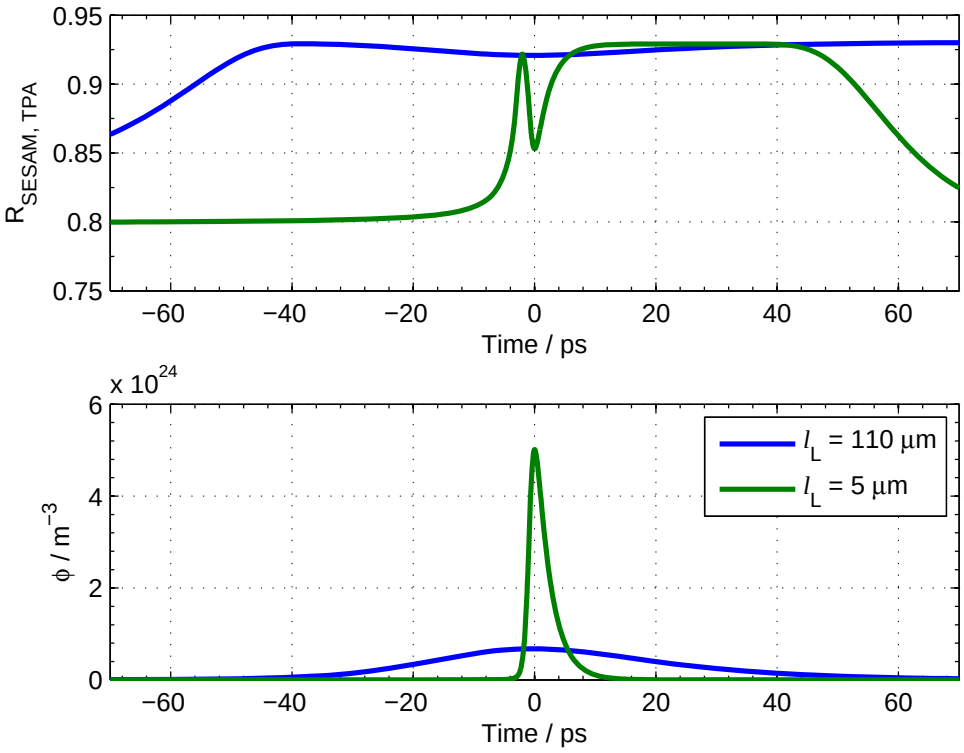

Figure 3.19: The TPA effect on SESAM reflectivities for cavity lengths of 5 µm and 110 µm.

Decreasing the resonator cavity length lowers the pulse duration while leaving the pulse energy unchanged. Its effect on the TPA-modified SESAM reflectivity is demonstrated in Figure 3.19 for 110 µm and 5 µm cavities, with cavity photon densities also shown to highlight the difference in pulse duration and intensity. The roll-over in the 110 µm cavity is shallow compared to that in the 5 µm cavity, with TPA affecting the short pulse much more. The TPA dependence on cavity length and its effect on laser output are examined further in Figure 3.20.

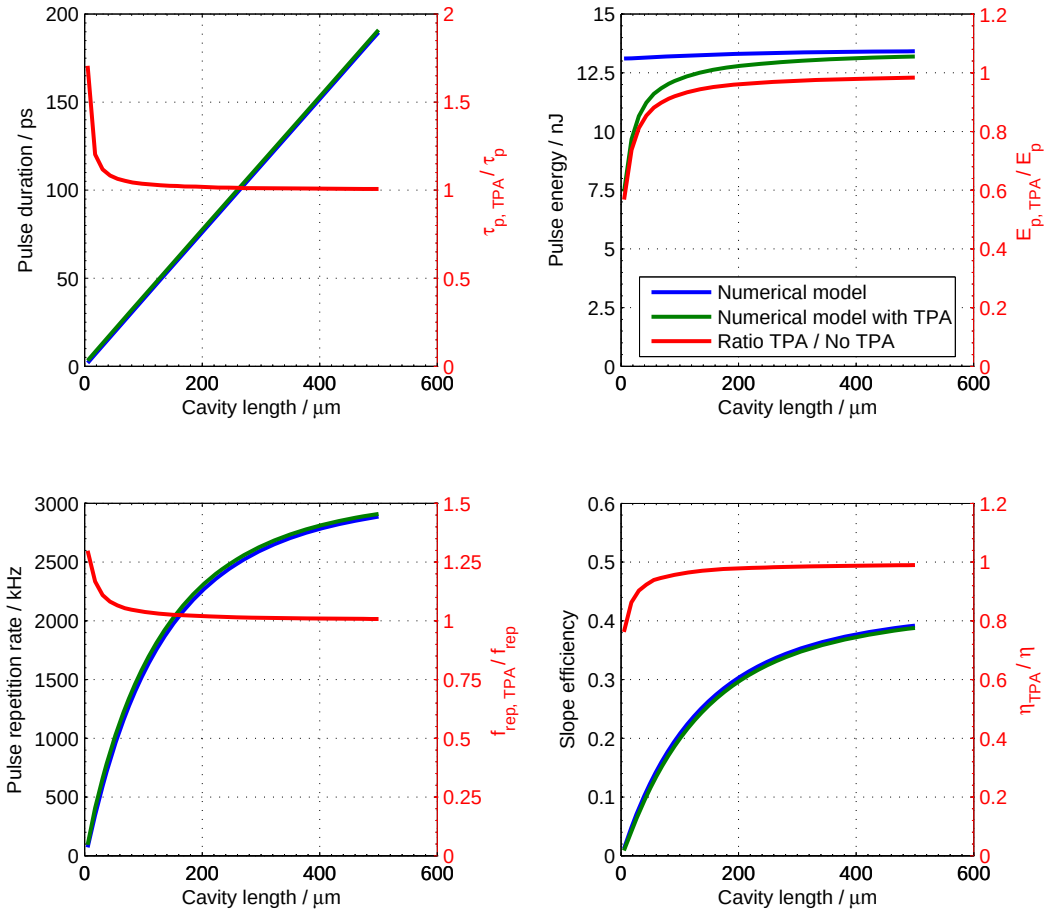

Figure 3.20: Modelled output parameters as a function of cavity length, showing the increased effect of TPA at short cavity lengths.

From Figure 3.20 it is clear that the presence of TPA in the SESAM is detrimental to the output of the laser; it serves to elongate the pulse duration, lower the pulse energy and lower the overall efficiency. The increased TPA effect at low cavity lengths, or high intra-cavity intensities, is also apparent. Low values of σ_{em} also increase TPA since the energy stored within the cavity is increased without elongating

the pulse. Previously, when TPA was not considered, pulse energy was independent of l_L, and pulse duration was independent of σ_{em}. However, TPA provides a mechanism through which these parameters can influence laser output properties that previously were unrelated, as shown in Figure 3.21.

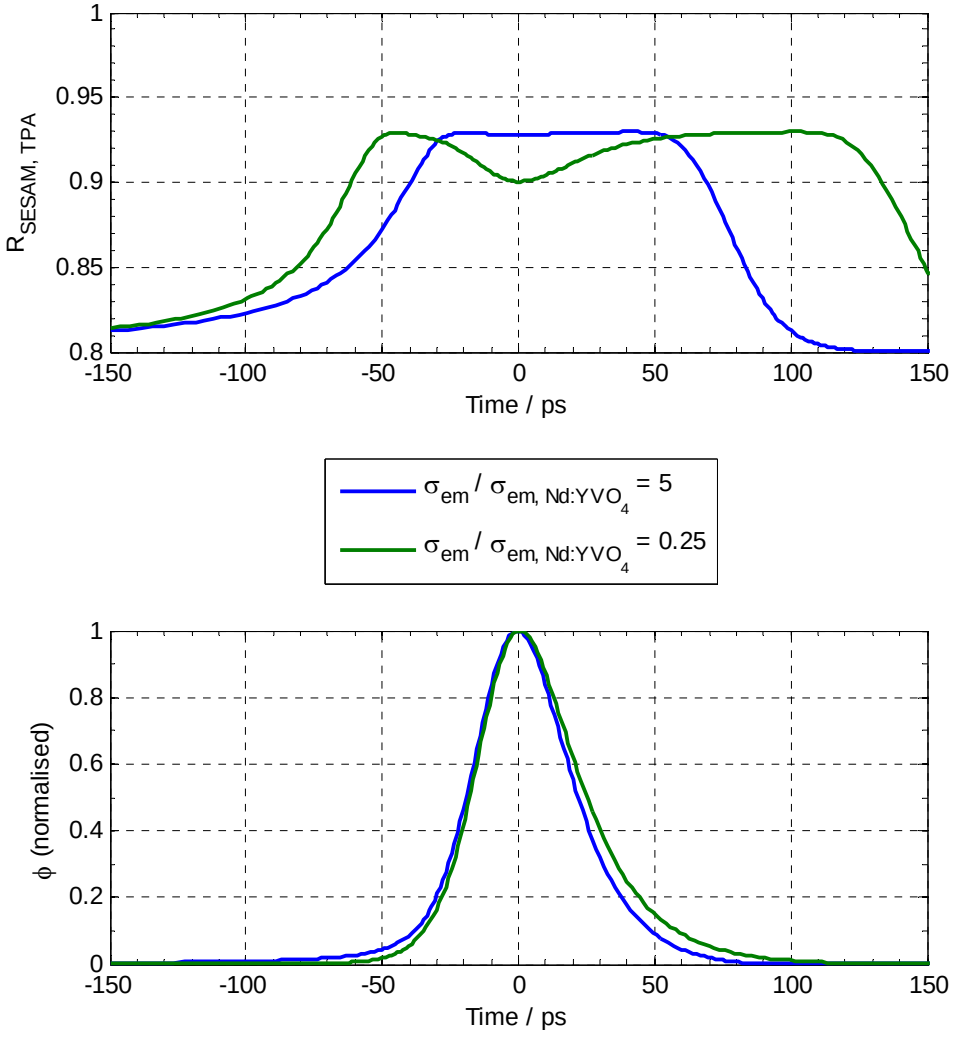

Figure 3.21: The TPA effect on SESAM reflectivity for low and high values of σ_{em}, showing extended pulse duration.

The mechanism by which TPA compromises the laser behaviour is again explainable by consideration of the $\delta n_{S\text{-}S}$ quantity defined in (3.40) and the plots in Figure 3.19 and Figure 3.21. Since the net reflectivity change of the SESAM is lessened by the TPA during the pulse, $\delta n_{S\text{-}S}$ is also compromised. Following the methods described in Section 3.7, this will elongate the pulse duration and decrease both pulse

energy and inter-pulse period. The pulse energy is lowered further owing to the additional loss factor that TPA effects on the cavity.

It is clear that the main regime where TPA is significant is for extremely short cavity lengths, where the expected pulse shortening is somewhat compromised. However, the trend to shorter pulses for shorter cavities certainly remains, and so TPA should not be a barrier to the goals of this work.

3.9 Etalons in SESAM Q-switched Microchip Lasers

If the Nd:YVO_4 gain crystal is not anti-reflection coated at the laser wavelength, there is a Fresnel reflectivity of 10.5% at the crystal/air interface. This creates two locations for air-gap etalons to form in the cavity: between the output coupler and gain crystal, and between the crystal and SESAM. The output coupler etalon serves to modify the output coupling efficiency of the resonator as a function of output coupler reflectivity and etalon thickness (for a constant gain medium refractive index). The effects of this can be predicted using the analytic expressions in Section 2.6 and the numerical modelling results in Section 3.7. However, the 'SESAM etalon' is more complex and has the potential to critically alter the Q-switching performance of the laser.

In order for it to be incorporated into the rate equations, the SESAM etalon is treated as a single entity that replaces the SESAM as the dynamic loss component in the cavity. Its net reflectivity is a function of etalon thickness, laser wavelength and the reflectivities of the two component interfaces – one of which is dynamic during the pulse cycle. We treat the SESAM as a surface, whose transmission corresponds to the SESAM absorption, and whose reflectivity is dynamic and obeys (3.20). Details of the etalon are given in Figure 3.22, showing the amplitudes of the transmitted and reflected waves, including phase changes from path length differences and reflection from high-index media. The reflectivity and transmission amplitude coefficients are r_1 and t_1, r_2 and t_2 for the crystal-air interface and air-SESAM interface respectively and are

defined in Figure 3.22. The phase change over a round-trip of the etalon for a wave of wavelength λ_L is $\delta = 4\pi n_{RI,air} d / \lambda_L$.

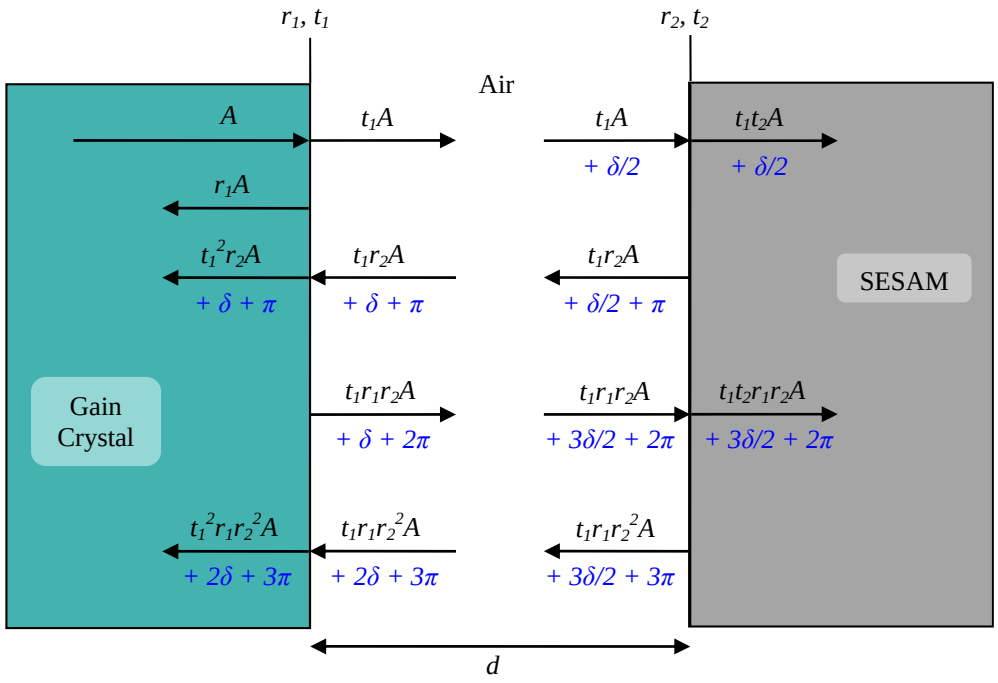

$$r_1 = \sqrt{R_{XTAL}},\ t_1 = \sqrt{1 - R_{XTAL}},\ R_{XTAL} = \frac{(n_{RI,XTAL} - n_{RI,AIR})^2}{(n_{RI,XTAL} + n_{RI,AIR})^2}$$

$$r_2 = \sqrt{R_{SESAM}},\ t_2 = \sqrt{1 - R_{SESAM}}$$

Figure 3.22: The air-gap etalon between gain crystal and SESAM, showing reflected/transmitted amplitudes and phase changes (in blue).

For a wave of amplitude A arriving at the crystal-air interface, the reflected amplitude is:

$$rA = \left[r_1 - r_2 t_1^2 e^{i\delta} \sum_{n=0}^{\infty} \left(r_1 r_2 e^{i\delta} \right)^n \right] A = \left[r_1 - r_2 t_1^2 e^{i\delta} \frac{1}{1 - r_1 r_2 e^{i\delta}} \right] A \qquad (3.43)$$

giving the net reflectivity of the SESAM etalon to the laser light as $R_{S\text{-}E,L} = \left| r^2 \right|$. The reflectivity of the SESAM etalon, primarily a function of SESAM reflectivity and etalon thickness, replaces the SESAM reflectivity in the photon density rate equation (3.22).

In addition, the SESAM etalon produces an enhancement of the field within the etalon at the SESAM face, essentially altering the effective saturation fluence of the SESAM and the rate at which the SESAM switches:

$$hA = \left[t_1 e^{i\frac{\delta}{2}} \sum_{n=0}^{\infty} \left(r_1 r_2 e^{i\delta} \right)^n \right] A = \left[t_1 e^{i\frac{\delta}{2}} \frac{1}{1 - r_1 r_2 e^{i\delta}} \right] A \tag{3.44}$$

where h and $H_{S\text{-}E} = \left| h^2 \right|$ are the amplitude and intensity enhancement coefficients respectively. The factor $H_{S\text{-}E}$ is again primarily a function of SESAM reflectivity and etalon thickness, and scales the intensity component of the effective fluence rate equation (3.23):

$$\frac{dF}{dt} = H_{S\text{-}E}\left(R_{SESAM}, d \right) \frac{\phi}{2} c_L h\nu_L - \frac{F}{\tau_{SESAM}} \tag{3.45}$$

The final effect of the SESAM etalon is to present a thickness-dependent reflectivity to the pump beam, for cases when the SESAM reflectivity at the pump wavelength is $< 100\%$. By setting $\delta = 4\pi n_{RI,air} d / \lambda_P$ and applying equation (3.43), the reflectivity of the SESAM etalon to the pump light, $R_{S\text{-}E,P}$, is determined. Its effect on the pump absorption is then included in the inversion population density rate equation (3.35).

Figure 3.23 shows the behaviour of the SESAM etalon Q-switch as a function of the etalon thickness (in integer numbers of incident wavelength) for the particular laser configuration used throughout this chapter, detailed in Table 3.3. In this instance, the SESAM reflectivity for the pump wavelength is taken from the measured value for the unit used in experiment. When d is of the order of a micron, the laser gain bandwidth is much narrower than the modulation width of Figure 3.23 so the laser is forced to operate at a particular point on these curves, governed by d.

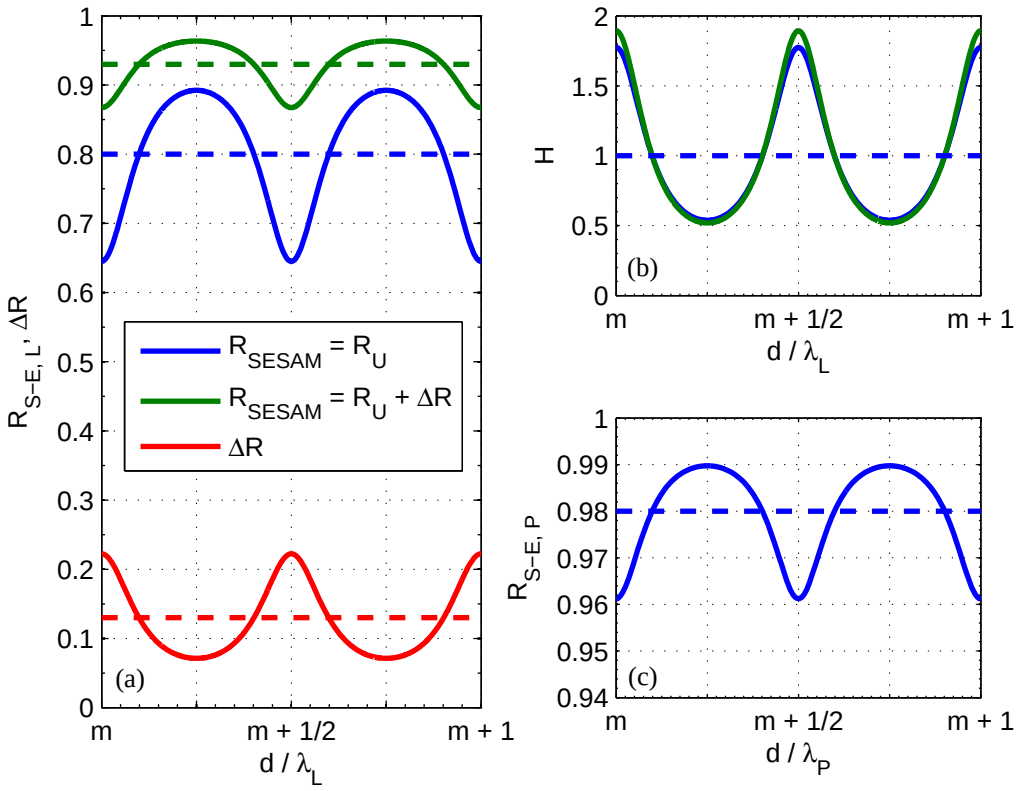

Figure 3.23: As a function of etalon thickness (m is integer): (a) The reflectivity of the SESAM etalon for switched (green) and un-switched (blue) SESAM reflectivities, also showing the resulting range of effective ΔR. (b) The field enhancement factor for a switched and un-switched SESAM. (c) The reflectivity of the SESAM etalon to the pump for a SESAM reflectivity of 98% at the pump wavelength. Non-etalon values are shown by dashed lines.

The effects of the intensity enhancement factor (Figure 3.23 (b)) on the laser behaviour are negligible in normal operation since the SESAM switches so early in the pulse formation. Equally, the change in pump reflectivity (Figure 3.23 (c)) only affects the repetition rate of the laser and is incomparable to changing the pump power. It is the change in the effective Q-switch loss range (Figure 3.23 (a)) offered by the varying etalon thickness that strongly impacts on the laser behaviour, with the initial Q-switch loss and modulation depth changing by large factors.

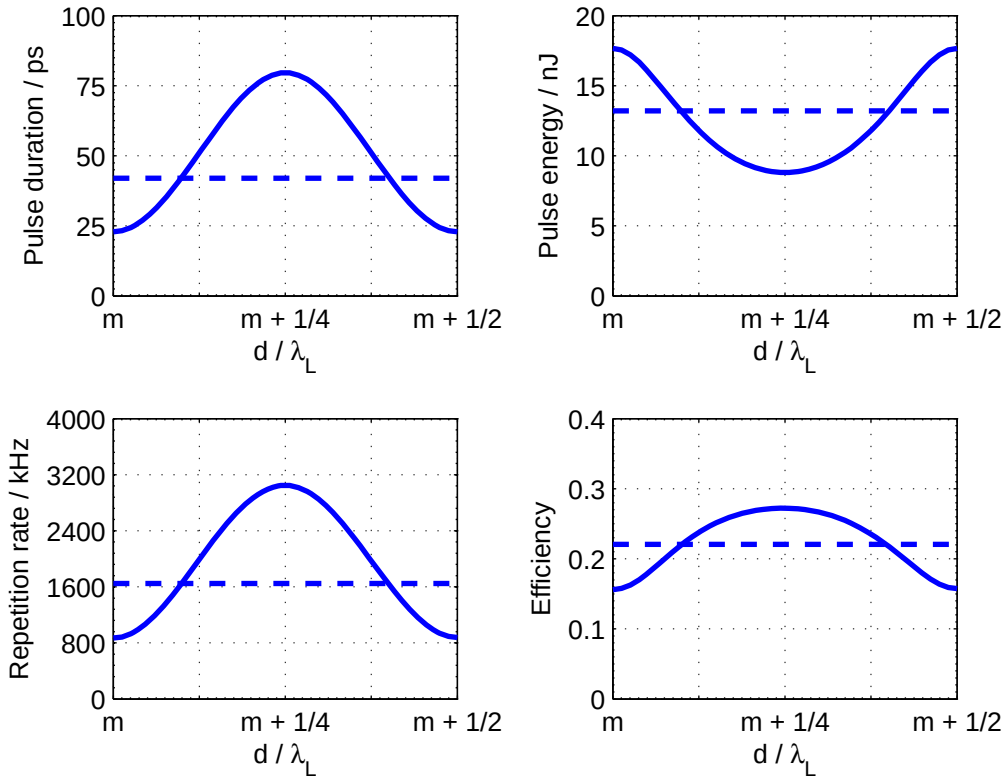

Figure 3.24: Output parameters of a SESAM Q-switched microchip, containing a SESAM etalon, as a function of the etalon thickness (expressed in terms of the laser wavelength, where m is integer). Non-etalon values are shown as dashed lines.

The effect of the SESAM etalon on laser performance (for the laser described in Table 3.3) is demonstrated in Figure 3.24 and compared to straight SESAM operation (dashed line). From Figure 3.23 and Figure 3.24 it is clear that the SESAM etalon strongly affects the apparent properties of the Q-switch, and hence the performance of the laser, with the extremes occurring when the thickness of the etalon is either resonant or anti-resonant with the laser radiation. In this particular configuration, the pulse duration and repetition rate can vary from their maxima by as much as 72% between resonant and anti-resonant etalons, with pulse energy changing by up to 50%.

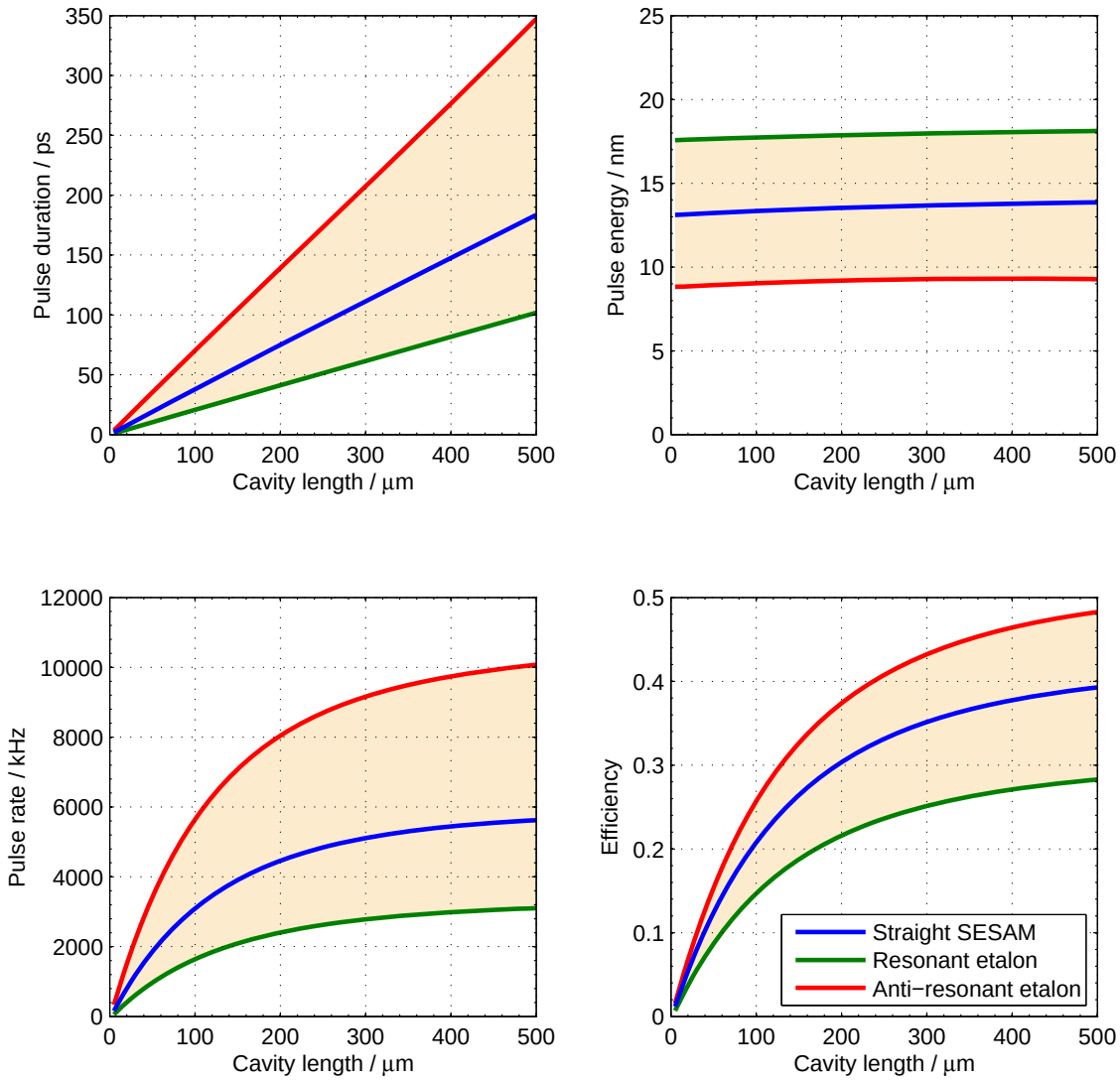

Figure 3.25: The effect of resonant and anti-resonant SESAM etalons on laser output behaviour for varying cavity length, compared to a straight SESAM case. For a given cavity length, any behaviour within the shaded range is achievable by changing the resonance of the SESAM etalon. $P_p = 200$ mW .

The implications of the presence of an etalon between the gain crystal and SESAM are clear in Figure 3.25. For a particular cavity length and SESAM, there is a range of output behaviour accessible, depending solely on the SESAM etalon thickness. When TPA in an etalon-affected SESAM microchip laser is also considered, the predicted ranges of output behaviour are modified further, as shown in Figure 3.26.

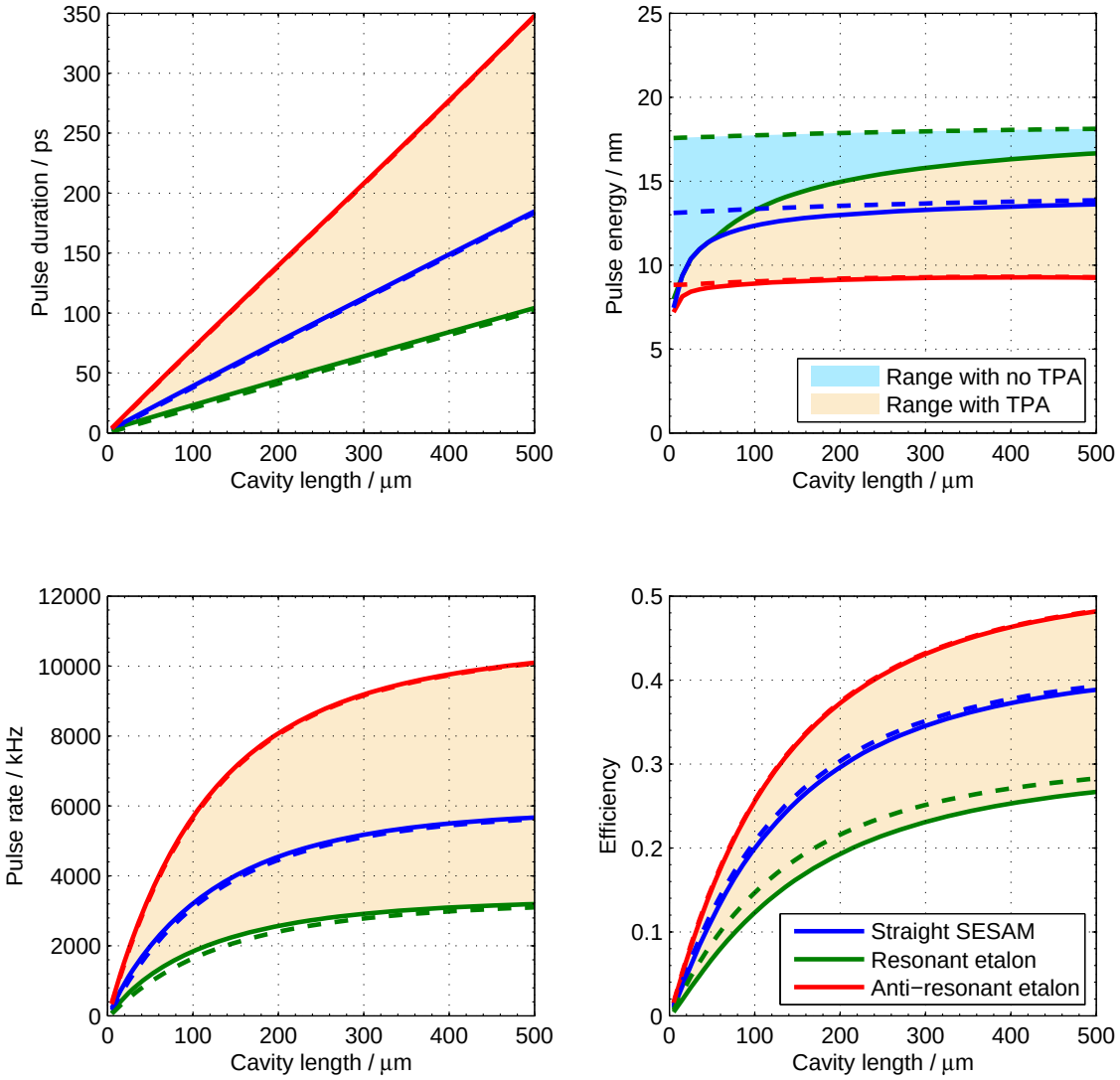

Figure 3.26: The effect of resonant and anti-resonant SESAM etalons on laser output behaviour for varying cavity length, also considering TPA. Dashed lines represent cases with no TPA, as displayed in Figure 3.25. $P_P = 200$ mW .

When taking the etalon effects into account, the contribution of TPA to the laser performance is greatly enhanced for the resonant etalon case. As with decreasing the cavity length described in Section 3.8, increasing the modulation depth of the combined etalon-SESAM Q-switch increases the intra-cavity intensity during the pulse, increasing the TPA effect and contributing more to cavity loss. In extremely short cavities, $l_L < 50$ µm , the ΔR -enhanced pulse energy of the resonant etalon actually drops below that of the un-enhanced case due to the increased TPA effect, as seen in the top-right plot in Figure 3.26. Where previously the pulse energy was thought to be independent

of cavity length, the presence of TPA, enhanced by a resonant etalon, changes the accessible range of pulse energy depending on the cavity length.

3.10 Partial switching and relaxation oscillations

While within the limits of real world components and designs, the ranges of parameters tested in order to draw the relationships in 3.7 were all fairly broad. This means that the modelled lasers were all quite robust and functioned well over a large parameter space. However, care was taken to ensure that sufficient pump power was supplied in order for the laser to produce well-defined Q-switched pulse trains.

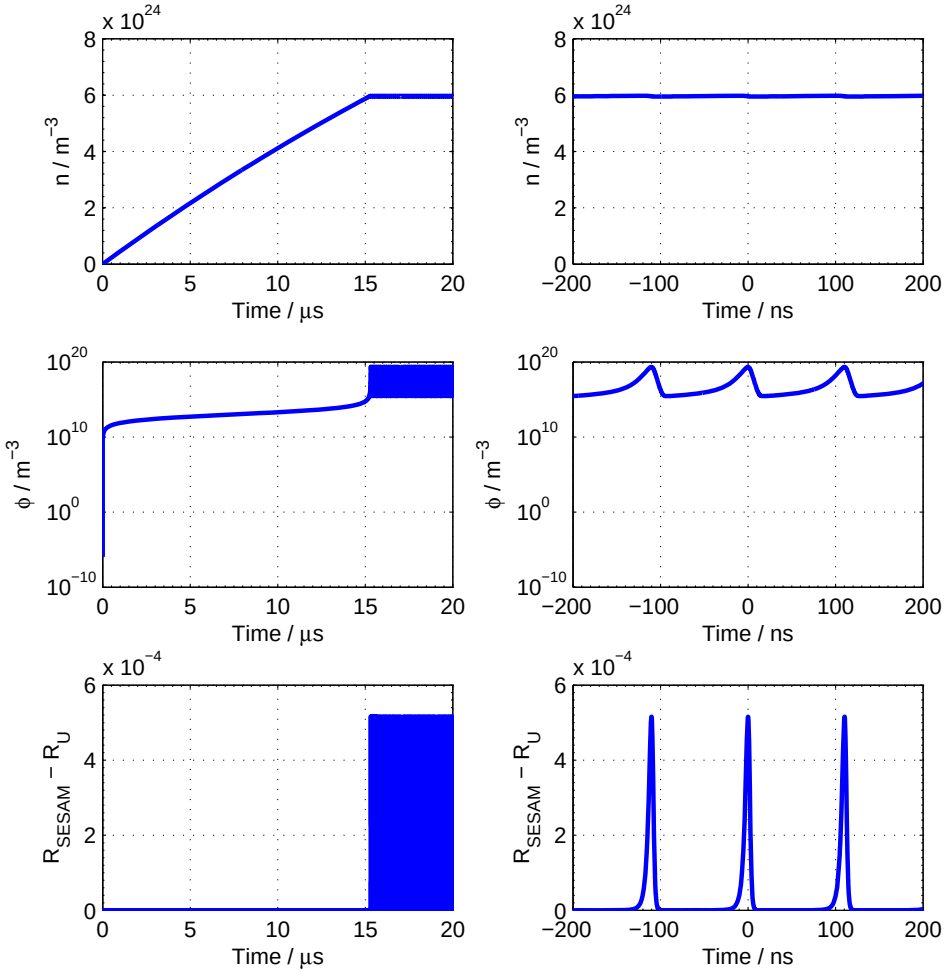

Figure 3.27: The evolution of the numerical model output variables over time for a case when the pump power (P_P = 6 mW) is insufficient to initiate Q-switched lasing.

Figure 3.27 presents the output behaviour of a modelled laser that has insufficient pump power to properly initiate switching of the SESAM. The plots for n and ϕ indicate that a low intensity, high repetition rate pulsed state has been reached and the reflectivity change of the SESAM, ~ 0.05%, is shown to be negligible compared to $\Delta R = 13\%$. The pulse duration in this instance is 6 ns, much longer than the 42 ps predicted for this cavity under fully-switched operation, and the repetition rate ~ 10 MHz compared to 1.7 MHz.

Using (3.34), and taking into account the split pumping term in (3.35), a threshold pump power of 1.2 mW is calculated. The data in Figure 3.27 were modelled at a pump power nearly five times the expected threshold value, but do not exhibit fully Q-switched operation. The SESAM reflectivity changes minutely, but the avalanche effect that leads to a full switch is not present. In this case, the inversion density is reaching threshold, but the CW cavity photon intensity is not sufficient to start the full SESAM switch. This behaviour will carry on indefinitely, outputting a high repetition rate, low power train of pulses with nanosecond duration.

Figure 3.28 shows an identical case to Figure 3.27 but the SESAM saturation intensity, $I_{SAT} = F_{SAT} / \tau_{SESAM}$, has been decreased by just over a factor of 5 by increasing τ_{SESAM} and well formed, fully switched SESAM behaviour is demonstrated. The results in Figure 3.28 are now similar to those in Figure 3.7, although the pulse repetition rate is lower due to the decreased pump power and the period of SESAM high reflectivity is extended owing to the increased relaxation time constant.

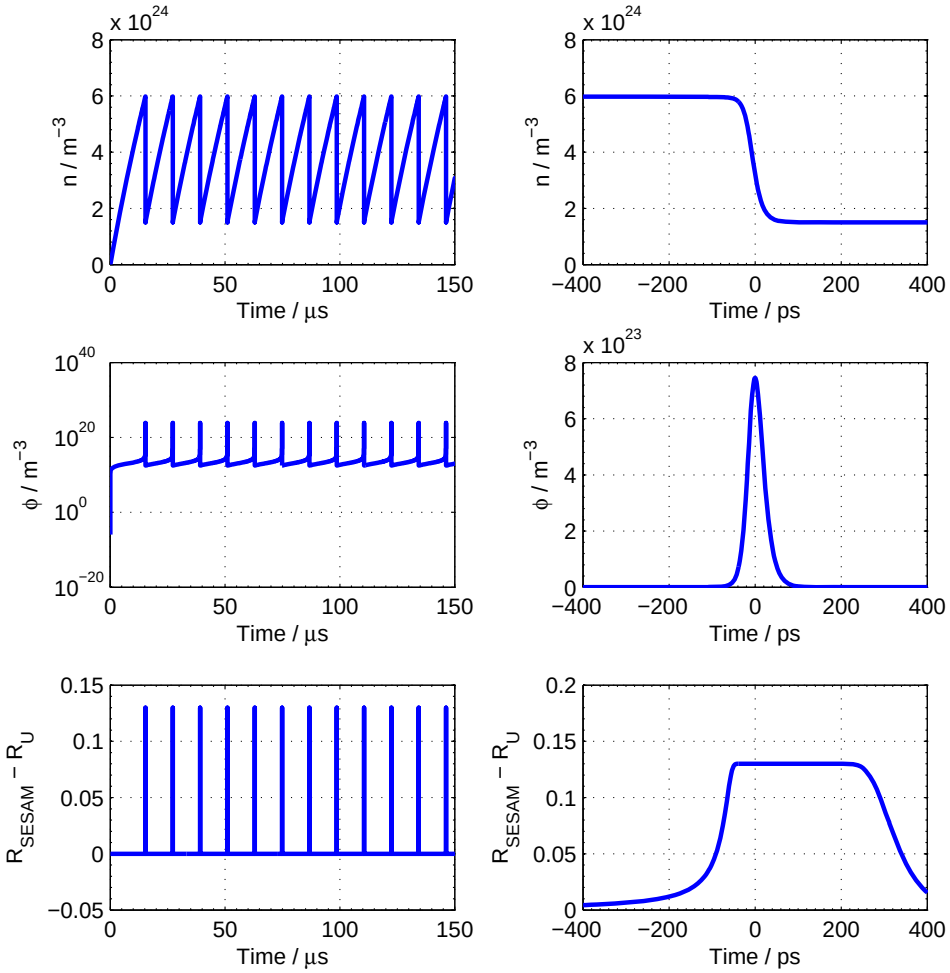

Figure 3.28: The case as in Figure 3.27 repeated, but with τ_{SESAM} = 50 ps and P_P = 6 mW .

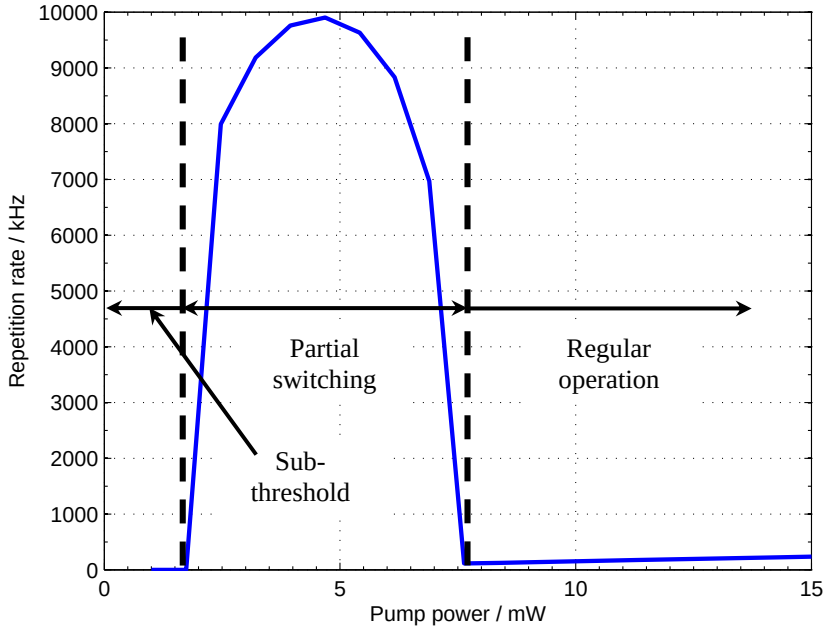

Figure 3.29: A plot identifying the quasi-Q-switched regime between true threshold and true Q-switched pulses, using pulse repetition rate as an indicator.

A true sub-threshold behaviour, demonstrating no pulse formation and no laser output, can be achieved at pump powers around the prescribed 1.2 mW. Between this threshold pump power and the pump power that generates proper Q-switched behaviour, there exists a middle ground where the SESAM is only partially switched. The range of pump powers that make up this regime, depicted in Figure 3.29 as the high repetition rate region, is governed by the SESAM saturation intensity value – a lower I_{SAT} value means a sooner onset of proper Q-switched pulses. However, this regime is very small compared to the ranges of pump powers in test and although its presence is interesting, it will unlikely have any bearing on real-world results.

An important parameter for determining whether a laser will Q-switch correctly is the ratio of the intensity for CW operation if the SESAM does not switch compared to the saturation intensity of the SESAM. We would expect that if this ratio is close to or greater than unity, then the laser will operate well. We find theoretically however that even if this ratio is as small as a few hundredths of a per cent, we can still observe correct Q-switching – we show now that this is attributable to the relaxation oscillation as the laser is turned on.

The effect of the relaxation oscillation spike on Q-switch behaviour is shown in Figure 3.30. In each case, the Q-switched response is compared to that of an identical laser configuration but with the SESAM replaced by a mirror with $R = R_U$ to generate relaxation oscillations. In Figure 3.30 (a) the pump power is sufficient to produce a relaxation oscillation spike with enough intensity to trigger the avalanche effect. This causes the intra-cavity intensity to depart from that of the relaxation oscillation, exceeding the I_{SAT} value and forming the fully-switched pulse. However, in the low pump power case of Figure 3.30 (b), identical to that of Figure 3.27, the relaxation oscillation is not intense enough to initiate the avalanche meaning that the SESAM only partially switches and the intra-cavity intensity never grows much beyond the relaxation oscillation value.

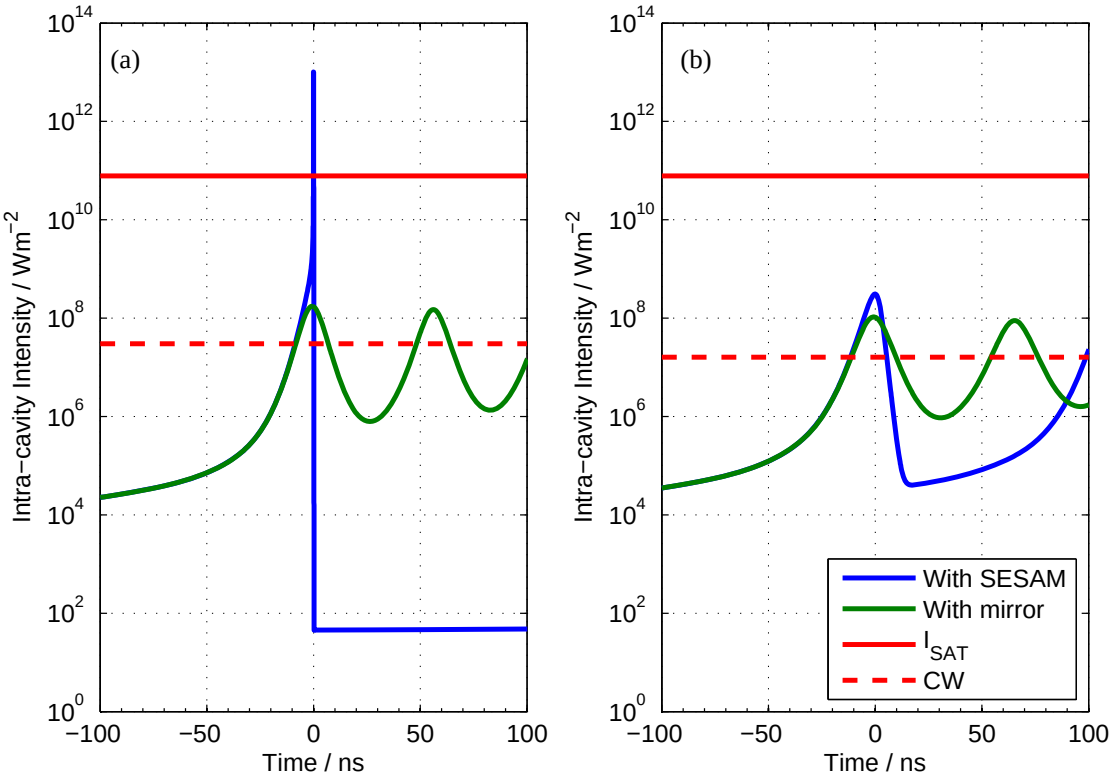

Figure 3.30: (a) The intra-cavity intensity during a full SESAM switch, ($P_P = 8$ mW) and (b) the intra-cavity intensity during a partial SESAM switch ($P_P = 6$ mW).

In reality, it is extremely unlikely that the partial switching as described above will be observed in an experimental laser system. The intensity of the partially-switched pulses is five orders of magnitude smaller than that of the fully-switched pulses and as such, is unlikely to be detected without extremely sensitive equipment. However, the intensity field suppression of an anti-resonant SESAM-etalon, as shown in Figure 3.23 (b), can inhibit the avalanche effect, preventing the SESAM from reaching its high-reflectivity state. In the anti-resonant case, the suppression factor increases with growing SESAM reflectivity during pulse formation, meaning that the avalanche effect is the cause of its own inhibition.

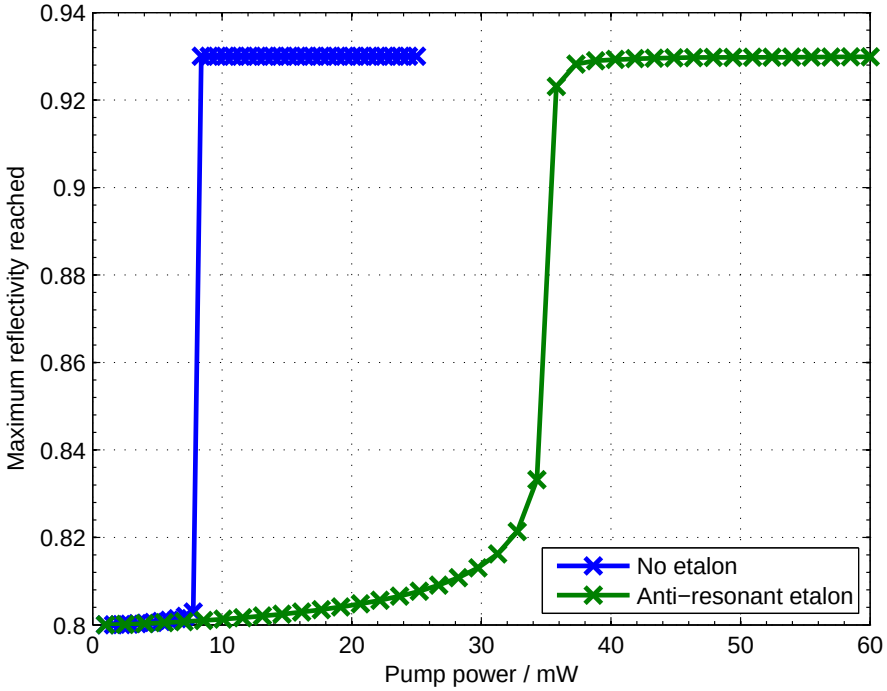

Figure 3.31: The maximum SESAM reflectivity reached during lasing as pump power is increased. $l_L = 310\ \mu\text{m}$.

The range of pump powers over which the SESAM is only partially switched for an anti-resonant SESAM etalon is shown in Figure 3.31. Before the anti-resonant case was considered, the partial switch of the SESAM was just 0.05%, with little practical possibility of achieving anything other than that or a full switch. By inserting an anti-resonant etalon between the SESAM and the gain crystal, a much broader range of switching extents is achievable by varying the pump power, a range which is accessible in experiment. Figure 3.31 is for a 310 μm cavity length to emphasize the partial-switching regime: at shorter cavity lengths, the intra-cavity intensity is higher and the regime is narrower.

3.11 Conclusion

Numerical solutions of the Q-switched laser rate equations have been used to predict the relationships between a laser's output behaviour and the characteristics of its components and provide guidelines for the design of extremely short prototype SESAM Q-switched microchip lasers.

In order to produce a laser that generates pulses of short duration, the design must have a short cavity as well as using a SESAM with a large modulation depth and a low initial reflectivity. Typically, the latter two criteria come hand-in-hand although at least some consideration must be given to the pulse energy, which is critically affected by the initial reflectivity. The minimum gain thickness, and hence minimum cavity length that can be used in this Q-switched microchip laser is 1.75 μm. At this thickness the pump efficiency is practically zero, $\eta_P \approx 0.006\%$, requiring extremely high pump powers to reach threshold. However, Q-switched operation is technically still possible and will produce pulses of sub-ps duration. Provided that efficiency is not a factor, the only limits to lowering pulse duration by decreasing cavity length are the practicalities of producing and handling thin crystals as well as providing sufficient heat management for the increased pump power required.

A key conclusion of the modelling is that these lasers are extremely robust and can successfully operate across a wide range of component parameters. This leads to a huge flexibility in choosing laser designs. It is clear that within the parameters of the SESAMs that are commercially available to us, the best way to reduce the pulse duration is to make thinner lasers, and lasers even an order of magnitude shorter than those in the literature are feasible, notwithstanding material handling issues.

Through use of a numerically-solved rate equation model, the presence of two-photon absorption in the semiconductor materials of a SESAM has been investigated and its effects on important laser output parameters examined. It has been shown to provide a mechanism for component parameters to exhibit control over output characteristics that were previously thought to be unrelated. For example, the presence of TPA causes a noticeable reduction in pulse energy at short cavity lengths when pulse energy otherwise would be independent of cavity length. In fact, any mechanism that shortens pulse duration or increases pulse energy, such as shortening the cavity or a resonant SESAM-etalon, will increase the TPA effect.

In broad terms, the presence of TPA has been shown not to cause great changes to laser behaviour in typical operating regimes, although it is important to be aware of its effects at short cavity lengths when designing SESAM Q-switched microchip lasers.

At cavity lengths around 100 µm, which is a region to be examined in experiment, pulse durations elongate and pulse energies drop considerably due to TPA. Since these Q-switched lasers employ SESAMs with large modulation depths, the TPA-induced reflectivity deficit is small by comparison. In mode-locked lasers where the SESAM modulation depths can be of the order of 1-2%, this loss of effective ΔR becomes more significant.

The presence of an etalon between the gain crystal and the SESAM can drastically change the output behaviour of the laser. The etalon can affect pump absorption in the cavity as well enhancing the intra-cavity intensity on the face of the SESAM although its main contribution to the laser behaviour is to modify the coupling of the cavity field into the SESAM, changing the effective Q-switch ΔR. By replacing the SESAM with the SESAM etalon as Q-switch and modelling one surface of the etalon as a SESAM, the behaviour of the etalon-affected laser was numerically modelled. For the design of laser described in Table 3.3, the pulse duration and repetition rate can vary by as much as 74% from their maxima and pulse energy by as much as 50%, with short pulse durations and high pulse energies obtained when the SESAM etalon is resonant with the laser radiation. We found that the most likely experimental scenario is that a wedged etalon will occur between the two components, providing a continuum of etalon thickness between resonant and anti-resonant across the transverse plane of the laser. This would make the entire range of behaviour shown in Figure 3.24 available by simply changing the position of the laser mode on the face of the laser.

We have shown that, in low-pump power cases, the SESAM can enter a regime of partial switching, made more accessible by the presence of an anti-resonant SESAM etalon. More importantly, we demonstrated that the CW intensity of the laser in its high-loss state is often many orders too low in itself to cause the SESAM to switch. Instead, the avalanche effect that leads to full-switching is triggered by the initial relaxation oscillation spike generated when the laser reaches threshold. Although the relaxation oscillation spike by itself is rarely enough to overcome the SESAM saturation intensity in normal operating regimes, it is certainly a big contributing factor in the initialisation

of Q-switched pulses and one which allows more flexibility when choosing components for a SESAM Q-switched microchip laser design.

4 Oscillator development

In this chapter, the SESAM Q-switched microchip laser design depicted in Figure 3.1, based around the parameters in Table 3.3, is investigated experimentally. The primary aim of these experiments is to minimise the pulse duration of the laser while monitoring other output characteristics such as pulse energy, repetition rate and slope efficiency and comparing these results to the output of the numerical model described in Chapter 3. A diagram of the extended set-up, from pump to laser analysis is shown in Figure 4.1.

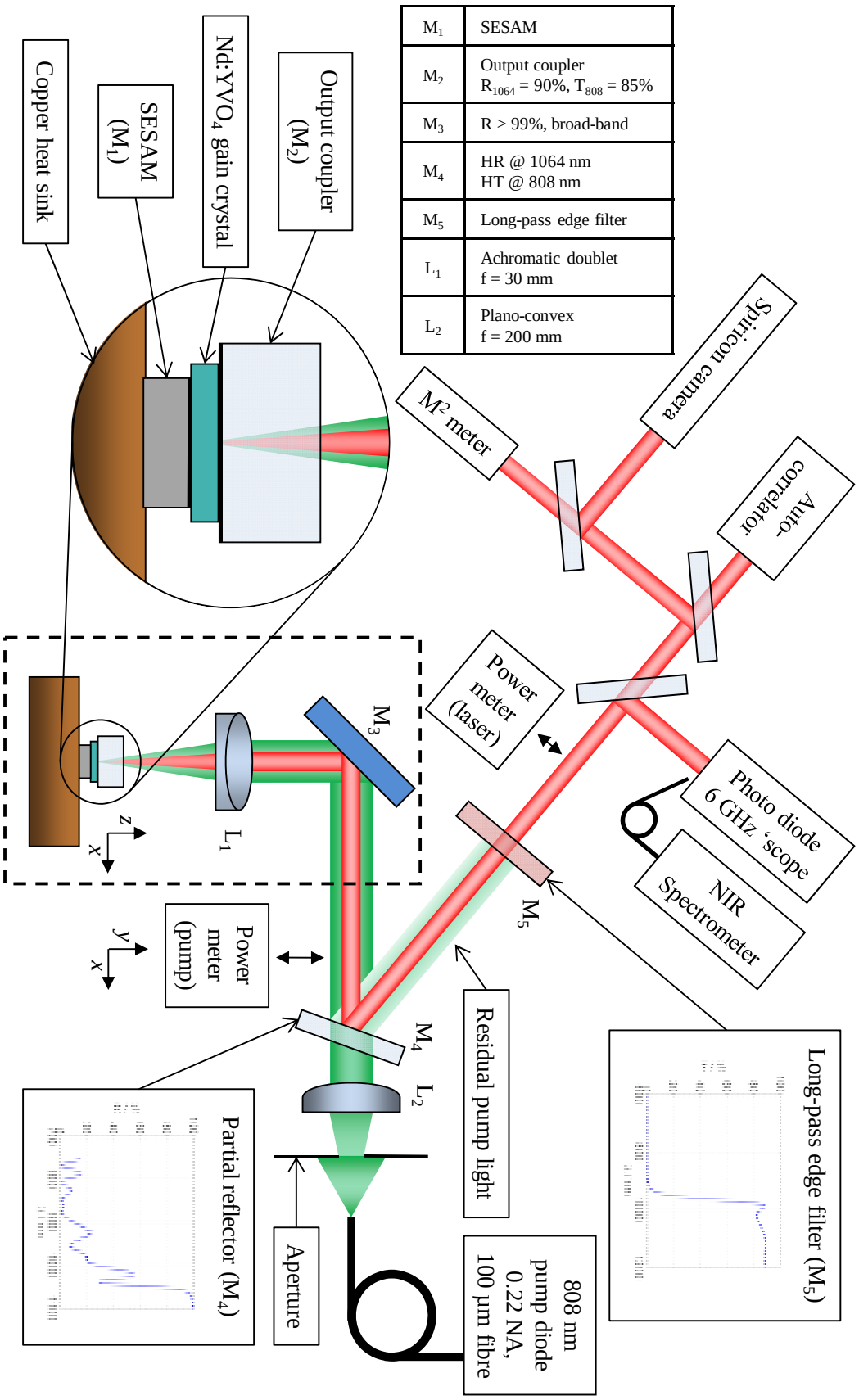

Figure 4.1: The extended set-up of the microchip laser system.

4.1 Set-up

The 808 nm pump source for these experiments was a Prolite Xt Corvus fibre-coupled diode laser bar, capable of delivering between 35 mW and 35 W of CW power through a 100 µm core diameter, 0.22 NA fibre. The diode exhibited small fluctuations (~ 10%) in output power at low operating currents so was typically operated at currents between 20 A and its maximum 50 A to reduce this effect. A variable aperture was placed in the far-field emission of the fibre, primarily to attenuate the high-power output, but with the added benefit of improving the beam quality from $M^2 \approx 40$ to an operating range of $M^2 \approx 2\text{-}4$, depending on how much pump power was required. The pump beam size and M^2 were measured using a Pulnix TM-745 CMOS camera with approximately 40x magnification and DataRay Inc. BeamScope P-7 scanning slit beam profiler respectively. The fibre output face was imaged into the laser crystal using a 200 mm collimating lens and a 30 mm focussing lens, resulting in a measured pump spot radius (at e^{-2}) of 10 µm at focus, for an aperture of ~ 5 mm diameter. Increasing the aperture did not change the focal spot size, but increased the M^2 of the beam.

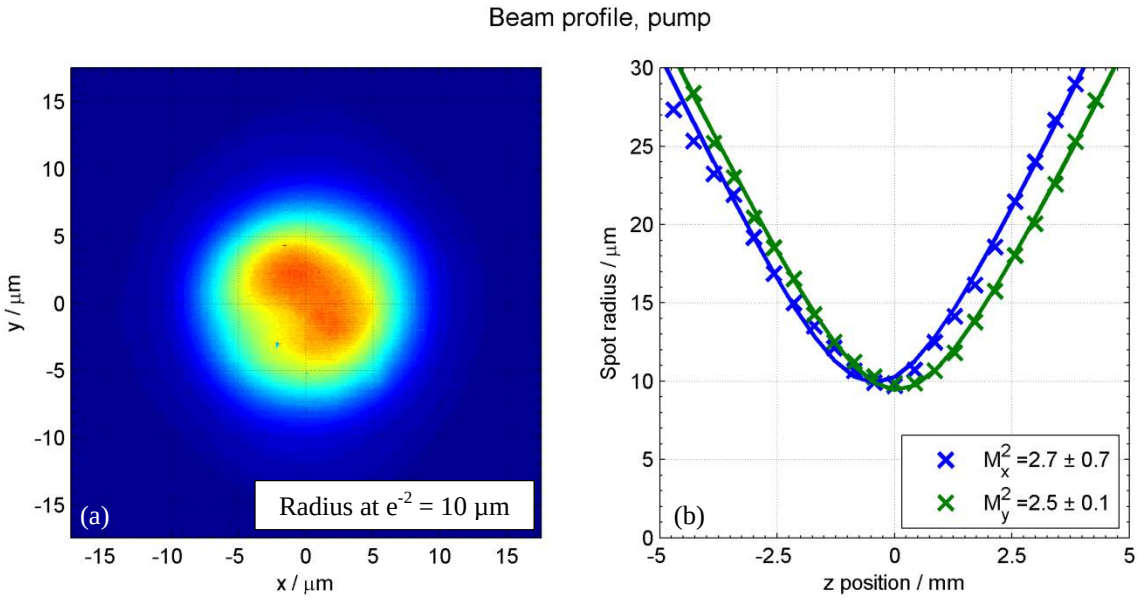

Figure 4.2: (a) Spot intensity profile at focus from Pulnix camera and (b) M^2 measurement of the pump beam from BeamScope profiler.

At this point we add a note about our use of the BeamScope profiler and Pulnix camera in measuring M^2 values and spot sizes for both pump and laser beams. Owing

to the BeamScope software's notoriously unreliable calculation of the M^2 parameter, the BeamScope was used purely to measure the beam diameter as a function of position along the beam propagation direction. These data were then converted to beam radii measurements and analysed separately by us to determine the M^2 factor, by fitting an expression for Gaussian beam propagation to the beam radius data:

$$\omega^2(z) = \omega_0{}^2 + \left(M^2\right)^2 \left(\frac{\lambda}{\omega_0 \pi}\right)^2 z^2 \tag{4.1}$$

where $\omega(z)$ is the beam radius as a function of distance from the beam waist position along the beam propagation direction and ω_0 is the beam radius at the beam waist. We took measures to ensure that the beam spot size on the BeamScope sensor was well above its resolution limit for all cases and we verified the spot size measurements of the BeamScope against measurements taken with the Pulnix camera, which in turn was calibrated by translating the laser spot a known distance across the camera sensor.

All lenses used were anti-reflection coated for broad-band NIR. Pump power in the collimated beam was monitored using a Coherent FieldMaxII power meter with PS10Q head and it is assumed that this is the power entering the laser output coupler. Both incoming pump and outgoing laser beams are reflected off turning mirror M_3 at 45° incidence. The reflectivity of mirror M_3 at 45° incidence is $\geq 99\%$ for the NIR range covering both the pump and laser wavelengths.

To ensure optimum absorption of the pump by the Nd:YVO_4 gain medium, the pump diode temperature was held at 18 °C, resulting in a peak emission wavelength of 807.8 nm, as measured by an Ocean Optics HR4000 spectrometer. The spectral bandwidth of the pump diode was measured to be 2 nm in the 15 – 30 °C range.

The assembly of the laser stack, inset Figure 4.1, is covered further in Section 4.2. In all of the following experiments, the output coupler reflectivity was $R_{OPC} = 90\%$ and the SESAM used was SESAM-6 from Table 4.1. From the analysis in Section 3.7, there exists an optimum output coupling reflectivity that results in shortest pulses for a particular laser design, with the added rule that lower reflectivities give higher pulse

energies. However, this dependence is weak and a comparatively high output coupler reflectivity was chosen based on the approaches taken in the literature (Table 2.2), to ensure that the laser easily reached threshold and performed reliably. The transmission of the bulk output coupler at the pump wavelength was measured to be 84%, which is accounted for when comparing results to the numerical model later in this chapter. For optimum efficiency in future systems, the output coupler should be AR-coated for the pump but this is unnecessary in our case since we have an abundance of pump power and it was convenient to use this off-the-shelf bulk-optic.

SESAM-	R_U / %	ΔR / %	F_{SAT} / Jm^{-2}	τ_{SESAM} / ps	I_{SAT} / 10^{10} Wm^{-2}
2	86	10	0.5	3	17
3	75	18	0.4	3	13
6	80	13	0.7	9	8
7	70	22	0.4	9	4

Table 4.1: The SESAMs considered for experiment and their parameters as measured by the manufacturer. The manufacturer's SESAM numbering system is not sequential and does not reflect any meaningful parameter or order.

The SESAMs shown in Table 4.1 are commercially available units and were purchased from BATOP GmbH [129]. SESAM-6 was found to give the most reliable and repeatable Q-switching results, owing to its low saturation intensity and low unsaturated loss. Each SESAM was given an additional coating to provide high reflectivity at the 808 nm pump wavelength and high transmission at the 1064 nm laser wavelength, shown in Figure 4.3.

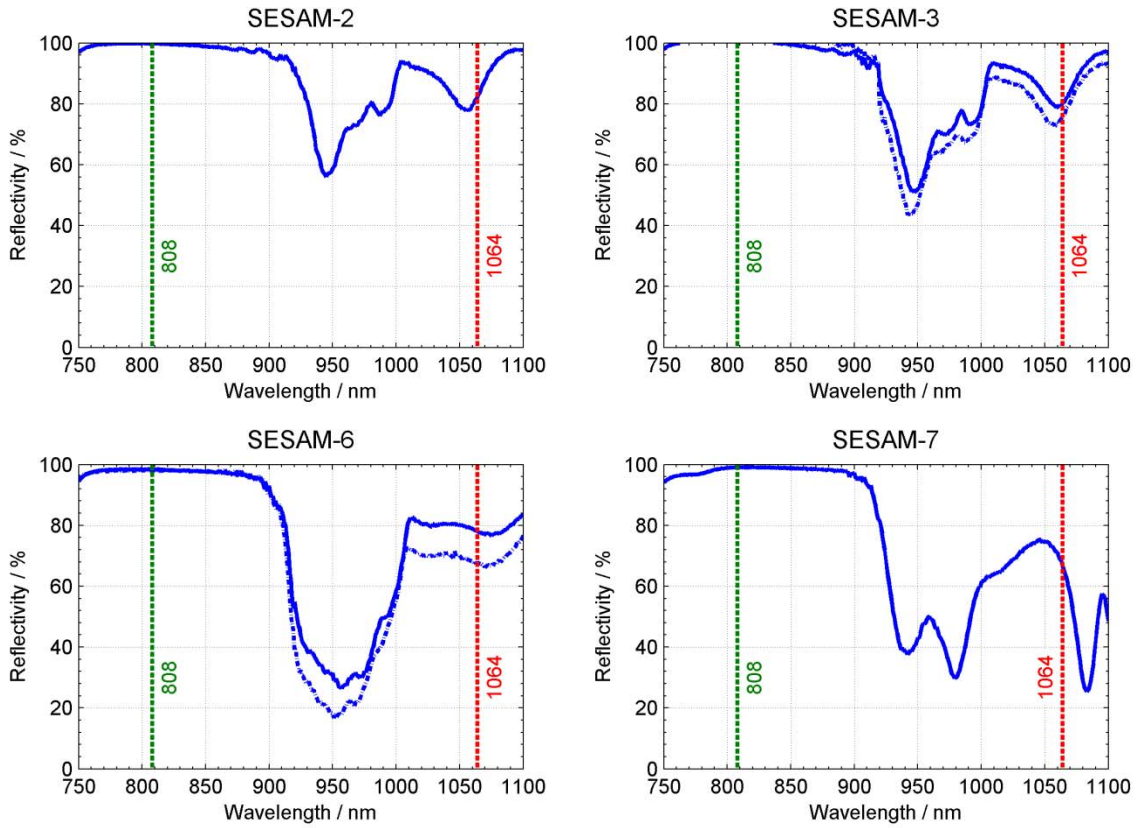

Figure 4.3: The un-switched reflectivities of the SESAMs, measured immediately post-coating. Dashed curves for SESAM-3 and SESAM-6 were re-measured 30 months after initial data were taken. All data measured using a Cary 5000 spectrophotometer.

There is a slight discrepancy between the un-switched reflectivity values provided by the manufacturer and those measured by us, although it is unclear whether this is due to variability in manufacture, degradation over time or to the applied 808 nm coating. The reflectivities of SESAM-3 and SESAM-6 were re-measured after two and a half years and the results are shown as dashed curves in Figure 4.3, showing a definite reduction in reflectivity at 1064 nm of about 10%. Although SESAM-6 had been used frequently in experiment in the period between measurements, suggesting damage and degradation through use, SESAM-3 was unused beyond brief feasibility testing, indicating SESAM degradation over time as the cause of the reflectivity drop.

In order to determine the effect of the degradation on SESAM performance, and accurately ascertain its switching parameters, at the end of this project we measured the SESAM reflectivity using a 30 ps mode-locked laser and varied the pulse fluence incident on the SESAM by translating the SESAM through beam focus. We were

looking for deviations from the manufacturer's specification, measured using a 220 fs laser, as well as making the measurement with a 30 ps laser that has a similar duration to the expected durations of the microchip laser. It was hoped that this approach would also demonstrate the effects of TPA roll-over, akin to those shown in Figure 3.3. The results are displayed in Figure 4.4, and do not closely match the expected curves.

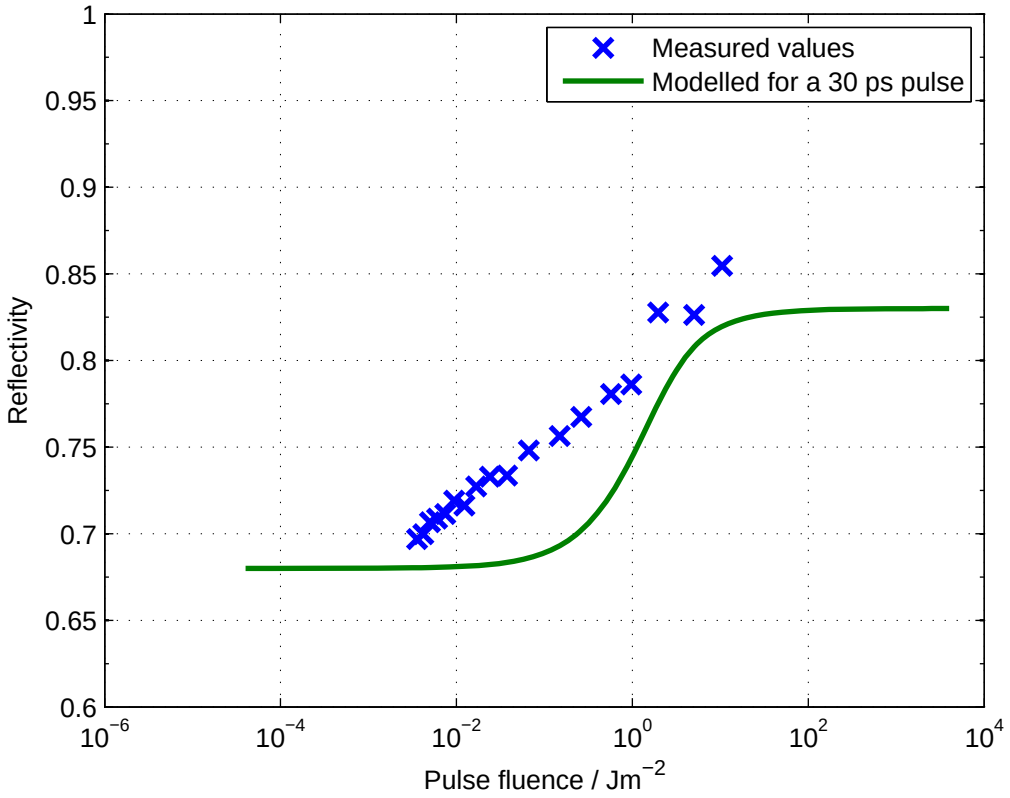

Figure 4.4: SESAM-6 reflectivity as a function of pulse fluence: measured values using a 30 ps pulse and determined by modelling for $F_{SAT} = 0.7$ Jm^{-2}, $R_U = 68\%$, $\Delta R = 15\%$ and 30 ps pulses.

For $F_{SAT} = 0.7$ Jm^{-2} and $\tau = 9$ ps, quoted for 220 fs pulses by the manufacturer, we expect the SESAM to be 63% switched for $F \approx 2$ Jm^{-2} for these 30 ps pulses which is consistent with this measurement, although we see an unexpected substantial change in reflectivity for fluences as small as 0.02 Jm^{-2} where we would expect to measure R_U. The lowest reflectivity measured of 69% is however consistent with the most recent measurement made using the spectrophotometer. The maximum fluence of 10 Jm^{-2} should be sufficient to closely approach $R_U + \Delta R$, but we could not increase the fluence to confirm the value of ΔR, or to observe TPA. While higher fluences are achieved

intra-cavity in the lasers presented below, they were not reproducible without causing damage to the SESAM using this particular laser source, or other sources readily available to us: the high 80 MHz repetition rate of this laser resulted in thermal damage for pulse fluences greater than 10 Jm^{-2}, even though we mechanically chopped the pulse train with a 1:90 duty cycle. We can conclude a lower limit of 15% for ΔR from the results in Figure 4.4. While this measurement of SESAM performance was not made using ideal sources that could access the entire range of SESAM operation without causing damage, clearly there is a substantial shift from the manufacturer's specification of $R_U = 80\%$ and $\Delta R = 13\%$.

The gain material used in all cases was a-cut 3 at.% at. Nd:YVO_4, acquired from CASIX Inc [177]. The samples were around 310 µm thick when delivered and we polished two samples down to 210 µm and 110 µm, all verified by optical profilometry.

The back face of the SESAM was attached to a copper disk using a silver-doped adhesive to provide good thermal conductivity between the two. The copper disk was rested on top of a larger copper block, which in turn was bolted to an x- and y-axis translation stage. This thermal management approach proved sufficient in as no effects attributed to heating were witnessed for the microchip laser oscillators.

The output laser beam was collected using the pump-focussing achromat, and separated from any unabsorbed pump light by near-normal reflection from a dichroic reflector, M_4, the reflectivity curve for which in Figure 4.1 was measured at normal incidence. Any remaining pump light was filtered from the beam by a long-pass edge filter. The edge filter is necessary since at the shortest cavity length tested, 50% of the pump light is unabsorbed and the reflectivity of the dichroic at 808 nm was small, but non-zero. We were not concerned about unabsorbed pump light re-entering the pump fibre since, although we were imaging the fibre face into the laser mode, the system was not well-enough aligned for pump light to re-enter the fibre after a complete round-trip through the set-up. The reflectivity of the dichroic and the transmission of the edge filter at 1064 nm were 97% and 86% respectively, as shown in Figure 4.5.

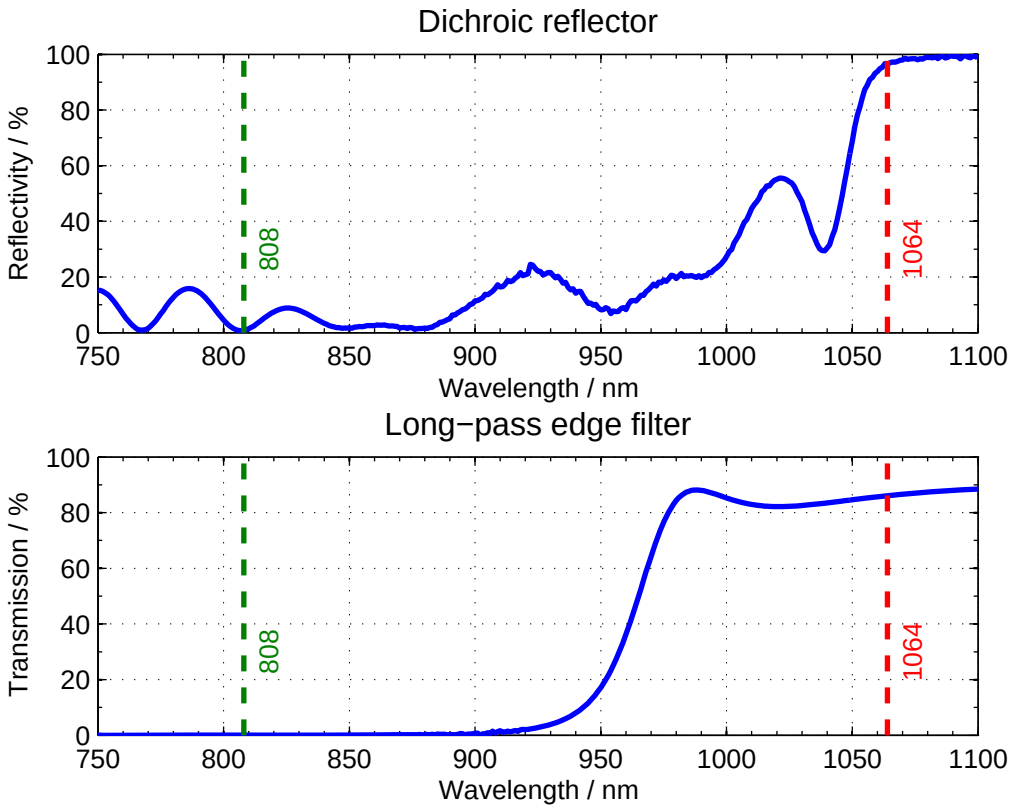

Figure 4.5: The reflectivity of the dichroic reflector and transmission of the edge filter.

Analysis of the pulsed laser beam occured after the edge filter. The output wavelength was monitored using the Ocean Optics spectrometer and the average output power was measured by the same power meter as for the pump. The pulse train was observed using an InGaAs photodiode and 6 GHz LeCroy sampling oscilloscope. Although the InGaAs photodiode has a relatively fast rise-time of 40 ps, the combination of oscilloscope and photodiode is insufficient to fully resolve sub-500 ps pulses. Measurement of the pulse duration itself was made using a modified Femtochrome FR-103HS spinning mirror autocorrelator. This uses, as one arm of a Mach-Zender interferometer, a double-pass through a pair of parallel mirrors that rotate to provide a variable path length as a function of rotation angle. Since we expected pulses of duration longer than 100 ps, we increased the length of one of the spinning mirrors in the pulse delay path to extend the path length difference, providing a sufficient range of delays to resolve these pulses. However, operating in this extended regime means that the relationship between the angle of the mirror spinner and the pulse delay provided by the spinning mirror pair became non-linear.

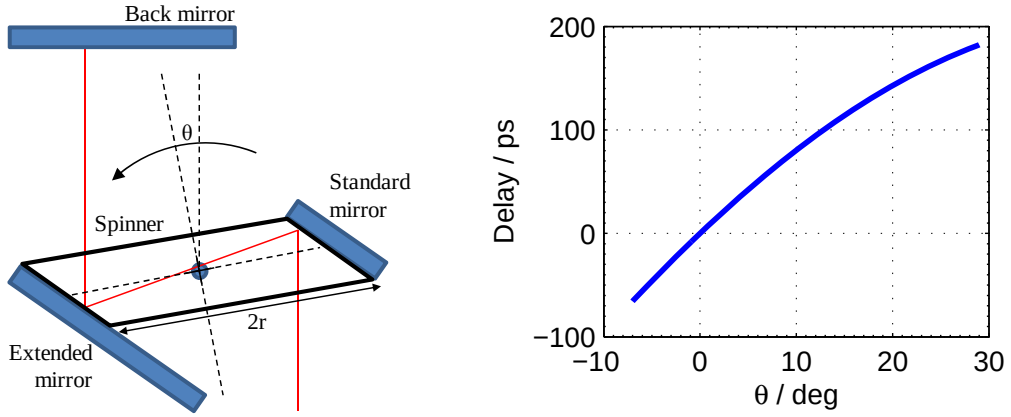

Figure 4.6: The spinning mirror pair in the scanning autocorrelator and the pulse delay as a function of rotation angle.

For the arrangement of Figure 4.6, for a mirror pair that are a distance $2r$ apart, the path length change relative to $\theta = 0°$, Δz is:

$$\Delta z = 2\left\{\frac{4r\cos\theta\sin\theta}{\cos\theta+\sin\theta} - \left[2r - \sqrt{4r^2\left(\cos\theta-\sin\theta\right)^2 + 16r^2\left(\frac{\cos\theta\sin\theta}{\cos\theta+\sin\theta}\right)^2}\right]\right\} \quad (4.2)$$

when the axis of the spinning plate is at an angle θ to the perpendicular of the direction of the incoming beam The angle limits of this arrangement are set by the mirror dimensions and were typically -7° to 29°, asymmetric about 0° due to the mirror elongation being in one direction only. The delayed pulse was combined with the original pulse in a 5 mm BBO frequency doubling crystal and the convolved intensity response measured by a photomultiplier.

The autocorrelator output signal, photomultiplier voltage as a function of time, was converted first to a function of spinner angle from knowing the rotational speed of the spinner and then to path length difference and finally delay, as shown in Figure 4.7. Note that the peak of the trace does not coincide with zero delay and zero path length difference in this case since the 0° position of the spinner, i.e. when the long spinner axis was perpendicular to the incoming beam, did not give the same total path length as that of the reference arm of the autocorrelator. Assuming a Gaussian-shaped pulse, the pulse duration is then calculated as $\tau_p = \tau_{ac}/\sqrt{2}$ where τ_{ac} was the FWHM duration of the autocorrelated response. Pulse duration measurement by autocorrelation is a well-

known method for measuring sub-nanosecond pulse durations and is described in detail in [178-181].

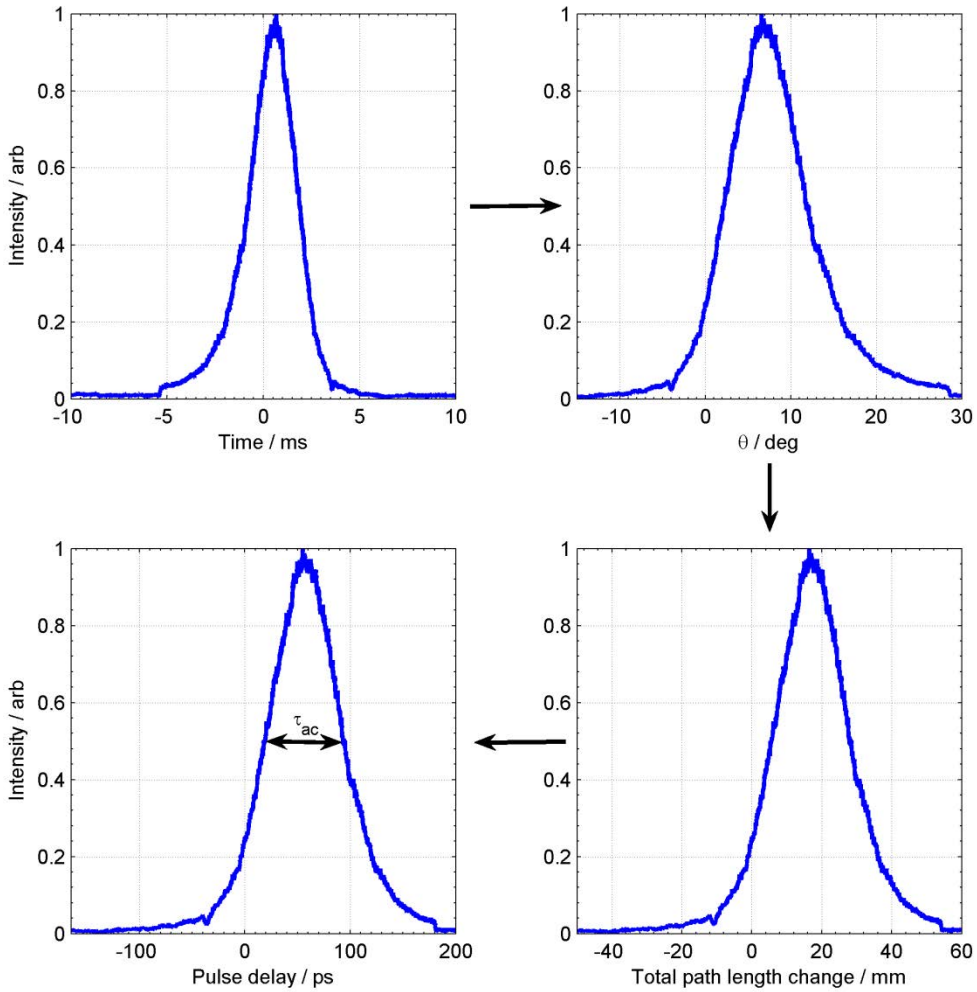

Figure 4.7: Clockwise from top left: the process for determining pulse duration from the raw output of the autocorrelator. The output of the photomultiplier in time is first converted to a function of angle from knowing the limits and angular velocity of the spinner, before being converted to a function of path length change by using equation (4.2) and finally to pulse delay, from which we can extract the pulse duration..

4.2 Laser assembly and testing procedure

The surfaces of the components in the laser stack were thoroughly cleaned to prevent contaminants interfering with the contacting between faces. The components were then simply compiled in a stack on top of one another in the order shown in Figure 4.1, the main contacting force being provided by the weight of the components themselves.

As mentioned in Section 3.9, the presence of a varying-thickness air-gap etalon between the gain crystal and SESAM provides access to a range of Q-switch behaviour. Evidence of a wedged etalon in experiment can be seen by the presence of a fringe pattern forming under sodium-lamp illumination. This is shown in Figure 4.8 where a 5 mm square gain crystal rests on top of the 4 mm square SESAM-6.

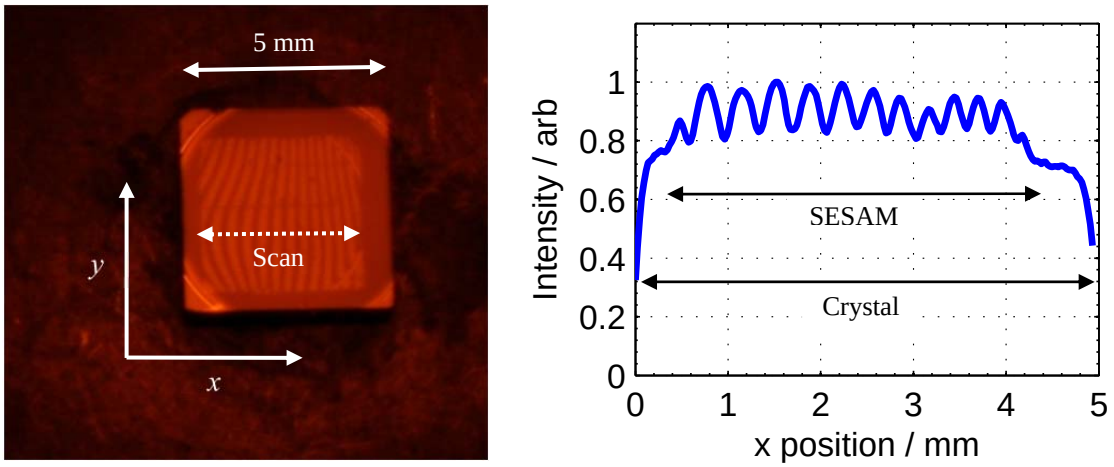

Figure 4.8: A microchip laser (310 µm-thick, coated-output-coupler crystal on top of SESAM-6) showing sodium fringes formed by the wedged etalon between components. The right hand plot is a line scan of the intensity of the photograph on the left, allowing the fringe spacing at the sodium lamp wavelength to be determined since crystal and SESAM dimensions are accurately known.

As the fringes in Figure 4.8 were formed using a sodium lamp ($\lambda = 589$ nm) the fringe spacing, and hence the periodicity of etalon resonance and changing SESAM-etalon behaviour, will be 1.8 times larger for 1064 nm radiation. In this particular example, there will be approximately 6 cycles of laser output behaviour achievable across the x-axis of the laser, which provides a good range to work with in experiment.

The components in the laser stack were gently manipulated until regular, clear interference patterns, similar to those in Figure 4.8, were discernible. This ensured that the etalons between SESAM and crystal and crystal and output coupler were wedged enough to provide a reasonable, though not excessive, range of behaviour. In early experiments, before the etalon effects were fully understood and taken into consideration, evaporation of fluids such as water and ethanol from between the components was investigated as a way to improve contacting between the components [182], reducing the inter-component spacing and removing the wedge from the etalon.

However, we were not successful in achieving a well-contacted bond between components and this process was found to adversely interfere with the operation of the laser, leaving residual deposits on the component faces, and so this method was abandoned. It is worth noting that shortly before this project concluded, we were given a demonstration of proper optical contacting technique by a colleague familiar with the process [183]. After detailed consultation with this individual, we suggest that optical contacting might be revisited in the future as a method to improve the robustness of the laser stack and could indeed remove the wedges from the air-gap etalons, reducing the etalon effects.

Completed laser stacks were placed under the 30 mm pump-focussing lens as shown in Figure 4.1. Apart from in the vertical laser stack and focussing lens (dotted area in Figure 4.1), all beams in the set-up were in the plane of the optical bench. As an initial guide, at low pump power the height of the pump spot inside the gain crystal was adjusted by moving the focussing lens until the visible upconversion fluorescence from the gain crystal appeared brightest. The pump power would then be increased until a laser spot was noticeable on an IR-viewing card placed after the edge filter. Due to etalon effects, it was sometimes necessary to raster the pump spot across the crystal in tandem with increasing the pump power in order to identify the point where threshold was lowest.

Once a regular pulse train was observed on the oscilloscope, the height of the pump spot was fine-tuned so that the highest pulse repetition rate was achieved. This ensures that the gain crystal is positioned at the focus of the pump beam since, from examination of equation (3.35), the smaller the pump volume, the faster the pump rate. When changing the pump spot height within the crystal, and hence changing the pump spot size, good overlap between the laser and pump modes is indicated by a maximum in output power since, as the pump power is kept constant, output power is directly proportional to efficiency. If the maxima in repetition rate and output power occur at the same spot height, it indicates that the pump spot size at focus is well matched to the laser mode size. This process is examined further in the following section.

4.3 General results

In this section, the general behaviour of the microchip laser design is investigated and the results presented. Unless otherwise stated, in the experiments in this section, the output coupler was a coating on the pump-input face of a 310 µm-thick crystal of 3 at.% Nd:YVO_4 rather than the bulk output coupler used in the other experiments in this chapter. This is to simplify the experiments by preventing a second etalon forming between crystal and bulk output coupler. In the following, the effect of varying the height of the pump spot in the gain crystal, a method used in the previous section to optimise the pump spot position, is quantified; the presence of an etalon between the gain crystal and SESAM is demonstrated and its effect on pulse duration and pulse energy is discussed; finally, the partial switching effect enabled by an anti-resonant SESAM-etalon is observed.

Optimising pump spot position

In establishing the best pump mode size to match the laser mode in Nd:YVO_4, we imaged the pump fibre output face using a range of lens combinations until the best possible matching was achieved (using the lens pair described in Section 4.1, $f_{col} = 200$ mm and $f_{foc} = 30\ mm$). We observed that when increasing the size of the pump mode, the laser mode size also increased, although not at the same rate. For all cases, the laser spot size was found to be almost independent of pump power, suggesting that thermal lensing is not the dominant factor in determining the laser mode size. The laser mode sizes for each cavity are shown in the following section.

Figure 4.9 shows the effect of adjusting the pump spot height within the gain crystal, effectively changing the pump spot size. As predicted in (3.35), the repetition rate reaches a maximum when the focal spot is centred in the gain crystal. The output power, and hence efficiency, is maximised at focus indicating best matching between the laser mode and pump mode sizes. Measurement showed that for our chosen pump waist of 10 µm, the laser mode was closely matched at between 8 and 10 µm. For larger pump spots, the laser mode did also get larger but did not fill the pump mode, resulting in an increasing pulse energy but a decrease in efficiency due to poor overlap. We have chosen to operate at the small, closely matched spot size to maximise efficiency; it

would be a reasonable choice to operate at larger spots to increase the output pulse energy.

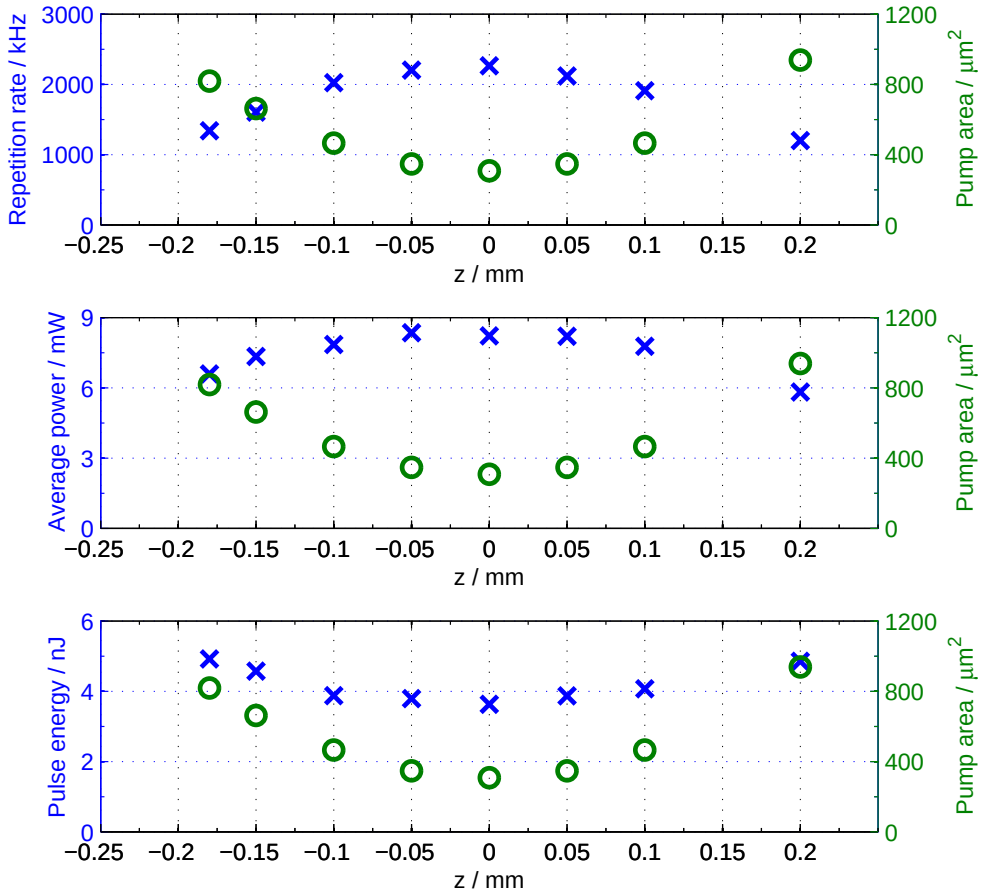

Figure 4.9: The laser output behaviour, X, and pump spot area, O, as functions of pump spot height within a 310 µm gain crystal.

In general, all laser designs tested in the following section were straightforward to construct and regular pulse trains were readily achievable, provided the right combination of etalon and pump power was found. For the spot sizes that we tested, between 300 – 1000 µm^2, the heat load in the laser crystal became destructive above 400 mW CW pump power. As the pump power was increased towards this limit, steady pulse trains with repetition rates in excess of 4 MHz were achieved for the thinner cavities under test, while the 310 µm cavity produced pulses at a rate in excess of 6 MHz.

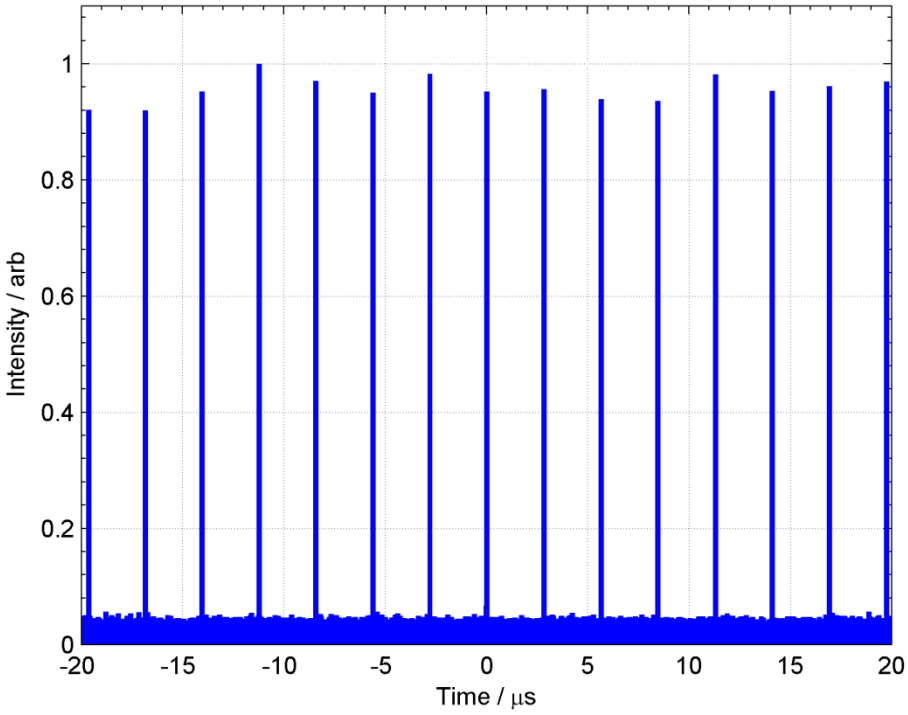

Figure 4.10: A pulse train from a 310 μm SESAM Q-switched laser. The repetition rate is 356 kHz.

A typical pulse train for a 310 μm laser is shown in Figure 4.10. Note that the pulse intensity appears inconsistent here because of an insufficient sampling rate. Pulse-to-pulse timing jitter was measured as the standard deviation of a large sample of inter-pulse period measurements using the equipment described in Section 4.1 and, when the laser was optimised for short pulse duration, was consistently found to be between 3 and 5% of the measured inter-pulse period. This value increased, i.e. jitter worsened, when operating away from SESAM etalon resonance. Although the pulse train measurement system as described in Section 4.1 is insufficient to resolve individual pulse peaks, it is capable of accurately determining the inter-pulse period, and hence jitter, provided that a large number of pulses are sampled.

Etalon effects

While scanning the pump spot along the scan line shown in Figure 4.8, and hence varying the thickness of the SESAM-etalon, as predicted in Figure 3.24 the pulse duration exhibited periodic variation between well-defined minima, around 45-50 ps in this case, and less well-defined maxima. The pulse duration maxima were more difficult to define since the pulse duration elongated beyond the limits of the autocorrelator and in this example were estimated to be of the order of several hundred picoseconds.

Measurement of the maxima was further complicated by the need to ensure full SESAM switching in an anti-resonant etalon: the pulse duration maxima can only be defined in relation to the minima if there is sufficient intra-cavity intensity to give a full SESAM switch. A pump power that delivered short pulses in a resonant etalon may be insufficient to achieve a full switch in an anti-resonant etalon, and it is impossible to distinguish between elongation due to partial switching and elongation due to modified Q-switch behaviour when moving from a resonant to an anti-resonant etalon.

The distance between the pulse duration minima locations for the laser in Figure 4.8 are plotted in Figure 4.11, alongside 1064 nm fringe spacing inferred from the sodium fringe pattern in Figure 4.8. The good agreement between these two measurements confirms that the pulse duration variations are indeed caused by the variation in thickness of the SESAM etalon. For all results in the following section, etalon thickness was optimised for short pulse duration. We explore further the effects of this etalon on other parameters of the laser in the discussion section below.

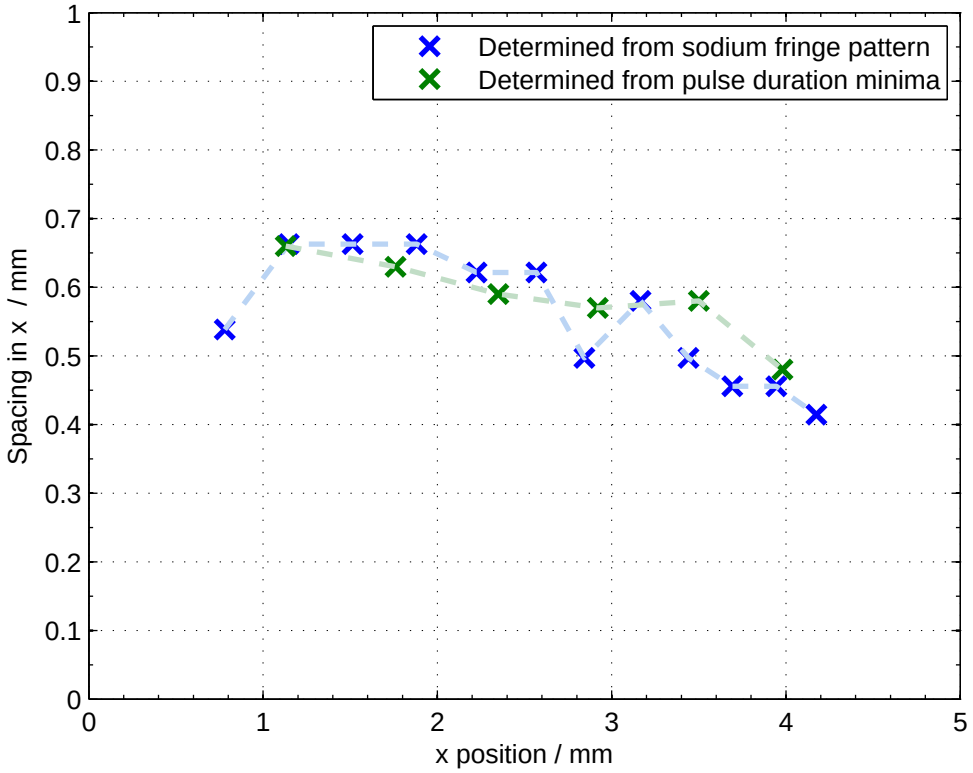

Figure 4.11: Fringe spacing and spacing of pulse duration minima as functions of x-position on the face of the laser.

Although clear periodicity of the pulse duration minima across the laser surface was observed, pulse energy did not follow a clear and obvious pattern, other than at shortest pulse durations, pulse energy seemed to reach a minimum. This is directly contrary to the prediction in Figure 3.24 where, owing to the SESAM etalon, the pulse energy should vary in the same cycle as pulse duration with energy *maxima* reached at the same locations as duration minima. At this point we distinguish between the SESAM etalon and the total cavity etalon as defined by the reflective surface of the output coupler and the SESAM surface. The cavity etalon determines the laser wavelength in relation to emission line centre and when varying the thickness of this etalon we see operation over a ~ 1 nm range as the cavity modes sweep through the gain peak. As the wavelength approaches line centre, as shown in Figure 4.12, the effective emission cross section is increased, reducing the pulse energy while leaving the pulse duration largely unaffected as per Figure 3.13 and Figure 3.11 respectively. As the cavity etalon tunes the laser line away from line centre, we expect the pulse energy to increase roughly as σ_{em}^{-1}, with little change in the pulse duration.

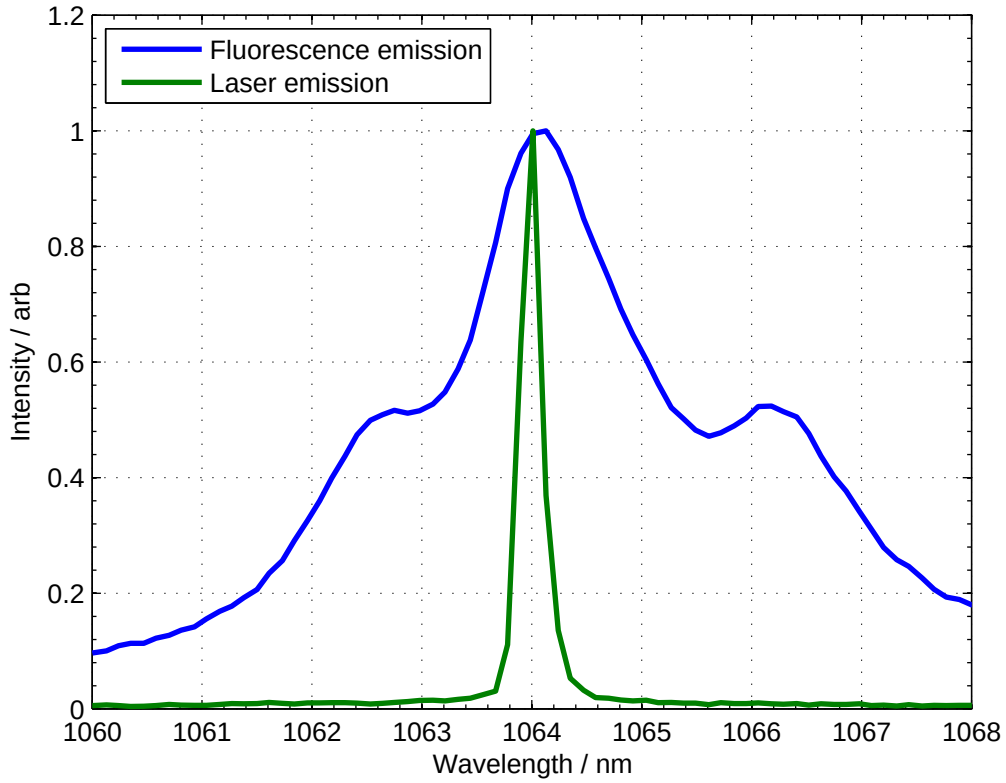

Figure 4.12: The fluorescence emission spectrum of Nd:YVO_4 and single frequency laser output.

The SESAM etalon is independent of the cavity etalon so, for a SESAM etalon optimised for short pulse duration, we should be able to change the cavity etalon (by altering the output coupler etalon or by exploiting minute variations in crystal thickness), shifting the wavelength and effective emission cross section and delivering short pulses at a range of pulse energies. The SESAM etalon remains resonant over the varying wavelength since the etalon thickness, estimated not to be greater than 10 μm, has a free spectral range of at least 30 nm. In practice however, the shortest pulses appear to be strongly correlated with operation at line centre, confining short pulses to low energy operation. We cannot currently explain why it is that shortest pulses always seem to correspond to line-centre operation, since nothing in our current theoretical understanding indicates that line-centre operation should shorten pulse duration. Note that these observations were with the output coupler directly coated on the gain crystal, and so there was no output coupler etalon to consider.

Partial Q-switching

In order to demonstrate partial switching, we optimised the position of the laser mode on the face of the laser to give long pulses, as judged first by the autocorrelator and then by the photodiode response, to ensure that the SESAM etalon was anti-resonant. The pump power was initially set high enough to give a regular train of pulses before being reduced while monitoring the photodiode response for longer, less intense pulses.

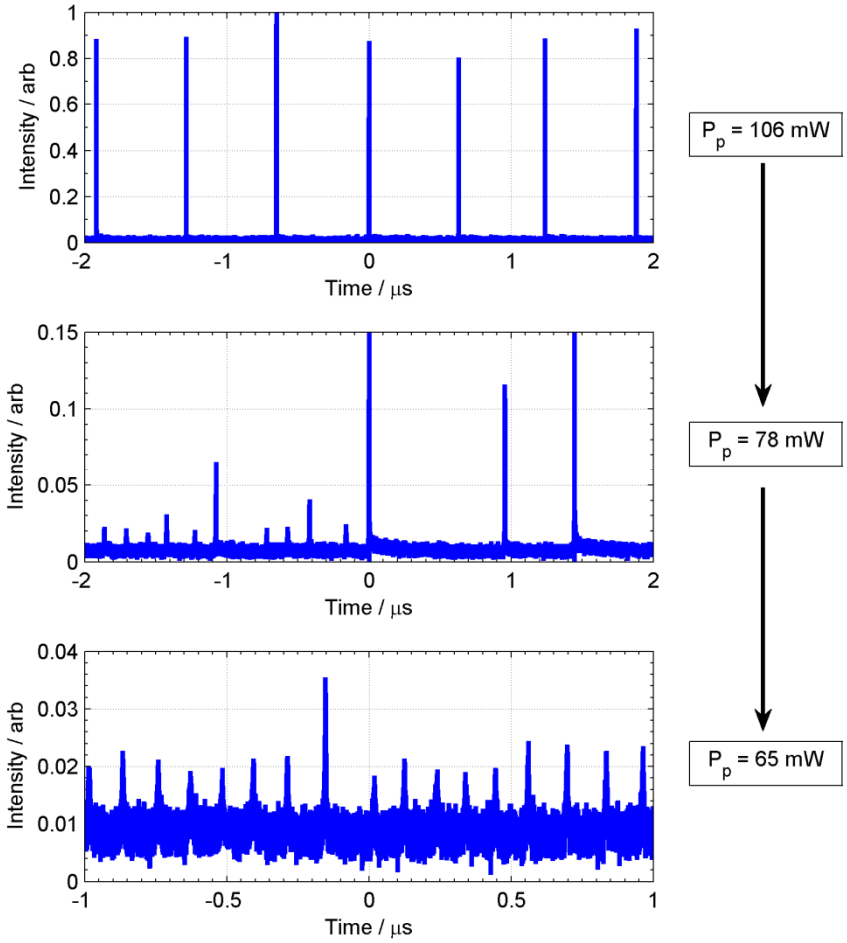

Figure 4.13: The pulse trains of a laser utilising an anti-resonant SESAM etalon for decreasing pump powers. The intensities of the plots are normalised to the maximum of the first. Note the change in axes scales between plots and that the two large pulses in the second plot are clipped by the oscilloscope.

The topmost plot in Figure 4.13 shows a regular pulse train, with pulses of similar intensities. The duration of these pulses was measured using the photodiode to be 330 ps at a repetition rate of 1.74 MHz. From comparison of the pulse duration with the etalon plot in Figure 3.26, we surmise that the SESAM-etalon is anti-resonant. In the subsequent plots, the pump power is reduced from 106 mW, and the onset of lower intensity, partially formed pulses was observed at around 96 mW. In the middle plot we see a range of partially switched pulses, with the smaller pulses having between 4 and 5 ns duration and a repetition rate around 5.7 MHz. In the bottom plot in Figure 4.13 the average pulse duration and repetition rate are 5.4 ns and 8.7 MHz respectively. There are variations in intensity, duration and inter-pulse period between pulses that are not seen in the numerical model predictions, most likely owing to thermal effects, although this variation was seen to lessen as pump power decreased. This is either due to the

decreased thermal load or because at lower pump powers the magnitude of the partial switch becomes less sensitive to fluctuations in pump power, as shown in Figure 3.31.

The elongated pulse duration, increased repetition rate and reduced intensity compared to fully-switched pulses confirm that partial switching of the SESAM is possible provided that an anti-resonant SESAM-etalon is present. A similar approach was attempted to induce partial switching for a resonant etalon case, but as the pump power was reduced, the laser either emitted a full and regular pulse train or nothing at all – there was no middle ground. Similarly, it was more difficult to observe a range of partial switching in the 210 µm cavity and impossible in the 110 µm cavity, since the intra-cavity intensity is higher, making it harder for the intensity suppression to overcome the avalanche effect.

4.4 Cavity length scaling results

Lasers with cavity lengths of 310 µm, 210 µm and 110 µm were assembled and operated according to the details in Sections 4.1 and 4.2. Pulse duration, repetition rate and average output power were recorded at varying pump powers for each, enabling slope efficiency to be determined.

These experiments used a bulk output coupler, and so there is an etalon formed by the air space between the output coupler and the gain crystal. Although we optimised the position of the pump mode in the laser plane for short pulse duration, the effect of the output coupler etalon on pulse duration is small compared to that of the SESAM etalon. For example, in a 310 µm cavity, the resonance of the output coupler etalon defines a pulse duration range of 6 ps compared to a 124 ps range defined by the SESAM etalon, making the effect of the output coupler etalon negligible. Since a solid conclusion regarding the resonance of the output coupler etalon cannot be drawn, both modelled extremes of resonance are included in the following plots for comparison.

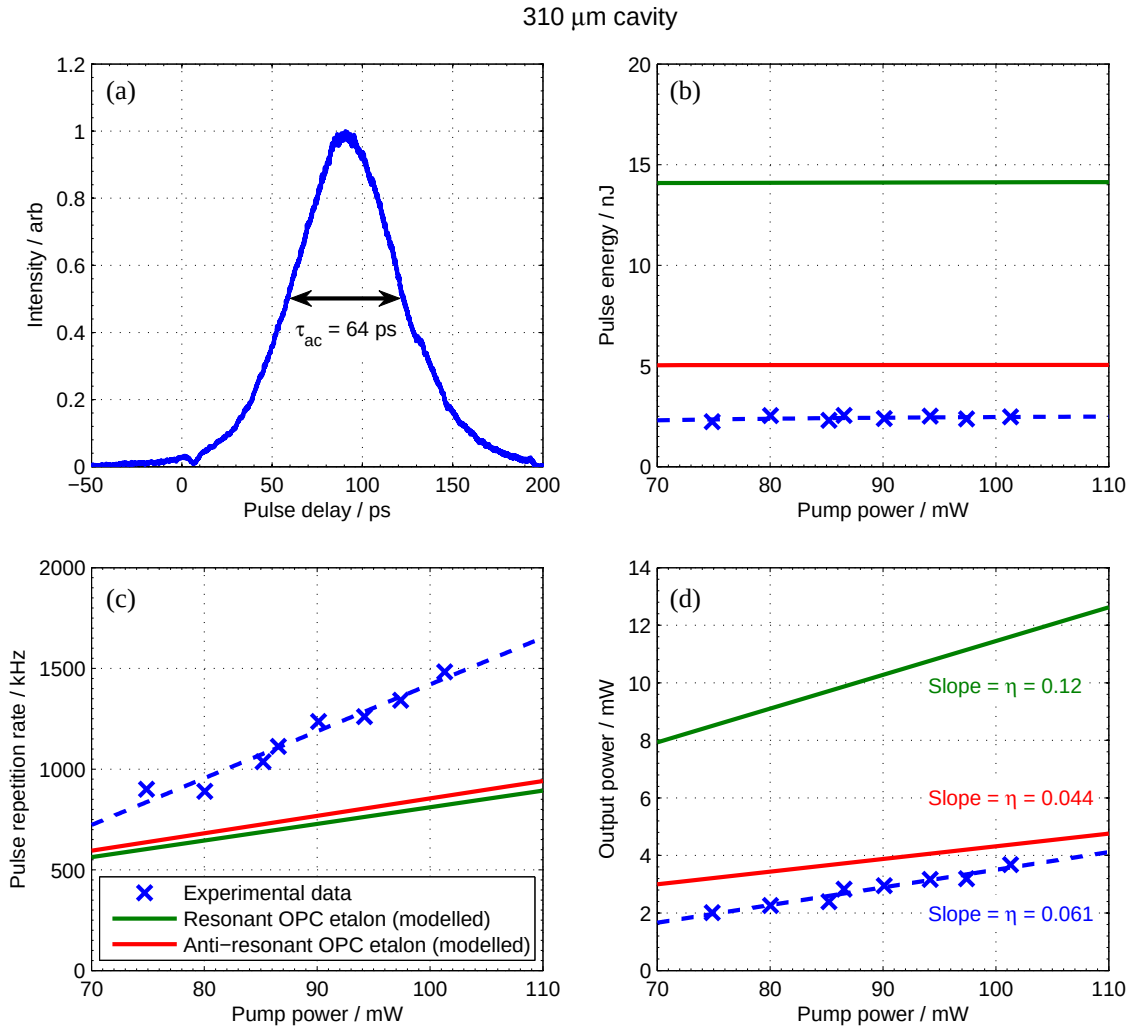

Figure 4.14: Results for the 310 µm cavity: (a) Autocorrelated pulse duration, (b) Pulse energy as a function of pump power, (c) Pulse repetition rate as a function of pump power and (d) Average output power as a function of pump power.

Figure 4.14 shows data taken using a 310 µm cavity. The key results taken from Figure 4.14 are the deconvolved pulse duration, $\tau_p = \tau_{ac}/\sqrt{2} = 45$ ps, and the optical conversion slope efficiency, $\eta = 6\%$. The pulse energy shows a small dependence on pump power but averages to 2.4 nJ in this pumping regime.

All data from the model have been generated using measured values for laser mode radius and the more recently measured SESAM reflectivity values in Section 4.1. As the pump mode is larger than the laser mode in all cases, the incident pump intensity in the model, which assumes perfect overlap between modes, is scaled down according to the ratio of laser to pump mode areas. Since we have optimised the cavity for short

pulses, we can be certain that we are utilising a resonant SESAM etalon, so this is the case in all modelled data.

Already in Figure 4.14 we observe some deviation from the numerical model predictions – particularly in pulse energy and repetition rate. At first glance, these effects appear to cancel each other out to deliver an average output power that falls close to prediction and a slope efficiency that actually falls within predictions. These deviations are discussed in detail towards the end of this section and in the following section.

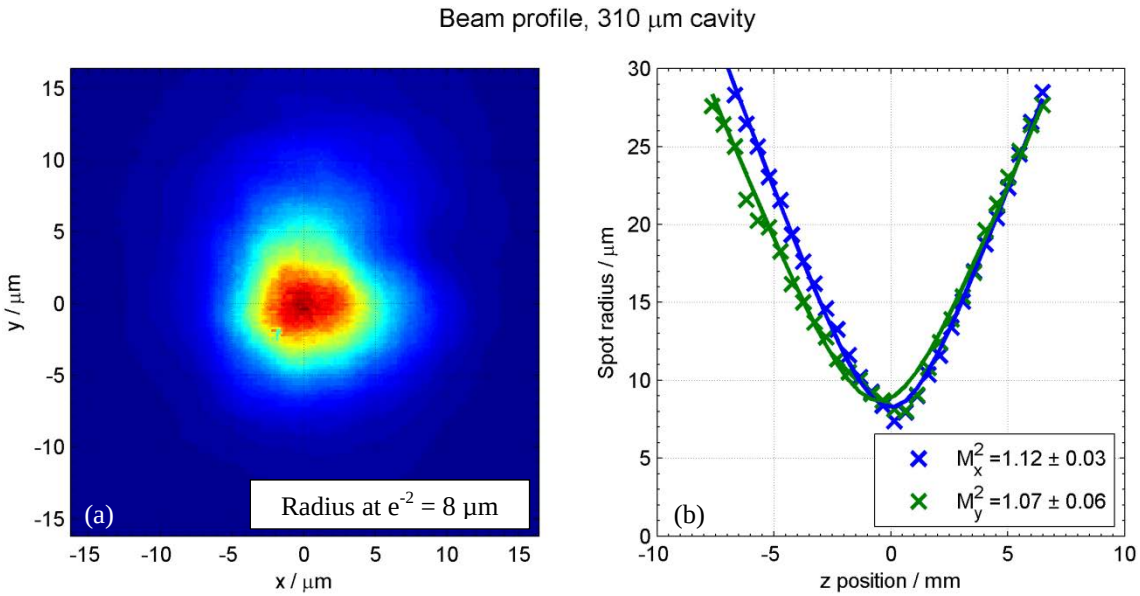

Figure 4.15: (a) Spot intensity profile at focus and (b) M^2 measurement of the laser beam for the 310 µm cavity.

The laser spot profile, shown in Figure 4.15 (a), shows an 8 µm mode radius in the Nd:YVO_4 crystal, and the M^2 value taken from Figure 4.15 (b) is 1.12 ± 0.03. This compares to a pump spot radius of 10 µm.

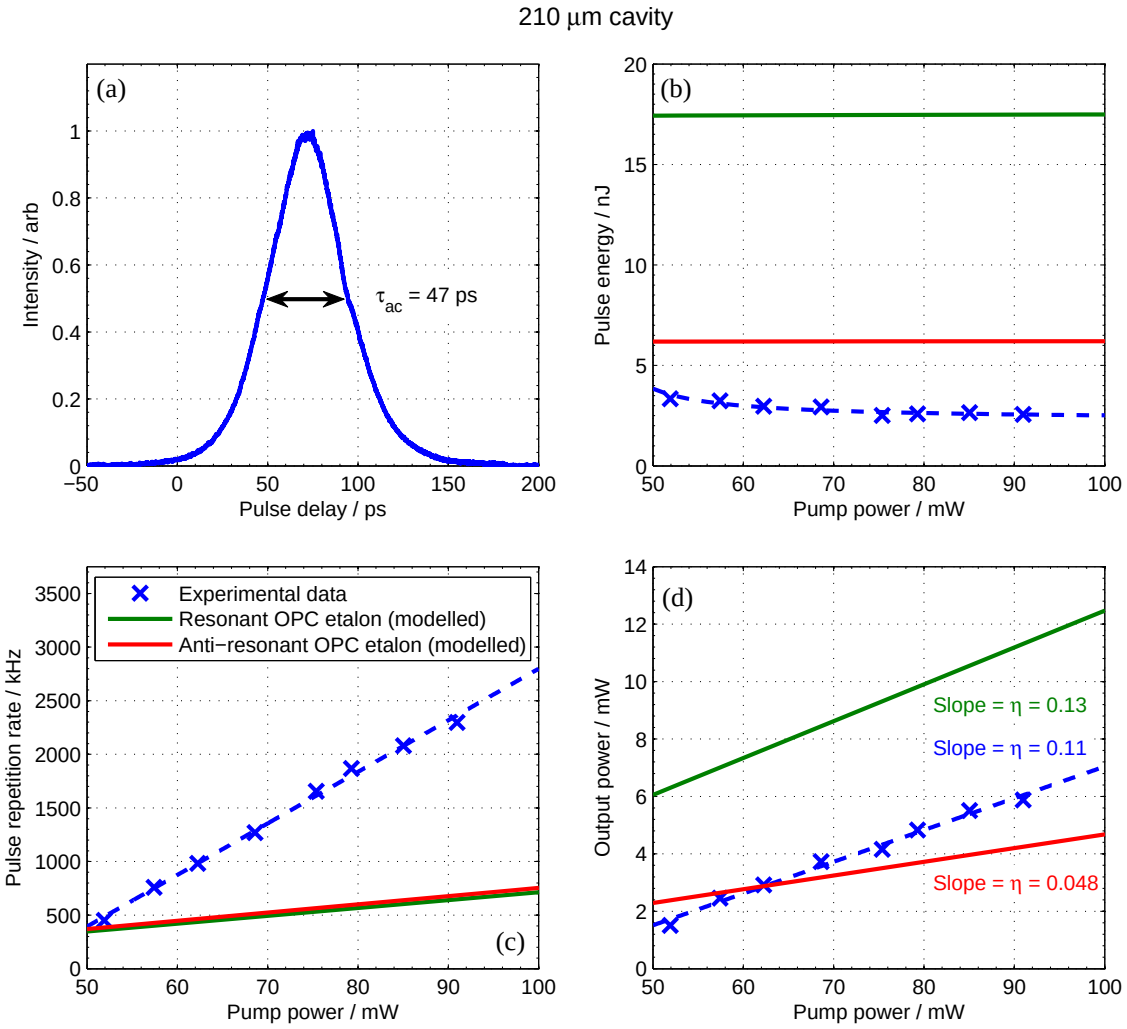

Figure 4.16: Results for the 210 µm cavity: (a) Autocorrelated pulse duration, (b) Pulse energy as a function of pump power, (c) Pulse repetition rate as a function of pump power and (d) Average output power as a function of pump power.

From the 210 µm cavity results shown in Figure 4.16, the shortest pulse duration was $\tau_p = \tau_{ac} / \sqrt{2} = 33$ ps, the slope efficiency 11% and 2.8 nJ pulse energy.

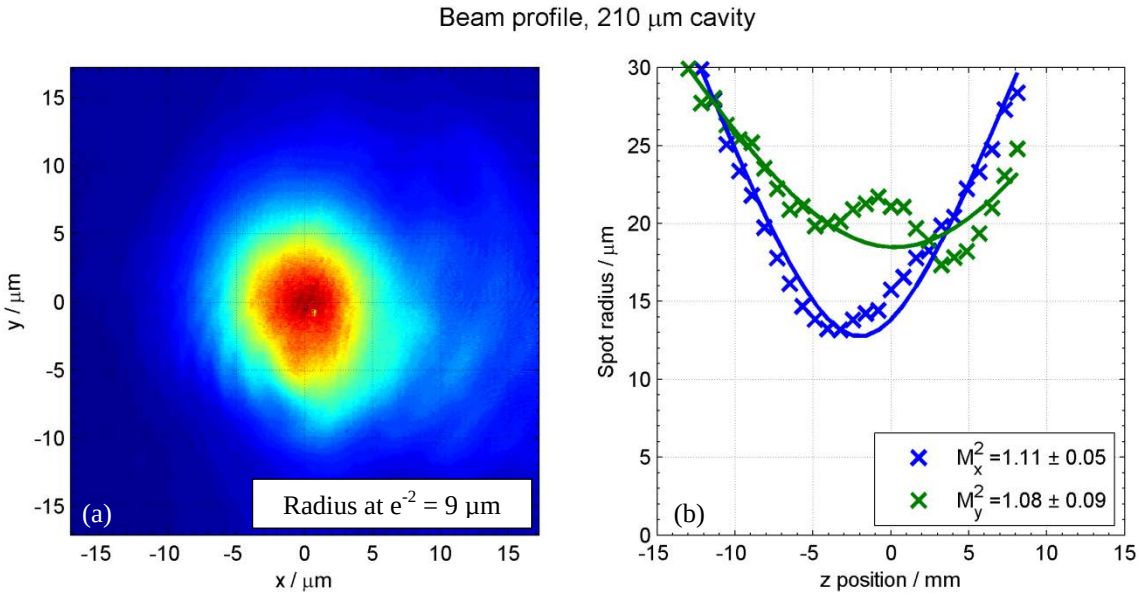

Figure 4.17: (a) Spot intensity profile at focus and (b) M^2 measurement of the laser beam for the 210 μm cavity.

The laser mode size within the 210 μm gain crystal was 9 μm from Figure 4.17 (a), with a beam quality of $M^2 = 1.11 \pm 0.05$ according to Figure 4.17 (b). The y profile in Figure 4.17 (b) is noticeably misshapen. This is due to a slight wedge, ~ 10 mrad (measured by an optical surface profiler), in the gain crystal, which causes a secondary, low intensity spot to form off-centre of the main laser spot when viewed away from the focal point. The result of this, as the M^2 scan moves away from the beam waist, is an apparent increase in the radius measurement at e^{-2}, as illustrated in Figure 4.18 (b). It is not until the BeamScope moves sufficiently far from the focal point that two distinct peaks are resolved and the measurement at e^{-2} applies solely to the primary beam, as in Figure 4.18 (c), in which z regime the M^2 property loses its meaning anyway. This can cause a 'W' shape in a beam radius measurement, as observed in Figure 4.17 (b) and Figure 4.20 (b). Luckily, in each case our secondary beam appears to exist mainly in one axis, suggesting that the crystal wedge is so oriented in relation to the BeamScope scanner that the secondary peak falls along just one BeamScope scan axis. This allows a more confident determination of M^2 in the unaffected scan axis, and we recommend that the M^2 value quoted for the distorted axis is ignored since it will bear little or no resemblance to the true beam quality parameter.

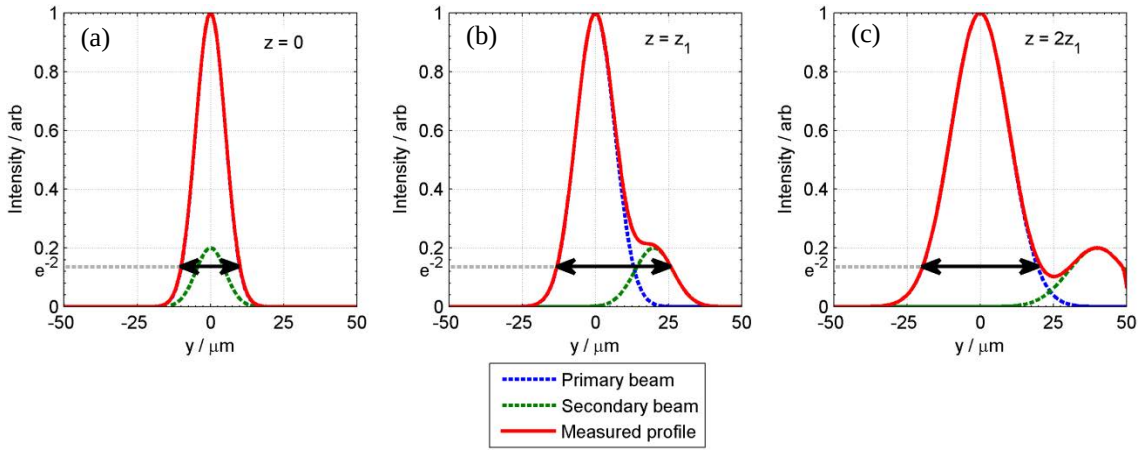

Figure 4.18: An intensity profile of a laser beam including a secondary low intensity beam, showing the e^{-2} diameter measured by the BeamScope, as a function of distance from the beam waist at $z = 0$. In this example the measurement at $z = 2z_1$ is nearly identical to the measurement at $z = z_1$.

A solution to making erroneous measurements of a beam containing a secondary, off-centre beam is either to remove the secondary beam by improving the parallelism of the laser crystal or to use a different method to quantify the beam radius. In the event that the crystal parallelism cannot be improved, a radius measurement made using the second moment of intensity distribution method, or D4σ method [184], may be more appropriate to accurately describe the beam radius than a measurement based on the intensity at e^{-2}. The D4σ method considers the entire energy distribution of a beam profile and is not so dependent on the exact evolution of the shape of the beam as the single e^{-2} characterisation method. It is then possible to scale the D4σ result to an equivalent ideal measurement at e^{-2}, which is a more commonly expressed quantity when describing a Gaussian beam shape. We leave the development of the measurement process to future work but for now make the best of our data by presenting the errors from our fitting of the M^2 parameter (95% confidence bounds) to our beam radius measurements to give an idea of the accuracy of our findings.

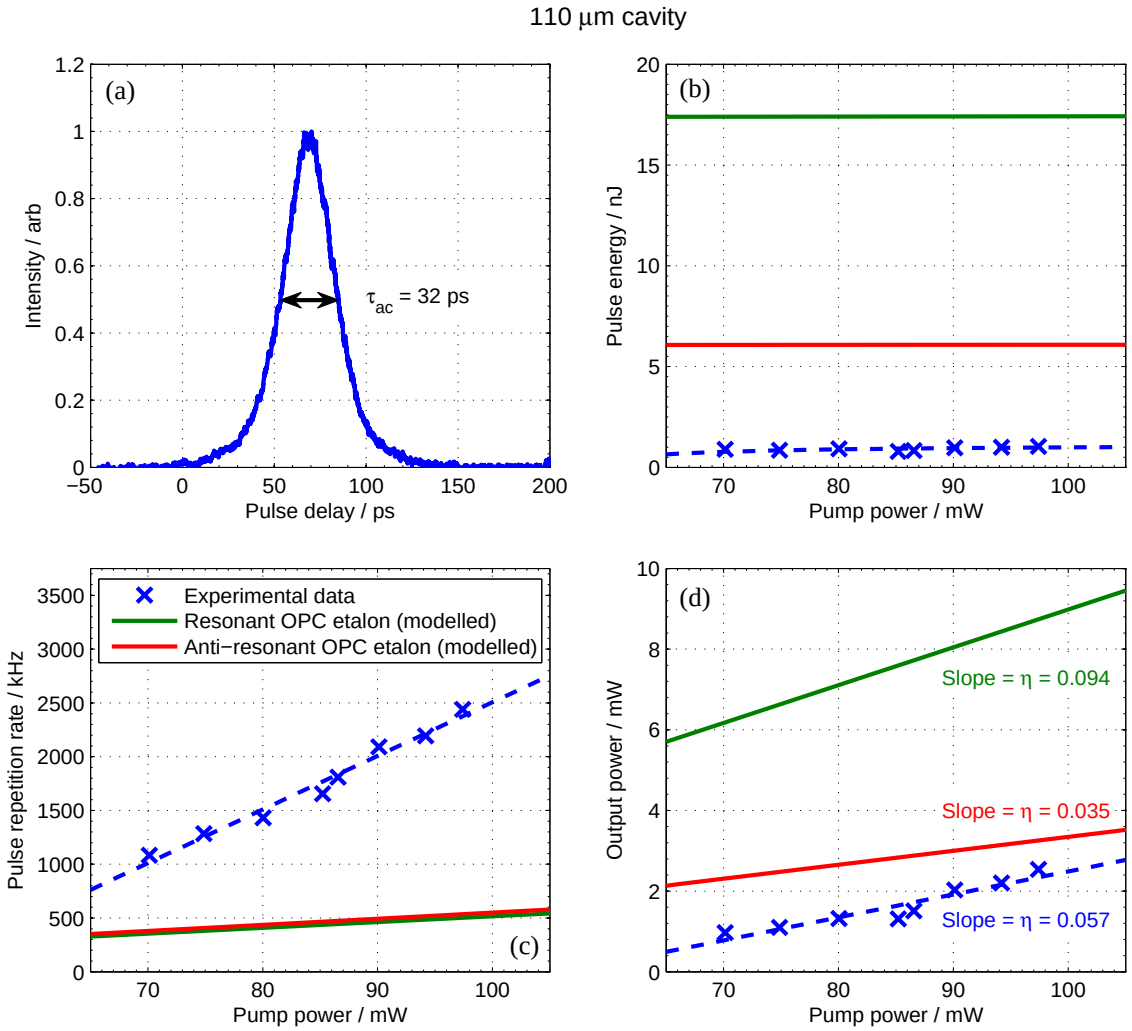

Figure 4.19: Results for the 110 µm cavity: (a) Autocorrelated pulse duration, (b) Pulse energy as a function of pump power, (c) Pulse repetition rate as a function of pump power and (d) Average output power as a function of pump power.

The pulse duration for the 110 µm cavity, taken from Figure 4.19 (a), is $\tau_p = \tau_{ac}/\sqrt{2} = 22$ ps. The slope efficiency from Figure 4.19 (d) is 6% and the average pulse energy in this pumping regime is 0.9 nJ.

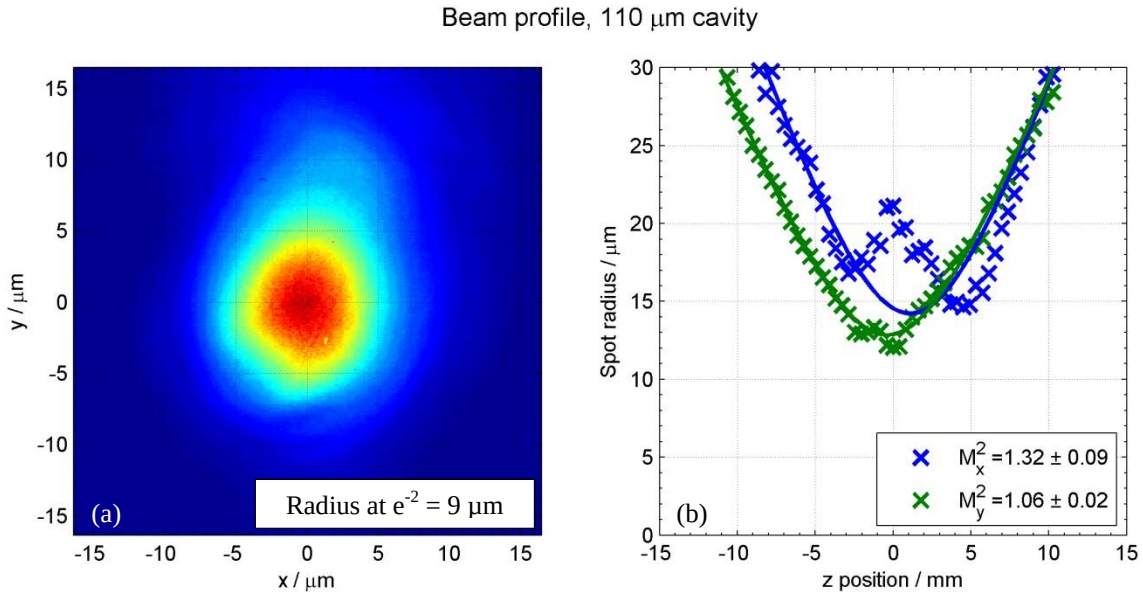

Figure 4.20: (a) Spot intensity profile at focus and (b) M^2 measurement of the laser beam for the 110 μm cavity.

The laser mode radius in the 110 μm cavity was 9 μm and the M^2 value was 1.06 ± 0.02. Again, a secondary spot is shown in the M^2 profile, as described above.

Cavity length / μm	Pulse duration / ps			Pulse energy / nJ				Slope efficiency / %		
	Exp.	Num. Mod.	Spühler 1999	Exp.	Exp. max	Num. Mod.	Spühler 1999	Exp.	Num. Mod.	Spühler 1999
310	45	45-47	63	2.4	16	5-14	4-11	6.1	4-12	4-12
210	33	31-33	43	2.8	24	6-18	5-15	11.1	5-13	5-13
110	22	17-18	22	0.9	4.1	6-17	6-16	5.7	4-9	4-10

Table 4.2: A summary of the experimental results and numerical and analytic modelling predictions. Ranged modelling values are predicted for anti-resonant and resonant output coupler etalons.

Table 4.2 contains a summary of all the experimental results shown in this section, with corresponding results from the numerical and analytic models. These results are also plotted in Figure 4.21, to show their relationships to cavity length scaling. For each cavity we also recorded the maximum pulse energy achievable, disregarding pulse duration. The pulse durations achieved when optimising for pulse energy were varied, but never approached that of the duration-minimised case and were typically of the order of 100s of picoseconds. We do not include pulse repetition rate figures in Table 4.2 since they are strongly pump power dependent and do not add significantly to the analysis at this point.

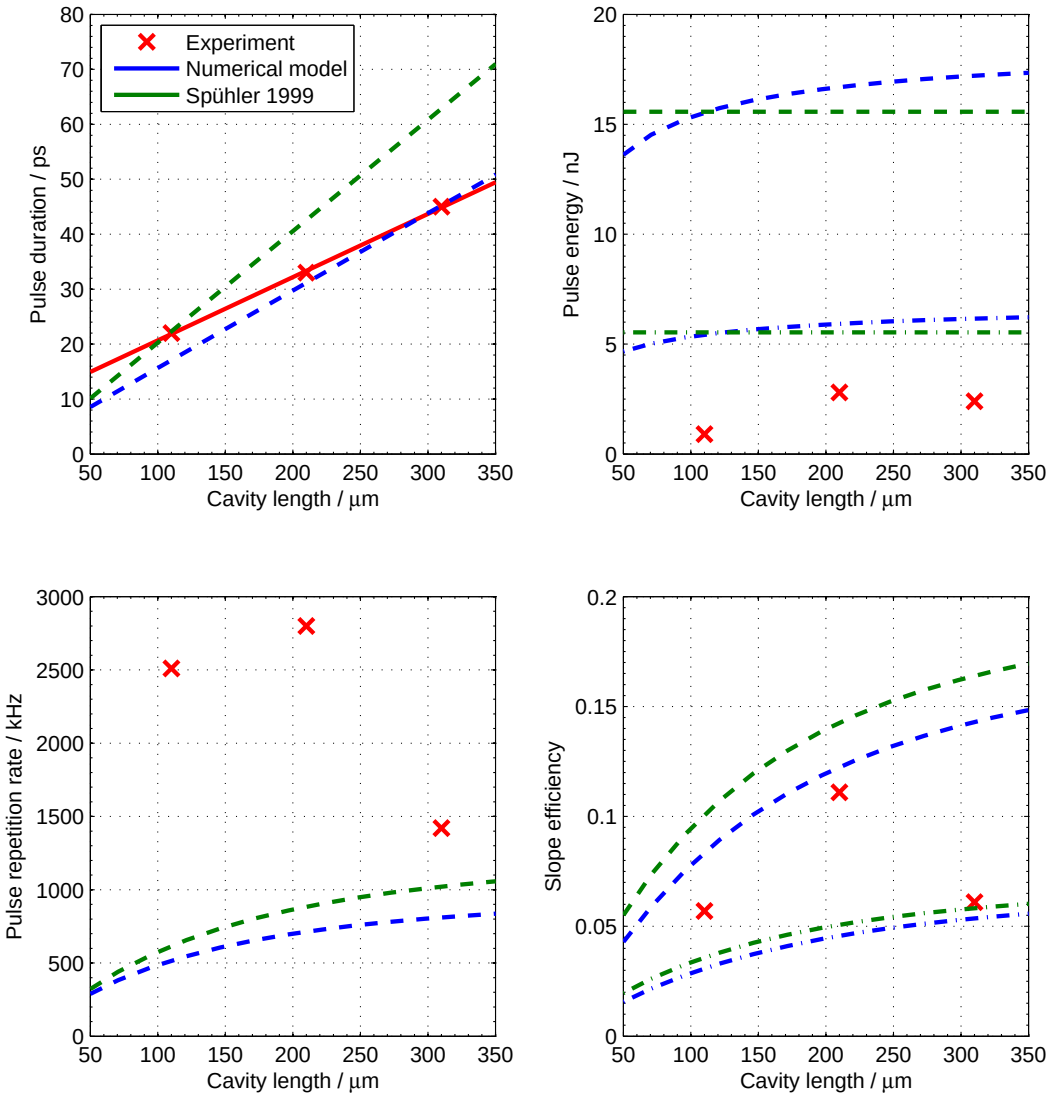

Figure 4.21: The laser results summarised in terms of cavity length scaling. Numerical and analytic modelling results are included for comparison. Resonant OPC etalon data are dashed lines, anti-resonant are dash-dotted.

4.5 Discussion

From the results in Figure 4.21 and Table 4.2, we see that the experimental pulse duration results show extremely good agreement with the numerical modelling predictions. The linear relationship is clearly evident and the measured values agree well with the numerical model predictions in this cavity length range. The relationships between pulse repetition rate and pump power in Figure 4.14, Figure 4.16 and Figure 4.19 show a linear dependence on pump power, although the values are not in the region

predicted by the models. The measured slope efficiencies are all within the predicted ranges, by virtue of increased repetition rate countering the observed deficiency in pulse energy.

In all cases the pulse energy was below the values predicted by both the analytic and numerical models, even when assuming for an anti-resonant output etalon. The pulse energy in the 110 µm cavity was consistently lower than that of the other two cavities, which in turn gave consistently similar pulse energy results to each other. In addition, the pulse repetition rate is above prediction for all cases, although the efficiency remains comparable. From these observations, we suspect that TPA is indeed present and suggest that it is more severe than we expected. While generally lowering the pulse energy for all cavity lengths, an increased consideration of TPA would impact more on the pulse energy at shorter cavity lengths while increasing repetition rate and leaving the efficiency relatively untouched, as shown in Figure 3.20 and Figure 3.26.

The maximum pulse energies in Table 4.2 actually exceed the range defined by modelling (6-12 nJ, depending on the output coupling etalon and for an anti-resonant SESAM etalon). We also must allow for the fact that the laser operates off line centre for maximum output energies: by scaling the modelled energy limits by a rough factor of 2 to account for a halved emission cross-section at ~ 1 nm from the line centre in Figure 4.12, these maximum energy values are consistent with the modelled ranges for an anti-resonant SESAM etalon. This reasonable agreement for the maximum pulse energies can be used as evidence of an increased TPA effect since TPA is not nearly as effective in an anti-resonant SESAM etalon case as it is for a resonant case, meaning that the maximum pulse energies measured in experiment will be less affected by increased TPA.

While at first glance severe TPA appears to be the solution for the pulse energy deficit, it cannot account for all of the deviations from our modelled predictions. In our TPA-modelling approach we would require an order of magnitude increase in the TPA coefficient, β, to bring the predicted pulse energy to a level close to the measured value. However, this boosted TPA concession increases the pulse duration prediction away from agreement with the measured values while not sufficiently increasing the

repetition rate to match the experimental data. Therefore, our treatment of TPA, or indeed the model's ability to comprehensively describe the workings of these lasers, is not complete and requires more development.

Although we identify that the model is lacking in its completeness, we also suspect that the SESAM loss is not behaving as prescribed in experiment. In re-measuring the un-switched reflectivity of the SESAM in Figure 4.3 and through our attempt to quantify the SESAM switching parameters, including TPA, in Figure 4.4 we identified that the SESAM is no longer performing at its manufacturer-specified values. It was not possible for us to exhaustively determine up-to-date SESAM parameters and as such, we cannot rule-out a degraded or damaged SESAM as a cause of the energy deficiency and pulse rate overshoot; either as a source of non-linear loss such as TPA or as a source of constant, non-saturable loss.

4.6 Conclusion

We have constructed three SESAM Q-switched microchip lasers of varying cavity lengths to investigate the effect of cavity length scaling on laser behaviour. In terms of our goal to generate pulses as short as possible, the key outcome of our work is that pulse duration is linearly dependent on cavity length, proven in both experiment and modelling. From the lasers that we tested, pulses of a record 22 ps duration were generated using a 110 µm cavity in a SESAM Q-switched microchip laser. Through this approach, it should be possible to generate a pulse of 10 ps duration at a cavity length of 80 µm; a thickness that poses some small difficulties to manufacture and handle, but is quite obtainable through current grinding and polishing processes.

As predicted by the numerical model, pulse repetition rate is linearly dependent on pump power, with little or no effect on pulse duration or energy. This is an extremely important result for applications where variable pulse rate, or even single pulse operation is desired.

The pulse energy achieved from these lasers is lower than the modelled predictions, although it can be seen from the literature that we are not the only group to experience a pulse energy below prediction [69]. We believe that it is due in part to the

unknown characteristics of a degraded SESAM, but also in part to a TPA contribution considerably stronger than our first estimations. Through our inclusion of TPA in the model, we are able to identify the effects of TPA on experimental SESAM Q-switched microchip lasers and recognise that we may have underestimated the extent of its effect in these types of lasers. We also realise that our first-approximation approach to TPA in the model may not be detailed enough to comprehensively model the effects of TPA in a structure as complex as a SESAM.

The modelled effects of a SESAM etalon have been shown to be reproducible in an experimental laser and the results show good agreement, at least in terms of pulse duration. By modifying the effective parameters of the cavity Q-switch, the varying-thickness SESAM etalon has been shown to give access to a range of pulse durations, as opposed to the SESAM delivering just one. An interesting side-effect of a non-resonant SESAM etalon is to restrict the switching avalanche effect, preventing the SESAM from switching fully and delivering a less intense, longer pulse. This mechanism has been predicted in modelling and successfully demonstrated in experiment.

We have shown that the numerical model can predict experimentally verified scaling relationships, such as the dependence of pulse duration on cavity length and pulse rate on pump power, and even indicate regimes of non-standard operation, such as the partial switching phenomenon. However, it is by no means detailed enough to offer an indisputable, or indeed accurate, prediction of a real-world laser’s performance. From our experimental findings we see there are mechanisms at work in SESAM Q-switched microchip lasers that are not yet understood and consequently our numerical model can only be considered a first step to guiding the design of these lasers.

5 Amplifier modelling and development

As discussed in Section 2.7 and demonstrated in Chapters 3 and 4, the pump-to-laser conversion efficiency of the minimal thickness microchip design is low, owing mainly to low absorption of the pump light. Two of our cavities tested are shorter than the absorption length of 3 at.% Nd:YVO_4, measured to be 250 µm for a pump source with 2 nm spectral bandwidth, leading to very poor absorption. By simply double-passing the pump light through the cavity we are improving the situation but as we push for shorter cavities to minimise pulse duration, this method is insufficient to provide reasonable efficiency.

The results in Chapters 3 and 4 also demonstrate pulse energies in the low nanojoule range, whereas the desired pulse energy from this laser system is at least in the 100s of nanojoule range. Through extension of the numerical model demonstrated

previously we will show that by applying a simple amplification architecture to the SESAM Q-switched microchip laser design, both efficiency and pulse energy can be greatly improved. We also present experimental data for the modelled amplifier designs.

5.1 Concept and design

In a similar approach to Zayhowski and Wilson [149], our energy scavenging amplifier design is extremely straightforward, in keeping with the simple design of the microchip laser. The amplifier takes the form of an additional slab of solid-state laser gain material, butted against the pump-input, laser-output face of the SESAM Q-switched microchip laser oscillator. The amplifier is pumped by the same pump beam as the oscillator, with pump light unabsorbed by the amplifier forming the pump source for the oscillator. Any residual pump light unabsorbed by the oscillator after being double-passed through the cavity re-enters the amplifier crystal for reabsorption. This reabsorption is the mechanism by which the oscillator efficiency might be reclaimed.

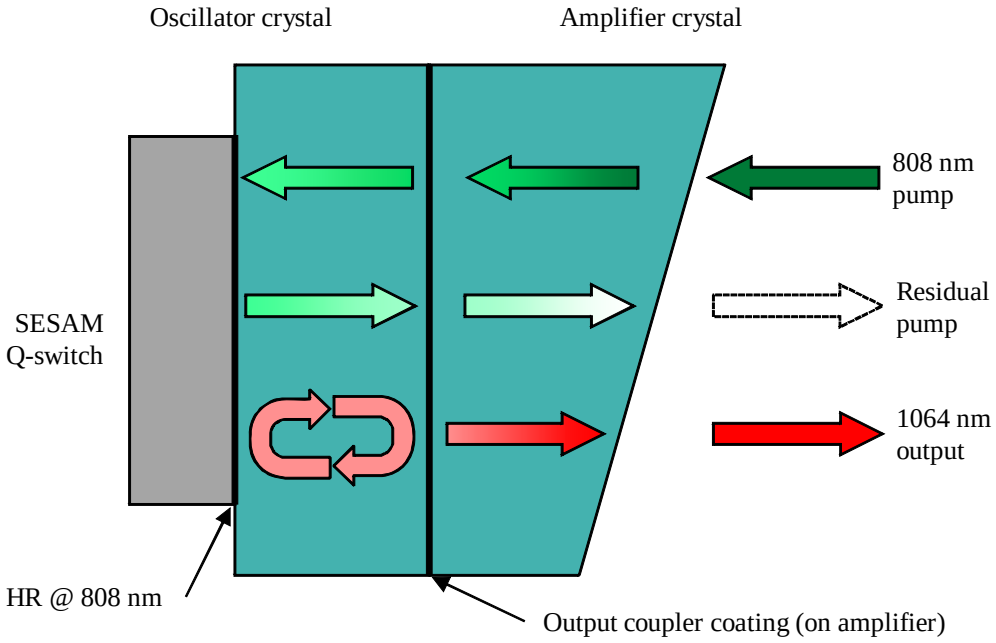

Figure 5.1: A schematic of the amplified SESAM Q-switched microchip laser. The bulk output coupler of Figure 3.1 has been replaced by a wedged, coated amplifier crystal.

The amplifier design is depicted in Figure 5.1, with the coated amplifier crystal replacing the bulk output coupler of Figure 3.1. A key consideration is the requirement

for a wedged amplifier crystal to prevent the Fresnel reflection from the uncoated amplifier-air interface from forming a CW resonator with the output coupler coating. Should the amplifier crystal lase by itself, it will prevent a large inversion density from building in both the amplifier and oscillator (as a coupled-cavity), as well as giving an unwanted background CW level to the output. An alternative to wedging the amplifier crystal is an AR coating, which would additionally prevent Fresnel losses of the output beam, but a wedge has the added benefit of being able to vary amplifier thickness by changing transverse mode position, which is useful in this proof-of-concept stage. In addition, standard AR coatings are rarely good enough by themselves to completely remove Fresnel reflections, so a wedge is preferable.

Since we are using the same pump source for oscillator and amplifier, we are limited to using Nd-doped materials although the amplifier material selection criteria are slightly different to those of the oscillator. Where previously a low emission cross-section was desirable for generating high pulse energies by raising the steady-state inversion threshold, in this instance the emission cross section should be high to give a greater amplification factor and lower saturation fluence. Since the pump has to travel through a highly absorbing medium before reaching the oscillator, the pump power incident on the amplifier will be higher to get comparable performance from the oscillator, requiring that the amplifier have a high thermal conductivity to dissipate the higher heat load. For these reasons, we again choose Nd:YVO_4 as the gain medium, although we will use 4 at.% Nd:YVO_4 for better absorption. For modelling purposes, we assume that the total ion density of 4 at.% Nd:YVO_4 is $4/3$ the value for 3 at.% Nd:YVO_4 as shown in Table 3.3, while the cross-sections remain the same. Again, we are using a-cut Nd:YVO_4, for its high absorption in the π polarisation. The absorption of a 4 at.% Nd:YVO_4 amplifier in single-pass configuration compared to that of a 3 at.% Nd:YVO_4 oscillator crystal in double-pass configuration is shown in Figure 5.2 (a).

To highlight the benefit of the pump-scavenging mechanism, in Figure 5.2 (b) we plot the total system absorption without including the scavenging component (i.e. absorption by initial amplifier pass and double pass through oscillator), and then the absorption including the scavenging component (i.e. initial amplifier pass, double pass through oscillator and second pass through amplifier) in Figure 5.2 (c). The benefit

becomes especially clear at shorter oscillator lengths: if we amplify our 110 µm oscillator system, the total system absorption increases from ~ 50% to nearly 90% by virtue of energy scavenging in just 150 µm of amplifier material.

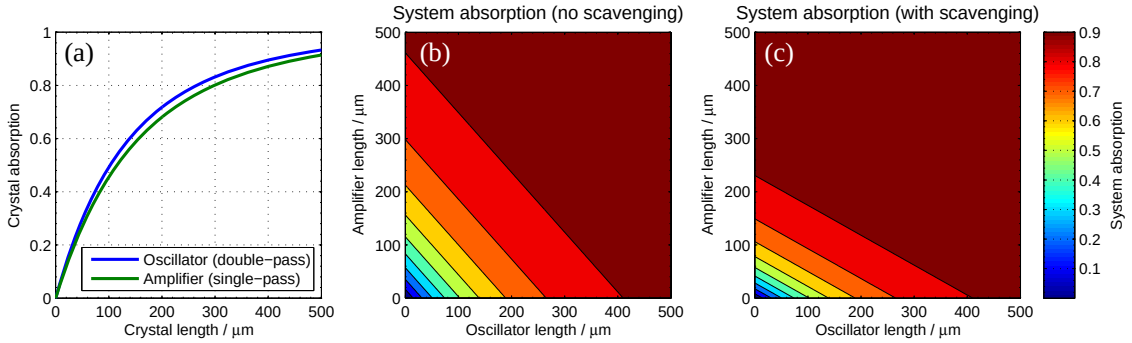

Figure 5.2: (a) The absorption of a 3 at.% Nd:YVO_4 oscillator in double-pass configuration and the absorption of a 4 at.% Nd:YVO_4 amplifier in single-pass. (b) The net system absorption as a function of oscillator and amplifier lengths, without the energy scavenging mechanism. (c) The net system absorption including the energy scavenging component.

We note that for oscillator and amplifiers of the same gain material and orientation, the properties of the oscillator mean that the input pulses for the amplifier will always be close to, but a little less than the saturation fluence for the material. The intracavity pulse fluence in the oscillator will be, by definition, of order of the saturation fluence, since we know it must pull down the oscillator gain as shown in the typical plots such as Figure 3.8. The pulse fluence exiting the oscillator is reduced by a factor of $\left(1-R_{OPC}\right)$ and so will likely be a little less than the saturation fluence for typical output couplers. The conclusion is that only a relatively small amplification factor of order $1/\left(1-R_{OPC}\right)$ is required for the pulse to begin to efficiently extract the stored energy in the amplifier, and for the overall efficiency of the oscillator-amplifier system to be dramatically increased.

5.2 Modifications to numerical model and general modelling results

Including the amplifier in the numerical model requires two main adaptations to be made to the rate equation model:

- Inversion density for the amplifier must be tracked as an additional coupled rate equation, accounting for pumping, pump scavenging and depletion.
- The effective pump power into the oscillator must be scaled-down to account for the presence of the amplifier.

We assume that the crystal axes of the amplifier and oscillator crystal are aligned, as this presents the highest amplifier emission cross-section to the polarised output of the oscillator. By operating at crossed-polarisations, we could increase the amount of π-polarised pump-light allowed through to the oscillator, improving the oscillator efficiency by making use of its large c-axis absorption cross-section. However, the pulse amplification factor is compromised by an orthogonal amplifier/oscillator arrangement since the π-polarised light emitted by the oscillator would only see the lower σ emission cross-section of the amplifier.

We assume that the laser and pump are collimated through the amplifier: this is experimentally not particularly well satisfied for the pump beam that has an M^2 of order 4, and for which the Rayleigh range of a 10 μm spot is just 100 μm. The model will thus overestimate the inversion density and thus the effectiveness of thick amplifiers to some extent, although higher brightness pump diodes may avoid this issue.

The rate equation for amplifier inversion density, n_A, in an amplifier of length l_A, is given:

$$\frac{dn_A}{dt} = -\frac{c_L}{l_A}\frac{\phi}{2}\left(1-R_{OPC}\right)\left(e^{\sigma_{em,A}n_A l_A}-1\right)+\frac{P_P}{h\nu_P}\frac{1}{\pi r_P{}^2 l_A}\eta_{P,\pi,A} + \frac{P_P}{h\nu_P}\frac{1}{\pi r_P{}^2 l_A}\eta_{P,\sigma,A}-\frac{n_A}{\tau_A} \tag{5.1}$$

where

$$\eta_{P,x,A} = \frac{1-e^{-l_A\alpha_{A,x}}+e^{-\left(l_A\alpha_{A,x}+2l_L\alpha_{L,x}\right)}-e^{-2\left(l_A\alpha_{A,x}+l_L\alpha_{L,x}\right)}}{2} \tag{5.2}$$

is the amplifier pump absorption efficiency and $\alpha_{A,x} = \left(n_{tot,A} - n_A\right)\sigma_{abs,x,A}$ and $\alpha_{L,x} = \left(n_{tot,L} - n_A\right)\sigma_{abs,x,L}$ are the single-pass absorption coefficients of the amplifier and laser oscillator respectively for polarisation x. The amplifier absorption efficiency is calculated as the fraction of incident pump power absorbed in the first pass, plus a contribution from absorption in the return pass of the pump power remaining after the transit through the oscillator. In our case, both the emission and absorption cross-sections are the same for both oscillator and amplifier, i.e. $\sigma_{abs,x,L} = \sigma_{abs,x,A}$ and $\sigma_{em,L} = \sigma_{em,A}$, but individual treatment is given for general applicability.

The first term on the right-hand side of (5.1) is the depletion of the amplifier as a function of the power output of the oscillator and is derived by considering the power into and out of the amplifier:

$$P_{out} = \pi r_L^{\,2} l_A h\nu_A \frac{dn_A}{dt} + P_{in} \tag{5.3}$$

where P_{out} is related to P_{in} by (3.1) (assuming common mode sizes between amplifier and oscillator) and P_{in} is calculated from (3.24). Since the wavelengths of the amplifier and oscillator are the same, $\nu_A = \nu_L$, the depletion term is derived. We do not need to account for the longitudinal variation in the inversion density through the amplifier, since the absorption and gain properties of such a slab are independent of this longitudinal profile, depending only on the integral of the oscillator inversion density.

The oscillator inversion density, equation (3.36), is modified to:

$$\begin{aligned}\frac{dn_L}{dt} = -c_L\sigma_{em,L}n_L\phi + \frac{P_P}{h\nu_P}\frac{1}{\pi r_P^{\,2} l_L}\eta_{P,\pi,L} \\ + \frac{P_P}{h\nu_P}\frac{1}{\pi r_P^{\,2} l_L}\eta_{P,\sigma,L} - \frac{n_L}{\tau_L}\end{aligned} \tag{5.4}$$

where the oscillator pump absorption efficiency is now given for a polarisation x:

$$\eta_{P,x,L} = \frac{e^{-l_A\alpha_{A,x}} - e^{-\left(l_A\alpha_{A,x} + 2l_L\alpha_{L,x}\right)}}{2} \tag{5.5}$$

and $\alpha_{A,x}$ and $\alpha_{L,x}$ are as before, giving the oscillator access only to that pump power that is transmitted through the amplifier slab.

The modified oscillator and amplifier differential equations can be solved for a time span to simulate a train of pulses as before. The resulting output power of the complete system is determined from (3.1) where the amplifier inversion density is the solution to (5.1) and using (3.24) as the input power. From this time-dynamic output power, we measure amplifier pulse duration and repetition rate, calculating energy by integration over a pulse and finally deriving overall slope efficiency by performing for a range of input pump powers.

In all the modelled results in this section and the next, the general laser design described in Chapter 3 forms the oscillator cavity and the amplifier length unless otherwise stated is 150 µm. We increase the standard pump power under test from 100 mW to 200 mW to approximately counter the absorption of the amplifier. At this stage TPA is not included in modelling results, as it is a fairly minor factor in dictating the oscillator behaviour. In terms of changing the oscillator behaviours that will most likely affect the amplified system performance, such as pulse energy and duration, other oscillator parameters, such as SESAM modulation depth, have a stronger effect.

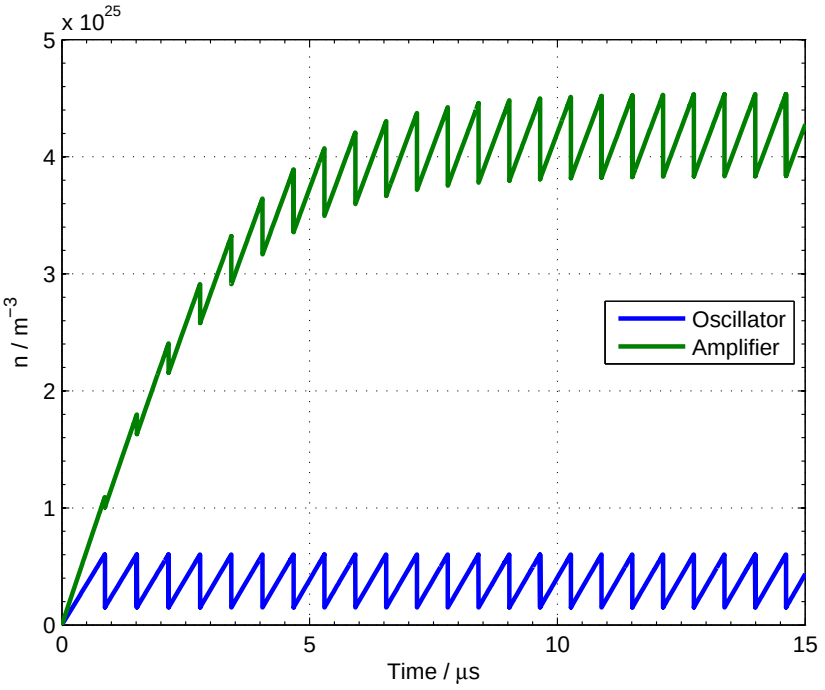

Figure 5.3: The inversion density of the amplifier and oscillator components of the laser over time.

The inversion in the amplifier compared to that of the oscillator for the general amplified design is shown in Figure 5.3. The inversion density of the oscillator performs as in Section 3.6, with periodic depletion by the pulse and re-pumping. The amplifier inversion behaves in much the same way although at a higher level and taking longer to reach equilibrium. This "warm-up" period, where the size of the amplifier inversion density, and hence the extent of its depletion, has not reached equilibrium with pump absorption, is also reflected in the intensity of the amplified pulses, shown in Figure 5.4. Through numerical modelling we find that the duration of the warm-up period is solely determined by the pump power.

During the amplifier pump and depletion cycle, the transmission of the amplifier crystal changes with the population inversion density, affecting the intensity of the pump through to the oscillator. The change in inversion density during the typical cycle shown in Figure 5.3, $\sim 7\times10^{24}$ m^{-3}, compared to the total ion density in 4 at.% ND:YVO_4, 5×10^{26} m^{-3}, is negligible, translating to a negligible change in amplifier transmission and hence oscillator pumping rate. While this mechanism is intrinsically incorporated into the numerical model, it appears to have no discernible effect.

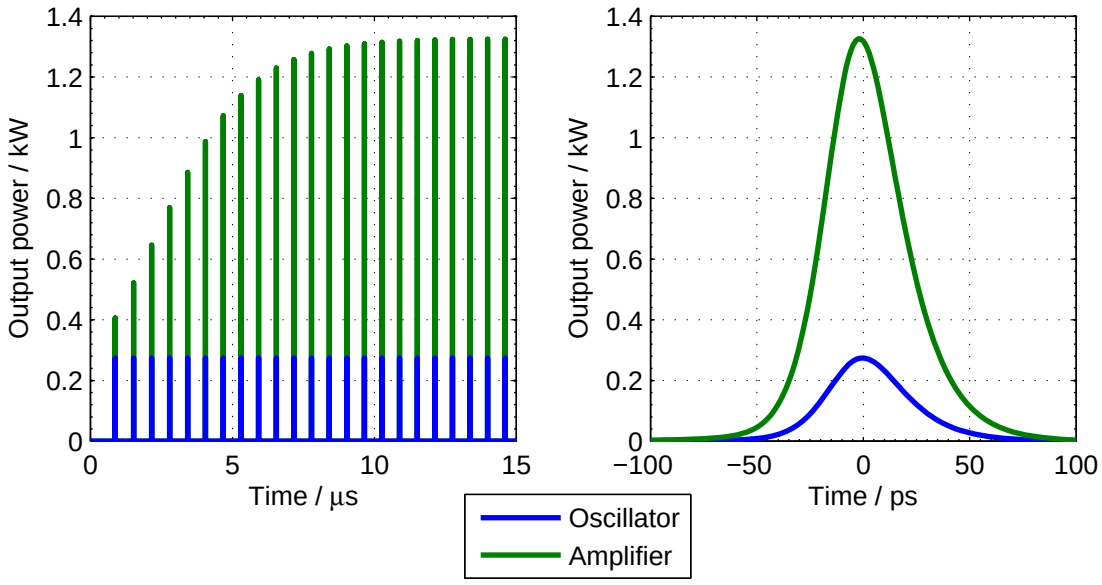

Figure 5.4: The output pulse trains of the amplifier and oscillator components, and pulse detail.

Figure 5.4 clearly shows the effect of the 150 μm-thick amplifier on the intensity of the pulse. In this instance, a pulse energy amplification of 4.8 is achieved to give a

pulse energy of 63 nJ at a repetition rate of 1.6 MHz and pulse duration 41 ps. The amplified pulse slightly precedes the oscillator pulse (in this example, by ~ 3.5 ps) owing to the leading edge of the oscillator pulse having sufficient intensity to trigger significant gain extraction in the amplifier, although the overall repetition rate of the amplifier output is identical to that of the oscillator. At this oscillator length, a small shortening of the pulse duration by 1.5% is predicted.

5.3 Modelling scaling relationships in the amplified laser

We now use the numerical model to examine the scaling relationships between oscillator and amplifier component parameters and the output behaviour of the amplified laser system. The guidelines for designing both the oscillator and amplifier components to optimise for overall system performance will be established.

In this analysis we make the distinction between the oscillator component of an amplified system, and an un-amplified laser as discussed in Chapters 3 and 4. While the performance of the amplifier component is typically characterised by comparing its output to its input from the oscillator component, we are mainly interested in the improvement of the complete amplifier system over that of an un-amplified laser with an identical oscillator cavity. However, this is not the same as comparing the amplifier system performance to that of its own oscillator component since the composition of the incident pump beams in terms of polarisation will be dissimilar. By passing through the amplifier, the π-polarised component of the pump beam is significantly reduced compared to the σ component, meaning that the oscillator component is pumped slightly less efficiently than in an un-amplified laser, for a given total pump power. To this end, although the cavities might be identical in design, the behaviours of the amplifier oscillator component and the un-amplified laser are not equivalent, especially for pump power-driven behaviour such as repetition rate. Therefore we make the decision to directly compare the amplifier system output to that of an un-amplified laser.

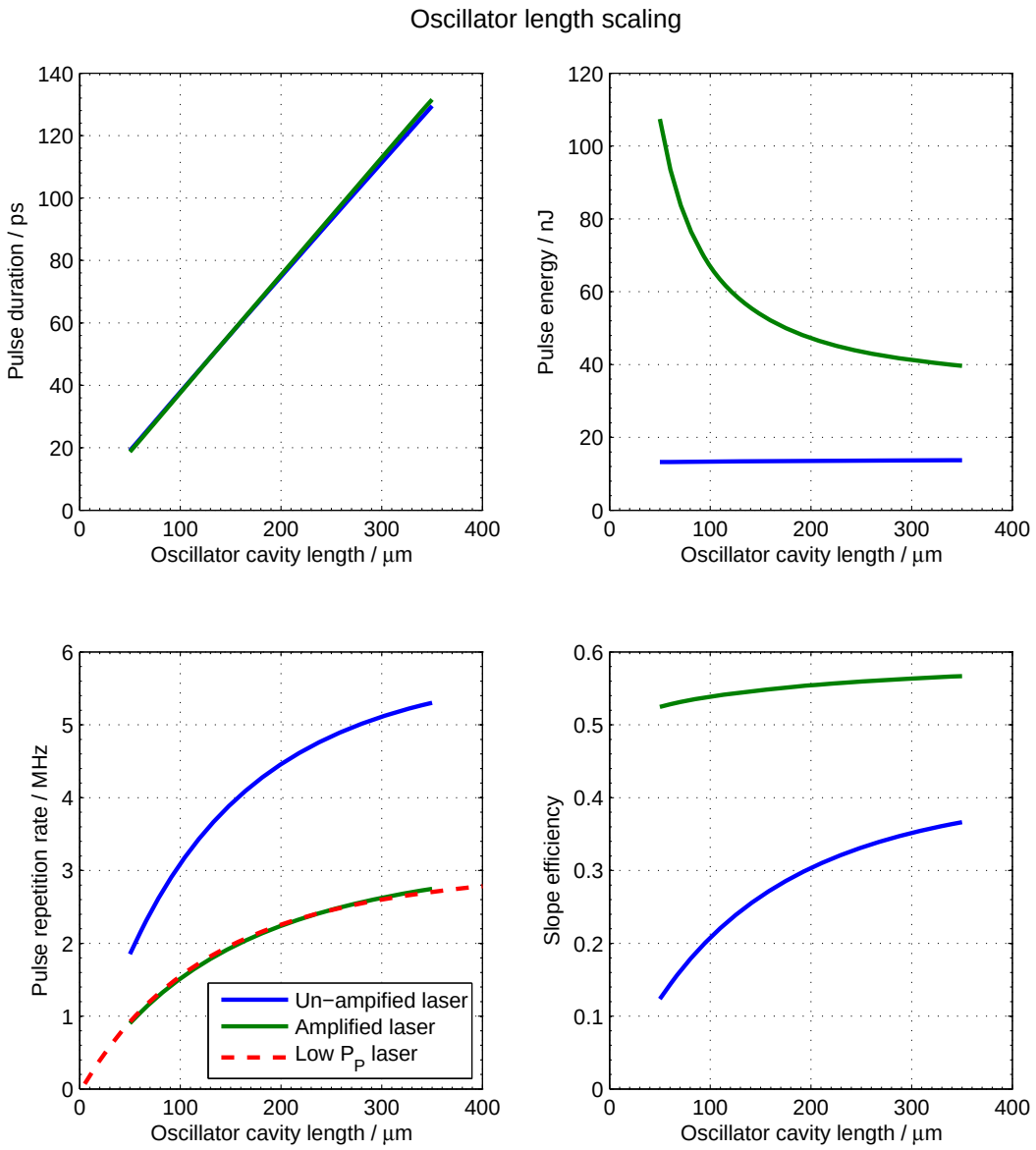

Figure 5.5: Amplifier system performance compared to an un-amplified laser as functions of oscillator cavity length. Amplifier length is fixed at 150 µm.

The effect of changing the oscillator cavity length on amplifier system performance is shown in Figure 5.5. The amplified pulse duration changes only marginally in relation to that of the un-amplified laser.

Amplifier pulse repetition rate behaves as expected: the presence of the amplifier effectively lowers the pump power reaching the oscillator and decreases the repetition rate. If the pump power of an un-amplified oscillator is chosen to deliver the same pulse repetition rate as the amplified system, shown by the dashed red line in

Figure 5.5, we show that the amplifier oscillator repetition rate behaves identically to a comparable un-amplified oscillator.

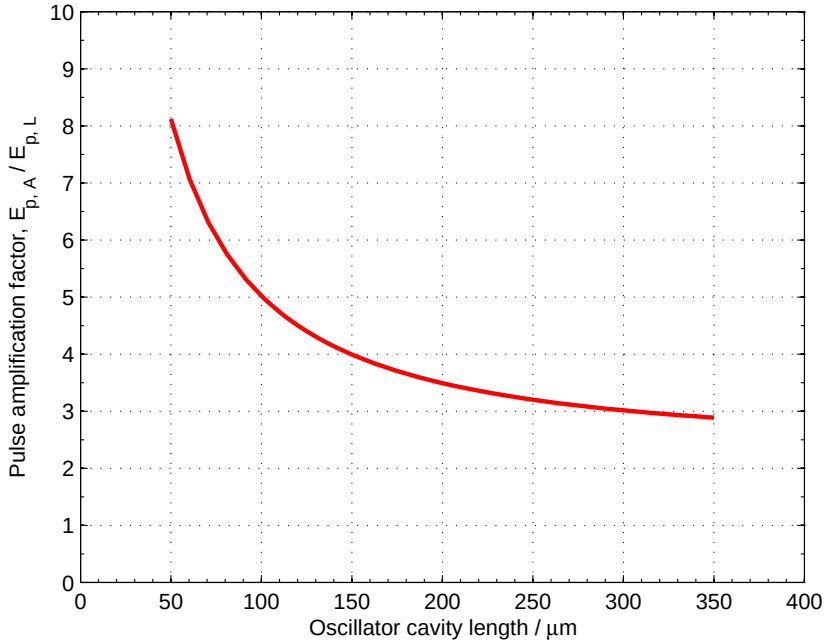

Figure 5.6: The ratio of amplified pulse energy to un-amplified pulse energy as a function of oscillator cavity length.

The effect of amplification on pulse energy is clear in both Figure 5.5 and Figure 5.6. Higher amplification factors are reached at shorter oscillator lengths because oscillator repetition rate, or amplifier depletion rate, is reduced since the oscillator is less absorbing. In order to maintain equilibrium between the reduced depletion rate and the unchanged pump absorption rate for the amplifier, the average amplifier inversion level increases, effectively increasing the magnitude of the depletion, as depicted in Figure 5.7. Since changing the oscillator length does not change the pulse energy into the amplifier, it is the magnitude of the amplifier inversion depletion that determines output pulse energy, and so the amplification factor is increased. Another factor reinforcing this trend is that the thinner oscillators absorb less of the incident pump power, therefore allowing more pump power to be absorbed on the return pass through the amplifier.

Where short oscillator length seriously compromised efficiency in un-amplified SESAM Q-switched microchip lasers, the introduction of a basic amplifier greatly lessens this effect. Note that the amplification factors ranging between 8 and 3 are

sufficient to boost the pulse fluence sufficiently to saturate the gain and extract the stored energy in the amplifier. The overall slope efficiency thus shows a strong improvement compared to that of an un-amplified laser, particularly at short oscillator lengths.

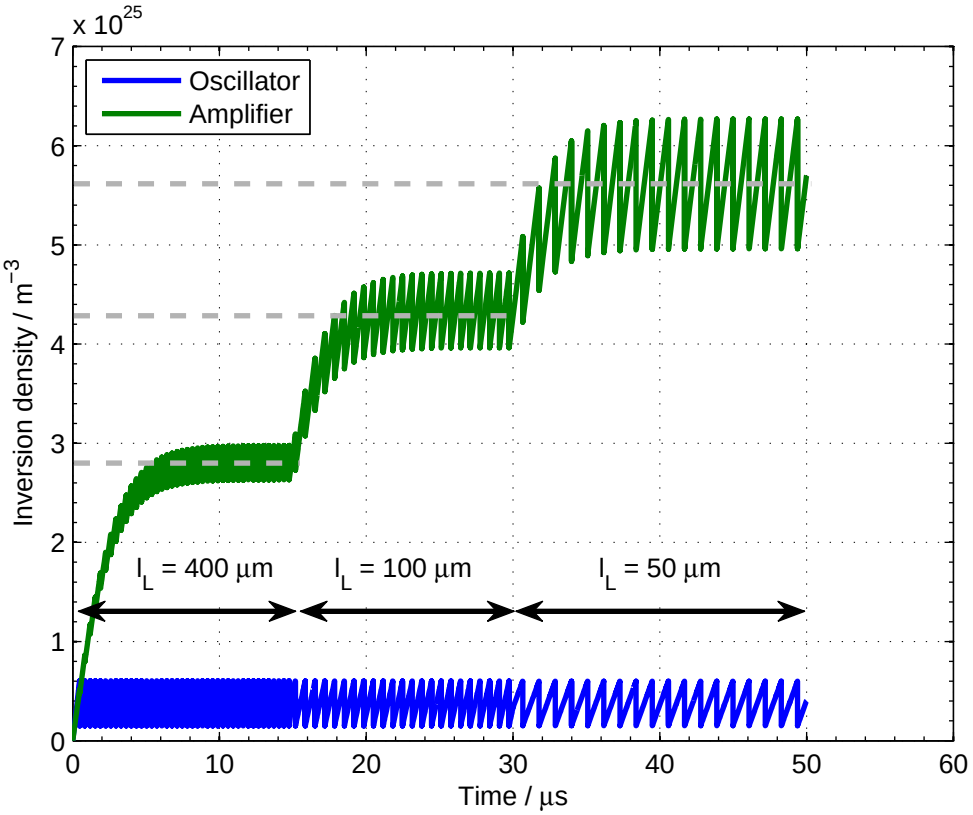

Figure 5.7: The comparative amplifier inversion densities for short and long cavity oscillators, when changed over time, showing increased amplifier inversion and inversion depletion for shorter, lower repetition rate oscillators. The average amplifier inversion levels at equilibriums are shown in dashed lines.

Figure 5.8 shows the effect of increasing pump power. The pump power absorbed by the oscillator increases so increasing the repetition rate, and increasing the depletion rate of the amplifier; the pump rate of the amplifier is also increased by the same factor however, resulting in a near-constant amplification factor E_A/E_L .

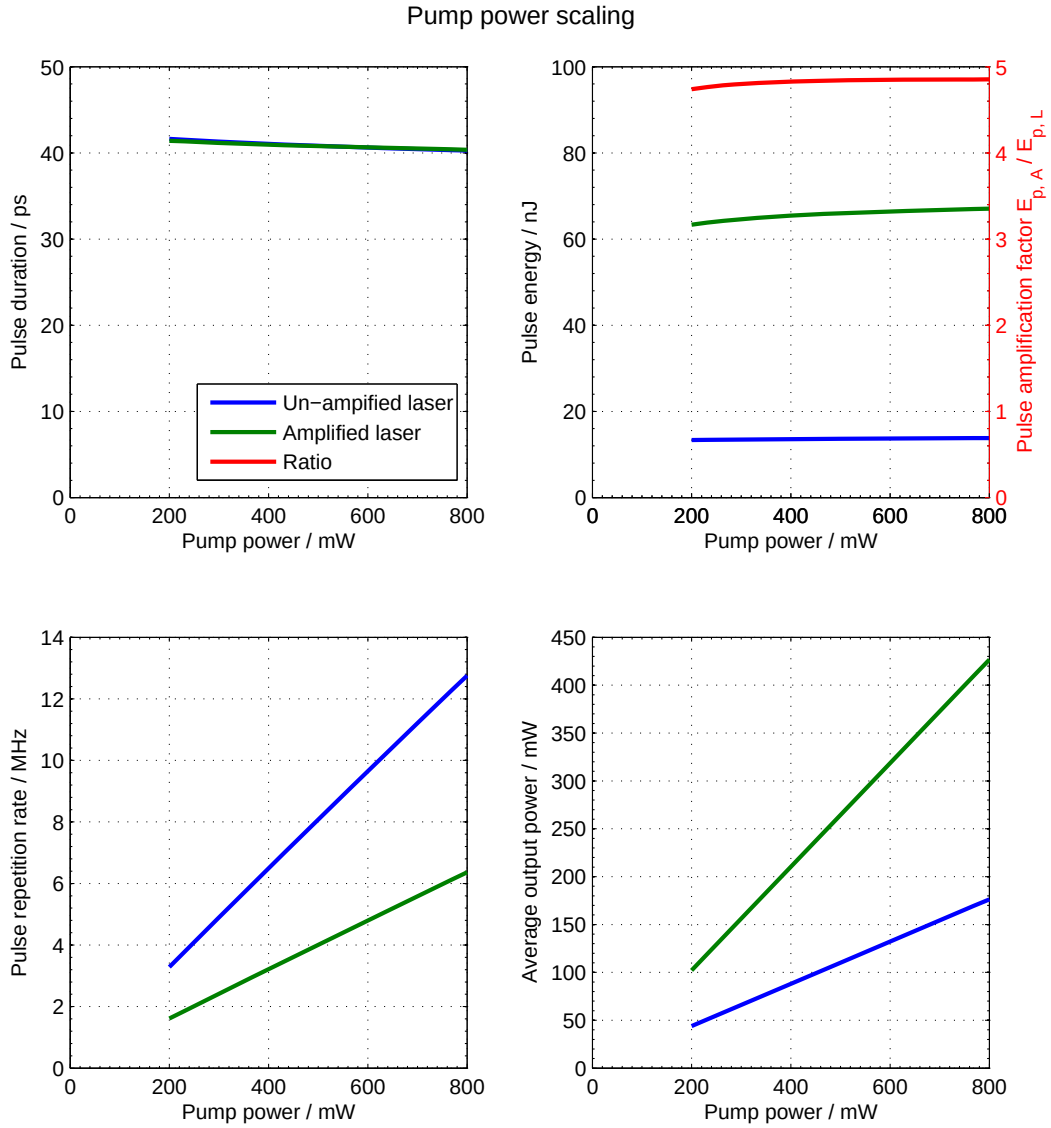

Figure 5.8: The scaling of amplified and un-amplified laser output behaviour with input pump power.

In general terms, any mechanism that gives a net increase in amplifier depletion rate will cause the amplifier inversion and so amplification factor to drop. Since the depletion rate is directly proportional to repetition rate, which in turn is proportional to the oscillator efficiency, the amplification factor is inversely related to the oscillator efficiency for a given amplifier. This gives us insight into the amplification dependence on oscillator parameters such as SESAM modulation depth, emission cross-section and output coupler reflectivity. In the following plots, the inverse relationship between oscillator efficiency and amplification factor is clear.

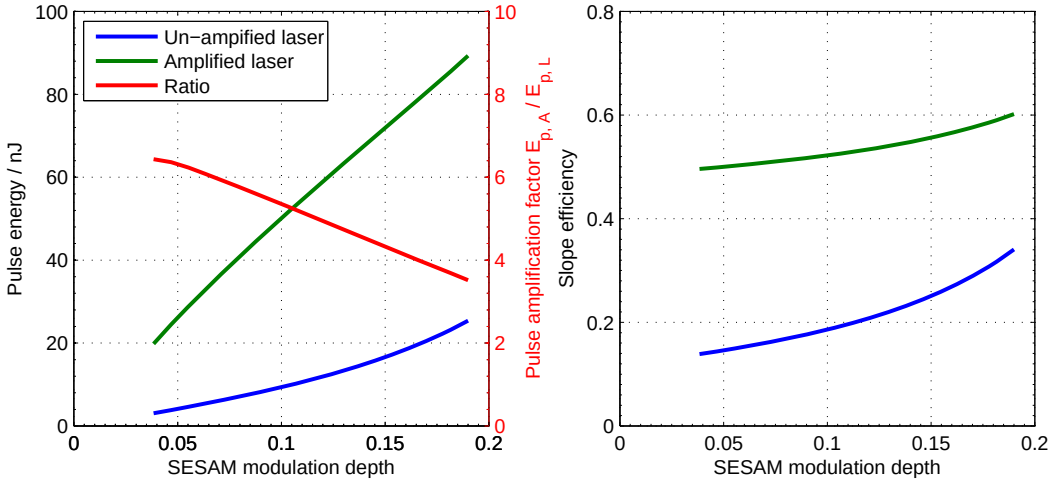

Figure 5.9: Amplifier scaling behaviour with SESAM modulation depth.

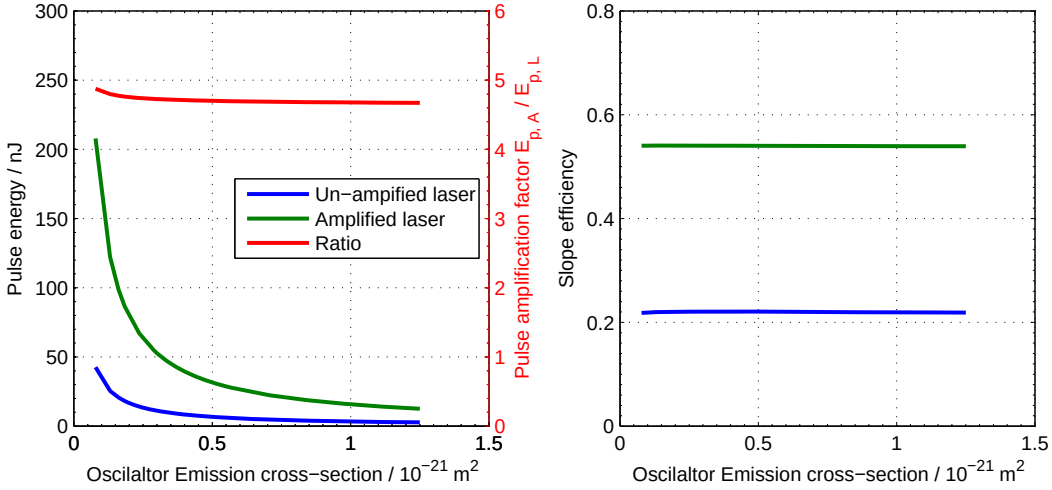

Figure 5.10: Amplifier scaling behaviour with oscillator emission cross-section.

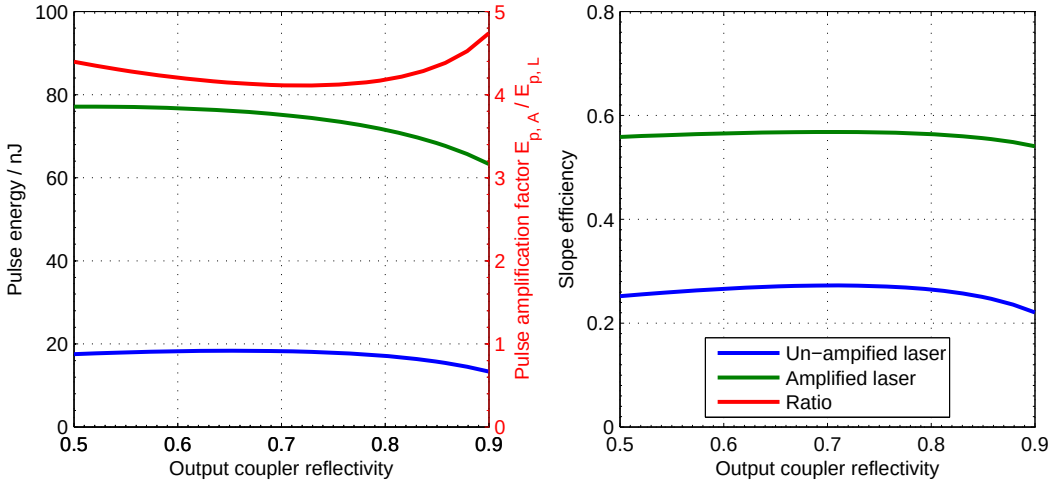

Figure 5.11 Amplifier scaling behaviour with output coupler reflectivity.

Finally, we examine the effects of SESAM etalon thickness on amplifier behaviour. A mix of changing the effective Q-switch modulation depth and the effective non-saturable Q-switch loss, the amplification factor is maximised for resonant etalons for which the effective ΔR is maximised, giving the lowest repetition rate and so maximum time to re-pump the amplifier.

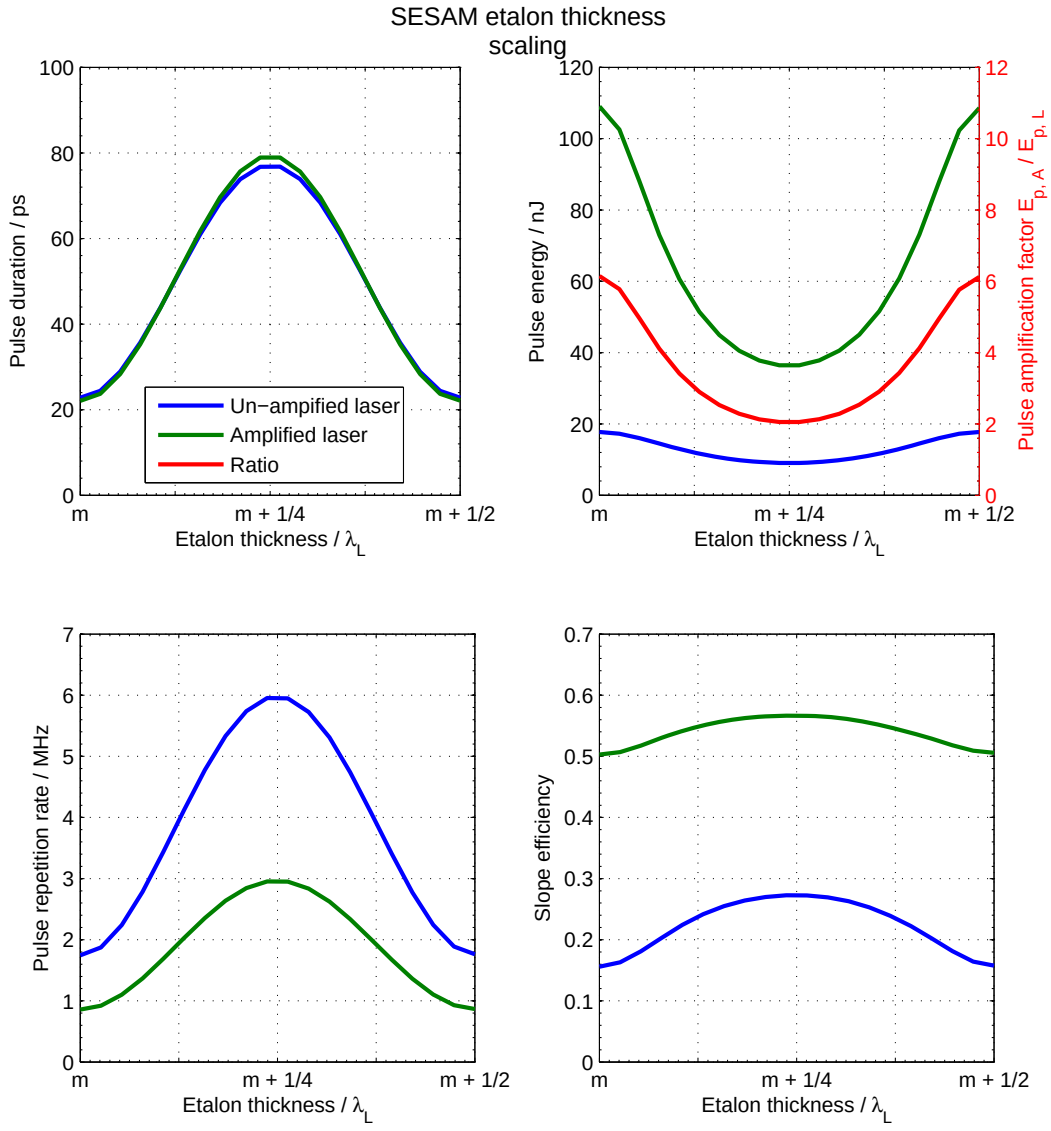

Figure 5.12: The effect of the oscillator SESAM etalon on amplifier performance.

In the remainder of this section, we examine the scaling relationships between amplifier properties and amplified system performance. The three main parameters to test are the amplifier length, its doping level and its emission cross-section. The effect of increasing the amplifier length is shown below.

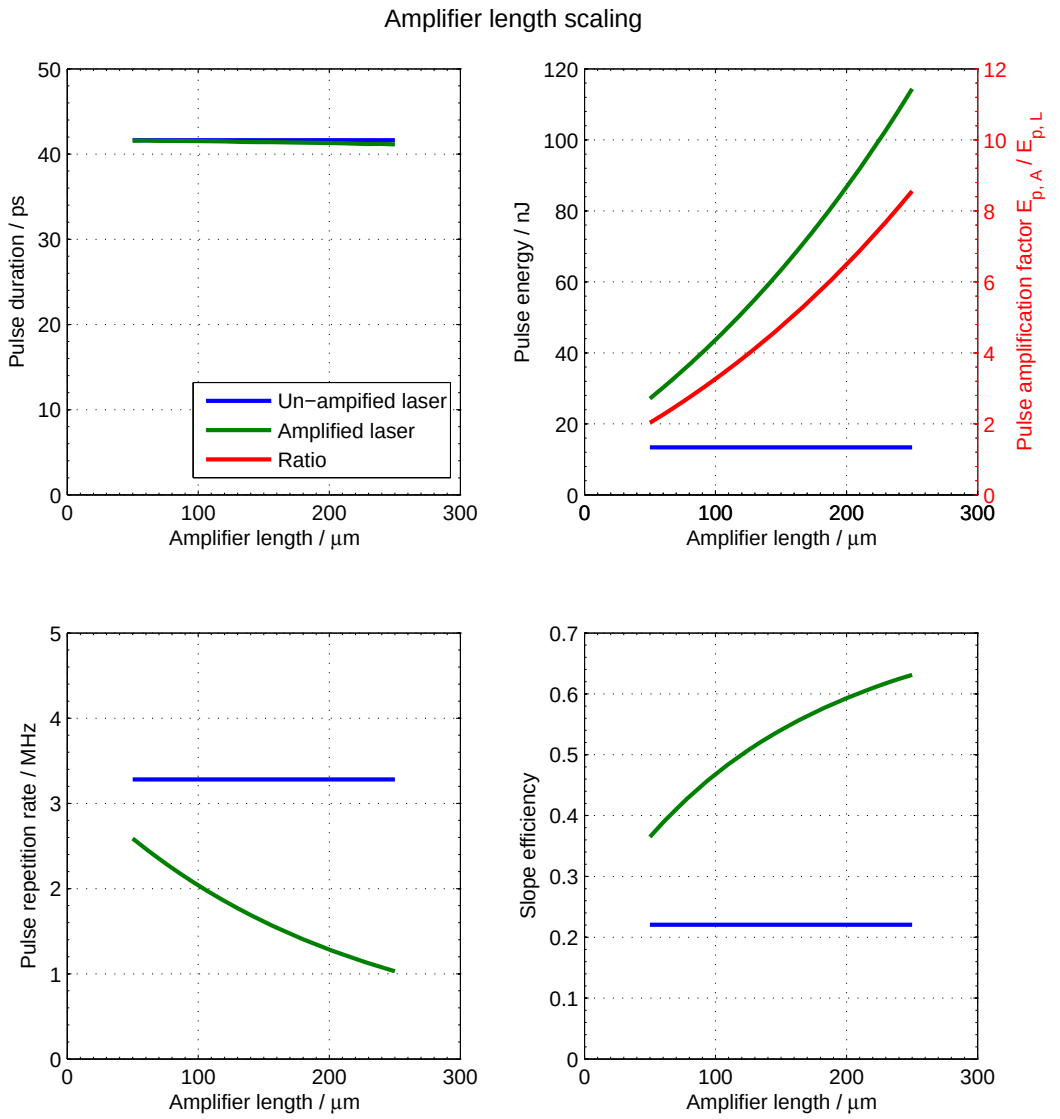

Figure 5.13: The effect of increasing the amplifier length on system output behaviour.

The results from Figure 5.13 are clear: increasing the amplifier length dramatically increases the pulse energy, amplification factor and system slope efficiency. Increasing the amplifier length will increase the amplifier absorption and so pump rate, as well as attenuating the pump power to the oscillator, lowering the repetition rate and increasing the inter-pulse pumping time. In Figure 5.14 we then see that increasing the amplifier length both increases the average amplifier inversion density and drastically increases the depletion magnitude as the increased amplification allows the output pulse to saturate the amplifier.

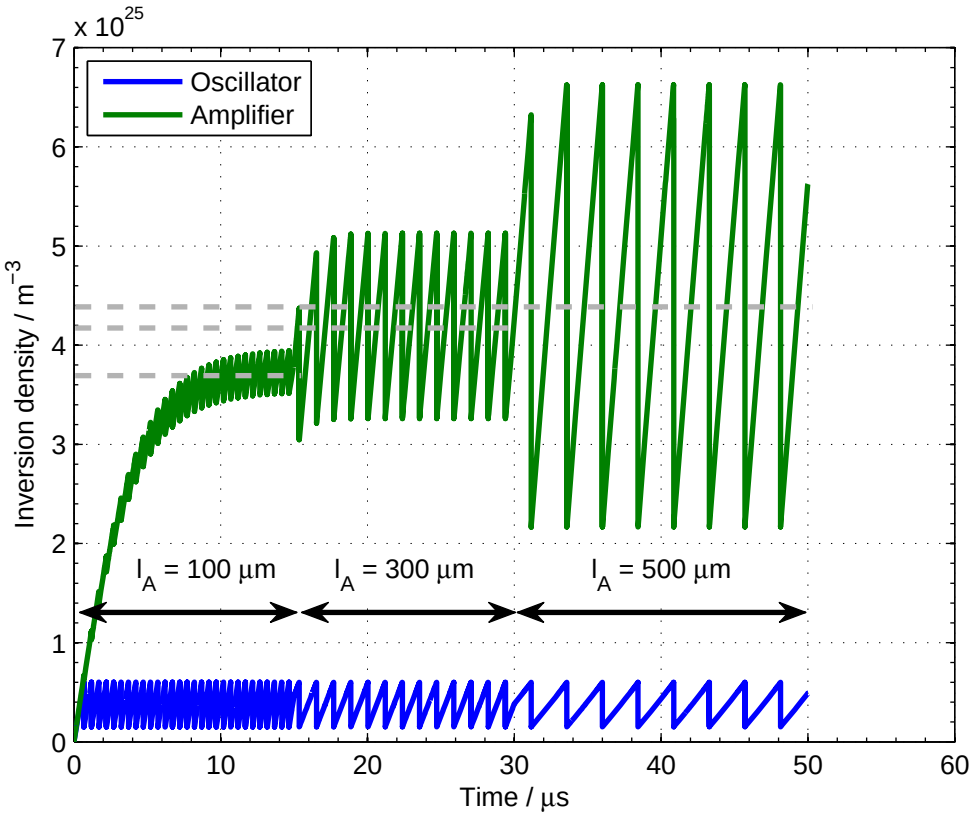

Figure 5.14: The inversion density of the amplifier and oscillator when amplifier length is changed over time. The average amplifier inversion levels at equilibriums are shown as dashed lines.

We see then that changing an amplifier absorption parameter, such as length or ion doping, changes both amplifier and oscillator behaviour (through pump power attenuation), meaning that their net effect is not intuitively obvious. The effect of a more heavily doped amplifier crystal is shown below, giving very positive results.

Slope efficiencies for increasing amplifier length and doping concentration will increase until they reach the quantum efficiency of the gain material, in this case $808/1064 = 76\%$. In terms of pulse energy, increasing the amplifier length and ion doping concentration seem to offer inexhaustible scaling. The real limitations in practice of course provide limits: diffraction of the pump beam limits the length of the amplifier that can be efficiently pumped; and increasing vanadate doping levels also increases losses and decreases the upper level lifetime. We will also see that thermal management becomes key when increasing the incident pump power to drive both the amplifier and oscillator.

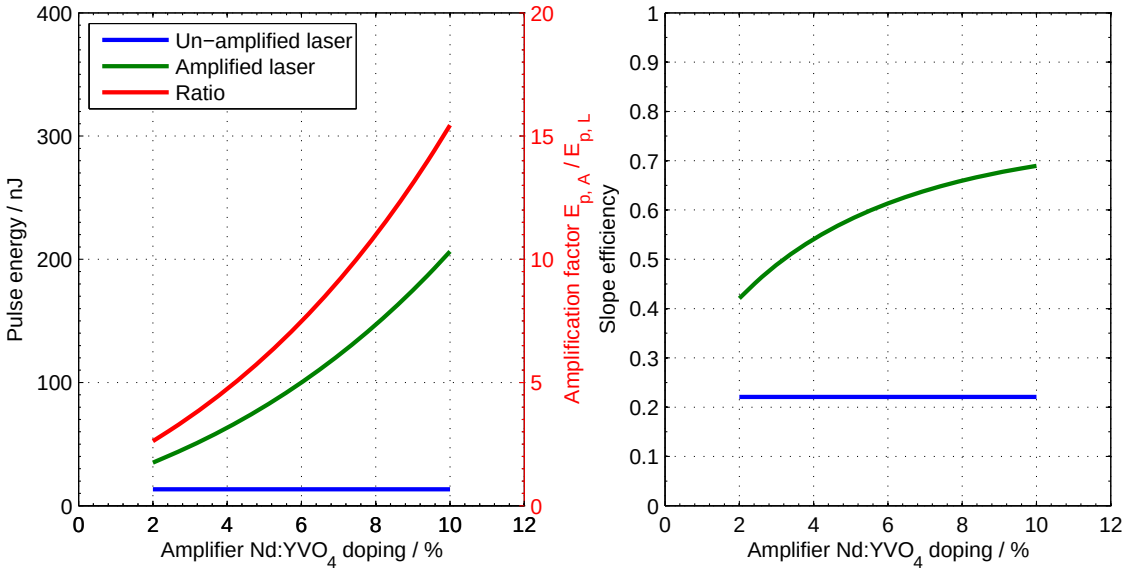

Figure 5.15: Pulse energy and slope efficiency increase through higher gain doping.

In summary, the numerical modelling results from this section provide clear guidelines for amplified SESAM Q-switched microchip laser design. When designing the amplifier, a thick, highly absorptive gain medium is desirable to give high pulse energies, high amplification factors and efficient operation. When optimising the oscillator design to give high pulse energy and high efficiency, short cavities employing SESAMs with large modulation depths are preferable, which aligns with the short-pulse generation requirements from Chapter 3. The presence of the amplifier has negligible effect on the pulse duration and we have shown that changing the pump power to moderate pulse repetition rate again has little effect over the output pulse energy or efficiency.

5.4 Proof of concept amplifier results

We constructed initial prototypes of the amplifier design discussed in Sections 5.1 and 5.3, comparing their performance to predictions using the numerical model described in the previous section. Amplifier construction and testing procedure followed the same processes as for an un-amplified laser as described in Sections 4.1 and 4.2, with the coated amplifier replacing the bulk output coupler, and using the same experimental set-up as in Figure 4.1. The pump-attenuating aperture was slightly wider than for the oscillator experiments to allow higher pump powers, with M^2 values

typically in the range 4-6. This corresponded to a Rayleigh range within the vanadate for the pump beam of approximately 150 µm, a fact that may well be the limiting factor in the success of these initial experiments.

Based on the guidelines from the previous section, we obtained a slab of 5 mm-square 4 at.% Nd:YVO4 from CASIX Inc. [177], and measured it to have a uniform thickness of 300 µm. CASIX applied an output coupler coating of 90% reflectivity at 1064 nm and high transmission at 808 nm. We polished the uncoated face of this crystal, resulting in a thickness of 275 µm at one edge, and 100 µm at the opposite edge. This formed a 2° wedge with varying thickness in the crystalline c-axis direction. The amplifier thickness under test was dictated by the performance of the oscillator, in particular the pulse duration and stability of the pulse train: We can choose a desired thickness of the amplifier, defining a contour on the amplifier surface along which we raster the pump beam while attempting to find a minimum pulse duration, but optimising for minimum pulse duration and stability took precedence.

The oscillator crystals used in these amplifier experiments were the 310 µm and 110 µm units tested in Chapter 4, to concentrate on the extremes of oscillator length scaling. The SESAM etalon was again optimised to deliver pulses as short as possible, with the focussing of the pump beam optimise to deliver the highest repletion rate, corresponding to having the pump focus centred within the oscillator.

All modelled data includes TPA modelling and is generated as for Section 4.4 by: assuming a resonant SESAM etalon; using the more recently measured SESAM parameters in Section 4.1; using the measured spot sizes, and for both resonant and anti-resonant output coupler etalons.

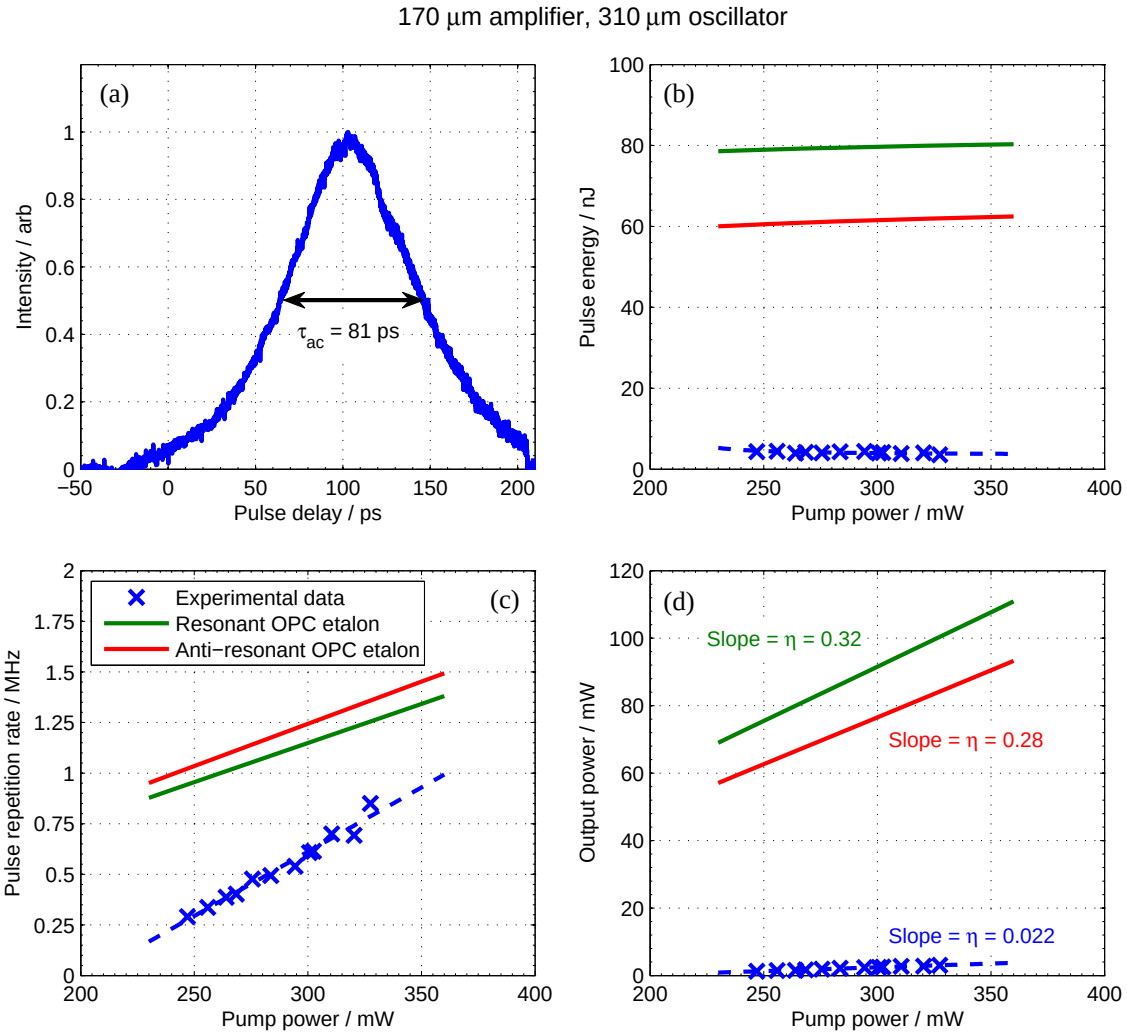

Figure 5.16: Results for the 310 µm oscillator with a 170 µm-thick amplifier: (a) Autocorrelated pulse duration, (b) Pulse energy as a function of pump power, (c) Pulse repetition rate as a function of pump power and (d) Average output power as a function of pump power.

The pump-power scaling results for an amplified laser utilising a 170 µm-thick amplifier and a 310 µm-long oscillator cavity are shown in Figure 5.16. The pulse duration was $\tau_p = \tau_{ac}/\sqrt{2} = 57$ ps, and the optical slope conversion efficiency $\eta = 2\%$. The measured output pulse energy was 4.1 nJ.

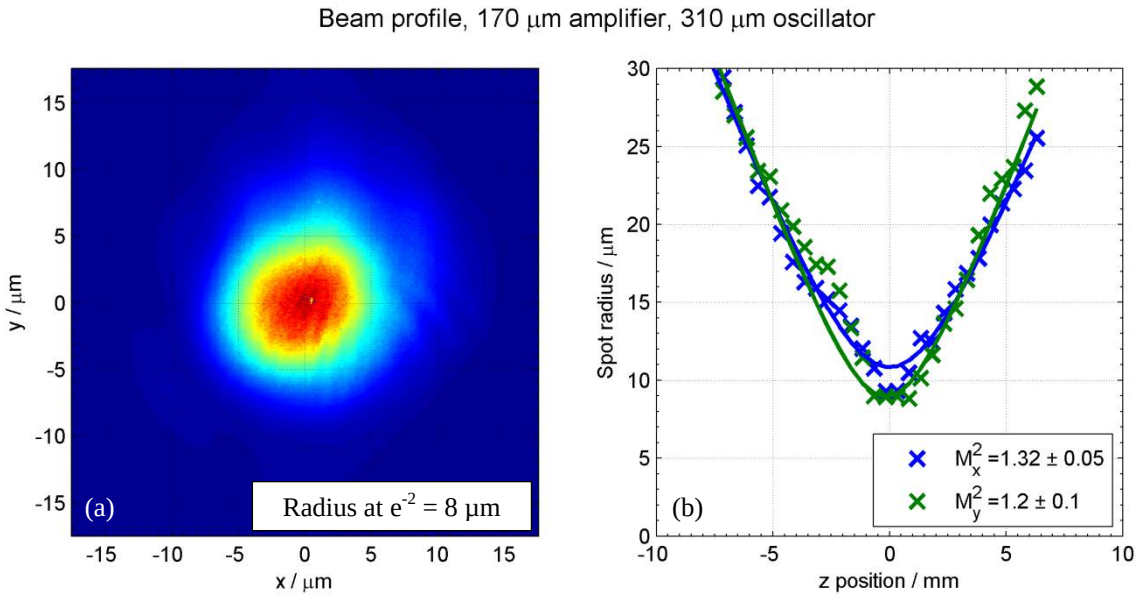

Figure 5.17: (a) Spot intensity profile at focus and (b) M^2 measurement of the amplified laser beam for the 170 μm amplifier on the 310 μm oscillator.

From Figure 5.17, the measured beam radius was 8 μm and the M^2 value was 1.32 ± 0.05.

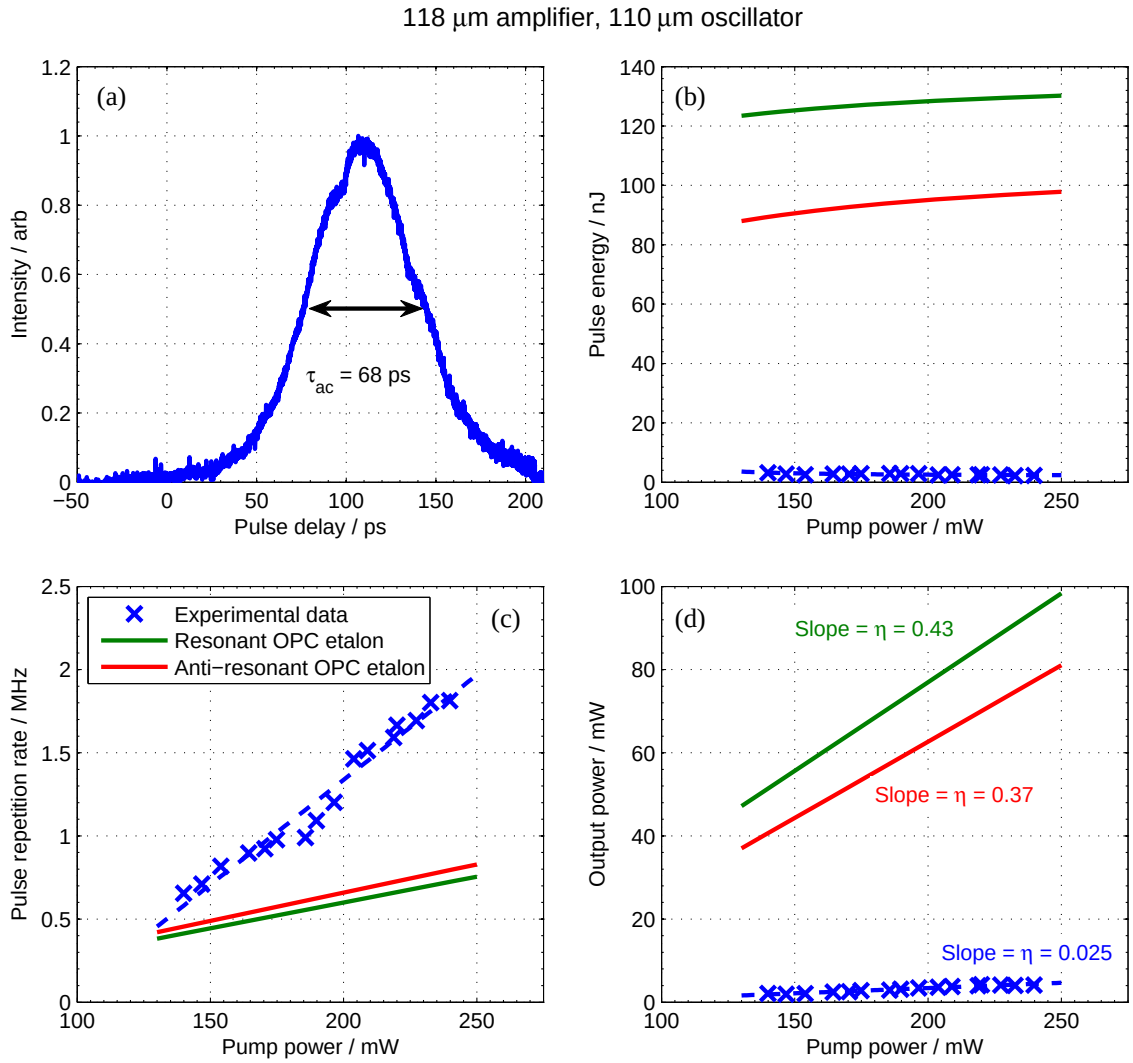

Figure 5.18: Results for the 110 µm oscillator with a 118 µm-thick amplifier: (a) Autocorrelated pulse duration, (b) Pulse energy as a function of pump power, (c) Pulse repetition rate as a function of pump power and (d) Average output power as a function of pump power.

The 110 µm oscillator with a 118 µm-thick amplifier yielded a pulse duration of $\tau_p = \tau_{ac}/\sqrt{2} = 48$ ps and optical slope conversion efficiency $\eta = 3\%$. The pulse energy for this amplified laser was 2.7 nJ.

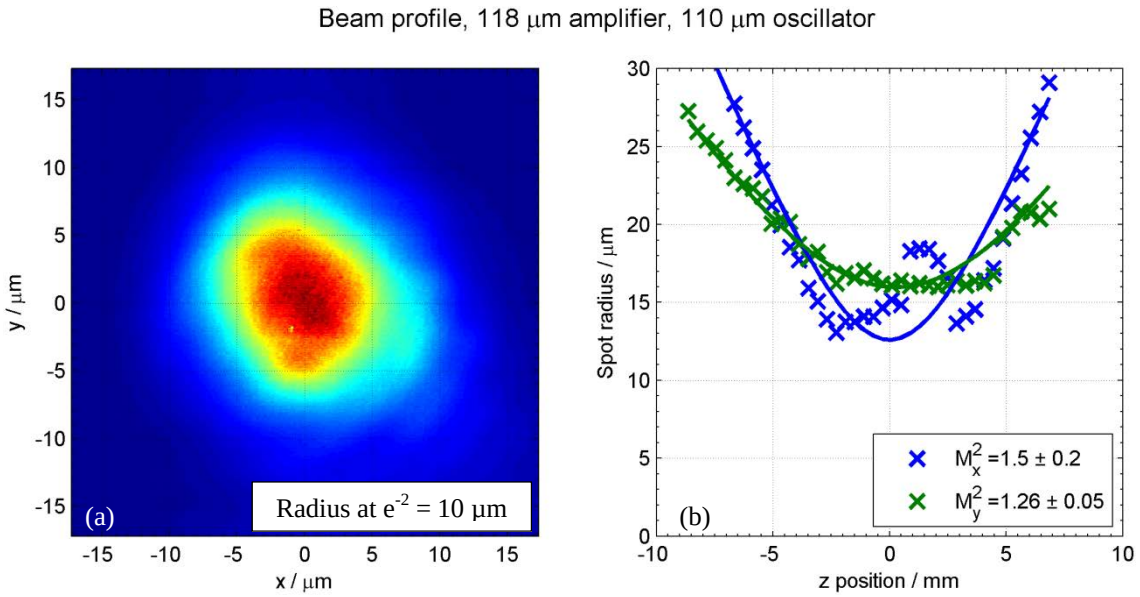

Figure 5.19: (a) Spot intensity profile at focus and (b) M^2 measurement of the amplified laser beam for the 118 μm amplifier on the 110 μm oscillator.

The measured beam radius of the amplified 110 μm oscillator was 10 μm and the M^2 value was 1.5 ± 0.2.

Osc. length / μm	Amp. length / μm	Pulse energy / nJ						Slope efficiency / %			
		Experiment			Numerical model			Experiment		Numerical model	
		No amp.	Amp.	Ratio	No amp.	Amp.	Ratio	No amp.	Amp.	No amp.	Amp.
310	170	2.4	4.1	1.7	5-14	62-80	5-12	6.1	2.2	4-12	28-32
110	118	0.9	2.7	3.0	6-17	95-130	8-16	5.7	2.5	5-13	37-43

Table 5.1: Summary of the amplified oscillator experiments.

The results for the amplified lasers and corresponding unamplified oscillators are shown in Table 5.1. For the 310 μm oscillator, we see an increase in output pulse energy by a factor of 1.7, with a larger increase for the 110 μm cavity by a factor of 3. For both systems, the slope efficiencies of the amplified systems are in fact *lower* than the unamplified lasers.

We can draw only tentative conclusions from these results, because of the significant breakdown of the modelling assumptions for these experimental conditions, specifically the assumption that the laser and pump beams are collimated through the laser system. The short Rayleigh range of the pump beam of just 150 μm means that its

beam area is greatly expanded through most of the amplifier compared to at focus: for the 310 µm oscillator and 170 µm amplifier, assuming the waist is at the centre of the oscillator, the beam area is almost six times larger at the entrance face of the amplifier. This increase in beam size will cause the inversion density to be correspondingly lower, reducing gain, and reducing overlap with the output beam that has far higher beam quality. These factors mean that most of the pump power absorbed by the amplifier cannot be extracted, and we might then expect the amplifier to reduce the overall efficiency of the system, despite the small increase in the output pulse energies.

The ratio of the pulse energy increase for the oscillators of different thickness is consistent with our expectations. The thinner 110 µm oscillator showed a larger gain than the 310 µm oscillator, despite having a thinner amplifier. The smaller fractional absorption of the thinner oscillator relative to that of the amplifier means that the amplifier receives more pump energy in each re-pumping time, and so shows higher gain – as predicted in Figure 5.6.

We make one cautionary note. The observed pulse durations from the amplified lasers were much longer than those from unamplified oscillators – for example in Chapter 4 we observed 22 ps pulses from a 110 µm laser, compared to 48 ps pulses for the amplified version. It is not clear why shorter pulses could not be obtained from the amplified system, and clearly there is doubt that the SESAM etalon was correctly optimised. This in turn makes it hard to convincingly compare the pulse energies of the amplified and un-amplified lasers with any conviction, and so we must leave to future work clear proof of amplification with this scheme.

In testing some designs with thicker amplifiers than those presented above, we noted a substantial thermal lensing effect present at high pump powers, causing critical instability in the operation of the laser oscillator. Pump powers significantly higher than those used in modelling were necessary to counter the absorption of the amplifier crystal, which is accounted for in the model, but also because the overlap between pump and laser modes across the system was so poor, as described above. Clearly, thermal lensing in the amplifier has the potential to distort the profile of the pump beam incident on the oscillator, as well as to alter the mode size of the laser. In order to avoid the thermal lensing effect, we were limited to operating at reduced pump powers, only

allowing us to test thinner amplifiers. Thorough investigation into the effects and management of thermal lensing in these amplifier crystals is left for future work.

5.5 Conclusion

We have used the modified rate equation model to track the inversion density of the amplifier, allowing us to make predictions of the amplified laser system performance based on various oscillator and amplifier parameters. We see that this basic design has the potential to vastly improve the pulse energy and efficiency of the SESAM Q-switched microchip laser. A sliver of amplifier material just 100 µm thick can boost pulse energy by a factor of 3 and nearly double the efficiency of a comparable standalone oscillator. We have provided guidelines to optimise both the amplifier and oscillator components of the amplified system.

Unfortunately our initial experiments have provided only weak support for these modelling conclusions, we believe owing to the high divergence of our pump source and to substantial thermal distortions of the pump and output beams. In this case, our model, which assumes a cylindrical pump beam matched to a cylindrical laser mode, cannot be used to confidently predict the performance of the amplified microchip systems tested here. However, it is fairly straightforward to include this overlap in the model and suggest that this would be an enlightening task for future work. In terms of experimental improvements, we suggest using pump sources with higher beam quality to more efficiently pump the amplifier and oscillator and hence lower the thermal load on the crystals. In addition, pumping at 880 nm and employing a heat spreading architecture will also reduce crystal heating and aid with thermal management. We are hopeful that this promising simple amplification scheme will still prove to be effective.

6 Conclusion

We have identified a regime of pulsed laser operation that is currently inaccessible to conventional mode-locked and Q-switched laser approaches. This region is defined by pulses of few-picosecond durations and near-microjoule energies. In Chapter 1 we have highlighted applications that would specifically benefit from the advent of a simple, cheap and efficient laser system that performs in this regime, specifically biological microscopy and imaging, and material processing.

Laser solutions that have so far been demonstrated to satisfy the ps-duration, µJ-energy requirements are predominantly thin-disk or amplified mode-locked laser systems. Owing to their complexity, these systems are expensive, difficult to maintain and operate and have large footprints. A technology that has shown promise to alleviate all of these drawbacks is Q-switched microchip lasers. The potential to generate shorter

and shorter pulses, potentially of picosecond duration, is afforded these systems by mechanisms such as cavity length scaling and Q-switch optimisation. From the analytic models and trends in the literature we find that short-cavity, SESAM Q-switched microchip lasers can potentially form the basis of a few-picosecond, microjoule pulsed laser system. SESAM Q-switched microchip lasers generating 100 ps, 80 µJ pulses after fibre amplification have already shown promising results in machining copper and steel.

To accurately model the limits of scaling the laser component parameters to achieve the shortest pulse durations, in Chapter 3 we devised a numerical model based on the coupled laser rate equations. We modified the common form rate equations for gain inversion and intra-cavity photon densities to include a time-dynamic loss term that constitutes a SESAM passive Q-switch, the loss of which is determined by an “effective fluence” that incorporates the SESAM recovery time. This approach enabled us to track the solutions of the rate equations over time, giving valuable insight into their interaction and ultimately demonstrating the inadequacy of the analytic models under certain conditions. After being used to demonstrate initial scaling relationships, the numerical model was extended to include the non-linear effects of two-photon absorption (TPA) in the semiconductor SESAM structure as well as the effects of air-gap etalons that modify the effective Q-switching properties.

The important scaling relationships derived from numerical modelling were: the linear dependence of pulse duration on cavity length and its inverse dependence on modulation depth; the inverse dependence of pulse energy on emission cross-section and its independence of cavity length and finally, the linear effect of pump power on repetition rate while not modifying pulse characteristics. TPA was shown only to cause a non-trivial effect at short cavity lengths, where the intensity was high enough to generate respectable TPA. The presence of a SESAM etalon was shown to have drastic consequences for the output behaviour of the laser through its modification of the effective Q-switch properties. One of the effects of a resonant SESAM etalon is to enhance the TPA effect, to the point where its detrimental effect to the laser must become a practical consideration, since the minimum pulse durations are achieved in conjunction with high energy and, hence high intensity, operation.

We show that relaxation oscillations are crucial for causing a switching avalanche and that SESAMs with I_{SAT} orders of magnitude above the CW operation level of the laser can still be used successfully. We have also predicted a regime where the SESAM produces only a partial switch. We further demonstrate that the intensity suppression mechanism of an anti-resonant SESAM etalon can inhibit the avalanche effect, leading to a practically attainable range of extents of SESAM switching, later demonstrated in an experimental setting.

In experimental work, we explored the general operation of SESAM Q-switched microchip lasers, observing strong evidence of etalon effects as pulse duration was found to be a function of mode position on the laser face. We then investigated the effects of cavity length scaling on laser performance, finding good agreement between modelled predictions for pulse duration and slope efficiency. We observed a deviation of repetition rates and a general deficiency in pulse energies compared to modelled predictions, indicating that our model is not a complete representation of the real-world lasers and requires more work if it is to be used to provide reliable design guidelines for these systems. As a first step to tackle the model shortcomings, we suggest that either TPA is more severe than we expected or its incorporation into the numerical model requires further development.

From experimental work we verified that the key relationship between cavity length and pulse duration was indeed linear and generated pulses of a record 22 ps duration from a SESAM Q-switched Nd:YVO_4 microchip laser with a 110 µm-long cavity. Our results are added to the literature summary plot from Section 2.5:

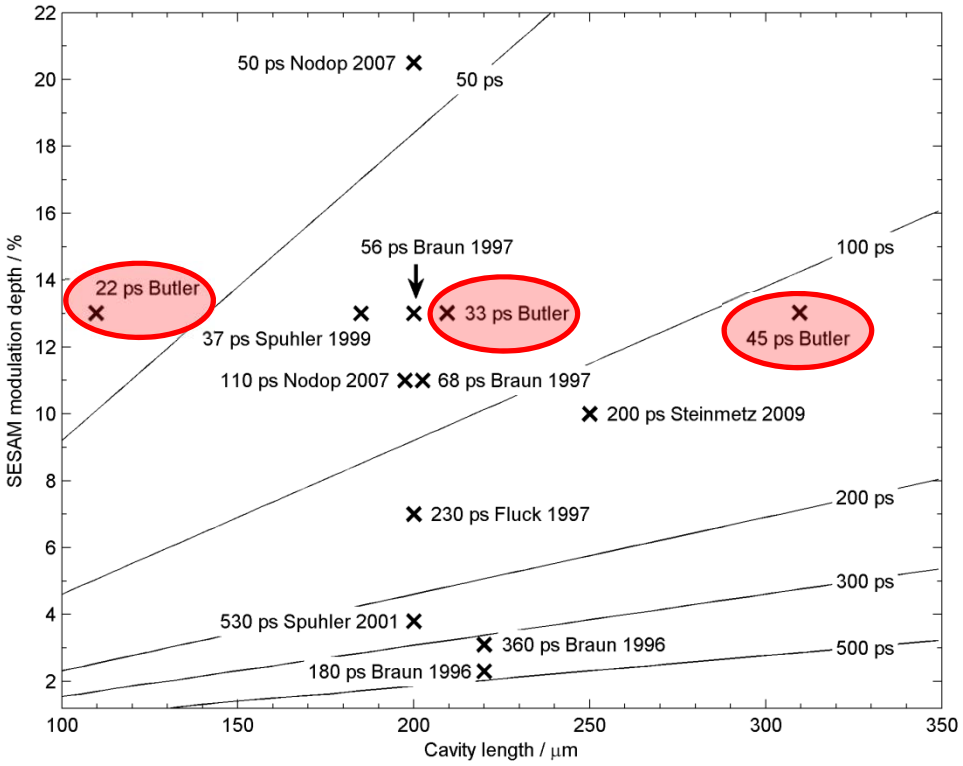

Figure 6.1: The field of work in sub-ns Q-switched microchip lasers, including our results from Chapter 4.

The possibility of reclaiming efficiency from the thin-gain oscillator through a novel, yet simple energy scavenging technique was discussed and numerically modelled in Chapter 5. We show that these amplifiers work efficiently, and the model scaling results indicate that thick amplifiers with short absorption lengths are required for maximising pulse energy and slope efficiency. An oscillator design that incorporates a short cavity with a high SESAM modulation depth will make best use of the amplifier gain. Conclusive experimental verification of these guidelines was unsuccessful, owing primarily to the unsuitability of our pump source to this amplification approach. We suggest that a higher quality pump beam could be successful and that consideration of the pump and mode overlap could be incorporated into the model with a high possibility of yielding informative results.

6.1 Implications of this work

The key result from this work is demonstration of the scaling relationships that enable shorter pulse duration. While pulses of 37 ps duration from a 185 µm cavity have

been reported [69], we demonstrate a further 40% improvement by further shortening the cavity length. In fact, from our experimental findings and numerically modelled predictions, the only boundaries to scaling down the cavity length are the practical limits of manufacturing and handling sub-100 μm gain crystals. Certainly in terms of pulse duration, SESAM Q-switched microchip lasers have the potential to perform comparably to mode-locked systems that are many times larger, more complex and expensive.

The range of commercially available SESAMs has, up until very recently, been dominated by devices specifically designed for use in mode-locked systems. They have high saturation intensities, low modulation depths and short recovery times. Their unsuitability to Q-switching is reflected in only one of our range of four sample SESAMs giving reliable, trouble-free operation. The amount of interest in the SESAM Q-switched field has grown dramatically in the 16 years since the first device was demonstrated, as their potential to perform in the picosecond, microjoule regime is realised. This interest and promising results have driven the first commercially available SESAMs designed specifically for Q-switching to be offered by the largest commercial SESAM producer, BATOP, earlier this year. These devices have modulation depths of between 5 and 15% with saturation intensities of the order of a magnitude lower than the unit we tested [129], providing strong suitability to short-pulse Q-switching under the guidelines we have identified.

Although the presence of a SESAM etalon has previously been suggested to modify the effective Q-switching behaviour [69], we believe we are the first group to account for it in modelling and experimentally demonstrate effects conclusively attributable to SESAM etalon variation. For each laser output parameter, the potential range of behaviour available simply by modifying the SESAM etalon thickness is substantial. For example, it can in theory cause pulse duration in a 110 μm cavity to vary between 17 ps and 70 ps, while causing similar modification of pulse energy. Without an understanding of the etalon effects, 42 ps would be all that is expected from such a cavity. In experiment we optimised the SESAM etalon in such a cavity to generate pulses of 22 ps duration, clearly showing the benefits of etalon modelling.

It is easy to imagine that the etalon mechanism can be beneficially employed to provide control over pulse behaviour without the need to drastically alter the laser design. However, accurately determining and controlling the SESAM etalon thickness in practice is unrealistic, and its unpredictability could cause more complication than benefit. Etalons are an interesting area of microchip behaviour but are best avoided to guarantee particular laser performance.

Two photon absorption in SESAMs has been investigated by a number of groups, although only in the context of mode-locked lasers. Our first-approximation approach to numerically modelling TPA in SESAMs in Q-switched lasers has shown that its effect on pulse energy can be substantial. This is further suggested by our conclusions from the energy deficiency observations in our oscillator development. As Q-switched cavities employing SESAMs are pushed shorter and shorter, in-depth understanding and appreciation of TPA effects become more and more pertinent.

Numerical modelling of a simple and compact, solid-state amplification approach has yielded promising possibilities of a 10 ps, 100 nJ laser. The prospect of a miniature combination Q-switched cavity and amplifier, contained in a sub-centimetre package, is extremely exciting. In our amplifier proof of concept experiments, we showed that although the concept is simple, the requirements of pump sources for effective use in such systems are more demanding than for un-amplified oscillators.

6.2 Future work

Throughout this project we have concentrated on a particular gain material, based on its specified properties and its use in the literature, and in experiment used one particular SESAM. Although using Nd:YVO_4 for its excellent absorptive and heat conductivity properties (in comparison to other solid state media, Table 3.1) is prudent in thin-gain microchip lasers, other solid-state materials are available and potentially bring benefits such as lower emission cross section for higher pulse energies. These materials have been tested in microchip lasers by other groups [66, 121, 135-139], although not with the express purpose of pushing the cavity lengths as short as possible. As mentioned in the previous section, SESAMs with favourable properties for Q-

switching are becoming readily commercially available. We suspect that the saturation intensity of the SESAMs in our selection was too high to allow repeatable pulse generation and so testing a range of new SESAMs would add valuable data-points to the literature plot in Figure 6.1.

With a view to making the cavities as short as possible, we identified that micron-length cavities were feasible. In the short term, there is still plenty of scope for investigating cavity lengths below 100 µm, with the 10 ps duration barrier expected to be broken at around 80 µm. From our experience with grinding and polishing Nd:YVO_4, tens of µm thickness are achievable through polishing. To go thinner still, we suggest that this could be achieved in principle by direct growing of gain crystals on an output coupler coating applied to an appropriate substrate but leave investigation of this idea to future work. Similarly, growth of the SESAM structure directly onto the gain crystal is another possibility that would result in a single, monolithic laser, additionally removing etalon-imposed uncertainties.

For practical continuation of the experiments that we have demonstrated, we highly recommend coating the surfaces of the components for the desired ranges of reflectivities required. While our bulk output coupling, uncoated gain crystal approach was useful to swap components in and out of the cavity, our experience with the 310 µm coated output coupler cavity used in Section 4.3 was that the results were more repeatable and the lack of an output coupler etalon made analysis more straightforward.

We mentioned in Section 3.3 that we had neglected spatial hole burning in the numerical model. While we argue that this is a reasonable approach for short cavities when not operating far above threshold, its incorporation into the model would provide a more complete representation of a miniature solid state laser. A good starting point is given by the inventor of the microchip laser in [173].

Finally, further work into generating conclusive results from our energy-scavenging amplifier technique is required. From analysis with the numerical model, the amplifier should behave fairly predictably and robustly, obviously showing some form of amplification. In our theoretical approach, we neglected divergence of the low beam quality of our pump diode and as such, saw reduced efficiencies and no definite sign of

amplification in experiments. An immediate improvement would be to use a high beam quality pump to deliver a near-cylindrical pump beam through both the oscillator and the amplifier. Including divergence in the model is possible and may yield informative results, but in practical terms, the amplifier and oscillator need to be pumped with similar spot sizes to optimise overall efficiency.

Although not in a state to be immediately useful in applications such as those described in Chapter 1, we believe that our lasers are another step towards few-ps microchip lasers, with the potential to fulfil these needs in the future.

7 References

1. M. D. Duncan, J. Reintjes, and T. J. Manuccia, "Scanning coherent anti-Stokes Raman microscope," Opt. Lett. **7**, 350-352 (1982).
2. C. L. Evans and X. S. Xie, "Coherent Anti-Stokes Raman Scattering Microscopy: Chemical Imaging for Biology and Medicine," Annual Review of Analytical Chemistry **1**, 883-909 (2008).
3. P. D. Maker and R. W. Terhune, "Study of Optical Effects Due to an Induced Polarization Third Order in the Electric Field Strength," Physical Review **137**, A801 (1965).
4. A. Zumbusch, G. R. Holtom, and X. S. Xie, "Three-Dimensional Vibrational Imaging by Coherent Anti-Stokes Raman Scattering," Physical Review Letters **82**, 4142 (1999).
5. C. L. Evans, E. O. Potma, M. Puoris'haag, D. Côté, C. P. Lin, and X. S. Xie, "Chemical imaging of tissue in vivo with video-rate coherent anti-Stokes Raman scattering microscopy," Proceedings of the National Academy of Sciences of the United States of America **102**, 16807-16812 (2005).
6. J.-x. Cheng, A. Volkmer, L. D. Book, and X. S. Xie, "An Epi-Detected Coherent Anti-Stokes Raman Scattering (E-CARS) Microscope with High Spectral Resolution and High Sensitivity," The Journal of Physical Chemistry B **105**, 1277-1280 (2001).

7. J. M. Dudley and J. R. Taylor, "Ten years of nonlinear optics in photonic crystal fibre," Nature Photonics **3**, 85-90 (2009).
8. W. Wadsworth, N. Joly, J. Knight, T. Birks, F. Biancalana, and P. Russell, "Supercontinuum and four-wave mixing with Q-switched pulses in endlessly single-mode photonic crystal fibres," Opt. Express **12**, 299-309 (2004).
9. S. Coen, A. H. L. Chau, R. Leonhardt, J. D. Harvey, J. C. Knight, W. J. Wadsworth, and P. S. J. Russell, "Supercontinuum generation by stimulated Raman scattering and parametric four-wave mixing in photonic crystal fibers," J. Opt. Soc. Am. B **19**, 753-764 (2002).
10. J. M. Dudley, L. Provino, N. Grossard, H. Maillotte, R. S. Windeler, B. J. Eggleton, and S. Coen, "Supercontinuum generation in air-silica microstructured fibers with nanosecond and femtosecond pulse pumping," J. Opt. Soc. Am. B **19**, 765-771 (2002).
11. W. J. Wadsworth, A. Ortigosa-Blanch, J. C. Knight, T. A. Birks, T. P. M. Man, and P. S. J. Russell, "Supercontinuum generation in photonic crystal fibers and optical fiber tapers: a novel light source," J. Opt. Soc. Am. B **19**, 2148-2155 (2002).
12. B. A. Cumberland, J. C. Travers, S. V. Popov, and J. R. Taylor, "Toward visible cw-pumped supercontinua," Opt. Lett. **33**, 2122-2124 (2008).
13. J. J. Zayhowski, "Passively Q-switched Nd:YAG microchip lasers and applications," Journal of Alloys and Compounds **303-304**, 393-400 (2000).
14. T. Baselt, T. Hammer, F. Basan, and P. Hartmann, "Application of a microchip laser-pumped photonic crystal fiber supercontinuum source for high-sensitive cavity ring down optical loss measurements," Proc. SPIE - Int. Soc. Opt. Eng. **7195**, 71951T (71955 pp.)-71951T (71955 pp.) (2009).
15. R. R. Alfano, *The Supercontinuum Laser Source,* 2 ed. (Springer, New York, 2006).
16. M. Amann, "Laser ranging: a critical review of usual techniques for distance measurement," Opt. Eng. **40**, 10 (2001).
17. A. J. Joblin, "Method of calculating the image resolution of a near-infrared time-of-flight tissue-imaging system," Appl. Opt. **35**, 752-757 (1996).
18. D.-H. Park, H.-H. Jeon, and S.-I. Oh, "Eyesafe microchip laser for laser range finder application," Chin. Opt. Lett. **5**, S243-S245 (2007).
19. A. Biernat and G. Kompa, "Powerful picosecond laser pulses enabling high-resolution pulsed laser radar," Journal of Optics **29**, 225 (1998).
20. M. A. Albota, R. M. Heinrichs, D. G. Kocher, D. G. Fouche, B. E. Player, M. E. Obrien, B. F. Aull, J. J. Zayhowski, J. Mooney, B. C. Willard, and R. R. Carlson, "Three-dimensional imaging laser radar with a photon-counting avalanche photodiode array and microchip laser," Appl. Opt. **41**, 7671-7678 (2002).
21. M. Elangovan, R. N. Day, and A. Periasamy, "Nanosecond fluorescence resonance energy transfer-fluorescence lifetime imaging microscopy to localize the protein interactions in a single living cell," Journal of Microscopy **205**, 3-14 (2002).
22. C. Wilkerson, "Detection and lifetime measurement of single molecules in flowing sample streams by laser-induced fluorescence," Appl. Phys. Lett. **62**, 2030 (1993).

23. J. V. Frangioni, "In vivo near-infrared fluorescence imaging," Current Opinion in Chemical Biology **7**, 626-634 (2003).
24. V. Ntziachristos, C. Bremer, and R. Weissleder, "Fluorescence imaging with near-infrared light: new technological advances that enable in vivo molecular imaging," European Radiology **13**, 195-208 (2003).
25. X. Liu, D. Du, and G. Mourou, "Laser ablation and micromachining with ultrashort laser pulses," Quantum Electronics, IEEE Journal of **33**, 1706-1716 (1997).
26. C. Momma, S. Nolte, B. N. Chichkov, F. v. Alvensleben, and A. Tünnermann, "Precise laser ablation with ultrashort pulses," Applied Surface Science **109-110**, 15-19 (1997).
27. B. C. Stuart, M. D. Feit, A. M. Rubenchik, B. W. Shore, and M. D. Perry, "Laser-Induced Damage in Dielectrics with Nanosecond to Subpicosecond Pulses," Physical Review Letters **74**, 2248 (1995).
28. S. Preuss, E. Matthias, and M. Stuke, "Sub-picosecond UV-laser ablation of Ni films," Applied Physics A: Materials Science & Processing **59**, 79-82 (1994).
29. S. Preuss, A. Demchuk, and M. Stuke, "Sub-picosecond UV laser ablation of metals," Applied Physics A: Materials Science & Processing **61**, 33-37 (1995).
30. B. N. Chichkov, C. Momma, S. Nolte, F. von Alvensleben, and A. Tünnermann, "Femtosecond, picosecond and nanosecond laser ablation of solids," Applied Physics A: Materials Science & Processing **63**, 109-115 (1996).
31. S. Nolte, C. Momma, H. Jacobs, A. Tünnermann, B. N. Chichkov, B. Wellegehausen, and H. Welling, "Ablation of metals by ultrashort laser pulses," J. Opt. Soc. Am. B **14**, 2716-2722 (1997).
32. C. Y. Chien and M. C. Gupta, "Pulse width effect in ultrafast laser processing of materials," Applied Physics A: Materials Science & Processing **81**, 1257-1263 (2005).
33. R. Le Harzic, D. Breitling, M. Weikert, S. Sommer, C. Föhl, S. Valette, C. Donnet, E. Audouard, and F. Dausinger, "Pulse width and energy influence on laser micromachining of metals in a range of 100 fs to 50ps," Applied Surface Science **249**, 322-331 (2005).
34. M. Perry, "Ultrashort-pulse laser machining of dielectric materials," J. Appl. Phys. **85**, 6803 (1999).
35. J. F. Seely and E. G. Harris, "Heating of a Plasma by Multiphoton Inverse Bremsstrahlung," Physical Review A **7**, 1064 (1973).
36. L. J. Frasinski, K. Codling, and P. A. Hatherly, "Covariance Mapping: A Correlation Method Applied to Multiphoton Multiple Ionization," Science **246**, 1029-1031 (1989).
37. M. Hashida, H. Mishima, S. Tokita, and S. Sakabe, "Non-thermal ablation of expanded polytetrafluoroethylene with an intense femtosecond-pulse laser," Opt. Express **17**, 13116-13121 (2009).
38. B. J. Johnston, Sydney (personal communication, 27/09/2011, 2011).
39. D. von der Linde, K. Sokolowski-Tinten, and J. Bialkowski, "Laser–solid interaction in the femtosecond time regime," Applied Surface Science **109-110**, 1-10 (1997).
40. A. Ancona, D. Nodop, J. Limpert, S. Nolte, and A. Tünnermann, "Microdrilling of metals with an inexpensive and compact ultra-short-pulse fiber amplified microchip laser," Applied Physics A: Materials Science & Processing (2008).

41. D. Breitling, "Fundamental aspects in machining of metals with short and ultrashort laser pulses," Proc. SPIE **5339**, 49 (2004).
42. A. DeMaria, "Self mode-locking of lasers with saturable absorbers," Appl. Phys. Lett. **8**, 174 (1966).
43. E. Ippen, "Passive mode locking of the cw dye laser," Appl. Phys. Lett. **21**, 348 (1972).
44. D. E. Spence, P. N. Kean, and W. Sibbett, "60-fsec pulse generation from a self-mode-locked Ti:sapphire laser," Opt. Lett. **16**, 42-44 (1991).
45. U. Keller, D. A. B. Miller, G. D. Boyd, T. H. Chiu, J. F. Ferguson, and M. T. Asom, "Solid-state low-loss intracavity saturable absorber for Nd:YLF lasers: an antiresonant semiconductor Fabry-Perot saturable absorber," Opt. Lett. **17**, 505-507 (1992).
46. D. H. Sutter, G. Steinmeyer, L. Gallmann, N. Matuschek, F. Morier-Genoud, U. Keller, V. Scheuer, G. Angelow, and T. Tschudi, "Semiconductor saturable-absorber mirror assisted Kerr-lens mode-locked Ti:sapphire laser producing pulses in the two-cycle regime," Opt. Lett. **24**, 631-633 (1999).
47. U. Keller, "Recent developments in compact ultrafast lasers," Nature **424**, 831-838 (2003).
48. W. Koechner, *Solid-State Laser Engineering*, 5 ed., Springer Series in Optical Sciences (Springer-Verlag, Berlin, 1999).
49. J. Herrmann, "Theory of Kerr-lens mode locking: role of self-focusing and radially varying gain," J. Opt. Soc. Am. B **11**, 498-512 (1994).
50. F. Salin, J. Squier, and M. Piché, "Mode locking of Ti:AI2O3 lasers and self-focusing: a Gaussian approximation," Opt. Lett. **16**, 1674-1676 (1991).
51. E. Innerhofer, T. Südmeyer, F. Brunner, R. Häring, A. Aschwanden, R. Paschotta, C. Hönninger, M. Kumkar, and U. Keller, "60-W average power in 810-fs pulses from a thin-disk Yb:YAG laser," in OSA Trends in Optics and Photonics (Optical Society of America, 2003), 152.
52. C. R. E. Baer, C. Kränkel, C. J. Saraceno, O. H. Heckl, M. Golling, R. Peters, K. Petermann, T. Südmeyer, G. Huber, and U. Keller, "Femtosecond thin-disk laser with 141 W of average power," Opt. Lett. **35**, 2302-2304 (2010).
53. I. N. Duling, T. Norris, T. Sizer, P. Bado, and G. A. Mourou, "Kilohertz synchronous amplification of 85-femtosecond optical pulses," J. Opt. Soc. Am. B **2**, 616-618 (1985).
54. P. Bado, M. Bouvier, and J. S. Coe, "Nd:YLF mode-locked oscillator and regenerative amplifier," Opt. Lett. **12**, 319-321 (1987).
55. C. J. Koester and E. Snitzer, "Amplification in a Fiber Laser," Appl. Opt. **3**, 1182-1186 (1964).
56. E. Desurvire, J. R. Simpson, and P. C. Becker, "High-gain erbium-doped traveling-wave fiber amplifier," Opt. Lett. **12**, 888-890 (1987).
57. J. Stone and C. A. Burrus, "Neodymium-Doped Fiber Lasers: Room Temperature cw Operation with an Injection Laser Pump," Appl. Opt. **13**, 1256-1258 (1974).
58. J. Limpert, T. Schreiber, T. Clausnitzer, K. Zöllner, H. Fuchs, E. Kley, H. Zellmer, and A. Tünnermann, "High-power femtosecond Yb-doped fiber amplifier," Opt. Express **10**, 628-638 (2002).

59. J. Limpert, F. Roser, T. Schreiber, and A. Tunnermann, "High-power ultrafast fiber laser systems," Selected Topics in Quantum Electronics, IEEE Journal of **12**, 233-244 (2006).
60. D. Herriott, H. Kogelnik, and R. Kompfner, "Off-Axis Paths in Spherical Mirror Interferometers," Appl. Opt. **3**, 523-526 (1964).
61. A. Fernandez, T. Fuji, A. Poppe, A. Fürbach, F. Krausz, and A. Apolonski, "Chirped-pulse oscillators: a route to high-power femtosecond pulseswithout external amplification," Opt. Lett. **29**, 1366-1368 (2004).
62. T. Sudmeyer, S. V. Marchese, S. Hashimoto, C. R. E. Baer, G. Gingras, B. Witzel, and U. Keller, "Femtosecond laser oscillators for high-field science," Nat Photon **2**, 599-604 (2008).
63. J. Neuhaus, D. Bauer, J. Kleinbauer, A. Killi, S. Weiler, D. H. Sutter, and T. Dekorsy, "Pulse energies exceeding 20 μJ directly from a femtosecond Yb:YAG oscillator," P. Corkum, S. Silvestri, K. A. Nelson, E. Riedle, and R. W. Schoenlein, eds. (Springer Berlin Heidelberg, 2009), pp. 729-731.
64. J. Neuhaus, D. Bauer, J. Zhang, A. Killi, J. Kleinbauer, M. Kumkar, S. Weiler, M. Guina, D. H. Sutter, and T. Dekorsy, "Subpicosecond thin-disk laser oscillator with pulse energies of up to 25.9 microjoules by use of an active multipass geometry," Opt. Express **16**, 20530-20539 (2008).
65. T. Südmeyer, S. V. Marchese, C. R. E. Baer, S. Hashimoto, M. Golling, A. G. Engqvist, D. J. H. C. Maas, G. Lépine, G. Gingras, B. Witzel, and U. Keller, "Femtosecond thin disk lasers with > 10 μJ pulse energy for high field physics at multi-megahertz repetition rates," P. Corkum, S. Silvestri, K. A. Nelson, E. Riedle, and R. W. Schoenlein, eds. (Springer Berlin Heidelberg, 2009), pp. 747-749.
66. J. J. Zayhowski and A. Mooradian, "Single-frequency microchip Nd lasers," Opt. Lett. **14**, 24-26 (1989).
67. J. Dong, K.-i. Ueda, H. Yagi, and A. Kaminskii, "Laser-diode pumped self-Q-switched microchip lasers," Optical Review **15**, 57-74 (2008).
68. D. Nodop, J. Limpert, R. Hohmuth, W. Richter, M. Guina, and A. Tünnermann, "High-pulse-energy passively Q-switched quasi-monolithic microchip lasers operating in the sub-100-ps pulse regime," Opt. Lett. **32**, 2115-2117 (2007).
69. G. J. Spühler, R. Paschotta, R. Fluck, B. Braun, M. Moser, G. Zhang, E. Gini, and U. Keller, "Experimentally confirmed design guidelines for passively Q-switched microchip lasers using semiconductor saturable absorbers," J. Opt. Soc. Am. B **16**, 376-388 (1999).
70. J. J. Zayhowski, "Ultraviolet generation with passively Q -switched microchip lasers," Opt. Lett. **21**, 588 (1996).
71. J. J. Zayhowski and C. DillI III, "Coupled-cavity electro-optically Q-switched Nd:YVO_4 microchip lasers," Opt. Lett. **20**, 716-718 (1995).
72. A. Steinmetz, D. Nodop, J. Limpert, R. Hohmuth, W. Richter, and A. Tünnermann, "2 MHz repetition rate, 200 ps pulse duration from a monolithic, passively Q-switched microchip laser," Applied Physics B: Lasers and Optics (2009).
73. J. J. Zayhowski and C. Dill III, "Diode-pumped microchip lasers electro-optically Q-switched at high pulse repetition rates," Opt. Lett. **17**, 1201-1203 (1992).

74. F. Di Teodoro and C. D. Brooks, "MW peak-power, mJ pulse energy, multi-kHz repetition rate pulses from Yb-doped fiber amplifiers," in *Fiber Lasers III: Technology, Systems, and Applications*, (SPIE, 2006), 61020K-61028.
75. A. V. Kir'yanov, S. M. Klimentov, I. V. Mel'nikov, and A. V. Shestakov, "Specialty Yb fiber amplifier for microchip Nd laser: Towards ~1-mJ/1-ns output at kHz-range repetition rate," Optics Communications **282**, 4759-4764 (2009).
76. D. Nodop, O. Schmidt, J. Limpert, and A. Tunnermann, "105 kHz, 85 ps, 3 MW microchip laser fiber amplifier system for micro-machining applications," in *Lasers and Electro-Optics, 2008 and 2008 Conference on Quantum Electronics and Laser Science. CLEO/QELS 2008. Conference on*, 2008), 1-2.
77. J. T. Mok, I. C. M. Littler, E. Tsoy, and B. J. Eggleton, "Soliton compression and pulse-train generation by use of microchip Q-switched pulses in Bragg gratings," Opt. Lett. **30**, 2457-2459 (2005).
78. A. Steinmetz, T. Eidam, D. Nodop, J. Limpert, and A. Tünnermann, "Nonlinear compression of Q-Switched laser pulses to the realm of ultrashort durations," Opt. Express **19**, 3758-3764 (2011).
79. A. A. Demidovich, S. V. Voitikov, L. E. Batay, A. S. Grabtchikov, M. B. Danailov, V. A. Lisinetskii, A. N. Kuzmin, and V. A. Orlovich, "Modeling and experimental investigation of short pulse Raman microchip laser," Optics Communications **263**, 52-59 (2006).
80. S. V. Voitikov, A. A. Demidovich, A. S. Grabtchikov, P. V. Shpak, M. B. Danailov, and V. A. Orlovich, "Two-Stokes generation and effect of multiwave mixing on output pulse parameters of a Q-switched Raman microchip laser," J. Opt. Soc. Am. B **27**, 1232-1241 (2010).
81. W. Koechner, "Solid-State Laser Engineering," in *Springer Series in Optical Sciences,* 5 ed., A. L. Schawlow, T. Tamir, and A. E. Siegman, eds. (Springer-Verlag, Berlin, 1999).
82. J. Gu, F. Zhou, W. Xie, S. C. Tam, and Y. L. Lam, "Passive Q-switching of a diode-pumped Nd:YAG laser with a GaAs output coupler," Optics Communications **165**, 245-249 (1999).
83. Z. Li, Z. Xiong, N. Moore, G. C. Lim, W. L. Huang, and D. X. Huang, "Pulse width reduction in AO Q-switched diode-pumped Nd:YVO4 laser with GaAs coupler," Optics Communications **237**, 411-416 (2004).
84. J. An, S. Zhao, G. Li, K. Yang, D. Li, J. Wang, and M. Li, "Doubly Q-switched intracavity-frequency-doubled c-cut Nd:$GdVO_4$/KTP green laser with AO and GaAs," Optik - International Journal for Light and Electron Optics **120**, 451-456 (2009).
85. Y. F. Li, S. Z. Zhao, Y. M. Sun, H. J. Qi, and K. Cheng, "Diode-pumped doubly passively Q-switched c-cut Nd:$GdVO_4$ 1.34 μm laser with V^{3+}:YAG and Co:LMA saturable absorbers," Optics & Laser Technology **43**, 985-988 (2011).
86. D. M. Andrauskas and C. Kennedy, "Tetravalent Chromium Solid-State Passive Q Switch for Nd:YAG Laser Systems," in OSA Proceedings Series (Optical Society of America, 1991), MT12.
87. H. Eilers, ouml, U. mmerich, S. M. Jacobsen, W. M. Yen, K. R. Hoffman, and W. Jia, "Spectroscopy and dynamics of Cr^{4+}:$Y_3Al_5O_{12}$," Physical Review B **49**, 15505 (1994).
88. M. Hercher, "An analysis of saturable absorbers," Appl. Opt. **6**, 947 (1967).

89. Z. Burshtein, P. Blau, Y. Kalisky, Y. Shimony, and M. R. Kokta, "Excited-state absorption studies of Cr^{4+} ions in several garnet host crystals," Quantum Electronics, IEEE Journal of **34**, 292-299 (1998).
90. A. M. Malyarevich, I. A. Denisov, K. V. Yumashev, V. P. Mikhailov, R. S. Conroy, and B. D. Sinclair, "V:YAG – a new passive Q-switch for diode-pumped solid-state lasers," Applied Physics B: Lasers and Optics **67**, 555-558 (1998).
91. F. Liu, J. He, B. Zhang, J. Xu, X. Dong, K. Yang, H. Xia, and H. Zhang, "Diode-pumped passively Q-switched Nd:$LuVO_4$ laser at 1.34μm with a V^{3+}:YAG saturable absorber," Opt. Express **16**, 11759-11763 (2008).
92. H.-T. Huang, B.-T. Zhang, J.-L. He, J.-F. Yang, J.-L. Xu, X.-Q. Yang, C.-H. Zuo, and S. Zhao, "Diode-pumped passively Q-switched Nd:$Gd_{0.5}Y_{0.5}VO_4$ laser at 1.34 μm with V^{3+}:YAG as the saturable absorber," Opt. Express **17**, 6946-6951 (2009).
93. A. Agnesi, A. Guandalini, G. Reali, J. K. Jabczynski, K. Kopczynski, and Z. Mierczyk, "Diode pumped Nd:YVO_4 laser at 1.34 μm Q-switched and mode locked by a V^{3+}:YAG saturable absorber," Optics Communications **194**, 429-433 (2001).
94. J. Sulc, J. Novak, H. Jelinkova, K. Nejezchleb, and V. Skoda, "Comparison of V:YAG and V:LuAG saturable absorbers for Nd:YAG 1338 nm microchip laser Q-switching," in *Solid State Lasers and Amplifiers IV, and High-Power Lasers*, (SPIE, 2010), 772119-772118.
95. K. V. Yumashev, "Saturable absorber Co^{2+}:$MgAl_2O_4$ crystal for Q Switching of 1.34 μm Nd^{3+}:$YAlO_3$ and 1.54 μm Er^{3+}:Glass Lasers," Appl. Opt. **38**, 6343-6346 (1999).
96. A. V. Podlipensky, V. G. Shcherbitsky, M. I. Demchuk, N. V. Kuleshov, V. I. Levchenko, V. N. Yakimovich, S. Girard, and R. Moncorgé, "Cr^{2+}:$Cd_{0.55}Mn_{0.45}Te$ crystal as a new saturable absorber for 2 μm lasers," Optics Communications **192**, 65-68 (2001).
97. W. Ge, H. Zhang, J. Wang, X. Cheng, M. Jiang, C. Du, and S. Yuan, "Pulsed laser output of LD-end-pumped 1.34 μm Nd: $GdVO_4$ laser with Co: $LaMgAl_{11}O_{19}$ crystal as saturable absorber," Opt. Express **13**, 3883-3889 (2005).
98. B. Denker, B. Galagan, E. Godovikova, M. Meilman, V. Osiko, S. Sverchkov, and I. Kertesz, "The Efficient Saturable Absorber for 1.54 μm Er Glass Lasers," in OSA Trends in Optics and Photonics (Optical Society of America, 1999), PD13.
99. S. Feng, C. Yu, L. Chen, S. Li, W. Chen, and L. Hu, "A cobalt-doped transparent glass ceramic saturable absorber Q-switch for a LD pumped Yb^{3+}/Er^{3+} glass microchip laser," Laser Physics **20**, 1687-1691 (2010).
100. D. P. Jiang, Y. Q. Zou, L. B. Su, H. L. Tang, F. Wu, L. H. Zheng, H. J. Li, and J. Xu, "A Co2+-doped alumina-rich Mg0.4Al2.4O4 spinel crystal as saturable absorber for a LD pumped Er: glass microchip laser at 1535 nm," Laser Physics Letters **8**, 343-348 (2011).
101. A. Malyarevich and K. Yumashev, "Saturable absorbers based on tetrahedrally coordinated transition-metal ions in crystals (Review)," Journal of Applied Spectroscopy **76**, 1-43 (2009).
102. S. Zhou, K. K. Lee, Y. C. Chen, and S. Li, "Monolithic self-Q-switched Cr,Nd:YAG laser," Opt. Lett. **18**, 511-512 (1993).

103. P. Wang, S.-H. Zhou, K. K. Lee, and Y. C. Chen, "Picosecond laser pulse generation in a monolithic self-Q-switched solid-state laser," Optics Communications **114**, 439-441 (1995).
104. J. Dong, P. Z. Deng, Y. P. Liu, Y.-H. Zhang, G.-S. Huang, and F.-X. Gan, "Performance of the Self-Q-Switched Cr,Yb:YAG Laser," Chinese Physics Letters **19**, 342-344 (2002).
105. Y. Zhou, Q. Thai, Y. C. Chen, and S. Zhou, "Monolithic Q-switched Cr,Yb:YAG laser," Optics Communications **219**, 365-367 (2003).
106. T. T. Kajava and A. L. Gaeta, "Q switching of a diode-pumped Nd:YAG laser with GaAs," Opt. Lett. **21**, 1244-1246 (1996).
107. J. Peng, H. Tan, Y. Wang, X. Ma, J. Miao, B. Wang, and L. Qian, "High repetition rate Q-switched microchip Nd:YVO4 laser with pulse duration as short as 1.1 ns," Optik - International Journal for Light and Electron Optics **119**, 657-660 (2008).
108. Y. P. Huang, Y. J. Huang, P. Y. Chiang, Y. F. Chen, and K. F. Huang, "Multi-millijoule, high-repetition-rate Q-switched Nd-doped vanadate laser with an AlGaInAs quantum-well saturable absorber," in *Photonics Global Conference (PGC), 2010*, 2010), 1-4.
109. X. Liu, E. U. Rafailov, D. Livshits, and D. Turchinovich, "Quantum well saturable absorber mirror with electrical control of modulation depth," in *Lasers and Electro-Optics/Quantum Electronics and Laser Science Conference: 2010 Laser Science to Photonic Applications, CLEO/QELS 2010*, 2010),
110. P. T. Guerreiro, S. Ten, N. F. Borrelli, J. Butty, G. E. Jabbour, and N. Peyghambarian, "PbS quantum-dot doped glasses as saturable absorbers for mode locking of a Cr:forsterite laser," Applied Physics Letters **71**, 1595-1597 (1997).
111. S. Y. Set, H. Yaguchi, Y. Tanaka, M. Jablonski, Y. Sakakibara, M. Tokomuto, H. Kataura, Y. Achiba, and K. Kikuchi, "A dual-regime mode-locked/Q-switched laser using a saturable absorber incorporating carbon nanotubes (SAINT)," in *Lasers and Electro-Optics, 2003. CLEO '03. Conference on*, 2003), 3 pp.
112. S. Y. Set, H. Yaguchi, Y. Tanaka, and M. Jablonski, "Laser mode locking using a saturable absorber incorporating carbon nanotubes," Lightwave Technology, Journal of **22**, 51-56 (2004).
113. E. U. Rafailov, M. A. Cataluna, and W. Sibbett, "Mode-locked quantum-dot lasers," Nat Photon **1**, 395-401 (2007).
114. F. Bonaccorso, Z. Sun, T. Hasan, and A. C. Ferrari, "Graphene photonics and optoelectronics," Nat Photon **4**, 611-622 (2010).
115. I. H. Baek, S. Y. Choi, H. W. Lee, W. B. Cho, V. Petrov, A. Agnesi, V. Pasiskevicius, D.-I. Yeom, K. Kim, and F. Rotermund, "Single-walled carbon nanotube saturable absorber assisted high-power mode-locking of a Ti:sapphire laser," Opt. Express **19**, 7833-7838 (2011).
116. D. Popa, Z. Sun, T. Hasan, F. Torrisi, F. Wang, and A. C. Ferrari, "Graphene Q-switched, tunable fiber laser," Applied Physics Letters **98**, 073106-073103 (2011).
117. X.-l. Li, J.-l. Xu, Y.-z. Wu, J.-l. He, and X.-p. Hao, "Large energy laser pulses with high repetition rate by graphene Q-switched solid-state laser," Opt. Express **19**, 9950-9955 (2011).

118. U. Keller, "Ultrafast all-solid-state laser technology," Applied Physics B: Lasers and Optics **58**, 347-363 (1994).
119. S. Tsuda, W. H. Knox, E. A. de Souza, W. Y. Jan, and J. E. Cunningham, "Low-loss intracavity AlAs/AlGaAs saturable Bragg reflector for femtosecond mode locking in solid-state lasers," Opt. Lett. **20**, 1406-1408 (1995).
120. B. Braun and U. Keller, "Single-frequency Q-switched ring laser with an antiresonant Fabry-Perot saturable absorber," Opt. Lett. **20**, 1020-1022 (1995).
121. B. Braun, F. X. Kartner, U. Keller, J. P. Meyn, and G. Huber, "Passively Q - switched 180-ps Nd:$LaSc_3(BO_3)_4$ microchip laser," Opt. Lett. **21**, 405 (1996).
122. B. Braun, F. X. Kärtner, G. Zhang, M. Moser, and U. Keller, "56-ps passively Q-switched diode-pumped microchip laser," Opt. Lett. **22**, 381-383 (1997).
123. M. Haiml, R. Grange, and U. Keller, "Optical characterization of semiconductor saturable absorbers," Applied Physics B: Lasers and Optics **79**, 331-339 (2004).
124. U. Keller, K. J. Weingarten, F. X. Kartner, D. Kopf, B. Braun, I. D. Jung, R. Fluck, C. Honninger, N. Matuschek, and J. Aus der Au, "Semiconductor saturable absorber mirrors (SESAM's) for femtosecond to nanosecond pulse generation in solid-state lasers," Selected Topics in Quantum Electronics, IEEE Journal of **2**, 435-453 (1996).
125. L. R. Brovelli, U. Keller, and T. H. Chiu, "Design and operation of antiresonant Fabry-Perot saturable semiconductor absorbers for mode-locked solid-state lasers," J. Opt. Soc. Am. B **12**, 311-322 (1995).
126. R. Häring, R. Paschotta, R. Fluck, E. Gini, H. Melchior, and U. Keller, "Passively Q-switched microchip laser at 1.5 μm," J. Opt. Soc. Am. B **18**, 1805-1812 (2001).
127. A. Jasik, J. Muszalski, K. Hejduk, and M. Kosmala, "The reduced temporal parameters of passivated semiconductor saturable absorber mirror," Thin Solid Films **518**, 171-173 (2009).
128. C. Hönninger, R. Paschotta, F. Morier-Genoud, M. Moser, and U. Keller, "Q-switching stability limits of continuous-wave passive mode locking," J. Opt. Soc. Am. B **16**, 46-56 (1999).
129. B. GmbH, "BATOP GmbH" (2011), retrieved http://www.batop.de/.
130. R. Ltd, "RefleKron Ltd" (2011), retrieved 2011, http://www.reflekron.com/.
131. J. J. Zayhowski, "Microchip lasers," Optical Materials **11**, 255-267 (1999).
132. B. Zhou, T. J. Kane, G. J. Dixon, and R. L. Byer, "Efficient, frequency-stable laser-diode-pumped Nd:YAG laser," Opt. Lett. **10**, 62-64 (1985).
133. A. Owyoung, G. R. Hadley, P. Esherick, R. L. Schmitt, and L. A. Rahn, "Gain switching of a monolithic single-frequency laser-diode-excited Nd:YAG laser," Opt. Lett. **10**, 484-486 (1985).
134. T. Taira, A. Mukai, Y. Nozawa, and T. Kobayashi, "Single-mode oscillation of laser-diode-pumped Nd:YVO_4 microchip lasers," Opt. Lett. **16**, 1955-1957 (1991).
135. G. J. Spühler, R. Paschotta, M. P. Kullberg, M. Graf, M. Moser, E. Mix, G. Huber, C. Harder, and U. Keller, "A passively Q-switched Yb:YAG microchip laser," Applied Physics B: Lasers and Optics **72**, 285-287 (2001).
136. J. Dong, K.-i. Ueda, and A. A. Kaminskii, "Efficient passively Q-switched Yb:LuAG microchip laser," Opt. Lett. **32**, 3266-3268 (2007).

137. H. Zhu, Y. Chen, Y. Lin, X. Gong, Z. Luo, and Y. Huang, "Efficient 1.06 μm laser operation in an unprocessed Nd3+:BaGd2(MoO4)4 cleavage microchip," Applied Physics B: Lasers and Optics **93**, 429-432 (2008).
138. B.-Q. Yao and et al., "Diode-End-Pumped Tm:Ho:$GdVO_4$ Microchip Laser at Room Temperature," Chinese Physics Letters **28**, 024210 (2011).
139. S. Zhuang, H. Yu, Z. Wang, H. Zhang, J. Wang, L. Guo, L. Chen, Y. Zhao, and X. Xu, "Passively Q-switched Nd:$Gd_{0.63}Y_{0.37}VO_4/Cr^{4+}$:YAG microchip laser," Journal of Crystal Growth **318**, 691-694 (2011).
140. J. J. Zayhowski, "Q-switched operation of microchip lasers," Opt. Lett. **16**, 575 (1991).
141. R. Fluck, B. Braun, E. Gini, H. Melchior, and U. Keller, "Passively Q-switched 1.34 μm Nd:YVO_4 microchip laser with semiconductor saturable-absorber mirrors," Opt. Lett. **22**, 991-993 (1997).
142. A. Inoue, J. Hayashi, T. Komikado, and S. Umegaki, "Polymeric saturable-absorber mirror for passive Q-switching of a laser-diode-pumped Nd^{3+}:YVO_4 microchip laser," Opt. Lett. **32**, 2807-2809 (2007).
143. J. J. Zayhowski and C. Dill III, "Diode-pumped passively Q-switched picosecond microchip lasers," Opt. Lett. **19**, 1427 (1994).
144. J. Dong, P. Deng, Y. Liu, Y. Zhang, J. Xu, W. Chen, and X. Xie, "Passively Q-Switched Yb:YAG Laser with Cr^{4+}:YAG as the Saturable Absorber," Appl. Opt. **40**, 4303-4307 (2001).
145. M. Liu, J. Liu, L. Li, and S. S. Liu, "Experimental study on pulse characteristics of diode-pumped Q-switched Nd:KGW laser," Laser Physics Letters **6**, 437-440 (2009).
146. S. Zhang, M. Wang, L. Xu, Y. Wang, Y. Tang, X. Cheng, W. Chen, J. Xu, B. Jiang, and Y. Pan, "Efficient Q-switched Tm:YAG ceramic slab laser," Opt. Express **19**, 727-732 (2011).
147. J. J. Zayhowski and P. L. Kelley, "Optimization of Q-switched lasers," Quantum Electronics, IEEE Journal of **27**, 2220-2225 (1991).
148. J. J. Zayhowski and A. L. Wilson, Jr., "Pump-induced bleaching of the saturable absorber in short-pulse Nd:YAG/Cr^{4+}:YAG passively Q-switched microchip lasers," Quantum Electronics, IEEE Journal of **39**, 1588-1593 (2003).
149. J. J. Zayhowski and J. A. L. Wilson, "Energy-scavenging amplifiers for miniature solid-state lasers," Opt. Lett. **29**, 1218-1220 (2004).
150. P. Langlois, M. Joschko, E. R. Thoen, E. M. Koontz, F. X. Kartner, E. P. Ippen, and L. A. Kolodziejski, "High fluence ultrafast dynamics of semiconductor saturable absorber mirrors," Applied Physics Letters **75**, 3841-3843 (1999).
151. E. R. Thoen, E. M. Koontz, M. Joschko, P. Langlois, T. R. Schibli, F. X. Kartner, E. P. Ippen, and L. A. Kolodziejski, "Two-photon absorption in semiconductor saturable absorber mirrors," Applied Physics Letters **74**, 3927-3929 (1999).
152. J. P. Meyn, T. Jensen, and G. Huber, "Spectroscopic properties and efficient diode-pumped laser operation of neodymium-doped lanthanum scandium borate," Quantum Electronics, IEEE Journal of **30**, 913-917 (1994).
153. S. V. Voitikov, A. A. Demidovich, L. E. Batay, A. N. Kuzmin, and M. B. Danailov, "Sub-nanosecond pulse dynamics of Nd:LSB microchip laser passively Q-switched by Cr:YAG saturable absorber," Optics Communications **251**, 154-164 (2005).

154. A. Brignon, G. Feugnet, J. P. Huignard, and J. P. Pocholle, "Compact Nd:YAG and Nd:YVO_4 amplifiers end-pumped by a high-brightness stacked array," Quantum Electronics, IEEE Journal of **34**, 577-585 (1998).
155. J. E. Geusic, H. M. Marcos, and L. G. Van Uitert, "Laser Oscillations in Nd-Doped Yttrium Aluminium, Yttrium Gallium And Gadolinium Garnets," Applied Physics Letters **4**, 182-184 (1964).
156. M. Tsunekane, T. Inohara, A. Ando, N. Kido, K. Kanehara, and T. Taira, "High Peak Power, Passively Q-switched Microlaser for Ignition of Engines," Quantum Electronics, IEEE Journal of **46**, 277-284 (2010).
157. J. R. O'Connor, "Unusual Crystal-Field Energy Levels and Efficient Laser Properties OF YVO_4:Nd," Applied Physics Letters **9**, 407-409 (1966).
158. G. M. Thomas and M. J. Damzen, "Passively Q-switched Nd:YVO_4 laser with greater than 11W average power," Opt. Express **19**, 4577-4582 (2011).
159. G. Huber, C. Kränkel, and K. Petermann, "Solid-state lasers: status and future [Invited]," J. Opt. Soc. Am. B **27**, B93-B105 (2010).
160. Y. F. Chen and Y. P. Lan, "Comparison between c-cut and a-cut Nd:YVO_4 lasers passively Q-switched with a Cr^{4+}:YAG saturable absorber," Applied Physics B: Lasers and Optics **74**, 415-418 (2002).
161. G. Muller and N. Neuroth, "Glass ceramic-a new laser host material," Journal of Applied Physics **44**, 2315-2318 (1973).
162. A. Ikesue, T. Kinoshita, K. Kamata, and K. Yoshida, "Fabrication and Optical Properties of High-Performance Polycrystalline Nd:YAG Ceramics for Solid-State Lasers," Journal of the American Ceramic Society **78**, 1033-1040 (1995).
163. A. Ikesue, "Polycrystalline Nd:YAG ceramics lasers," Optical Materials **19**, 183-187 (2002).
164. Y. Feng, J. Lu, K. Takaichi, K.-i. Ueda, H. Yagi, T. Yanagitani, and A. A. Kaminskii, "Passively Q-Switched Ceramic Nd3+:YAG/Cr4+:YAG Lasers," Appl. Opt. **43**, 2944-2947 (2004).
165. A. Ikesue and Y. L. Aung, "Ceramic laser materials," Nat Photon **2**, 721-727 (2008).
166. R. Lan, Z. Wang, H. Liu, H. Yu, L. Guo, L. Chen, S. Zhuang, X. Xu, and J. Wang, "Passively Q-switched Nd:YAG ceramic laser towards large pulse energy and short pulse width," Laser Physics **20**, 187-191 (2009).
167. I. Shoji, S. Kurimura, Y. Sato, T. Taira, A. Ikesue, and K. Yoshida, "Optical properties and laser characteristics of highly Nd^{3+}-doped $Y_3Al_5O_{12}$ ceramics," Applied Physics Letters **77**, 939-941 (2000).
168. A. Pirri, G. Toci, D. Alderighi, and M. Vannini, "Effects of the excitation density on the laser output of two differently doped Yb:YAG ceramics," Opt. Express **18**, 17262-17272 (2010).
169. J.-l. Li, K.-i. Ueda, M. Musha, L.-x. Zhong, and A. Shirakawa, "Radially polarized and pulsed output from passively Q-switched Nd:YAG ceramic microchip laser," Opt. Lett. **33**, 2686-2688 (2008).
170. O. Svelto, *Principles of Lasers*, 4 ed. (Plenum Press, New York, 1998).
171. E. Raikkonen, S. C. Buchter, and M. Kaivola, "Modeling the Time-Dynamics of Miniature Passively Q-switched Lasers," Quantum Electronics, IEEE Journal of **45**, 1563-1570 (2009).
172. L. F. Shampine and M. W. Reichelt, "The MATLAB ODE Suite," SIAM Journal on Scientific Computing **18**, 1-22 (1997).

173. J. J. Zayhowski, "Limits imposed by spatial hole burning on the single-mode operation of standing-wave laser cavities," Opt. Lett. **15**, 431-433 (1990).
174. Z. Xingyu, Z. Shengzhi, W. Qingpu, B. Ozygus, and H. Weber, "Modeling of diode-pumped actively Q-switched lasers," Quantum Electronics, IEEE Journal of **35**, 1912-1918 (1999).
175. T. R. Schibli, E. R. Thoen, F. X. Kärtner, and E. P. Ippen, "Suppression of Q-switched mode locking and break-up into multiple pulses by inverse saturable absorption," Applied Physics B: Lasers and Optics **70**(2000).
176. R. Grange, M. Haiml, R. Paschotta, G. J. Spühler, L. Krainer, M. Golling, O. Ostinelli, and U. Keller, "New regime of inverse saturable absorption for self-stabilizing passively mode-locked lasers," Applied Physics B: Lasers and Optics **80**, 151-158 (2005).
177. C. Inc, "CASIX Inc" (2011), retrieved 2011, http://www.casix.com/.
178. J. A. Armstrong, "Measurement of picosecond laser pulse widths," Applied Physics Letters **10**, 16-18 (1967).
179. D. J. Bradley and G. H. C. New, "Ultrashort pulse measurements," Proceedings of the IEEE **62**, 313-345 (1974).
180. K. Sala, G. Kenney-Wallace, and G. Hall, "CW autocorrelation measurements of picosecond laser pulses," Quantum Electronics, IEEE Journal of **16**, 990-996 (1980).
181. R. K. Jain, J. E. Brown, and W. P. Robinson, "Simple distortion-free real-time optical pulse correlator," Appl. Opt. **21**, 4073-4076 (1982).
182. Z. L. Liau, "Semiconductor wafer bonding via liquid capillarity," Applied Physics Letters **77**, 651-653 (2000).
183. G. Bonner, University of Strathclyde, Glasgow (personal communication, 2011).
184. ISO, "11146: Lasers and laser-related equipment - Test methods for laser beam widths, divergence angles and beam propagation ratios," (2005).